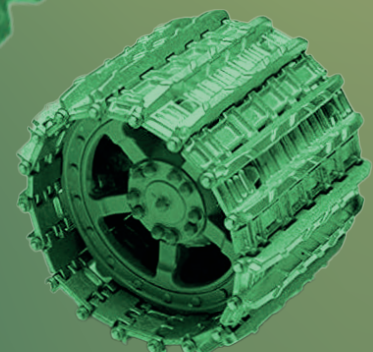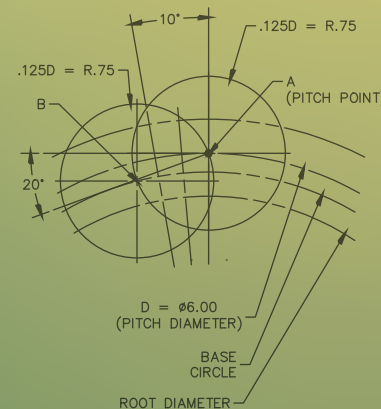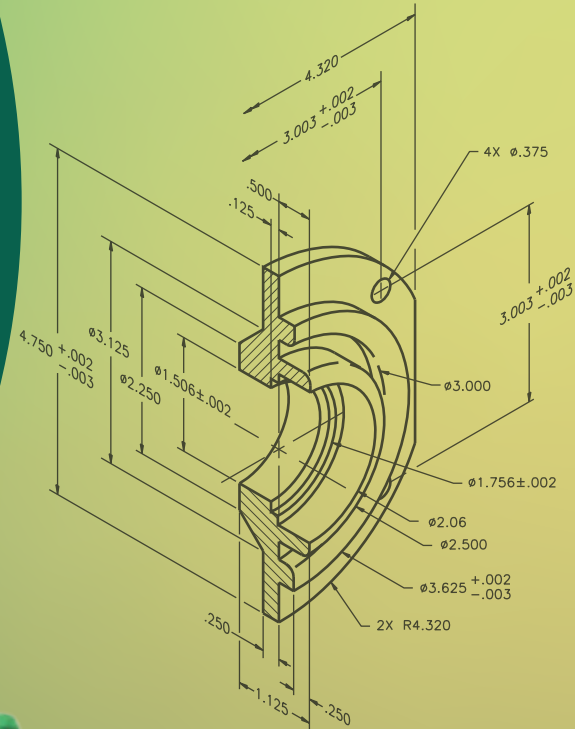June **2025**
Volume **9** · Issue **2**

Exploring Innovations in
Mechanical Science and Engineering

› Evaluation of tool radius and machining parameters on cutting forces and surface roughness for AA 6082 aluminum alloy

› Low velocity impact responses of symmetric and asymmetric curved foam core sandwich panels

› Unravelling quadcopter frame dynamics: A study on vibration analysis and harmonic response

› Microstructural investigation of geopolymer composites obtained from recyclable waste materials

An International Journal Covering Advances in
Mechanical Engineering and Applied Sciences

97726367450090

OPEN ACCESS

Indexed / Abstracted in:

TR-Dizin, EBSCO, Scilit, Index Copernicus, The Open Ukrainian Citation Index (OUCI), Paperity Open Science, Asian Science Citation Index

Aims and Scopes

European Mechanical Science (EMS) is an international, peer-reviewed journal that publishes full-length original research papers, and reviews related to all areas of Mechanical Engineering such as Solid Mechanics, Material, Automotive, Fluid Mechanics, Thermal, Engine and Power, Dynamics and Control, Robotics and Mechatronics, Transportation, Computational Mechanics, Design, Systems, Manufacturing, Biomedical, Process, and Aerospace published four times a year in March, June, September, and December. This is an open-access journal which means that all content is freely available without charge to the user or author's institution. EMS is a quarterly published journal operating an online submission and peer review system. It allows authors to submit articles online and track their progress via its web interface. This journal is a peer-reviewed open-access engineering journal published four times a year.

For inquiries and communication, please contact us at: emsjournal01@gmail.com

https://dergipark.org.tr/ems

Contents

– Research Articles

NO$_x$ conversion efficiency of an SCR system with V$_2$O$_5$-WO$_3$/TiO$_2$ catalyst and C$_2$H$_5$OH reductant: An experimental study

Erdi Tosun[1]* [ID]

[1]Çukurova University, Faculty of Engineering, Department of Automotive Engineering, 01250, Adana, Türkiye

Abstract: Internal combustion engines (ICEs) have long been the dominant power source in the transportation sector due to their high power-to-weight ratio. However, their widespread use poses significant environmental challenges, primarily due to the emission of harmful gases. To mitigate these emissions, stringent regulations necessitate the development of advanced after-treatment systems. In this study, a SCR (Selective Catalytic Reduction) system integrated with a diesel engine was investigated using V$_2$O$_5$-WO$_3$/TiO$_2$ as the catalyst and C$_2$H$_5$OH as the reductant. Engine tests were conducted under three different load conditions -no load (0 kW), 2 kW, and 4 kW- within an exhaust temperature range of 150-240 °C. NO$_x$ conversion efficiency was evaluated with respect to engine load and temperature variations. Additionally, catalyst characterization was performed using Energy-Dispersive X-ray Spectroscopy (EDS), Scanning Electron Microscopy (SEM), Brunauer-Emmett-Teller (BET), and X-ray Diffraction (XRD) analyses. The results indicate that increasing engine load and exhaust gas temperature enhances , likely due to the higher hydrocarbon (HC) content in the exhaust at increased load levels and improved catalytic activity at elevated temperatures. The highest of 93.28% was achieved at 4 kW and 240°C.

Keywords: diesel engine; emission; NO$_x$; selective catalytic reduction.

1. Introduction

Internal combustion engines (ICEs) have been the primary power source for the transportation sector for decades but they pose significant challenges to environmental sustainability. Despite their dominance, largely due to their high power-to-weight ratio, one of the most critical issues associated with these engines is the release of harmful gases as byproducts of combustion. These emissions are regulated through stringent emission standards that compel manufacturers to keep them within permissible limits.

The combustion of fossil fuels plays a major role in environmental degradation, releasing pollutants such as carbon dioxide (CO$_2$), carbon monoxide (CO), hydrocarbon (HC), oxides of nitrogen (NO$_x$), particulate matter (PM) and other harmful gases [1,2]. Among all these emissions, NO$_x$ is a significant emission produced by ICEs that has harmful impacts on both human health and the environment. Reducing NO$_x$ emissions is therefore of critical importance [3]. Therefore, strict regulations and various reduction methods are being imple-

mented to mitigate their adverse effects.

NO$_x$ emissions can be reduced through effective methods like Exhaust Gas Recirculation (EGR), Lean NO$_x$ Trap (LNT), Selective Catalytic Reduction (SCR), or by using water-emulsified fuels without engine modification [4]. SCR is one of the most critical technologies for reducing NO$_x$ emissions as it introduces a reductant into the exhaust stream where it reacts with NO$_x$ in the presence of a catalyst to form harmless products. SCR systems are classified by the reductant used. As the most popular and commercialized one, Urea-SCR systems are designed with the target of reducing NO$_x$ emissions by injecting AdBlue (a solution of 32.5% urea and 67.5% deionized water) as reductant into the exhaust gases. Urea (CO(NH$_2$)$_2$) is subjected to thermal decomposition, producing gaseous ammonia (NH$_3$) and isocyanic acid (HNCO) at higher exhaust temperature levels. NH$_3$ produced from CO(NH$_2$)$_2$ as a precursor acts as the active reductant and reacts with NO$_x$ to produce harmless nitrogen (N$_2$) and water (H$_2$O). AdBlue is preferred over pure ammonia because it is safer to store and less toxic, making it more suitable for passenger ve-

hicles. On the other hand, the V_2O_5-WO_3/TiO_2 catalyst is used in commercialized Adblue systems as a catalyst [5,6]. Unfortunately, NH_3 negatively impacts both the environment and human health, causing toxicity, corrosion, undesirable odor, eye irritation, and respiratory issues. To address these challenges, researchers have directed their efforts toward both the development of catalysts and also the investigation of alternative reductants. [7].

Besides NH_3, various reducing gases like HCs, CO, and hydrogen (H_2) are being studied as potential SCR reductants for the removal of NO_x from the exhaust stream [8]. HC examples include methane (CH_4), iso-propanol (C_3H_8O), octane (C_8H_{18}), and pentane (C_5H_{12}) [9]. With HCs as reductants in SCR systems, an effective solution is provided to problems related to NH_3, such as NH_3 slip, the need for large urea tanks, and the complexity and cost of the injection system [10].

Upon reviewing the literature, it has been observed that HCs are widely used as reductants in various studies. Keskin [11] investigated the NO_x conversion performance of the SCR system with Ce/TiO_2 and Au-doped Ce/TiO_2 catalysts in real exhaust conditions. Low temperature characteristics of the catalysts were evaluated under 200-300 °C temperature intervals. The results indicated that Ce/TiO_2 catalysts were more effective at reducing NO_x than Au-Ce/TiO_2 catalysts. The addition of Au decreased the catalyst's surface properties, leading to reduced activity in the Au-Ce/TiO_2 catalysts. Ahmad et al. [12] studied the low exhaust gas temperature performance of an SCR system utilizing ethanol (C_2H_5OH)/H_2O blends with different ratios (100% C_2H_5OH (E), 96% C_2H_5OH + 4% H_2O (E4W), 92% C_2H_5OH + 8% H_2O (E8W)) as reductants. The results were also evaluated with respect to two different space velocity (SV) values (20000 h^{-1}, and 40000 h^{-1}). Increased engine load caused to slight rise in NO_x conversion rates. %68 as the highest NO_x conversion rate was obtained with the use of 100% C_2H_5OH as reductant. Furthermore, it was determined that adding H_2O to C_2H_5OH negatively impacts NO_x conversion rates. Özarslan [13] utilized an Ag-Ni-TiO_2/Cordierite catalyst in a C_2H_5OH-SCR system for the purpose of NO_x reduction in a compression ignition engine. NO_x reduction measurements were performed within the temperature range of 190 to 270 °C, at intervals of 20 °C. The tests were conducted with engine loads of 1 kW and 3 kW, and a SV of 30000 h^{-1}. It was shown that the Ag-Ni-TiO_2/Cordierite catalyst, using C_2H_5OH as a reductant, achieved 93.8% efficiency of NO_x conversion () at 270 °C and 3 kW. Kass et al. [14] aimed to reduce NO_x emissions from a diesel engine using a C_2H_5OH-SCR system. NO_x reductions of 90% and 80% were achieved at SVs of 21000 h^{-1} and 57000 h^{-1}, respectively, within a catalyst temperature range of 360 - 400 °C. The study revealed that C_2H_5OH was quickly converted to acetaldehyde by the silver-loaded alumina catalyst. However, significant amounts of acetaldehyde bypassed the catalyst at an SV of 57,000 h^{-1}. Gu et al. [15] assessed the H_2

addition effects on via HC-SCR system with different reductants at low temperature values. In this study, H_2 has been employed in HC-SCR systems to improve NO_x conversion efficiencies, especially at low temperatures between 245°C and 315°C. The tests were conducted at temperatures below 315°C using a 2.5 wt.% Ag/Al_2O_3 catalyst. Propene (C_3H_6), heptane (C_7H_{16}), and dodecane ($C_{12}H_{26}$) were employed as reductants in the tests to assess the impact of various chemical structures and chain lengths. C_7H_{16} showed the highest of 43% at 315°C without H_2. However, with the addition of H_2, $C_{12}H_{26}$ achieved the greatest efficiency, reaching 58% at the same temperature. In the engine experiments, it was found that using diesel fuel as the reductant led to a maximum of 79% at 315°C and 76% at 245°C. Dong et al. [16] investigated the NO_x reduction performance of a C_2H_5OH -based SCR system using Ag/Al_2O_3 catalysts in both engine bench and real-road exhaust conditions. High NO_x conversion (up to 90%) was observed between 350 - 450 °C under controlled test bench conditions, whereas in real-road bus demonstrations, conversion efficiency dropped below 15%. The results highlighted that sulfur poisoning and catalyst thermal inertia significantly affected catalyst performance. Additionally, the Ag/Al_2O_3 catalyst reduced soluble organic fractions in PM emissions but showed minimal effect on dry soot and variable effects on sulfate formation depending on temperature. Kruczyński et al. [17] evaluated the NO_x reduction performance of metal-based catalysts (Cu, Ag, Au) supported on Al_2O_3–SiO_2 carriers using C_3H_6 as the reducing agent under real diesel exhaust conditions. Catalysts were evaluated for NO, NO_2, and HC conversion, as well as CO and N_2O formation. All catalysts achieved nearly 100% NO_2 and C_3H_6 conversion, but NO conversion was highest with Ag/Al_2O_3–SiO_2 (81%) at around 480 °C. The Ag-based catalyst also showed the lowest N_2O formation compared to Au and Cu variants. The study concluded that although metals on acidic supports can be effective, their full application in low-temperature NO_x control remains limited.

In this study, engine tests were conducted on a SCR system coupled with a diesel engine using V_2O_5-WO_3/TiO_2 as the catalyst and C_2H_5OH as the reductant. were determined by calculating the NO_x reduction rates under three different engine load conditions as no load (0 kW), 2 kW, and 4 kW within an exhaust temperature range of 150-240°C. Catalyst characterization was also achieved via Energy-Dispersive X-ray Spectroscopy (EDS), Scanning Electron Microscopy (SEM), Brunauer-Emmett-Teller (BET), and X-ray diffraction (XRD) analyses.

2. Materials and Methods

The engine tests were conducted in the Engine Test Laboratory while the catalyst preparation processes were carried out in the Fuel Analysis Laboratory, both located within the Automotive Engineering Department of Çukurova University. In addition, the catalyst

characterization tests were performed in the Central Research Laboratory of Çukurova University.

2.1. Preparation of Catalyst

In the SCR system used for NO_x reduction purpose, V_2O_5-WO_3/TiO_2 was employed as the catalyst and C_2H_5OH was used as the reducing agent.

The SCR catalyst was synthesized through the conventional wet impregnation method, following a previously reported study by Keskin et al. [18] with certain modifications. The cordierite was used as the main carrier structure in catalyst production. Initially, a pre-treatment was applied using a solution containing 250 g of oxalic acid and 500 mL of distilled water to enhance the surface area providing extra binding sites for catalytic materials. This treatment was carried out using a heated magnetic stirrer at a temperature range of 95-100°C for about 4 hours. Subsequently, a washing step was performed with distilled water until the pH reached approximately 7 which corresponds to a neutral condition. In the next step, a drying process was carried out at 120 °C using a furnace. Finally, specimens were exposed to the calcination process at 550 °C for 2 hours to get rid of impurities.

V_2O_5-WO_3/TiO_2 catalyst includes V_2O_5, WO_3, and TiO_2 with molar ratios of 1.62, 1, and 45.41, respectively [19], and the preparation of the catalyst began by mixing the materials in these molar ratios and corresponding weights in 300 mL of distilled water using an ultrasonic stirrer for 15 minutes. Then, the mixture was transferred to a heater, and the stirring process continued until the water contained in the mixture evaporated. The resulting mud-like structure was dried at 120°C for 1 hour, then subjected to calcination at 500°C for 1 hour using a muffle furnace. The obtained structure was ground into a powder. The powder catalyst was mixed with 10% of its weight in colloidal silica and stirred for 1 hour in 300 mL of water using a magnetic stirrer to improve binding between materials. Then, the cordierite structure was immersed in this mixture to ensure it was fully wet. Next, drying was applied in an oven at 120°C for 1 hour. The impregnation subsequent drying process was repeated three times consecutively. At last, the cordierite coated with catalyst material was prepared through calcination at 500°C for 3 hours.

The entire process can be summarized in three main stages: cordierite pre-treatment, production of powdered catalyst, and catalyst-coated cordierite production.

2.2. Characterization of Catalyst

The chemical characterization and the surface morphologies of the catalysts were analyzed using EDS and SEM techniques, respectively, with an FEI brand Quanta 650 FEG SEM device. Additionally, the measurement of the catalysts' surface area was based on the BET theory via N_2 gas adsorption analysis using a Sorptometer 1042 instrument. On the other hand, the crystallographic properties were evaluated using XRD analysis. This analysis was performed with the PANalytical Empyrean XRD device.

2.3. Test Rig and Experiments

Load and emission tests were done in 2 cylinders, water-cooled compression ignition engine. The technical specifications of the test engine are summarized in ▶**Table 1**. The test set-up was schematized in the following ▶**Figure 1**. In tests, diesel was utilized as fuel and values were evaluated using V_2O_5-WO_3/TiO_2 catalyst and C_2H_5OH as a reductant under engine loads of 0 kW, 2
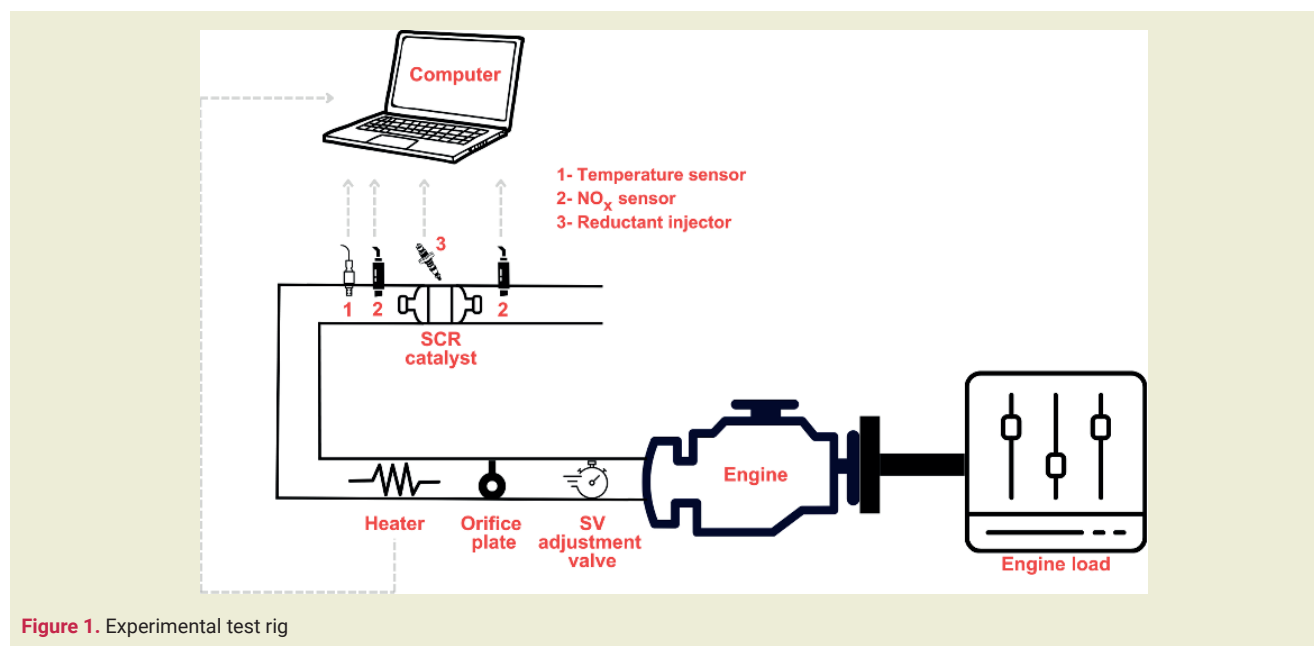
Figure 1. Experimental test rig

kW, and 4 kW. These load values were obtained from a 10 kW electrically controlled loading unit based on current and voltage measurements. As seen in ▶**Figure 1**, the exhaust flow rate required for SV determination (the ratio of exhaust flow rate to the volume of catalyst) is adjusted via an orifice, while the exhaust temperature is regulated using a heater in the exhaust line. The tests were also conducted at temperatures from 150 °C to 240 °C with 10 °C increments and an SV value of 40000 h^{-1}. A K-type thermocouple is installed immediately before the SCR to measure the exhaust temperature. Additionally, Continental UniNO$_x$ sensors are placed both before and after the SCR to determine calculated with the following formula:

$$\eta_{NO_x} = \frac{\left(NO_{x_{in}} - NO_{x_{out}}\right)}{NO_{x_{in}}} \, x \, 100 \tag{1}$$

Table 1. Engine specifications

Brand / Model	AKSA / A2CRX08
Number of cylinders	2
Engine speed	3000 rpm
Cylinder volume	830 cm³
Bore / Stroke	80 / 79 mm
Compression ratio	23/1
Cooling	Water-cooled

3. Results and Discussions

3.1. Catalyst Characterization Results

SEM-EDS analysis was conducted to evaluate the micromorphology and surface structure of the catalyst, revealing that the surfaces were coated with catalytic elements. ▶**Figure 2** illustrates the surface morphology of the catalyst coated cordierite structure with 5000x/10000x magnifications. The porous structure of cordierite can easily be seen from the images. The catalyst material is distributed within an irregular structure of cordierite.

The elemental overlay was determined by EDS analysis as shown in ▶**Figure 3** and the distribution of elements contained in the catalyst can be seen. Total EDS imaging identified two predominant colors: yellow and turquoise, representing Si and Ti, respectively. Elemental distribution analysis determined the proportions of Si, Al, O, Mg, Ti, W, and V as 34%, 8%, 13%, 4%, 33%, 2%, and 7%, respectively.

XRD analysis was used to characterize the catalysts, exploring the crystallization and distribution of catalytic elements on the cordierite surface. As a result of the XRD analysis, it was determined that cordierite has an orthorhombic crystal structure, anatase and vanadium have a tetragonal crystal structure, and tungsten has a monoclinic crystal structure. As can be seen in ▶**Figure 4**, each chemical used in catalyst production has dis-
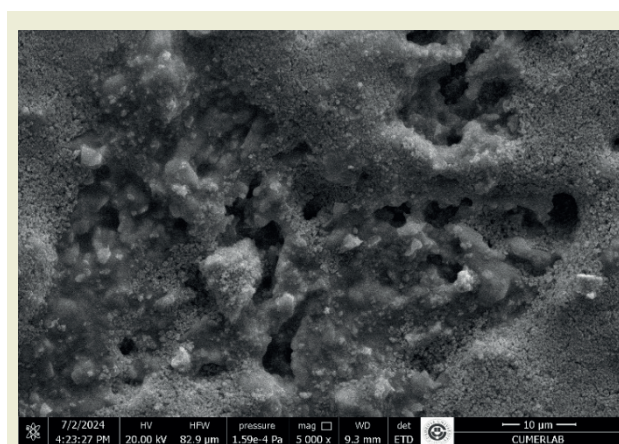
(a)
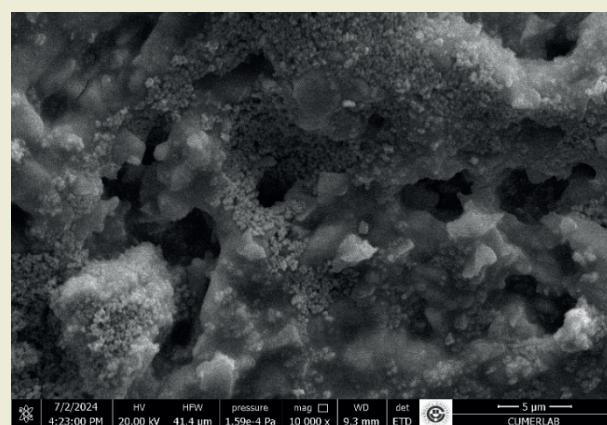
(b)

Figure 2. SEM results of V$_2$O$_5$-WO$_3$/TiO$_2$ catalyst/cordierite structure (a) 5000x (b) 10000x
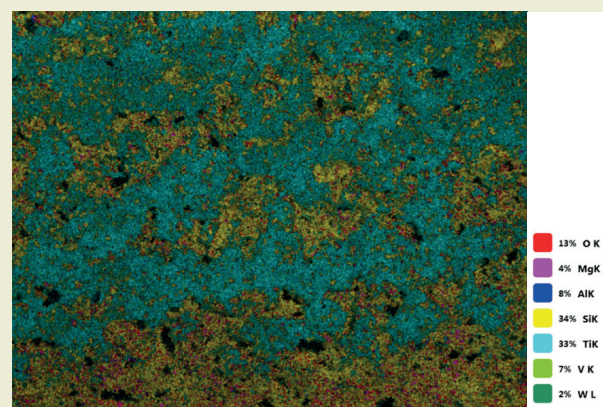
Figure 3. Elemental overlay of V$_2$O$_5$-WO$_3$/TiO$_2$ catalyst/cordierite structure through EDS analysis

tinct characteristic peaks at specific angles. In the pattern, the characteristic diffraction peaks of cordierite were determined at 10.33, 18.01, 21.63, 26.27, 28.34, 29.35, 33.79, and 54.15° (Ref. Code: 98-007-5635), consistent with earlier studies [20, 21]. The characteristic peaks of anatase were observed at 25.22, 36.87, 38.43, and 47.97 (Ref. Code: 98-000-9853). Similar peaks were also observed in previous studies [22, 23]. The peaks corresponding to vanadium and tungsten were detected at 36.87°, 39.44°, 54.99°, 64.32°, and 69.59°
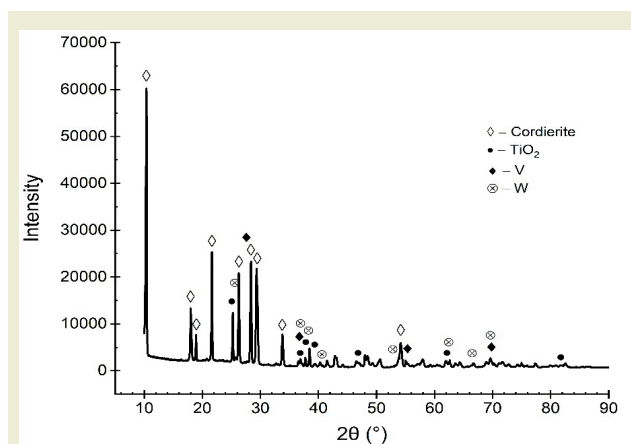
Figure 4. XRD results of V_2O_5-WO_3/TiO_2 catalyst/cordierite structure

Figure 5. versus temperature at various engine loads

(Ref. Code: 98-023-7337), and at 25.77°, 36.87°, 37.72°, 41.47°, 57.87°, and 69.59° (Ref. Code: 98-008-0829), respectively. These peaks exhibit relatively low diffraction intensities, indicating that the active metal species are highly dispersed on the catalyst surface [24, 25].

BET surface area is generally crucial for catalyst performance, as a larger surface area increases active sites, enhances component dispersion, and promotes reactant adsorption, thereby improving catalytic activity. BET analysis revealed that the surface area of the catalyst was found as 43.58 m^2/g, while the cordierite surface area was nearly 0.5 m^2/g. The approximately 87 times increase in active surface area significantly enhances catalytic activity.

3.2. NO$_x$ Conversion Efficiency Results

The of the catalyst was evaluated with respect to varying engine load and temperature as illustrated in ▶**Figure 5**. In tests, the 0 kW case was compared with 2 kW and 4 kW load conditions. The tests were repeated with exhaust gas temperatures ranging from 150 °C to 240 °C rising in increments of 10 °C. It is obvious that an increase in engine load and exhaust gas temperature cause to obtain higher . As the engine load increases, HC content in the exhaust gases also rises. Due to their reducing properties, HCs contribute to the NO$_x$ conversion process that improve [6,26]. Besides that, the increase in exhaust gas temperature clearly demonstrates a positive effect on . This may possibly be explained by the fact that higher exhaust temperatures enhance catalytic activity, leading to improved conversion efficiency [10]. Within the 150-240 °C temperature range, average values of 87.98%, 90.4%, and 91.41% were achieved under no-load, 2 kW, and 4 kW conditions, respectively. The average values at 2 kW and 4 kW loads resulted in a 2.75% and 3.9% improvement in compared to the 0 kW condition. The highest was achieved at 240 °C compared to lower temperature values under all load conditions. Furthermore, the highest of 93.28% was observed at 4 kW and an exhaust temperature of 240°C.
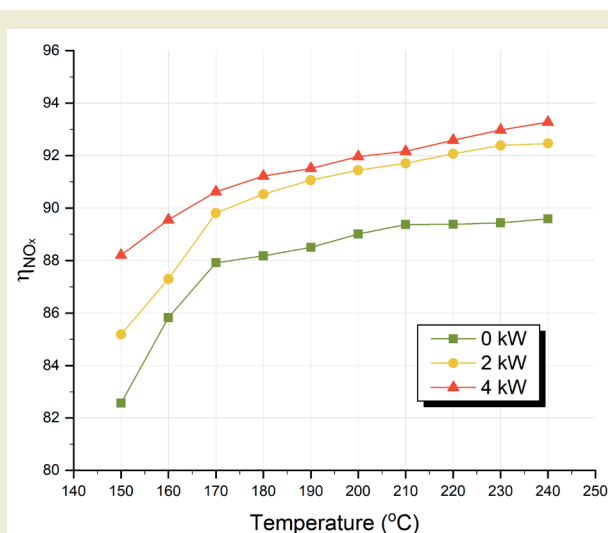
4. Conclusions

At the conclusion of the study, the following findings were made:

- SEM-EDS analysis confirmed the successful coating of the catalyst on the cordierite surface.

- Elemental distribution identified Si, Ti, Al, O, Mg, W, and V as the main components.

- XRD analysis revealed that cordierite has an orthorhombic crystal structure, anatase and vanadium have a tetragonal structure, and tungsten has a monoclinic structure.

- BET analysis showed a significant increase in surface area from 0.5 m^2/g (cordierite) to 43.58 m^2/g (catalyst), enhancing catalytic activity.

- Increasing engine load and exhaust gas temperature improved .

- The highest (93.28%) was achieved at 4 kW load and 240°C conditions.

Research ethics

Not applicable.

Author contributions

The author solely conducted all stages of this research.

Competing interests

The author state(s) no conflict of interest.

Research funding

None declared.

Data availability

Not applicable.

Peer-review

Externally peer-reviewed.

Orcid

Erdi Tosun (iD) https://orcid.org/0000-0001-5733-2047

References

[1] Yu, J., Feng, R., Wang, S., & Deng, B. (2024). The influence of particle oxidation catalyst (POC) mode on emissions reduction of a turbo-charging non-road diesel under wide operating conditions. Thermal Science and Engineering Progress, 47, 102357. https://doi.org/10.1016/j.tsep.2023.102357

[2] Sonachalam, M., Manieniyan, V., Senthilkumar, R., Ramis, M.K., Warimani, M., Kumar, R., Kedia, A., Yunus Khan, T.M., & Almakayeel, N. (2024). Experimental investigation of performance, emission, and combustion characteristics of a diesel engine using blends of waste cooking oil-ethanol biodiesel with MWCNT nanoparticles. Case Studies in Thermal Engineering, 61, 105094. https://doi.org/10.1016/j.csite.2024.105094

[3] Tosun, E., & Özcanlı, M. (2021). Hydrogen enrichment effects on performance and emission characteristics of a diesel engine operated with diesel-soybean biodiesel blends with nanoparticle addition. Engineering Science and Technology, an International Journal, 24(3), 648-654. https://doi.org/10.1016/j.jestch.2020.12.022

[4] Çalık, A., Tosun, E., Akar, M.A., & Özcanlı, M. (2023). Combined effects of hydrogen and TiO2 nanoparticle additive on terebinth oil biodiesel operated diesel engine. Science and Technology for Energy Transition (STET), 78(9), 1-6. https://doi.org/10.2516/stet/2023007

[5] Scicluna, T., & Farrugia, M. (2024). Experimental investigation of an Adblue® injection system and implementation on a dual-fuel (diesel/lpg) engine. 21st Int. Conf. Mechatronics - Mechatronika, IEEE 1-8. https://doi.org/10.1109/ME61309.2024.10789645

[6] Yakaryılmaz A.C., & Özgür, T. (2024). NOx emission reduction through selective catalytic reduction using copper-based Y zeolite catalyst: experimental investigation and characterization. International Journal of Automotive Engineering and Technologies, 13(3), 84-90. https://doi.org/10.18245/ijaet.1453469

[7] Sümer, Ş.U.H., Keiyinci, S., Keskin, A., Özarslan, H., & Keskin, Z. (2023). The effect of fusel oil as a reductant over the multi-metallic catalyst for selective catalytic reduction of NOx in diesel exhaust at low-temperature conditions. Petroleum Science and Technology, 41(20), 1901-1917. https://doi.org/10.1080/10916466.2022.2097262

[8] Keskin, Z., Özgür, T., Özarslan, H., & Yakaryılmaz, A.C. (2021). Effects of hydrogen addition into liquefied petroleum gas reductant on the activity of Ag-Ti-Cu/Cordierite catalyst for selective catalytic reduction system. International Journal of Hydrogen Energy, 46(10), 7634-7641. https://doi.org/10.1016/j.ijhydene.2020.11.200

[9] Chen, Z., Liu, Q., Liu, H., & Wang, T. (2024). Recent advances in SCR systems of heavy-duty diesel vehicles—low-temperature NOx reduction technology and combination of SCR with remote OBD. Atmosphere, 15(3), 997. https://doi.org/10.3390/atmos15080997

[10] Keskin, Z. (2021). The effect of H2O on the use of ethanol as reductant in the SCR system. European Mechanical Science, 5(1), 34-38. https://doi.org/10.26701/ems.780324

[11] Keskin, Z. (2021). Investigation of deactivation effect of Au addition to Ce/TiO2 catalyst for selective catalytic reduction using real diesel engine exhaust samples at low temperature conditions. Journal of Chemical Technology & Biotechnology, 96(8), 2275-2282. https://doi.org/10.1002/jctb.6753

[12] Ahmad, M.A.C.M., Keskin, A., Özarslan, H., & Keskin, Z. (2024). Properties of ethyl alcohol-water mixtures as a reductant in a SCR system at low exhaust gas temperatures. Energy Sources, Part A: Recovery, Utilization, and Environmental Effects, 46(1), 5584-5595. https://doi.org/10.1080/15567036.2020.1733142

[13] Özarslan, H. (2024). Preparation and NOx reduction performance of Ag-Ni-TiO2/Cordierite catalyst for HC-SCR system. Cukurova University Journal of the Faculty of Engineering, 39(2), 339-347. https://doi.org/10.21605/cukurovaumfd.1514048

[14] Kass, M.D., Thomas, J.F., Lewis, S.A., Storey, J.M., Domingo, N., Graves, R.L., Panov, A., & Park, P. (2003). Selective catalytic reduction of NOx emissions from a 5.9 liter diesel engine using ethanol as a reductant. SAE Transactions Journal of Fuels and Lubricants, 112(4), 2584-2593. https://doi.org/10.4271/2003-01-3244

[15] Gu, H., Chun, K.M., & Song, S. (2015). The effects of hydrogen on the efficiency of NOx reduction via hydrocarbon-selective catalytic reduction (HC-SCR) at low temperature using various reductants. International Journal of Hydrogen Energy, 40(30), 9602-9610. https://doi.org/10.1016/j.ijhydene.2015.05.070

[16] Dong, H., Shuai, S., Zhang, W., Li, R., Wang, J., Shi, X., & He, H. (2007). An Ethanol SCR for NOx Purification: Performance Evaluation on Engine Bench and Demonstration on Bus. SAE Technical Paper, 2007-01-1240. https://doi.org/10.4271/2007-01-1240

[17] Kruczyński, S.W., Orliński, P., & Ślęzak, M. (2022). The comparative analysis of catalytic properties of Group 11 elements in NOx reduction by hydrocarbons in the presence of oxygen. Eksploatacja i Niezawodnosc – Maintenance and Reliability, 24(1), 170-176. https://doi.org/10.17531/ein.2022.1.19

[18] Keskin, A., Yaşar, A., Candemir, O.C., & Özarslan, H. (2020). Influence of transition metal based SCR catalyst on the NOx emissions of diesel engine at low exhaust gas temperatures. Fuel, 273, 117785. https://doi.org/10.1016/j.fuel.2020.117785

[19] Long, Y., Su, Y., Xue, Y., Wu, Z., & Weng, X. (2021). $V_2O_5-W_O3/TiO_2$ catalyst for efficient synergistic control of NOx and chlorinated organics: insights into the arsenic effect. Environmental Science & Technology, 55(13), 9317-9325. https://doi.org/10.1021/acs.est.1c02636

[20] Keskin, Z. (2021). Enhancing of low-temperature OHC-SCR activity of Ag/TiO2 with addition of MnO2 nanoparticles, and performance evaluation using diesel engine exhaust gases. Environmental Technology & Innovation, 21, 101205. https://doi.org/10.1016/j.eti.2020.101205

[21] Li, F., Shen, B., Tian, L., Li, G., & He, C. (2016). Enhancement of SCR activity and mechanical stability on cordierite supported $V_2O_5-W_O3/TiO_2$ catalyst by substrate acid pretreatment and addition of silica. Powder Technology, 297, 384-391. https://doi.org/10.1016/j.powtec.2016.04.050

[22] Dong, G., Zhao, Y., & Zhang, Y. (2014). Preparation and performance of V-Wreparation and performance of V-W/x(Mn-Ce-Ti)/y(Cu-Ce-Ti)/cordierite catalyst by impregnation method in sequence for SCR reaction with urea. Journal of Fuel Chemistry and Technology, 42(9), 1093-1101. https://doi.org/10.1016/S1872-5813(14)60044-X

[23] Pang, L., Fan, C., Shao, L., Yi, J., Cai, X., Wang, J., Kang, M., & Li, T. (2014). Effect of V_2O_5/W_O3TiO_2 catalyst preparation method on NOx removal from diesel exhaust. Chinese Journal of Catalysis, 35(12), 2020-2028. https://doi.org/10.1016/S1872-2067(14)60218-7

[24] Chen, M., Zhao, M., Tang, F., Ruan, L., Yang, H., & Li, N. (2017). Effect of Ce doping into $V_2O_5-W_O3/TiO_2$ catalysts on the selective catalytic reduction of NOx by NH_3. Journal of Rare Earths, 35(12), 1206-1215. https://doi.org/10.1016/j.jre.2017.06.004

[25] Yu, B., Liu, X., Wu, S., Yang, H., Zhou, S., Yang, L., & Liu, F. (2024). Study on Novel SCR Catalysts for Denitration of High Concentrated Nitrogen Oxides and Their Reaction Mechanisms. Catalysts, 14(7), 406. https://doi.org/10.3390/catal14070406

[26] Reşitoğlu, İ.A., Keskin, A., Özarslan, H., & Bulut, H. (2019). Selective catalytic reduction of NOx emissions by hydrocarbons over Ag–Pt/Al2O3 catalyst in diesel engine. International Journal of Environmental Science and Technology, 16, 6959-6966. https://doi.org/10.1007/s13762-019-02266-x

Research Article

Data-driven optimization of MIG welding: A synergistic approach for superior joint quality

Raviram R[1]* iD, Ranjith Raj A[1] iD, Shashang G[1] iD, Shameer Mohamed S[1] iD

[1]Department of Mechanical Engineering, Sri Venkateswara College of Engineering, Sriperumbudur, Tamil Nadu, India

Abstract: A data-driven approach was applied in this research to determine input parameters for producing high-quality welds in mild steel sheets. By utilizing an L16 orthogonal array, the signal-to-noise (S/N) ratio and analysis of variance (ANOVA) techniques were used to optimize weld characteristics. The Multi-Objective Optimization based on Ratio Analysis (MOORA) method was used to rank these conflicting objectives according to their importance in different scenarios. From principal component analysis (PCA), setting the voltage at 42V, welding current at 250A, wire feed rate at 8 mm/min, and gas flow rate at 15 L/min results in ideal characteristics: penetration of 2.961 mm, reinforcement of 5.658 mm, bead width of 12.753 mm, and dilution percentage of 4.183%. Through the MOORA method, it was determined that a voltage of 40V, welding current of 175A, wire feed rate of 4 mm/min, and gas flow rate of 10 L/min would yield optimal weld bead geometry with penetration of 0.884 mm, reinforcement of 6.489 mm, bead width of 11.715 mm, and dilution percentage of 1.218%. This study effectively optimized welding parameters for superior welding in sheet metal fabrication for small and medium-sized enterprises.

Keywords: MIG, Taguchi method, MOORA method, PCA, analysis of variance, optimization

1. Introduction

Many small-scale and medium-scale industries utilize Metal Inert Gas (MIG) welding to manufacture sheet metal components. However, there is a need to utilize the design of experiments to identify the optimum process parameters for improved welding. In MIG welding, heat is applied to fuse a consumable electrode and the base plate metal, which then solidify together to form a robust joint. Mild steel is a readily accessible material, reasonably priced, and finds extensive use in numerous engineering applications [1]. This welding technique offers numerous benefits, including reasonable production speed, optimal cost of the product, strength, and improved surface quality [2,3]. The Metal Inert Gas (MIG) welding process is also referred to by way of Gas Metal Arc Welding (GMAW) [3]. In this procedure, metallic components are melted through the application of heat by an electric arc, while utilizing a consumable wire electrode. The welding gun consistently feeds the filler wire into the weld pool, facilitating the joining of the main materials [4]. A shielding atmosphere, comprising carbon dioxide gas, is established in the working area to safeguard the weld deposit from contaminants [5].

Hot-rolled mild steel has been utilized as the base metal for this study. This material finds use in structural components, railways, agricultural equipment, and various components in machinery and equipment. The voltage, current, wire filler rate, and gas flow rate have important effects on weld joints [6-9].

2. Experiment and Methods

The MIG welding process utilized a Toshweld MIG 400IJ DC inverter source (±2A current stability) and an IGBT Module wire feeder. The gas cylinder was fitted with a gas flow meter (±0.1 L/min). For the experiment, mild steel sheet metal (IS 2062 GR E250) of 2 mm thickness was cut to the desired dimensions of 28×150mm using a punching machine. Plate surfaces were cleaned using wire brushes and emery paper to eliminate any rust. A single bead was then applied to two clean plates using 1.2 mm diameter copper-coated mild steel wire (ER70S-6) while maintaining a pure carbon dioxide gas flow rate and positive electrode polarity to form a butt joint. The chemical compositions of the base material are detailed in ▶Table 1, while those of the wire can be found in ▶Table 2. All experimental analyses were conducted utilizing Minitab software (version 21.4.2) (RRID:SCR_014483). ▶Figure 1 illustrates the weld bead geometry.

Table 1. Chemical composition of E250

C	Mn	Si	P	S
0.2	1.5	0.04	0.04	0.04

Table 2. Chemical composition of ER70S-6

C	Mn	Si	P	S	Ni	Cr	Mo	V	Cu
0.08	1.625	0.975	0.009	0.035	0.15	0.15	0.15	0.03	0.5

Area A = added metal
Area B = base metal melted
%Dilution = [B/(A+B)] x100
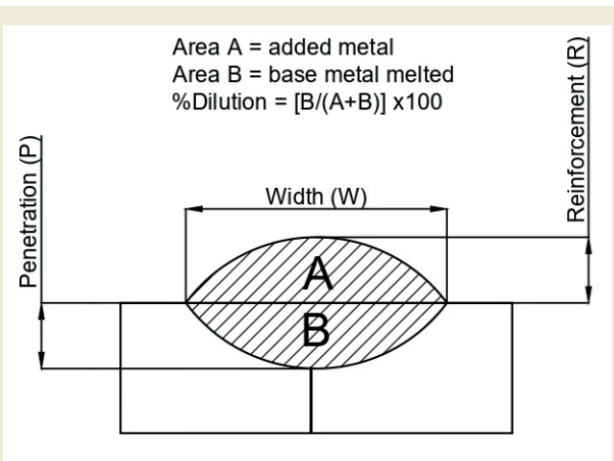
Figure 1. Weld bead geometry

centage by examining the melted areas of both the base material and the material utilized for weld bead height. Detailed results are presented in ▶**Table 4**, while ▶**Figure 2** illustrates the weld bead specimens.

Figure 2. Welded specimens

2.1. Selection of process parameters

In order to establish the extent of the input variables, experimental welds were conducted. The key characteristics analyzed for this study include voltage, welding current, gas flow rate, and wire feed speed [6-9]. ▶**Table 3** presents the specific input variables by their corresponding levels.

Table 3. Levels of process parameters

Parameters	Level 1	Level 2	Level 3	Level 4
Voltage V, V	40	42	44	46
Current I, A	175	200	225	250
Wire feed rate S, mm/min	4	6	8	10
Gas flow rate G, lpm	10	15	20	25

2.2. Orthogonal array and recording of data

Table 4 presents data showing that sixteen experiments in total were carried out using an L16 orthogonal array. These experiments were carried out randomly to avoid any potential inaccuracies associated with a systematic testing approach [10]. Following the completion of the welding process, cross-sections from the optimal section, typically the middle, of each welded sample were obtained. The weld beads were subsequently analyzed with an Epson L3150 image scanner (5760 × 1440 dpi resolution), which was used to capture individual measurements from the scans. ImageJ software (1:54i03 version) was utilized to determine the dilution per-

2.3. Taguchi Method

The Taguchi technique is an effective tool designed for solving issues that can significantly reduce the cost and duration of experiments while improving the performance of the system, layout, procedure, and product [11]. This approach, which blends the concepts of quality loss function and experimental design theory, has been used in the manufacturing sector to solve a number of challenging issues and carry out reliable process and product design. Additionally, this method identifies the characteristics that have the greatest impact on the total performance.

The Taguchi approach yields optimal parameters for the process that are not affected by variations in the surrounding conditions or other noise elements [12]. As the process variables rise, so does the number of experiments. The Taguchi technique uses an orthogonal array arrangement for analyzing the complete process parameters with a restricted number of experiments in order to overcome this complexity. For evaluating quality attributes, S/N ratio is utilized in Taguchi method. The mean (or desired value) of the output characteristics, is represented by the phrase "signal," and the unwanted value, or the square of the deviation, is represented by the term "noise." Consequently, the ratio of mean to the square of the deviation is known as the S/N ratio [13–18]. In the examination of the (Signal/Noise) ratio, Taguchi establishes three categories of quality characteristics, i.e. the lower-the-better, the larg-

Table 4. Layout of L16 orthogonal array with experiment values

No.	V	I	S	G	Penetration, mm	Reinforcement, mm	Bead Width, mm	Dilution Percentage
1	40	175	4	10	0.884	6.489	11.715	1.218
2	40	200	6	15	0.775	5.117	9.38	1.292
3	40	225	8	20	0.548	4.173	7.373	1.254
4	40	250	10	25	1.04	3.405	13.023	2.659
5	42	175	6	20	1.733	6.879	11.058	2.092
6	42	200	4	25	1.25	6.127	13.9	1.716
7	42	225	10	10	1.491	5.529	13.046	2.245
8	42	250	8	15	2.961	5.658	12.753	4.183
9	44	175	8	25	1.767	7.124	13.831	2.103
10	44	200	10	20	1.096	7.258	14.023	1.265
11	44	225	4	15	1.386	5.397	15.471	2.175
12	44	250	6	10	1.47	4.956	15.96	2.499
13	46	175	10	15	1.25	7.858	16.681	1.343
14	46	200	8	10	1.491	9.316	16.117	1.345
15	46	225	6	25	2.08	5.768	12.661	2.928
16	46	250	4	20	2.108	5.046	12.479	3.444

er-the-better, and the nominal-the-better. The optimal bead geometry requires smaller the better characteristics for depth of penetration and dilution, while larger the better characteristics for bead width and reinforcement are crucial for optimal design.

The S/N ratio is expressed as follows:

Nominal-the-best,

$$S/N = -10 log\, y_i^{-2}/s^2 \qquad (1)$$

Smaller-the-better,

$$S/N = -10 log(\frac{1}{n}\sum_{i=1}^{n} y_i^2) \qquad (2)$$

Larger-the-better,

$$S/N = -10 log(\frac{1}{n}\sum_{i=1}^{n} 1/y_i^2) \qquad (3)$$

From a sequence of n simulated trials, y_i is the result of the ith trial.

2.4. MOORA method

A method of concurrently improving two or more competing attributes while conforming to specific limitations is called multi-objective optimization [19]. One such multi-objective optimization strategy is the MOORA method, which Brauers first presented [20]. It is a useful tool for resolving a wide range of complicated decision-making problems related to manufacturing settings [19]. The decision matrix that displays the performance of the various alternatives in relation to different characteristics is the primary step when using MOORA method [21–27].

$$X = \begin{bmatrix} X_{11} & X_{12} & \dots & \dots & \dots & \dots & X_{1q} \\ X_{21} & X_{22} & \dots & \dots & \dots & \dots & X_{2q} \\ \dots & \dots & \dots & \dots & \dots & \dots & \dots \\ \dots & \dots & \dots & \dots & \dots & \dots & \dots \\ X_{p1} & X_{p2} & \dots & \dots & \dots & \dots & X_{pq} \end{bmatrix} \qquad (4)$$

Where p is the number of alternatives, q is the number of attributes, and X_{ij} is the performance measure of the ith alternative on the jth attribute [19]. Next, a ratio arrangement is developed where the performance of each alternative on an attribute is compared with a denominator that represents all the different alternatives on that attribute. According to the findings of Brauers et al. [21], the most favorable option for this denominator involves calculating the square of the total squared values for each attribute. The resulting is an equation for this ratio:

$$\overset{a}{X}_{ij} = X_{ij}/\sqrt{\sum_{i=1}^{m} X_{ij}^2}\,(j=1,2,\dots,n) \qquad (5)$$

Here X_{ij} represents a dimensionless number which indicates the normalized performance of the ith alternative on the jth attribute and lies inside the interval [0, 1] [19]. These normalized performances are included for multi-objective optimization while maximizing helpful qualities and removed when minimizing non-beneficial attributes. The optimizing problem now changes to

$$Y_i = \sum_{j=1}^{g} \overset{a}{X}_{ij} - \sum_{j=g+1}^{n} \overset{a}{X}_{ij} \qquad (6)$$

Where Y_i is the normalized value of the ith alternative with regard to every attribute, g is the number of qualities to be maximized, and (n−g) is the number of qualities to be minimized. It is often observed that certain

characteristics are more important than others in certain circumstances. A property is multiplied by its corresponding weight to increase its importance [8]. Considering attribute weights to be taken into account, Eq. (6) is modified as follows:

$$Y_i = \sum_{j=1}^{g} W_j \cdot \overset{a}{X}_{ij} - \sum_{j=g+1}^{n} W_j \cdot \overset{a}{X}_{ij} (j = 1,2,....,n) \quad (7)$$

Where W_j is the weight of the jth attribute, which is calculated by applying the entropy method. Based on the total of the maximum and minimum values in the decision matrix, the Y_i value may be positive or negative in research. The ultimate preference of Y_i is displayed through an ordered ranking. As a result, the poorest alternative has the lowest Y_i value, and the greatest alternative has the highest Y_i value.

2.5. GRA and PCA

The integration of Grey Relational Analysis (GRA) with Principal Component Analysis (PCA) significantly enhances multi-optimization in welding processes [28]. This integration allows for the improvement of multiple quality responses, such as penetration, reinforcement, bead width, and dilution percentage, simultaneously. The weighted response analysis helps determine the relative importance of different quality responses, providing a more accurate representation of their impact on the overall optimization process [28]. This combination also allows for more informed decision-making regard-

ing the selection of welding parameters, as PCA helps to classify the most significant parameters based on weighted responses. The integration of GRA and PCA has been proven to yield effective results in finding optimal combinations of welding parameters for multiple response optimizations, improving various quality responses in welding processes. This approach represents a novel and valuable contribution to the field, offering new insights and solutions for improving weld quality. Overall, the integration of GRA and PCA in welding optimization enables researchers to handle multiple responses, determine weighted influences of parameters, make informed decisions, achieve successful results, and contribute to the advancement of knowledge in the optimization of the welding process.

3. Results and Discussion

3.1. Probability plots

The experimental data distribution, as shown in ▶Table 4, is assessed using probability plots. The normality assumption is confirmed through Anderson-Darling test, a robust statistical method commonly used to detect outliers from a normal distribution [29]. ▶Figure 3 shows that the data of all experiments and responses closely align with the fitted line, low Anderson-Darling statistics values, and a p-value greater than 0.05 [28], indicating that further analysis of the data is appropriate.
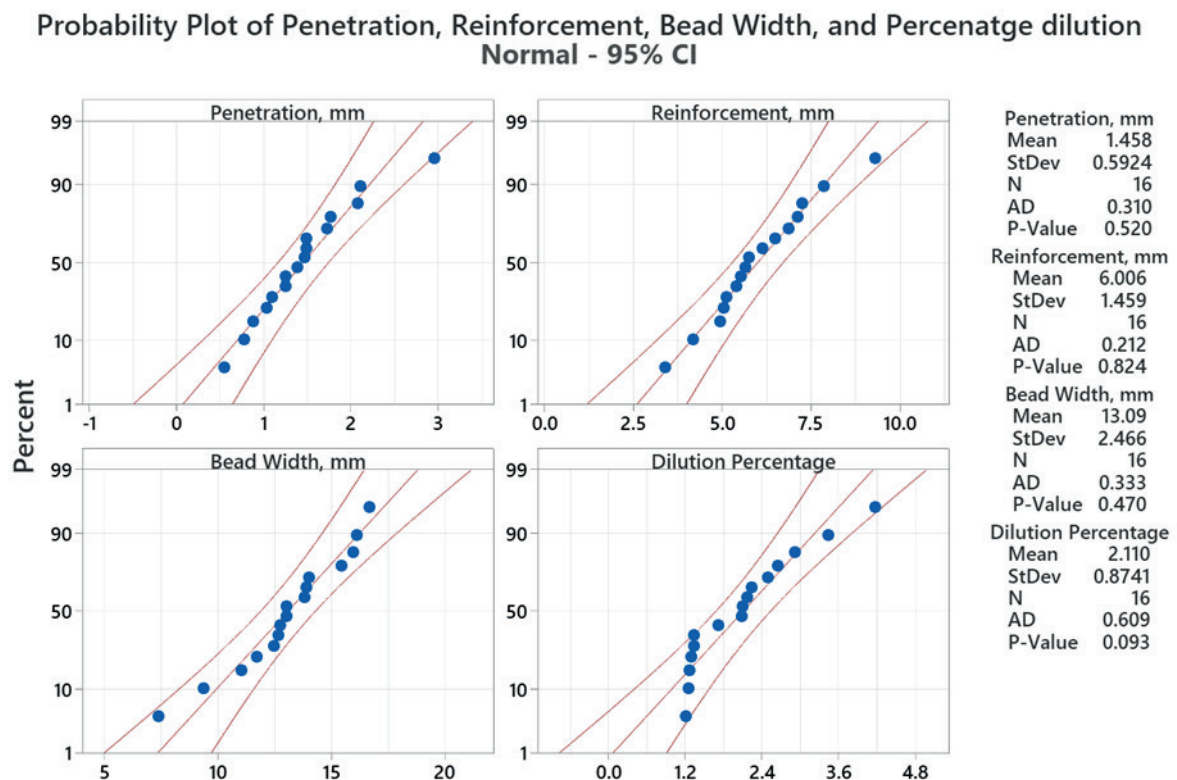
Figure 3. Probability plot for responses

3.2. Mean of Response

The influence of various welding parameters on the S/N ratio is individually examined as a result of the orthogonal design of the experiments. Graphs known as response curves illustrate how performance characteristics vary as input parameter levels change [10]. The graphs for response means are displayed in ▶Figures 4 to 7. Weld bead geometry quality attributes are influenced by process variables, as seen by the response graphs from the Taguchi experiment. Consequently, a thorough examination of how these factors affect the geometry of the weld bead is given in the sections that follow.
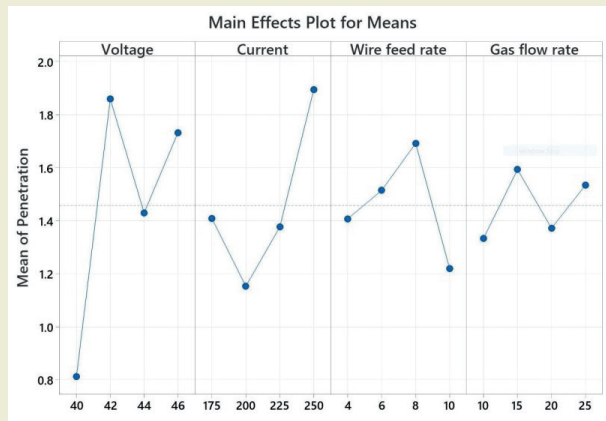
Figure 4. Main effect plots for mean of penetration
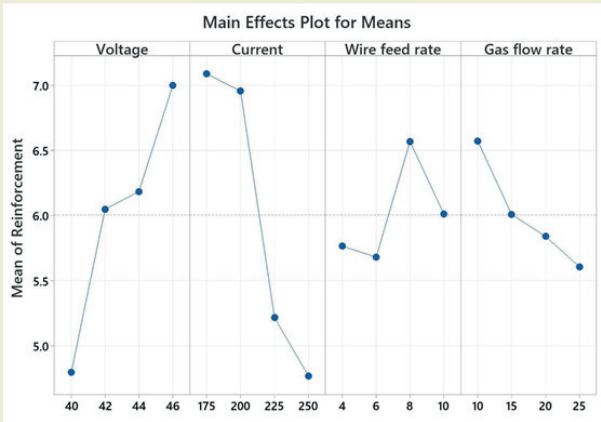
Figure 5. Main effect plots for mean of reinforcement
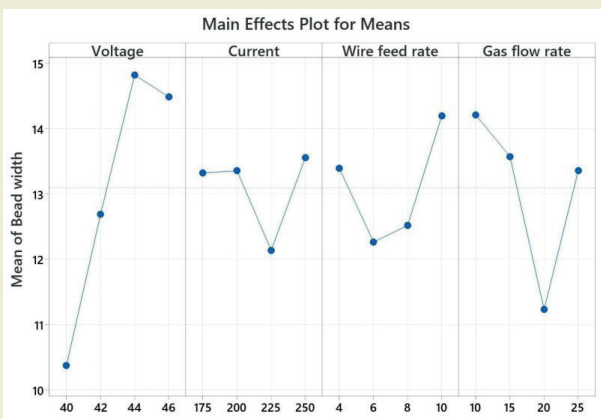
Figure 6. Main effect plots for mean of bead width
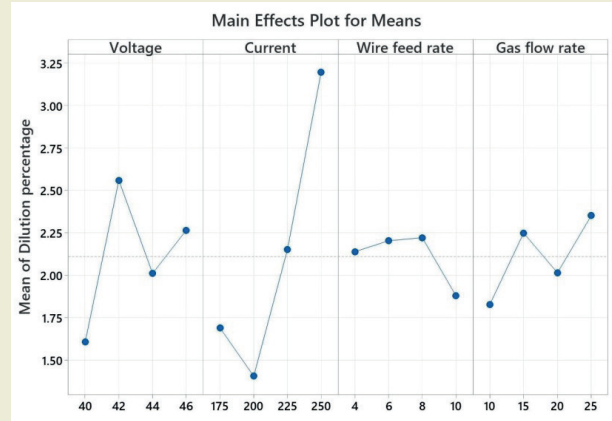
Figure 7. Main effect plots for mean of dilution percentage
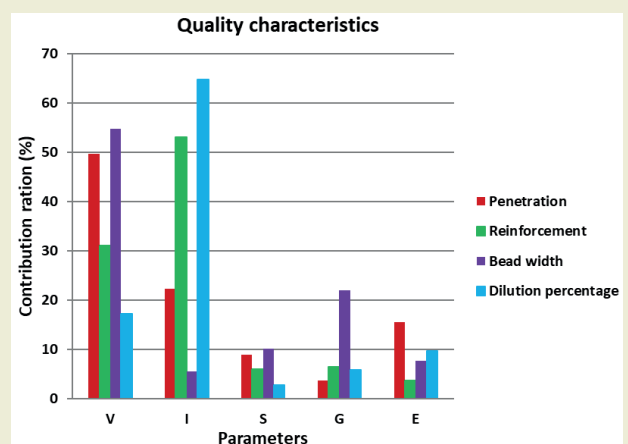
Figure 8. Pareto diagram for responses

3.3. ANOVA and contribution ratio

Table 5 provides the details of the calculation of the contribution ratio, which is derived from the total sum square of the difference. A method for identifying the significant process variables is Pareto analysis, which is also a quick and simple technique to analyze experiment findings [10]. The Pareto diagram's significant factors are chosen from the left side, where they collectively contribute 90%. It is clear from ▶Tables 5 and 6 that the depth of penetration and bead width is mostly determined by the Voltage. But out of all of these factors, welding current followed by voltage has the bigger impact on other parameters which include reinforcement, and dilution percentage. ▶Figure 8 displays the extracts of Pareto diagram.

4. MOORA

The weights of the variables are calculated and given in ▶Table 7. ▶Table 8 displays the normalized performance scores for various alternatives across specific attributes. These scores were determined using Equation (5). By applying Equation (7), the normalized values (Y_i) for every alternative were calculated based on these attributes. The table also presents the results of

MOORA method, organizing the alternatives in descending order of their assessment values. According to this method, experiment number 1 attained the top rank, following process parameters set at Voltage=40 V (level 1), Current=175 A (level 1), wire feed rate=4 mm/min (level 1), and gas flow rate 10 lpm (level 1).

5. Grey Rational Analysis

Maximizing reinforcement and bead width is of interest, depending on the aim of this article. Consequently, for these quality attributes, the larger-the-better criterion is chosen, and Equation (8) is used to express the normalized results.

$$y_j^*(q) = \frac{y_j(q) - min y_j(q)}{max y_j(q) - min y_j(q)} \quad (8)$$

It is also necessary to decrease penetration and dilution percentage, hence, as Equation (9) states, the smaller the better is used.

$$y_j^*(q) = \frac{max y_j(q) - y_j(q)}{max y_j(q) - min y_j(q)} \quad (9)$$

Where the generated grey relational values are denoted by $y_j^*(p)$, and the highest and lowest values of $y_j(q)$ for the qth observation are represented by max $y_i(q)$ and min $y_i(q)$, respectively. The number of response variables is q = 4. The sixteen observations are listed in the comparable sequence $y_i(q)$, with j = 1, 2…,16. A greater value of normalized results is anticipated for improved performance, as the optimal normalized values equals 1.

After normalizing the data, Grey Relational Coefficients (GRC) are computed to demonstrate the correlation between the actual experimental outcomes and the desired ones. The expression for GRC $\xi_j(q)$ is provided in Equation (10).

$$\xi\big(y_j^*(q), y_0^*(q)\big) = \frac{\Delta_{min}(q) + \zeta \Delta_{max}(q)}{\Delta_{0j}(q) + \zeta \Delta_{max}(q)} \quad (10)$$

Where $|(q) + \zeta \Delta_{max}(q)|$ is the deviation sequence, defined as the absolute difference between reference sequence $y_0^*(q)$ and comparability sequence $y_j^*(q)$ [28]. The value of the identification or distinguishing coefficient (ξ) is between [0, 1], which in this paper was fixed at 0.5 [28]. Grey Relational Grade (GRG) is calculated from the weighted mean of the corresponding GRCs

Table 5. S/N response

Factors			V	I	S	G	Error	Total
Penetration	Sum at factor levels	1	2.042	-2.647	-2.545	-2.304		-10.403
		2	-4.903	-0.998	-3.067	-2.997		
		3	-2.981	-1.860	-3.155	-1.706		
		4	-4.562	-4.898	-1.636	-3.396		
	Sum of squares of differences		2.617	1.171	0.469	0.187	0.817	5.263
	Contribution ratio, %		49.724	22.250	8.911	3.553	15.523	100
Reinforcement	Sum at factor levels	1	13.370	16.990	15.170	16.100		61.310
		2	15.600	16.630	15.010	15.450		
		3	15.700	14.280	15.980	15.110		
		4	16.640	13.410	15.150	14.670		
	Sum of squares of differences		9.918	16.917	1.920	2.035	1.139	31.929
	Contribution ratio, %		31.063	52.983	6.013	6.374	3.567	100
Bead width	Sum at factor levels	1	20.120	22.380	22.490	22.970		88.700
		2	22.040	22.350	21.610	22.450		
		3	23.400	21.380	21.610	20.770		
		4	23.140	22.600	23.000	22.510		
	Sum of squares of differences		49.944	4.982	9.262	20.008	6.989	91.185
	Contribution ratio, %		54.772	5.464	10.157	21.942	7.665	100
Dilution percentage	Sum at factor levels	1	-3.600	-4.286	-5.974	-4.816		-23.343
		2	-7.640	-2.884	-6.482	-5.993		
		3	-5.800	-6.269	-5.856	-5.291		
		4	-6.303	-9.905	-5.031	-7.243		
	Sum of squares of differences		1.960	7.424	0.302	0.668	1.106	11.461
	Contribution ratio, %		17.101	64.776	2.635	5.828	9.650	100

for each experimental run, which gives data about the strength of correlation among the welding runs. The GRG value ranges from 0 to 1. The ideal scenario is typically an experimental run with a greater GRG, which shows how strongly relevant experiments correlate with the idealized value. Equation (11) is used to calculate the GRG when all quality responses are given equal weights.

$$\gamma_j(y_0^*, y_j^*) = \frac{1}{n} \sum_{q=1}^{n} \xi(y_j^*(q), y_0^*(q)) \qquad (11)$$

In certain practical uses, the weights of quality attributes vary similarly to the weights derived from PCA. Under these cases, Equation (11) undergoes a modification to become Equation (12) [28]:

$$\gamma_j(y_0^*, y_j^*) = \frac{1}{n} \sum_{q=1}^{n} Wq \, \xi(y_j^*(q), y_0^*(q)) \qquad (12)$$

Where $\gamma_j(y_0^*, y_j^*)$ is GRG for j^{th} experiment and n is the number of quality responses, Wq is the weight of qth quality response, and $\sum_{q=1}^{n} Wq = 1$

5.1. Principal Component Analysis

Principal Component Analysis is considered a reliable statistical method used to optimize several objectives simultaneously [28]. It simplifies and consolidates numerous related datasets into a few uncorrelated arrays and principal components, reducing complexity, correlation, vagueness, and dimensions of information [30]. A linear transformation is used in PCA to preserve as much distinctive information [31]. Therefore, PCA converts multi-response optimization to single-response optimization without varying the existing data [32]. It is achieved by constructing linear arrangements

Table 6. Results of ANOVA

Analysis of Variance for Penetration						
Source	DF	Adj SS	Adj MS	F-Value	P-Value	Rank
Voltage	3	2.617	0.87233	3.2	0.182	1
Current	3	1.1716	0.39055	1.43	0.387	2
Wire feed rate	3	0.4697	0.15658	0.57	0.67	3
Gas flow rate	3	0.1878	0.06259	0.23	0.871	4
Error	3	0.8172	0.27241			
Total	15	5.2634				
Analysis of Variance for reinforcement						
Source	DF	Adj SS	Adj MS	F-Value	P-Value	Rank
Voltage	3	9.918	3.3061	8.71	0.054	2
Current	3	16.917	5.6389	14.86	0.026	1
Wire feed rate	3	1.92	0.6401	1.69	0.339	4
Gas flow rate	3	2.035	0.6784	1.79	0.323	3
Error	3	1.139	0.3795			
Total	15	31.929				
Analysis of Variance for Bead width						
Source	DF	Adj SS	Adj MS	F-Value	P-Value	Rank
Voltage	3	49.944	16.648	7.15	0.07	1
Current	3	4.982	1.661	0.71	0.606	4
Wire feed rate	3	9.262	3.087	1.33	0.411	3
Gas flow rate	3	20.008	6.669	2.86	0.205	2
Error	3	6.989	2.33			
Total	15	91.185				
Analysis of Variance for Dilution percentage						
Source	DF	Adj SS	Adj MS	F-Value	P-Value	Rank
Voltage	3	1.9604	0.6535	1.77	0.325	2
Current	3	7.4238	2.4746	6.71	0.076	1
Wire feed rate	3	0.3021	0.1007	0.27	0.843	4
Gas flow rate	3	0.6679	0.2226	0.6	0.656	3
Error	3	1.1063	0.3688			
Total	15	11.4605				

Table 7. Weights of responses

Parameters	Penetration, mm	Reinforcement, mm	Bead Width, mm	Dilution Percentage
Weights	0.382	0.140	0.090	0.387

Table 8. Results of multi-criteria analysis and normalized decision-making matrix

Exp. no.	Weight Normalized matrix				$\bar{y}$	Rank
	Penetration	Reinforcement	Bead width	Dilution percentage		
1	0.054	0.037	0.020	0.318	-0.315	1
2	0.047	0.029	0.016	0.338	-0.340	4
3	0.033	0.024	0.012	0.328	-0.325	2
4	0.063	0.019	0.022	0.694	-0.716	13
5	0.106	0.039	0.019	0.546	-0.594	9
6	0.076	0.035	0.024	0.448	-0.466	7
7	0.091	0.031	0.022	0.586	-0.624	11
8	0.181	0.032	0.022	1.092	-1.219	16
9	0.108	0.041	0.023	0.549	-0.593	8
10	0.067	0.041	0.024	0.330	-0.332	3
11	0.084	0.031	0.026	0.568	-0.596	10
12	0.090	0.028	0.027	0.653	-0.687	12
13	0.076	0.045	0.028	0.351	-0.354	5
14	0.091	0.053	0.027	0.351	-0.362	6
15	0.127	0.033	0.021	0.765	-0.837	14
16	0.129	0.029	0.021	0.900	-0.978	15

for a variety of responses. The GRC (Generalized Reduced Coefficient) of the output variable is utilized for developing a matrix denoted by Equation (13).

$$y = \begin{bmatrix} y_1(1) & y_1(2) & \cdots & y_1(k) \\ y_2(1) & y_2(2) & \cdots & y_2(k) \\ \cdots & \cdots & \cdots & \cdots \\ \cdots & \cdots & \cdots & \cdots \\ y_j(1) & y_j(2) & \cdots & y_j(k) \end{bmatrix} \quad (13)$$

In this work, $y_a(q)$ denotes the GRC of an individual response, in which a is the total number of experiments (a = 1, 2, …j) and b is the total number of quality responses (b = 1, 2, . . . k). In this study, j is equal to 16, and k is equal to 4. Subsequently, the equation that follows can be utilized for creating the correlation coefficient matrix:

$$R_{jl} = \left(\frac{Cov(y_a(b), y_a(l))}{\sigma_{ya}(b) * \sigma_{ya}(l)}\right) b = 1,2, \ldots k; l = 1,2, \ldots, k \quad (14)$$

The expression where $Cov(y_a(b), y_a(l))$ represents the covariance among the sequences $y_a(b)$ and $y_a(l)$, while $\sigma_{ya}(b)$ and $\sigma_{ya}(l)$ represent the standard deviation of sequences $y_a(b)$ and $y_a(l)$, individually. The eigenvalues and eigenvectors were calculated from the R_{jl} array using Equation (15)

$$(R - \lambda_k I_j)V_{pk} = 0 \quad (15)$$

Consequently, Equation (16) is used to develop the uncorrelated principal components (PCs) from the eigenvalues (λ_k) and eigenvectors (V_{pk}) of the square matrix R

$$Z_{jk} = \sum_{i=1}^{n} Y_j(p) \times V_{pk} \quad (16)$$

In this equation, Z_{jk} refers to the kth principal component. The initial eigenvalue related to the first principal component (PC) explains the major contribution of variance, where the eigenvalues and principal components are organized in descending order based on their described variance. ▶**Table 9** presents the eigenvalues associated with the eigenvectors.

Table 9. Principal Component Analysis

Component	PC1	PC2	PC3	PC4
Eigenvalue	1.9199	1.5786	0.4939	0.0076
Variation (%)	0.48	0.395	0.123	0.002
Cumulative (%)	0.48	0.875	0.998	1
Eigen Vector	0.688	0.118	-0.363	0.617
	-0.082	0.723	-0.57	-0.382
	0.208	0.642	0.734	0.077
	0.69	-0.225	0.073	-0.684

5.2. Optimization of multiple variables by utilizing GRA and PCA

Because every response variable in GRA has identical weights, choosing decisions may be difficult. Thus, PCA has been utilized for determining the relative weights of quality responses [33]. This study compares the multi-objective optimization processes carried out by PCA and GRA. The section on optimization methodology goes into comprehensive detail on the steps. Equations (8) and (9) are first used to normalize the S/N ratios. Equation (10) is utilized to calculate the Grey relationship coefficient of individual response. ▶Table 9 displays the Eigen values and Eigen vectors for PCA, which were computed using Equation (15) and PC from Equation (16). The Eigenvectors of the first PC are squared to yield relative weights of the quality responses. Using the weights determined by PCA and GRCs that are listed in ▶Table 9 are computed for sixteen experiments using Equation (11).

Sample number eight yields the maximum GRG value. ▶Table 10 makes it clear that the first PC contributes up to 47.33% of the variance for four quality attributes. The squares of the eigenvectors of the first PC, which are selected as weights of quality responses, are shown in ▶Table 10 and are determined to be, in the order of penetration, reinforcement, bead width, and dilution percentage of 0.4733, 0.0067, 0.0433, and 0.4761 respectively. Thus, with regard to individual GRG, the ideal multi-objective optimization can be accomplished. Hence, from GRG, $A_2B_4C_3$ that is, Voltage=42 V (level 2), Current=250 A (level 4), wire feed rate=8 mm/min (level 3), and gas flow rate 15 lpm (level 2) represents the ideal collection of input parameter values for optimum responses.

6. Conclusion

The SN ratio is used to identify interactions among input and process parameters. MOORA method ranks parameters based on calculated weights while GRA with PCA assigns equal weights to all parameters to determine the optimized parameters. This study compares these methods, enabling industries to select the suitable optimization process from the available methods based on their specific requirements. The results contributed to reducing the welding defect in the small-scale industry where the experiments were conducted. By reducing the number of experiments and associated costs, it is possible to identify optimized solutions for the existing welding machines and the given job.

- Using S/N ratio for single objective optimization concludes that:

- For reduced penetration, V=42 V, I=250 A, S=8 mm/min, and G=15 lpm

- For enlarged reinforcement, V=46 V, I=200 A, S=8 mm/min, and G=10 lpm

- For enlarged bead width, V=46 V, I=175 A, S=10 mm/min, and G=15 lpm

- For reduced dilution percentage, V=42 V, I=250 A, S=8 mm/min, and G=15 lpm.

- Predominantly voltage affects penetration and bead width whereas welding current affects reinforcement and dilution percentage.

- Through the MOORA method, it was determined

Table 9. Calculated Normalized GRC, and GRG for 16 experiments

Exp. No.	Normalization				Grey Relational Coefficient				GRG	Rank
1	0.283	0.641	0.567	0.000	0.411	0.582	0.536	0.333	0.466	14
2	0.205	0.405	0.295	0.048	0.386	0.456	0.415	0.344	0.401	15
3	0.000	0.202	0.000	0.024	0.333	0.385	0.333	0.339	0.348	16
4	0.380	0.000	0.697	0.633	0.446	0.333	0.623	0.577	0.495	13
5	0.682	0.699	0.496	0.439	0.612	0.624	0.498	0.471	0.551	9
6	0.489	0.584	0.777	0.278	0.494	0.546	0.691	0.409	0.535	12
7	0.593	0.482	0.699	0.496	0.551	0.491	0.624	0.498	0.541	11
8	1.000	0.505	0.671	1.000	1.000	0.502	0.603	1.000	0.776	1
9	0.694	0.733	0.771	0.443	0.620	0.652	0.685	0.473	0.608	7
10	0.411	0.752	0.787	0.031	0.459	0.668	0.702	0.340	0.542	10
11	0.550	0.458	0.908	0.470	0.526	0.480	0.844	0.485	0.584	8
12	0.585	0.373	0.946	0.582	0.546	0.444	0.902	0.545	0.609	6
13	0.489	0.831	1.000	0.080	0.494	0.747	1.000	0.352	0.648	3
14	0.593	1.000	0.958	0.080	0.551	1.000	0.922	0.352	0.706	2
15	0.791	0.524	0.662	0.711	0.705	0.512	0.597	0.634	0.612	5
16	0.799	0.391	0.645	0.843	0.713	0.451	0.584	0.761	0.627	4

Table 10. Variance contribution of response variables for first PC

Response Variable	Contribution
Penetration	0.4733
Reinforcement	0.0067
Bead width	0.0433
Dilution percentage	0.4761

that a voltage of 40V, welding current of 175A, wire feed rate of 4 mm/min, and gas flow rate of 10 lpm would yield optimal weld bead geometry with penetration of 0.884 mm, reinforcement of 6.489 mm, bead width of 11.715 mm, and dilution percentage of 1.218%.

• From PCA and GRA, setting the voltage at 42V, welding current at 250A, wire feed rate at 8 mm/min, and gas flow rate at 15 lpm results in ideal characteristics: penetration of 2.961 mm, reinforcement of 5.658 mm, bead width of 12.753 mm, and dilution percentage of 4.183%.

Research ethics

Not applicable.

Author contributions

Methodology – Raviram R, Ranjith Raj A; Formal Analysis – Raviram R, Shashang G, Shameer Mohamed S; Investigation – Raviram R, Shashang G; Resources – Raviram R, Ranjith Raj A; Data Curation – Raviram R; Writing – Original Draft Preparation – Raviram R; Writing – Review & Editing – Raviram R, Ranjith Raj A; Visualization – Raviram R, Shashang G, Shameer Mohamed S; Supervision – Ranjith Raj A; Project Administration – Raviram R, Ranjith Raj A; Funding Acquisition – Raviram R.

Competing interests

The author state(s) no conflict of interest.

Data availability

Not applicable.

Peer-review

Externally peer-reviewed.

Orcid

Raviram R https://orcid.org/0009-0005-5837-1239
Ranjith Raj A https://orcid.org/0000-0003-3125-8146
Shashang G https://orcid.org/0009-0007-9673-1674
Shameer Mohamed S https://orcid.org/0009-0005-7444-9657

References

[1] Baskoro, A. S., Hidayat, R., Widyianto, A., Amat, M. A., & Putra, D. U. (2020). Optimization of Gas Metal Arc Welding (GMAW) Parameters for Minimum Distortion of T Welded Joints of A36 Mild Steel by Taguchi Method. Materials Science and Engineering, 1000, 356–363. doi: 10.4028/www.scientific.net/msf.1000.356

[2] Ramarao, M., King, M. F., Sivakumar, A., Manikandan, V., Vijayakumar, M., & Subbiah, R. (2022). Optimizing GMAW parameters to achieve high impact strength of the dissimilar weld joints using Taguchi approach. Materials Today: Proceedings, 50, 861–866.

[3] Adin, M. Ş., & İşcan, B. (2022). Optimization of process parameters of medium carbon steel joints joined by MIG welding using Taguchi method. European Mechanical Science, 6(1), 17–26.

[4] Madavi, K. R., Jogi, B. F., & Lohar, G. S. (2022). Metal inert gas (MIG) welding process: A study of effect of welding parameters. Materials Today: Proceedings, 51, 690–698.

[5] Titinan, M., Masaya, S., Manabu, T., Rinsei, I., Muneo, M., & Tokihiko, K. (2017). Diagnostic of heat source characteristics in gas metal arc welding using CO2 shielding gas. 溶接学会論文集, 35(2), 103s–107s.

[6] Narwadkar, A., & Bhosle, S. (2016). Optimization of MIG welding parameters to control the angular distortion in Fe410WA steel. Materials and Manufacturing Processes, 31(16), 2158–2164.

[7] Sankar, B. V., Lawrence, I. D., & Jayabal, S. (2018). Experimental study and analysis of weld parameters by GRA on MIG welding. Materials Today: Proceedings, 5(6), 14309–14316.

[8] Pal, A. (2015). MIG welding parametric optimisation using Taguchi's orthogonal array and analysis of variance. International Journal of Research Review in Engineering Science and Technology, 4(1), 211–217.

[9] Kumar, P., & Roy, B. K. (2013). Parameters Optimization for Gas Metal Arc Welding of Austenitic Stainless Steel (AISI 304) & Low Carbon Steel using Taguchi's Technique. International Journal of Engineering and Management Research, 3(4), 18–22.

[10] Palani, P. K., Murugan, N., & Karthikeyan, B. (2006). Process parameter selection for optimising weld bead geometry in stainless steel cladding using Taguchi's approach. Materials Science and Technology, 22(10), 1193–1200.

[11] Montgomery, D. C. (2006). Design and analysis of experiments (4. baskı). New York: John Wiley & Sons.

[12] Ross, P. J. (1988). Taguchi techniques for quality engineering. New York: Tata McGraw Hill.

[13] Park, S. H. (1996). Robust design and analysis for quality engineering (1. baskı). Londra: Chapman & Hall.

[14] Ross, P. J. (1996). Taguchi techniques for quality engineering. New York: McGraw-Hill.

[15] Belavendran, N. (1995). Quality by design. Londra: Prentice Hall.

[16] Yang, W. H., & Tarng, Y. S. (1998). Design optimization of cutting parameters for turning operations based on the Taguchi method. Journal of Materials Processing Technology, 84, 122–129.

[17] Songa, Y. A., Parka, S., & Chaeb, S. W. (2005). Optimization of the injection molding process for part warpage using Taguchi method.

International Journal of Machine Tools & Manufacture, 45(1), 1−7.

[18] Syrcos, G. P. (2003). Die casting process optimization using Taguchi methods. Journal of Materials Processing Technology, 135, 68−74.

[19] Gadakh, V. S., Shinde, V. B., & Khemnar, N. S. (2013). Optimization of welding process parameters using MOORA method. The International Journal of Advanced Manufacturing Technology, 69, 2031−2039.

[20] Brauers, W. K. M. (2004). Optimization methods for a stakeholder society: A revolution in economic thinking by multiobjective optimization. Boston: Kluwer Academic.

[21] Brauers, W. K. M., Zavadskas, E. K., Peldschus, F., & Turskis, Z. (2008). Multi-objective decision-making for road design. Transport, 23, 183−193.

[22] Brauers, W. K. M., Zavadskas, E. K., Peldschus, F., & Turskis, Z. (2008). Multi-objective optimization of road design alternatives with an application of the MOORA method. Proceedings of the 25th International Symposium on Automation and Robotics in Construction, Lithuania, 541−548.

[23] Brauers, W. K. M. (2008). Multi-objective contractor's ranking by applying the MOORA method. Journal of Business Economics and Management, 4, 245−255.

[24] Brauers, W. K. M., & Zavadskas, E. K. (2009). Robustness of the multiobjective MOORA method with a test for the facilities sector. Technological and Economic Development of Economy, 15(2), 352−375.

[25] Kalibatas, D., & Turskis, Z. (2008). Multicriteria evaluation of inner climate by using MOORA method. Information Technology and Control, 37, 79−83.

[26] Brauers, W. K. M., & Zavadskas, E. K. (2010). Project management by MULTIMOORA as an instrument for transition economies. Technological and Economic Development of Economy, 16(1), 5−24.

[27] Lootsma, F. A. (1999). Multi-criteria decision analysis via ratio and difference judgement. Londra: Springer.

[28] Qazi, M. I., Akhtar, R., Abas, M., Khalid, Q. S., Babar, A. R., & Pruncu, C. I. (2020). An integrated approach of GRA coupled with principal component analysis for multi-optimization of shielded metal arc welding (SMAW) process. Materials, 13(16), 3457.

[29] Stephens, M. A. (1974). EDF statistics for goodness of fit and some comparisons. Journal of the American Statistical Association, 69, 730−737.

[30] Seong, W.-J. (2019). Prediction and characteristics of angular distortion in multi-layer butt welding. Materials, 12, 1435.

[31] Armentani, E., Esposito, R., & Sepe, R. (2007). The influence of thermal properties and preheating on residual stresses in welding. International Journal of Computational Materials Science and Surface Engineering, 1, 146−162.

[32] Ramasamy, N., Jeyasimman, D., Kathiravan, R., & Raju, N. (2019). Influence of Welding Sequence on Residual Stresses Induced in As-Welded Plug Weld of Low-Carbon Steel Plate. Transactions of the Indian Institute of Metals, 72, 1361−1369.

[33] Chate, G. R., Patel, G. M., Kulkarni, R. M., Vernekar, P., Deshpande, A. S., & Parappagoudar, M. B. (2018). Study of the effect of nano-silica particles on resin-bonded moulding sand properties and quality of casting. Silicon, 10, 1921−1936.

Investigation of the effects of binary hybrid nanofluids and different arrangements of corrugated tubes on thermal performance

Fatma Oflaz¹* iD

¹Firat University, Faculty of Technology, Automotive Engineering, Elazığ, Türkiye

Abstract: This research examined the effects of corrugation distance and nanofluid volume concentration on pressure drop, Nusselt number, and thermal performance in a circular tube. Binary nanofluid ($MWCNT/Al_2O_3$, 60:40) with volume fractions of 0.25%, 0.5%, and 1% was tested in corrugated tubes with distances of 10 mm, 20 mm, and 30 mm under constant heat flux (20 kW/m²) for Reynolds numbers between 10,000 and 40,000. 3D single-phase model was developed using ANSYS 19 with the standard k-ε turbulence model and validated against equations from the literature. Results revealed that heat transfer improved with increasing Reynolds number, primarily due to elevated flow rates and intensified mixing induced by the corrugated surfaces. Compared to smooth tubes, the corrugated tubes exhibited higher Nusselt numbers, signifying better convective heat transfer performance. Nonetheless, this improvement was accompanied by increased friction factors and pressure drops, especially at shorter corrugation distances. Shorter corrugation distances intensified turbulence and mixing, enhancing heat transfer, while longer distances diminished turbulence, lowering the Nusselt number. The highest thermal performance, with a performance evaluation criterion of 1.27, was achieved at a corrugation distance of 10 mm and an $MWCNT/Al_2O_3$ nanofluid concentration of 1%. For the same nanofluid concentration, the performance evaluation criterion was 1.24 at a corrugation distance of 20 mm and 1.21 at 30 mm, respectively.

Keywords: Binary nanofluid, Corrugated tube, Heat transfer, Performance Evaluation Criteria, Pressure drop

1. Introduction

Corrugation on tube walls enhances heat transfer by inducing turbulence and swirl flows, which increase fluid mixing and improve interaction with the tube surface. The swirling motion helps clean the inner surface, reducing fouling, while the increased surface area allows for more efficient heat exchanger. These combined factors reduce the fouling factor and enhance overall heat transfer efficiency [1]. Additionally, corrugated tubes increase the wetted perimeter without changing the cross-sectional area, which provides more surface area for heat transfer. Corrugated surfaces improve heat transfer by enhancing turbulence and fluid mixing but cause a higher pressure drop due to increased flow resistance. Corrugated tubes are generally utilized in heating and cooling systems, waste heat recovery, and chemical reactors due to their improved heat transfer efficiency [2]. Corrugated tubes have gained significant attention in research due to their simpler manufacturing and assembly process. Their practical advantages make them a preferred choice for enhancing heat transfer efficiency. Cauwenberge et al. [3] investigated helical heat exchangers using corrugated tubes and found that these tubes experienced a pressure drop 5.6 to 6.7 times higher than that of smooth tubes. They also observed a substantial improvement in heat transfer performance, with increases between 83% and 119%. Andrade et al. [4] examined the characteristics of heat transfer and pressure drop in corrugated tubes. They found that corrugated tubes exhibit a more gradual shift in frictional behavior compared to smooth tubes, demonstrating greater effectiveness in handling transitional flow regimes. Navickaitė et al. [5] studied numerical analyses to evaluate the thermal performance of corrugated tubes subjected to constant power inputs. The results revealed that double-corrugated tubes significantly improve thermal efficiency while maintaining the same pressure drop. The numerical simulations predicted a 400% increase in thermal efficiency, with a volumetric flow rate 4.2 times lower in double-corrugated tubes. Additionally, PEC increased by up to 14% for tubes

Nomenclature

D diameter (mm)

ΔV differential voltage, v

Q rate of heat transfer (W)

h convective heat transfer coefficient (W/m^{2}K)

q heat flux (W/m^2)

cp specific heat (J kg /K)

ΔP pressure drop [Pa]

T temperature (K)

U average velocity (m/s)

ρ density (kg/m^3)

k thermal conductivity (W/mK)

Nu Nusselt number

$\dot{m}$ mass flow rate (kg/s)

EG ethylene glycol

L length (mm)

e thick (mm)

MWCNT multi-walled carbon nanotubes

Al_2O_3 aluminum oxide

η overall enhancement efficiency

θ kinematic viscosity (m^2/s)

Greek symbols

f friction factor

Re Reynolds number

Pr Prandtl number

φ volume concentration, %

μ dynamic viscosity (kg/ms)

Subscripts

bf base fluid

f fluid

nf nanofluid

p nanoparticle

with an ellipse-base and 11% for those with a super ellipse-base. Wongcharee and Eiamsa-ard [6] performed experimental studies to examine the combined impact of using CuO/water nanofluids, twisted tapes, and corrugated tubes with various flow configurations. The results showed that nanofluids in smooth tubes exhibited a heat transfer improvement ranging from 2.64% to 16.9% over water under identical conditions. Additionally, the use of corrugated tubes resulted in a more significant enhancement, with heat transfer increasing by 4.8% to 66.3%. Ekiciler [7] examined the impact of wall corrugation and the use of Zn:Ag/EG-H$_2$O hybrid nanofluid on heat transfer and flow in a turbulent pipe flow. Different wall corrugation patterns were compared to a smooth pipe, with Reynolds numbers ranging from 13000 to 28000. The results demonstrated that adding wall corrugations significantly enhanced heat transfer and affected flow characteristics. Ajeel et al. [8] examined various corrugated channels using nanofluids in turbulent flow conditions with a constant heat flux. The results revealed that the modified channels substantially improved the heat transfer rate, with the greatest enhancement occurring in a trapezoidal corrugated channel using 2% silica nanofluids. Wang et al. [9–12] developed innovative external helical corrugated tubes to optimize heat transfer, pressure drop, and energy efficiency. The findings indicate that secondary flow plays a key role in reducing the irreversibility of both heat dissipation and viscous dissipation. Compared to transverse corrugated tubes with similar geometric characteristics, the spiral corrugated tubes demonstrated superior overall performance. Studies show that adding nanoparticles to a base fluid to create "nanofluids" can significantly increase the fluid's thermal conductivity [13]. This improvement makes nanofluids more effective for heat transfer applications, offering potential benefits in systems like industrial cooling and electronics.

MWCNTs are preferred as nanofluids due to their high thermal conductivity, large surface area, and strong mechanical properties, which enhance heat transfer performance. MWCNTs also offer good stability in suspension and have a low density, minimizing pressure drop and improving overall thermal efficiency. These attributes make MWCNT nanofluids ideal for heat exchange and thermal management applications. In their study, Palanisamy et al. [14] explored the heat transfer and pressure drop characteristics of a cone-shaped helically coiled tube heat exchanger utilizing MWCNT/water nanofluid. Results revealed that the Nusselt numbers, representing the heat transfer efficiency, increased by 22%, 41%, and 52% for nanofluids with volume fractions of 0.1%, 0.3%, and 0.5%, respectively, in comparison to water. This improvement was linked to the enhanced thermal conductivity of MWCNT nanofluids and increased turbulence within the fluid. Ibrahim et al. [15] examined the mixed convection heat transfer behavior of hybrid nanofluids, focusing on how varying nanoparticle compositions impact heat transfer across different flow conditions. Their analysis highlighted the influence of distinct nanoparticle combinations on thermal performance in various flow regimes. They created and evaluated three hybrid nanofluids with distinct Al$_2$O$_3$ and MWCNT ratios. Of these, the nanofluid containing 60% Al$_2$O$_3$ and 40% MWCNT showed the greatest improvement in heat transfer performance, achieving a Nusselt number increase of more than 5% relative to the other formulations. Painuly et al. [16] carried out an experimental investigation to assess the friction factors and convective heat transfer efficiency of a helically corrugated tube equipped with inserts, specifically under laminar flow conditions. The working fluid was water-ethylene glycol mixture with hybrid nanofluids composed of Al$_2$O$_3$ and MWCNT. The results showed that increasing the Al$_2$O$_3$-MWCNT

concentration in the hybrid nanofluid, along with reducing the helix ratio of the tube inserts, significantly enhanced both the heat transfer rate and the thermal performance factor. The Al_2O_3-MWCNT hybrid nanofluid demonstrated Nusselt number increases of 42.5%, 49.47%, and 56.2% over the base fluid at volume fractions of 0.1%, 0.5%, and 1%, respectively. Najafabadi et al. [17] examined three-dimensional simulations of steady-state laminar flow within a horizontal pipe, utilizing engine oil as the base fluid mixed with CuO and multi-walled carbon nanotubes nanoparticles. The objective was to evaluate and compare the impact of varying nanoparticle volume concentrations, using CuO and MWCNT in 1:1 and 1:2 ratios, on convective heat transfer performance. The results showed that increasing the nanoparticle concentration led to significant improvements in both the convective heat transfer coefficient and the Nusselt number, with MWCNT contributing more substantially to the enhancements than CuO. Scott et al. [18] conducted research on the preparation of alumina–multiwalled carbon nanotube/water hybrid nanofluid using a two-step method across different volume concentrations. The findings indicated that increasing the volume concentration initially enhanced heat transfer, with a maximum improvement of 49.27% observed at a volume concentration of 0.10%,

compared to the base fluid. However, beyond this point, further increases in concentration resulted in a decline in natural convection heat transfer performance.

Based on the above studies, most research has focused on the effects of nanofluid types and mass/volume fractions on heat transfer. Some studies have investigated the effects of MWCNT, Al_2O_3 nanofluids, and corrugated tubes separately; however, no study has been found that has investigated their combined effect in the same study. Corrugated tubes are known to enhance heat transfer by disrupting the thermal boundary layer, increasing turbulence and improving fluid mixing. For this purpose, this study aims to analyze the combined effects of MWCNT/Al_2O_3 hybrid nanofluids with two different corrugation spacings and three different volume concentrations on thermal performance.

2. Materials and methods

2.1. Physical model

The study focuses on a numerical analysis of heat transfer and fluid flow within a 3D corrugated tube. The key objective is to investigate how the corrugated
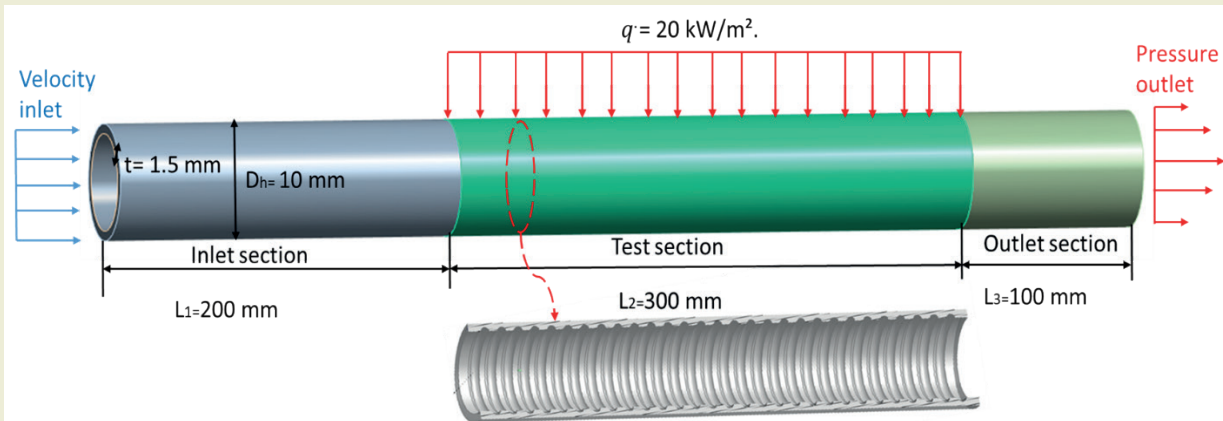

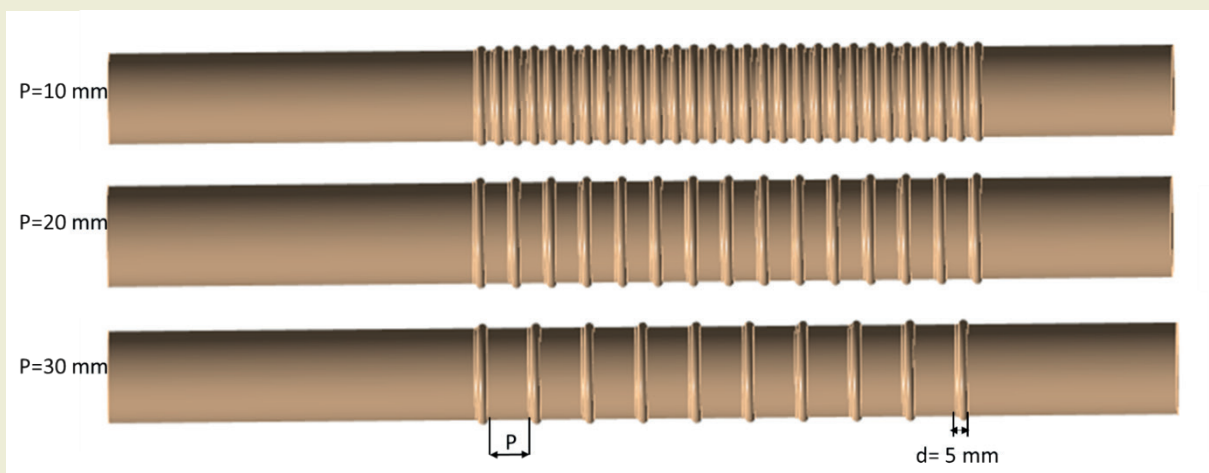**Figure 1.** Schematic diagram of corrugated tube

Fig. 2. View of corrugated distances of corrugated tubes

tube's structure affects fluid flow and heat transfer under specified boundary conditions. Two distinct tube geometries were analyzed: a smooth tube and a corrugated tube. The smooth tube served as the baseline for comparison against the performance of the corrugated tube. ▶Figure 1 provides a visual representation of the corrugated tube, illustrating its structure and the associated computational domain. The ▶Figure 1 highlights the corrugated section, as well as the smooth walled inlet and outlet regions that are part of the flow domain used for the analysis. The smooth tube used has the same dimensions as the corrugated tube, except it does not have any corrugations.

The tube is 600 mm long with a 10 mm hydraulic diameter and 1.5 mm wall thickness. It consists of an inlet (200 mm), a heated corrugated test section (300 mm), and an outlet (100 mm). Corrugation spacings are 10 mm, 20 mm, and 30 mm. The inlet ensures fully developed flow (velocity inlet at 300.15 K), while the outlet prevents backflow (pressure outlet). The corrugated walls are heated at 20 kW/m². The flow domain includes smooth inlet/outlet sections and a heated test section for analysis.

2.2. Thermophysical properties of nanofluids

The general equations utilized to determine the thermophysical properties of nanofluids can also be applied to hybrid nanofluids with appropriate modifications. In this context, the base fluid is denoted by (bf), the nanoparticles by (np), and the nanofluid by (nf). Symbols (p$_1$) and (p$_2$) specifically refer to MWCNT nanoparticles and Al$_2$O$_3$ nanoparticles, respectively.

The volume fraction of the hybrid nanofluid is calculated as follows:

$$\varphi_{hnf} = \varphi_{p1} + \varphi_{p2} \tag{1}$$

The density of the nanofluid is determined using the Pak and Cho [19] correlation, as presented in Equation (2)

$$\rho_{hnf} = \rho_{bf}.(1-\varphi) + \rho_{np}. \; \varphi \tag{2}$$

The dynamic viscosity of the hybrid nanofluid is calculated using the well-known Brinkman [20] equation (3), as follows:

$$\mu_{hnf} = \mu_{bf}(1 - \varphi_{p1} - \varphi_{p2})^{-2.5} \tag{3}$$

The thermal conductivity of the hybrid nanofluid was obtained using the commonly used Maxwell [21] equation, as described in equation (4) as follows:

$$k_{hnf} = \frac{(\varphi_{p1} k_{p1} + \varphi_{p2} k_{p2})/\varphi_{nf} + 2k_{bf} + 2(\varphi_{p1} k_{p1} + \varphi_{p2} k_{p2}) - 2(\varphi_{nf} k_{bf})}{(\varphi_{p1} k_{p1} + \varphi_{p2} k_{p2})/\varphi_{nf} + 2k_{bf} - 2(\varphi_{p1} k_{p1} + \varphi_{p2} k_{p2}) + \varphi_{nf} k_{bf}} \tag{4}$$

In this study, nanofluids were prepared at three different volume concentrations (0.25%, 0.5% and 1%) using water as the working fluid and MWCNT-Al$_2$O$_3$

Table 1. The characteristics of water and the nanoparticles utilized in this study.

Properties	Water [22]	MWCNT [23]	Al$_2$O$_3$ [22]
ρ (kg/m³)	998.2	2100	3980
C_p (J/kg K)	4182	710	777
k (W/mK)	0.6	2000	38

nanoparticles at a ratio of (60:40). A 60:40 hybridization ratio was selected based on the experimental findings of Krishnan et al. [24], which investigated the thermal properties of Al$_2$O$_3$-MWCNT/DI water hybrid nanofluids at different particle weight ratios and identified 60:40 as the most thermally efficient composition.

2.3. Data reduction

The findings are evaluated and expressed through the average friction factor (f), Reynolds number (Re), and Nusselt number (Nu), each represented by the following equations:

The constant heat flux applied to the test tube can be expressed as follows:

$$q^{.} = \frac{Q}{\pi D_h L} \tag{5}$$

Here, $q^{.}$ represents the constant heat flux and D_h is the hydraulic diameter of the tube.

The convective heat transfer coefficient in the tube is described as follows:

$$h = \frac{q^{.}}{(T_w - T_b)} \tag{6}$$

Here T_w represents the local wall temperature and T_b represents the temperature of the mass.

$$Re = \frac{\rho U D_h}{\mu} \tag{7}$$

Here U represents the mean fluid velocity.

$$Nu = \frac{h D_h}{k} \tag{8}$$

$$f = \frac{\Delta P}{\frac{1}{2}\rho U^2 \frac{L}{D_h}} \tag{9}$$

The pressure difference (ΔP) is determined by subtracting the average outlet pressure (P_{outlet}) from the average inlet pressure (P_{inlet}), as described in Equation (10).

$$\Delta P = P_{inlet} - P_{outlet} \tag{10}$$

A non-dimensional parameter, PEC is generally defined

as the ratio of increased heat transfer performance to increased friction losses in a heat exchange system. It evaluates whether a particular enhancement technique (e.g. turbulators, vortex generators, nanofluids, extended surfaces) provides an overall benefit in thermal-hydraulic performance. PEC value greater than 1 indicates that the heat transfer improvement outweighs the increase in flow resistance, making the enhancement effective. On the other hand, if PEC is less than 1, the increase in pressure drop is more significant than the thermal gain, rendering the modification inefficient. The Performance Evaluation Criteria, shown in Equation 11, is applied to evaluate the heat transfer efficiency and fluid flow characteristics of tubes with varying surface roughness. It combines the Nusselt number (representing heat transfer) and the friction factor (representing flow resistance) to evaluate overall performance. The PEC assesses whether the increase in heat transfer efficiency is sufficient to offset the additional fluid friction. Here Nu represents corrugated tube and Nu_s represents smooth tube.

$$\text{PEC} = \frac{(Nu/Nu_s)}{(f/f_s)^{1/3}} \tag{11}$$

2.4. Governing equations

Finite volume numerical simulations were conducted using ANSYS Fluent 19. To enhance the accuracy in capturing turbulent flows and to improve the modeling of fluid mixing and flow instabilities, the k-ε RNG turbulence model was employed under single-phase flow conditions. The pressure and velocity fields were solved iteratively using the SIMPLE algorithm to ensure fluid stability. The QUICK (Quadratic Upstream Interpolation for Convective Kinematics) scheme was employed to enhance accuracy in convective flow calculations, providing smooth flow modeling. The convergence criterion was set to 1×10⁻⁵ with the relevant equations used generally outlined.

Mass Conservation

$$\nabla(\rho\vec{V}) = 0 \tag{12}$$

Momentum Conservation

$$\nabla(\rho\vec{V}\vec{V}) = -\nabla P + \nabla(\mu\nabla\vec{V}) \tag{13}$$

Energy Conservation

$$\nabla(\rho c_p \vec{V}T) = \nabla(k\nabla T) \tag{14}$$

The k-ε turbulence model defines the turbulence kinetic energy (k) and the dissipation rate (ε) by solving differential equations that describe the behavior of these turbulent properties.

$$\frac{\partial(\rho k)}{\partial t} + \nabla.(\rho U k) = \nabla.\left(\left(\mu + \frac{\mu_t}{\sigma_k}\right)\nabla k\right) + P_k - \rho\varepsilon \tag{15}$$

$$\frac{\partial(\rho\varepsilon)}{\partial t} + \nabla.(\rho U\varepsilon) = \nabla.\left(\left(\mu + \frac{\mu_t}{\sigma_\varepsilon}\right)\nabla\varepsilon\right) + \frac{\varepsilon}{k}(C_{\varepsilon 1}(P_k) - C_{\varepsilon 2}\rho\varepsilon) \tag{16}$$

P_k is defined as;

$$P_k = \mu_t \nabla U.(\nabla U + \nabla U^T) - \frac{2}{3}\nabla.U(3\mu_t \nabla.U + \rho k) \tag{17}$$

In this turbulence model, the constant coefficients are as follows: Cμ=0.09, Cε₁=1.44, Cε₂=1,92, σk=1, σε=1.3

$$\mu_t = \rho c_\mu k^2/\varepsilon \tag{18}$$

2.5. Boundary conditions

This numerical simulation was conducted under the assumptions that the flow is three-dimensional, steady, and fully developed. Natural convection and heat loss to the surroundings were considered negligible, and gravitational effects were ignored. The velocity profile at the inlet was assumed to be smooth, while the thermophysical properties of the hybrid nanofluid were regarded as constant and unaffected by temperature variations. The inlet boundary conditions were set with a defined flow velocity and a temperature of 300.15 K.

Inlet boundary:

$$u = u_{in}, v=w=0, k_{in} = \frac{3}{2}(Iu_{in})^2, \varepsilon_{in} = C_\mu^{3/4}\frac{K^{3/2}}{L_t} \tag{19}$$

Outlet boundary:

The pressure is set to atmospheric pressure, which corresponds to a gauge pressure of zero.

$$\frac{\partial u}{\partial z} = \frac{\partial v}{\partial z} = \frac{\partial w}{\partial z} = 0, \frac{\partial T}{\partial z} = 0, \frac{\partial k}{\partial x} = \frac{\partial\varepsilon}{\partial x} = 0 \tag{20}$$

At the wall:

$$u = v = w=0, q^. = q_{wall} \tag{21}$$

2.6. Grid independence and code validation

A steady-state, 3D model was developed to simulate flow dynamics in a corrugated tube. Mesh generation is a critical step in numerical simulations, impacting both accuracy and computational efficiency. Due to the complex flow near the corrugated surface, capturing this region properly is essential for analyzing pressure drop and the Nusselt number. The mesh was created using ANSYS Workbench 19.0 with an unstructured grid, refined near the walls to accurately resolve the laminar viscous sublayer. The y⁺ parameter was used to ensure proper mesh quality, especially for turbulent flows, where the boundary layer consists of multiple zones.

- Viscous sublayer (y⁺<5), where viscous forces dominate.

- Buffer layer and log-law region for higher y⁺.

For accurate results, especially when using a turbulence

model like k$-\epsilon$, it's important to keep y⁺ less than 5 near the wall to properly resolve the viscous sublayer and avoid errors in predicting flow properties [25].

$$y^+ = \frac{yu_\tau}{v} \tag{22}$$

Here, y⁺ shows the non-dimensional distance from the wall, where y is the physical distance to the wall, u_τ is the friction velocity, and v is the kinematic viscosity of the fluid. This study evaluated different mesh structures at Reynolds number of 10000 to ensure that the model provided accurate results. The specific mesh structure with 2.1 million elements was chosen for all analyses because it produced consistent results for the Nusselt number (Nu) and the friction factor (f), with deviations remaining below 2%. This indicates that increasing the mesh density further did not significantly improve the accuracy, making this mesh both efficient and accurate. Additionally, the y⁺ value of 2.46 for this mesh indicates that the mesh near the wall was fine enough to accurately capture the flow characteristics, especially within the viscous sublayer, where y⁺ values below 5 are recommended. Since this mesh successfully balances accuracy (with minimal deviation in results) and computational cost, it was chosen for further study, as shown in ▶Figure 3.

Different mesh sizes were tested to ensure grid independence. The mesh sizes ranged from 0.4 mm to 0.09 mm, and the results for the Nusselt number and friction factor were plotted. Upon comparing the results, it was found that the percentage difference in Nusselt
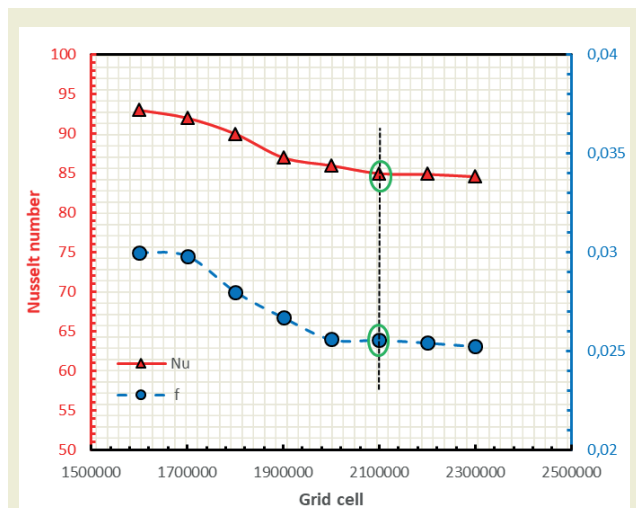
Figure 3. Grid Independence test for Nusselt number and Friction factor at Re=10000

number and friction factor between the finer meshes (0.1 mm, 0.09 mm, and 0.08 mm) was only 1–3%. This small variation indicates that further refining the mesh beyond 0.1 mm would not significantly improve the accuracy of the results but would increase computational cost and time. Thus, the 0.1 mm mesh size was selected as the most appropriate for further analysis. ▶Figure 4 illustrates the mesh configuration for the smooth pipe and the corrugate positioned at three different spacing intervals (P = 10 mm, P = 20 mm, and P = 30 mm) using the 0.1 mm mesh structure.

Figure 4. Mesh generation view of smooth tube and tube with different corrugated distances

2.7. Validation of Numerical Study

To ensure the precision and reliability of the numerical method, the results obtained from the simulation of fully developed turbulent water flow in a smooth tube are evaluated against well-known empirica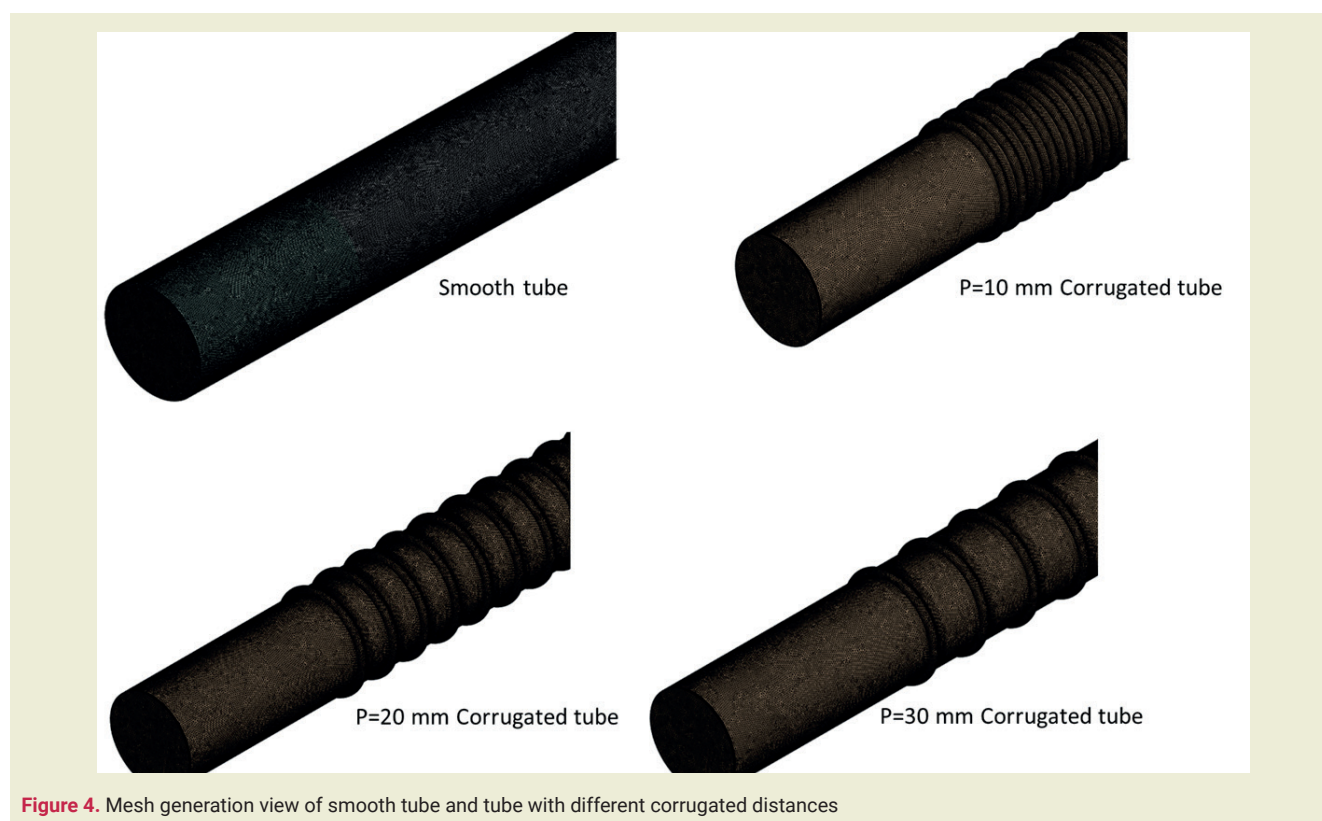l models. The comparisons involved various correlations for the Nusselt number, such as Dittus-Boelter [26] correlation (Equation 23), Gnielinski [27] correlation (Equation 24), and the Pak and Cho [19] correlation (Equation 25), as well as for the friction factor, including Blasius [28] correlation (Equation 26), McAdams [29] correlation (Equation 27), and Petukhov [30] correlation (Equation 28). The CFD simulation results of the Nusselt number and friction factor of the straight pipe were compared with the literature. They were validated against the established literature by showing maximum deviations of ±9% and ±11% respectively, as shown in ▶Figure 4. This validation confirmed the reliability of the numerical approach in predicting heat transfer and flow resistance under turbulent conditions.

$$Nu = 0.024\, Re^{0.8} Pr^{0.4} \tag{23}$$

$$Nu = \frac{(f/8)(Re_D - 1000)Pr}{1 + 12.7(f/8)^{1/2}(Pr^{2/3} - 1)} \tag{24}$$

$$Nu = 0.021 Re_b^{0.8} Pr_{nf}^{0.5}\; ;\; 10^4 \leq Re_b \leq 10^5 \tag{25}$$

$$f = 0.316 Re^{-0.25} \tag{26}$$

$$f = 0.18\, Re^{-2} \tag{27}$$

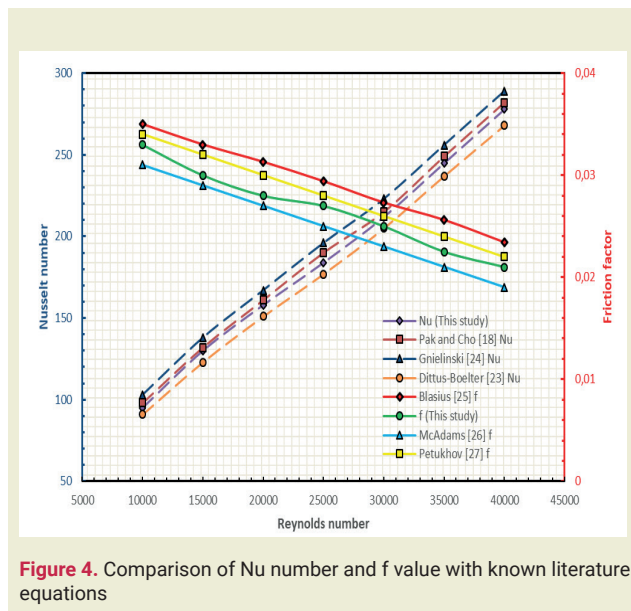$$f = (0.29 \ln Re - 1.64\,)^2 \tag{28}$$

Figure 4. Comparison of Nu number and f value with known literature equations

3. Results and discussion

First, experiments were carried out with water to evaluate the thermal performance of the corrugated pipe without using nanofluid. As shown in ▶Figure 5(a), cor-

rugated tubes exhibited higher Nusselt numbers than smooth tubes due to enhanced turbulence, flow separation, and recirculation, which intensified mixing and reduced thermal boundary layer thickness. Heat transfer increased by 37.6%, 32.5%, and 26.3% for corrugation distances of 10 mm, 20 mm, and 30 mm, respectively. ▶Figure 5(b) shows that the friction factor remained higher in corrugated tubes due to continuous boundary layer disruption, leading to periodic flow separation, reattachment, and increased resistance.

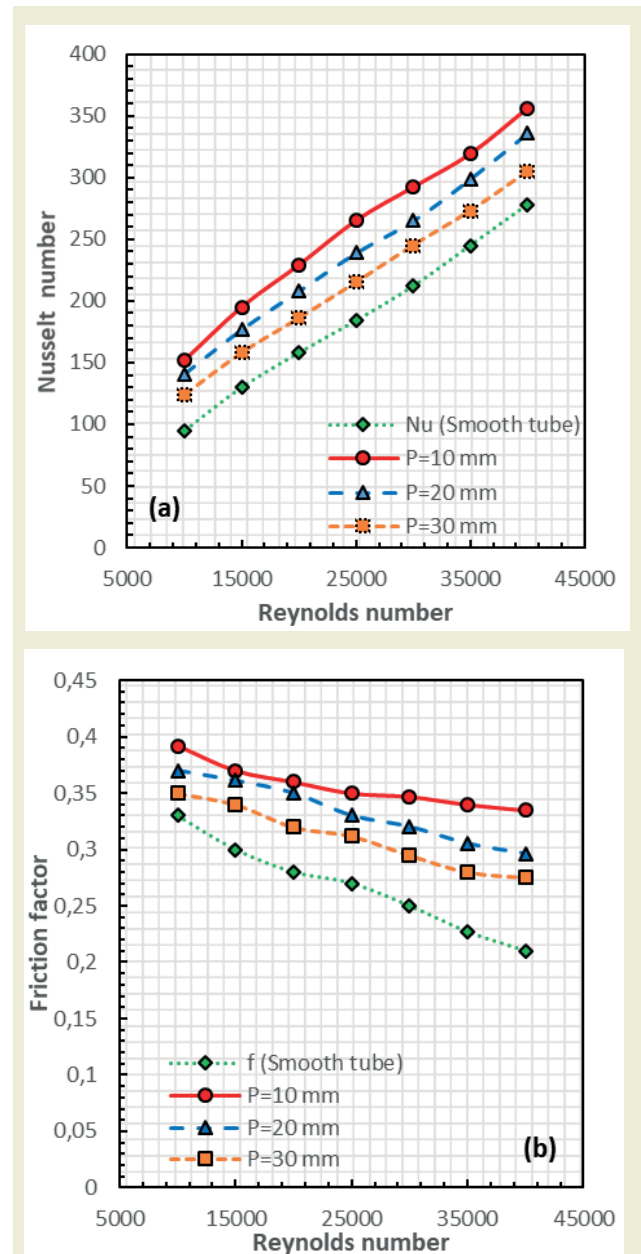**Figure 5.** The variation of (a) Nu, (b) f via Reynolds numbers at different corrugation distances for water

The intensified mixing in corrugated tubes enhances heat transfer by transporting cooler fluid from the core to the heated wall and rapidly removing heated fluid. This process reduces the thermal boundary layer thickness, minimizing heat transfer resistance and increasing convective efficiency. As a result, at the same Reyn-

olds number, corrugated tubes achieved higher Nusselt numbers than smooth tubes, with enhancements of 37.6%, 32.5%, and 26.3% for corrugation distances of 10 mm, 20 mm, and 30 mm, respectively. The increased friction factor in corrugated tubes, shown in ▶**Figure 5**(b), is attributed to boundary layer disruption caused by surface geometry. Unlike smooth tubes, where the friction factor decreases with the Reynolds number due to a thinning viscous sublayer, corrugated tubes experience persistent turbulence, flow separation, and recirculation. The repeated formation of low-pressure zones and reattachment points along the corrugated surface further amplifies flow resistance [31].
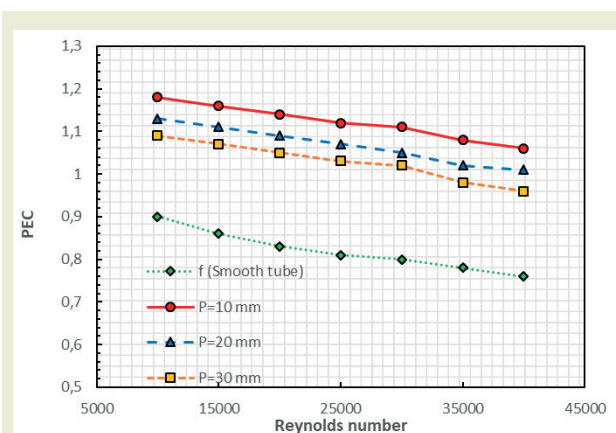

Figure 6. Variation of PEC at different corrugate distances for water

Figure 7. Variation of Nusselt number of MWCNT/Al$_2$O$_3$ nanofluids at different volume fractions at different corrugate distances at 40000 Reynolds number

The friction factor in the tube with a corrugate distance of P = 10 mm was found to be 15.81 times higher than in the smooth tube. As the distance (P) increases, the interruptions become less frequent, which slightly reduces the friction factor, as seen with P = 20 mm and P = 30 mm. This shows how strongly the corrugate distance influences flow resistance. However, the friction factor remains significantly higher than that of smooth tubes because each corrugate still induces flow separation and turbulence. Therefore, as the corrugate distance decreases, the flow encounters greater resistance, which is reflected in increasing friction factor values. ▶**Figure 6** illustrates the PEC for various Reynolds numbers across corrugate distances. Each corrugate distance follows a similar pattern within the Reynolds number range, with PEC values decreasing consistently as Reynolds numbers increase. Among the tested corrugate distances, P=10 mm achieves the highest PEC value at 1.18, while P=30 mm yields the lowest at 1.09. This suggests closer corrugate distances provide better hydrodynamic performance, whereas higher Reynolds numbers correspond to lower PEC values. These findings emphasize the significant role that corrugate distances play in enhancing flow performance, underscoring the importance of selecting optimal corrugate distance to improve flow efficiency in corrugated tubes.

After analyses conducted on corrugated tubes using water as the working fluid, the thermohydraulic per-
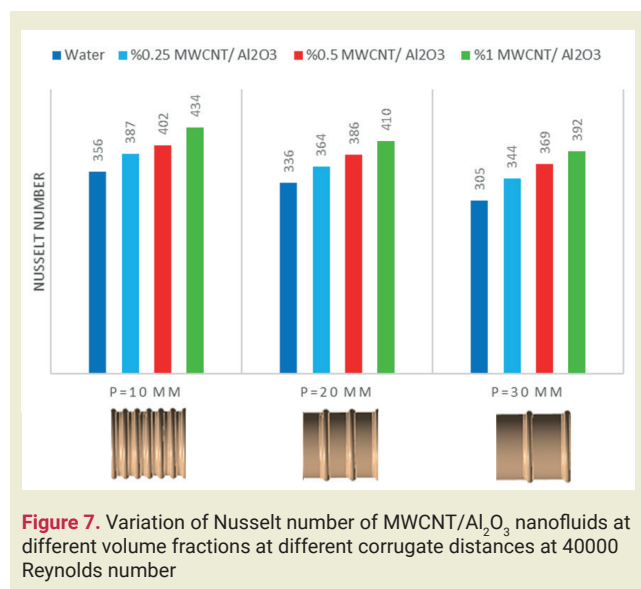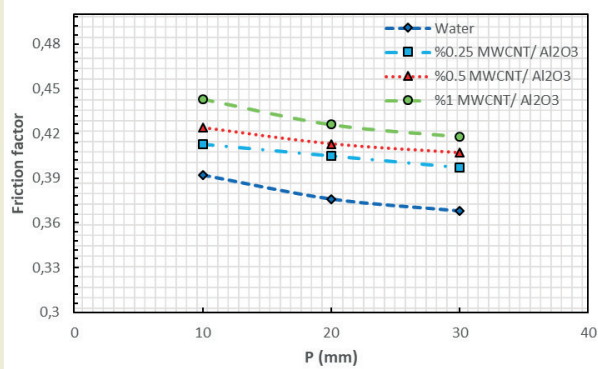
formance of MWCNT/Al$_2$O$_3$ nanofluids mixed in a %60-40 ratio was examined at three different volume fractions (0.25%, 0.5%, and 1%). As shown in ▶**Figure 7**, the highest Nusselt number was obtained with the nanofluid containing a 1% volume fraction with a P=10 mm pitch. In the corrugated tube with a P=10 mm pitch, the 1% MWCNT/Al$_2$O$_3$ nanofluid recorded a 17.97% increase in the Nusselt number compared to water. Relative to a smooth, non-corrugated tube, this increase was 35.94%. It was observed that reducing the pitch of the corrugations was more effective than increasing the nanofluid volume fraction. This can be attributed to the fact that refining the physical design of the tube (such as by reducing the corrugate distance) enables efficient enhancement of both convective and conductive heat transfer processes with minimal extra energy input. In contrast, higher nanoparticle concentrations often yield diminishing returns, as they increase the fluid's viscosity and the associated pumping energy needed to maintain flow.

▶**Figure 8** shows the change in the friction factor of MWCNT/Al$_2$O$_3$ nanofluid and water at different volume fractions as the corrugate distance increases with a Reynolds number of 10000. The friction factor decreases with increasing corrugate distance but increases as the nanofluid volume fraction increases. The highest friction factor was obtained in the corrugated tube with a 1% MWCNT/Al$_2$O$_3$ volume fraction and a corrugate distance of P=10 mm. Compared to the case using water, it was observed that using a 1% MWCNT/Al$_2$O$_3$ nanofluid increased the friction factor by 11.51%. This indicates that the use of corrugates causes more friction increase than the use of nanofluids.

▶**Figure 9** shows the performance of MWCNT/Al$_2$O$_3$ nanofluids with three different volume concentrations at three different corrugate distances. The highest performance evaluation criterion was obtained with the

maximum PEC value was recorded at approximately 1.09.

Figure 8. Effect of the corrugate distance on the friction factor of MWCNT/Al$_2$O$_3$ nanofluid and water at different volume fractions at 10000 Reynolds number
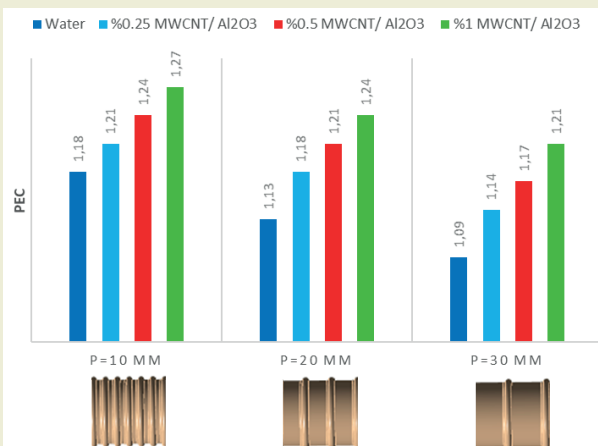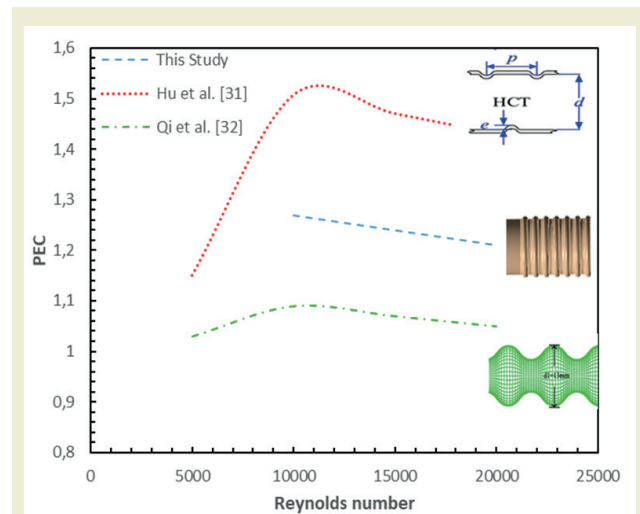

Figure 9. Change in performance evaluation criteria (PEC) of MWCNT/Al$_2$O$_3$ nanofluid with different volume fraction at different corrugate distances at 10000 Reynolds number

Figure 10. Comparison with literature studies using corrugated tube

MWCNT/Al$_2$O$_3$ nanofluid with 1% volume concentration at P = 10 mm groove distance with a value of 1.27. The lowest value was obtained with the MWCNT/Al$_2$O$_3$ nanofluid with 0.25% volume concentration at P = 30 mm groove distance with a value of 1.14.

Finally, a comparison was made with experimental studies in the literature to evaluate the performance of this study. As seen in ▶**Figure 10**, the thermal performance of studies conducted using different corrugated tubes was assessed. Qi et al. [32] examined flow resistance and heat transfer performance of TiO$_2$-water nanofluids in corrugated and circular tubes using experimental and numerical methods. The results showed that adding nanoparticles did not significantly increase the resistance, but the corrugated tube combined with nanofluids increased the heat transfer by up to 53.95%. Hu et al. [33] studied the effects of corrugated tubes parameters on thermal-hydraulic performance using three different corrugated tubes and air and helium as working fluids. It was observed that the Nusselt number (Nu) increased with decreasing p/d ratio. The best-performing corrugated tube exhibited a 60% higher Nu value compared to the smooth tube. Additionally, the

4. Conclusions

This study investigated the effects of corrugation distance on the performance of MWCNT/Al$_2$O$_3$ nanofluid with different volume concentrations in corrugated tubes. For corrugations with distances of P=10 mm, P=20 mm, and P=30 mm, MWCNT/Al$_2$O$_3$ nanofluids mixed at a 60:40 ratio were analyzed at volume fractions of 0.25%, 0.5%, and 1% using the ANSYS Workbench 19.0 program. The Reynolds numbers ranged from 10000 to 40000. This analysis aimed to examine the interaction between heat transfer, friction factor, and pressure drop, providing important insights for improving and optimizing such systems. The main conclusions derived from this study are as follows:

- Corrugated tubes demonstrated superior Nusselt numbers compared to smooth tubes, attributed to enhanced recirculation, backflow, and the formation of a thinner boundary layer. The Nusselt number in corrugated tubes increased significantly compared to the smooth tube, with enhancements of 37.6% for a corrugation distance of 10 mm, 32.5% for 20 mm, and 26.3% for 30 mm.

- Corrugated surfaces increase friction factors compared to smooth tubes. The corrugated surfaces disrupt the normally smooth viscous sublayer, causing greater interaction between the flow and the tube walls, which increases flow resistance and friction. The tube with a corrugation distance of 10 mm exhibited a friction factor 15.81 times higher than that of the smooth tube. Increasing the corrugation distance to 20 mm and 30 mm reduced the frequency of flow disruptions, leading to a slight decrease in the friction factor.

- Reducing corrugate distance increases turbulence and fluid mixing, leading to higher Nusselt numbers, indicating improved heat transfer. In contrast, increasing corrugate distance produces less turbulence and mixing, resulting in lower Nusselt numbers and reduced heat transfer efficiency.

- Smaller corrugate distances improve hydrodynamic performance. However, as the Reynolds number increases, the performance evaluation criteria (PEC) values decrease for all corrugate distances. The maximum performance evaluation criterion of 1.27 was achieved using the MWCNT/Al_2O_3 nanofluid with a 1% volume concentration at a groove distance of 10 mm.

- Increasing the volume fraction of a nanofluid enhances heat transfer through better thermal conductivity, while changes in corrugation distance have a more significant impact on heat transfer by altering the flow structure, increasing turbulence, and strengthening convection.

- This study evaluated the thermal performance of MWCNT/Al_2O_3 hybrid nanofluids at concentrations of 0.25%, 0.50%, and 1%, with the most effective heat transfer observed at 1%. Although increasing the concentration beyond this value may further enhance thermal conductivity, it could also result in undesirable effects such as higher viscosity, increased energy consumption for fluid circulation, and nanoparticle clustering, which may deteriorate flow stability and overall system efficiency.

Future studies could explore the existence of an optimal concentration (peak point) by examining a wider range of concentrations and evaluating the trade-offs between thermal performance and fluid flow characteristics.

Research ethics

Not applicable.

Author contributions

The author solely conducted all stages of this research.

Competing interests

The author state(s) no conflict of interest.

Research funding

None declared.

Data availability

Not applicable.

Peer-review

Externally peer-reviewed.

Orcid

Fatma Oflaz https://orcid.org/0000-0002-9636-5746

References

[1] Kalendar, A., Galal, T., Al-Saftawi, A. and Zedan, M. (2011) Enhanced tubing thermal performance for innovative MSF system. Journal of Mechanical Science and Technology, 25, 1969–77. https://doi.org/10.1007/s12206-011-0524-7

[2] Kareem, Z.S., Mohd Jaafar, M.N., Lazim, T.M., Abdullah, S. and Abdulwahid, A.F. (2015) Passive heat transfer enhancement review in corrugation. Experimental Thermal and Fluid Science, Elsevier Inc. 68, 22–38. https://doi.org/10.1016/j.expthermflusci.2015.04.012

[3] Van Cauwenberge, D.J., Dedeyne, J.N., Van Geem, K.M., Marin, G.B. and Floré, J. (2018) Numerical and experimental evaluation of heat transfer in helically corrugated tubes. AIChE Journal, 64, 1702–13. https://doi.org/10.1002/aic.16038

[4] Andrade, F., Moita, A.S., Nikulin, A., Moreira, A.L.N. and Santos, H. (2019) Experimental investigation on heat transfer and pressure drop of internal flow in corrugated tubes. International Journal of Heat and Mass Transfer, Elsevier Ltd. 140, 940–55. https://doi.org/10.1016/j.ijheatmasstransfer.2019.06.025

[5] Navickaitė, K., Cattani, L., Bahl, C.R.H. and Engelbrecht, K. (2019) Elliptical double corrugated tubes for enhanced heat transfer. International Journal of Heat and Mass Transfer, 128, 363–77. https://doi.org/10.1016/j.ijheatmasstransfer.2018.09.003

[6] Wang, G., Qi, C., Liu, M., Li, C., Yan, Y. and Liang, L. (2019) Effect of corrugation pitch on thermo-hydraulic performance of nanofluids in corrugated tubes of heat exchanger system based on exergy efficiency. Energy Conversion and Management, 186, 51–65. https://doi.org/10.1016/j.enconman.2019.02.046

[7] Ekiciler, R. (2024) Analysis and Evaluation of the Effects of Uniform and Non-uniform Wall Corrugation in a Pipe Filled with Ternary Hybrid Nanofluid. Arabian Journal for Science and Engineering, Springer Berlin Heidelberg. 49, 2681–94. https://doi.org/10.1007/s13369-023-08459-4

[8] Ajeel, R.K., Saiful-Islam, W., Sopian, K. and Yusoff, M.Z. (2020) Analysis of thermal-hydraulic performance and flow structures of nanofluids across various corrugated channels: An experimental and numerical study. Thermal Science and Engineering Progress, 19. https://doi.org/10.1016/j.tsep.2020.100604

[9] Wang, W., Zhang, Y., Lee, K.S. and Li, B. (2019) Optimal design of a double pipe heat exchanger based on the outward helically corrugated tube. International Journal of Heat and Mass Transfer, Elsevier Ltd. 135, 706–16. https://doi.org/10.1016/j.ijheatmasstransfer.2019.01.115

[10] Wang, W., Zhang, Y., Li, B. and Li, Y. (2018) Numerical investigation of tube-side fully developed turbulent flow and heat transfer in outward corrugated tubes. International Journal of Heat and Mass Transfer, Elsevier Ltd. 116, 115–26. https://doi.org/10.1016/j.ijheatmasstransfer.2017.09.003

[11] Wang, W., Zhang, Y., Liu, J., Li, B. and Sundén, B. (2018) Numerical investigation of entropy generation of turbulent flow in a novel outward corrugated tube. International Journal of Heat and Mass Transfer, Elsevier Ltd. 126, 836–47. https://doi.org/10.1016/j.ijheatmasstransfer.2018.06.017

[12] Wang, W., Zhang, Y., Li, Y., Han, H. and Li, B. (2018) Multi-objective

optimization of turbulent heat transfer flow in novel outward helically corrugated tubes. Applied Thermal Engineering, Elsevier Ltd. 138, 795–806. https://doi.org/10.1016/j.applthermaleng.2017.12.080

[13] Oflaz, F., Keklikcioglu, O. and Ozceyhan, V. (2022) Investigating thermal performance of combined use of SiO2-water nanofluid and newly designed conical wire inserts. Case Studies in Thermal Engineering, Elsevier Ltd. 38, 102378. https://doi.org/10.1016/j.csite.2022.102378

[14] Palanisamy, K. and Kumar, P.C.M. (2017) Heat transfer enhancement and pressure drop analysis of a cone helical coiled tube heat exchanger using MWCNT/water nanofluid. Journal of Applied Fluid Mechanics, 10, 7–13. https://doi.org/10.36884/jafm.10.SI.28265

[15] Umar Ibrahim, I., Sharifpur, M. and Meyer, J.P. (2024) Mixed Convection Heat Transfer Characteristics of Al2O3 − MWCNT Hybrid Nanofluid under Thermally Developing Flow; Effects of Particles Percentage Weight Composition. Applied Thermal Engineering, Elsevier Ltd. 249, 123372. https://doi.org/10.1016/j.applthermaleng.2024.123372

[16] Painuly, A., Joshi, G., Negi, P., Zainith, P. and Mishra, N.K. (2025) Experimental analysis of W/EG based Al2O3-MWCNT non-Newtonian hybrid nanofluid by employing helical tape inserts inside a corrugated tube. International Journal of Thermal Sciences, Elsevier Masson SAS. 208, 109399. https://doi.org/10.1016/j.ijthermalsci.2024.109399

[17] Khalili Najafabadi, M., Hriczó, K. and Bognár, G. (2024) Enhancing the heat transfer in CuO-MWCNT oil hybrid nanofluid flow in a pipe. Results in Physics, 64. https://doi.org/10.1016/j.rinp.2024.107934

[18] Scott, T.O., Ewim, D.R.E. and Eloka-Eboka, A.C. (2023) Experimental study on the influence of volume concentration on natural convection heat transfer with Al2O3-MWCNT/water hybrid nanofluids. Materials Today: Proceedings, Elsevier Ltd. c, 0–6. https://doi.org/10.1016/j.matpr.2023.07.290

[19] Pak, B.C. and Cho, Y.I. (1998) Hydrodynamic and heat transfer study of dispersed fluids with submicron metallic oxide particles. Experimental Heat Transfer, 11, 151–70. https://doi.org/10.1080/08916159808946559

[20] H.C., B. (1952) The viscosity of concentrated suspensions and solutions. J Chem Phys 20 571,.

[21] Xu, J.Z., Gao, B.Z. and Kang, F.Y. (2016) A reconstruction of Maxwell model for effective thermal conductivity of composite materials. Applied Thermal Engineering, 102, 972–9. https://doi.org/10.1016/j.applthermaleng.2016.03.155

[22] Oflaz, F. (2025) Evaluation of the thermo - hydraulic behavior of water - based graphene and Al2O3 hybrid nanofluids in a circular tube through CFD simulations. Journal of Thermal Analysis and Calori-

metry, Springer International Publishing. https://doi.org/10.1007/s10973-025-13993-4

[23] Keklikcioglu, O. (2023) Optimization of thermal and hydraulic characteristics of a heat exchanger tube using ternary hybrid nanofluids with various configurations. Journal of Thermal Analysis and Calorimetry, Springer International Publishing. 148, 7855–67. https://doi.org/10.1007/s10973-023-12263-5

[24] Suseel Jai Krishnan, S., Momin, M., Nwaokocha, C., Sharifpur, M. and Meyer, J.P. (2022) An empirical study on the persuasive particle size effects over the multi-physical properties of monophase MWCNT-Al2O3 hybridized nanofluids. Journal of Molecular Liquids, Elsevier B.V. 361, 119668. https://doi.org/10.1016/j.molliq.2022.119668

[25] Ao, S.I., Castillo, O., Douglas, C., Dagan Feng, D. and Korsunsky, A.M. (2017) Proceedings of the international multiconference of engineers and computer scientists 2017. Lecture Notes in Engineering and Computer Science, 2227.

[26] F.W. Dittus, L.M.K.B. (1930) Heat transfer in automobile radiators of the tubular type. The University of California Publications on Engineering, 2, 443–61.

[27] Gnielinski, V. (1976) New equations for heat and mass transfer in turbulent pipe and channel flow. International Chemical Engineering, 27, 359–368.

[28] H. Blasius. (1913) The Law of Similarity for Frictions in Liquids, "Notices of research in the field of engineering. Not Res F Eng, 131, 1–41.

[29] McAdams, W.H. (1942) Heat Transmission. (Second Ed), McGraw-Hill, New York,.

[30] B.S. Petukhov. (1970) Heat Transfer and Friction in Turbulent Pipe Flow with Variable Physical Properties. Advances in Heat Transfer, 6, 503–64.

[31] Togun, H., Homod, R.Z., Yaseen, Z.M., Abed, A.M., Dhabab, J.M., Ibrahem, R.K. et al. (2022) Efficient Heat Transfer Augmentation in Channels with Semicircle Ribs and Hybrid Al2O3-Cu/Water Nanofluids. Nanomaterials, 12. https://doi.org/10.3390/nano12152720

[32] Hu, Q., Qu, X., Peng, W. and Wang, J. (2022) Experimental and numerical investigation of turbulent heat transfer enhancement of an intermediate heat exchanger using corrugated tubes. International Journal of Heat and Mass Transfer, Elsevier Ltd. 185, 122385. https://doi.org/10.1016/j.ijheatmasstransfer.2021.122385

[33] Qi, C., Wan, Y.L., Li, C.Y., Han, D.T. and Rao, Z.H. (2017) Experimental and numerical research on the flow and heat transfer characteristics of TiO2-water nanofluids in a corrugated tube. International Journal of Heat and Mass Transfer, Elsevier Ltd. 115, 1072–84. https://doi.org/10.1016/j.ijheatmasstransfer.2017.08.098

Evaluation of tool radius and machining parameters on cutting forces and surface roughness for AA 6082 aluminum alloy

Ayşe Sena Yamaner[1*] (iD), **Bahar Sayın Kul**[1] (iD)

[1]Selçuk University, Faculty of Technology, Department of Mechanical Engineering, Türkiye

Abstract: In this study, the effects of machining parameters on surface roughness and cutting forces during the machining of AA6082 aluminum alloy, which is widely utilized in automotive, manufacturing and aerospace industries, on a conventional lathe were investigated. Tool corner radius (0.4 mm and 0.8 mm), depth of chip (0.25-0.5 mm), feed rate (0.1-0.2 mm/rev) and cutting speed (65-105 m/min) were used as input variables. Surface roughness and cutting forces were evaluated as outputs; effective parameters and optimum process conditions were determined by analysis of variance (ANOVA) and S/N ratios. The results show that tools with a corner radius of 0.8 mm provide lower cutting forces and better surface quality, and the study provides practical optimization data for the machinability of AA6082 alloy, making original contributions to both academic literature and industrial applications.

Keywords: AA 6082; machinability; turning; surface roughness; cutting force; ANOVA.

1. Introduction

In the manufacturing sector, it is common to encounter areas where materials that do not contain any other metal in their composition are used, but alloys have a much stronger place. Each alloy has its own unique properties that put it ahead of others. This can sometimes be corrosion resistance, sometimes casting ability, sometimes mechanical properties, etc. The inherent recyclability and reusability of aluminum without any loss of properties gives it a head start in manufacturing processes over less economical materials such as steel [1]. In addition, being a material that offers both lightness and durability, it is used as a substitute for steel in many engineering applications. This results in not only pure aluminum but also alloyed aluminum becoming more and more common in many sectors. AA6082, an alloy of the aluminum, which is the most easily machined of non-ferrous metals, is widely preferred due to its low density, lightness, low cost, high strength (the highest strength of the 6000 series alloys), high corrosion resistance and its structure that allows forging [2-4]. This material may not respond well to machinability due to its high thermal expansion coefficients and tendency to form build-up edges, as well as its poor ductility [5]. At this point, the priority needs in the machining process, which is a multifaceted pro-cess where many factors such as cost effectiveness, quality, applicability, cutting force, energy consumption, tool wear, surface quality, production speed, maintenance are effective, should be analyzed, and the process should be brought to a state that will meet these needs with optimum parameter/level selections. Machining is a multi-faceted process influenced by numerous factors such as cost effectiveness, surface quality, tool wear, energy consumption, production speed, and maintenance requirements. A key component of machining optimization involves modeling and analyzing the relationship between input parameters (such as cutting speed, feed rate, depth of cut, and tool geometry) and output responses (such as cutting force, surface roughness, material removal rate, and tool life). Optimization approaches such as S/N ratios as well as statistical methods such as ANOVA and multi-criteria decision-making tools play an important role in the development of robust prediction models for machining processes. These methods allow the systematic evaluation of factor influences, interaction effects, and identification of optimal parameter settings for achieving desired machining outcomes. General machining processes are turning, milling, drilling, grinding, reaming, honing, rolling, forging, casting, etc., and turning is responsible for an average of 45% of the workload caused by such machining processes [6]. Therefore, a literature

summary of machining processes, primarily turning, involving AA6082 alloy is presented below.

In the study by Saravanan and Mahendran [3], the machinability of AA6082 alloy produced with boron carbide (B4C) reinforcement at different weight percentages was investigated by computer numerical control (CNC) turning process. In the study, which presented evaluations in terms of tool wear and surface roughness at the center of depth of cut, feed rate and cutting speed it was reported that boron carbide reinforcement improved the machinability. Jebaraj, Pradeep Kumar [4] conducted a study to evaluate the impact of machining parameters, one being cooling media (dry, wet, cryogenic CO_2 and cryogenic LN_2) on surface finish, tool wear and cutting forces during milling of 6082-T6 alloy. It was emphasized that while the best machining performance is obtained with wet cooling, cryogenic cooling can extend tool life by preventing high temperature generation but at the same time, it can compromise tool wear. The study by Yapan, Türkeli [5] is an example of the use of minimum quantity lubrication (MQL) processes using GNP-added nanofluid (N-MQL) in the milling of Al6082 alloy. In the study where the cutting temperature, force, feed force, roughness and chip morphology as well as carbon emission and total processing cost were evaluated, it was found that the use of N-MQL improved all parameters compared to dry cutting and MQL. In the study by Chowdhury, Das and Chakraborty [6], the effects of parameters such as cutting speed, feed rate and depth of cut on machinability and surface quality in CNC turning operations of Aluminum 6082-T6 alloy were analyzed using Fuzzy multi-criteria decision-making methods. While it was reported that decision-making methods can be used as a powerful tool for the optimization of parameters, it was stated that the material is suitable for machinability in CNC. Singh, Chauhan [7] aimed to reduce the roughness of the surface resulting from the machinability of Al-6082 T-6 on a CNC lathe in their study. It was observed that there is a ranking among the parameters in terms of their effects on roughness as follows: speed, feed rate, depth of chip. Turan et al. [8] investigated the effects of tool coating, cutting speed and feed rate on surface roughness and geometric tolerances in dry drilling of Al 6082-T6 alloy. The experimental results showed that uncoated tools gave the lowest surface roughness, while TiAlN coated tools gave the lowest cylindricity error. They also reported that among the prediction models, the Artificial Neural Network (ANN) achieved the highest accuracy. Işık et al [9] fabricated AlSi10Mg samples by selective laser melting (SLM) and investigated the effects of scanning distance (SD), scanning speed (SS) and laser power (P) as fabrication parameters on quality outputs such as surface roughness, diameter change, circularity change and concentricity. According to the results obtained, the increase in laser power improved the roughness and diameter change, while the increase in scanning distance and scanning speed had negative effects on circularity and concentricity; moreover, the most suitable production parameter combination was

determined as A2B1C3 (0.10 mm, 1450 mm/s, 370 W) by the gray relationship analysis (GRA) method. According to ANOVA analysis, it was determined that the most effective parameter on surface roughness was laser power with a rate of 53.22%. Özlü [10] investigated the effects of cutting speed and feed rate on cutting forces and surface roughness in turning Sleipner cold work tool steel. Increasing feed rate increased the forces and roughness, while higher cutting speeds decreased these values. As a result of the experiment, the lowest cutting force and the best surface finish were obtained with a cutting speed of 150 m/min and a feed rate of 0.1 mm/rev. Binali et al [11] investigated the effects of cutting speed, feed rate, chip depth and cutting media parameters on surface roughness, cutting force and tool wear in the machining of Al6082 alloy. They concluded that the nano-SiO_2-doped olive oil-based MQL method showed superior performance by providing the lowest cutting force, temperature and surface roughness values. The results reported that nano-doped biobased MQL systems offer an effective alternative for sustainable and highly efficient machining.

Kartal, Yerlikaya and Gökkaya [12] studied the extent to which the machining of Al-6082 T6 aluminum alloy by abrasive water jet (AWJ) method causes changes in terms of surface roughness and macro surface characteristics. As a result of the evaluation carried out for different levels of cutting parameters such as distance, abrasive flow rate, spindle speed and nozzle feed rate, it was found that the most effective parameter on surface quality was the nozzle feed rate.

Stanojković and Radovanović [13] investigate the effects of the parameters of speed, feed and depth of chip on the force, moment and surface roughness during the milling process of AA-6082-T6 alloy. As a result of the experiments studied out using solid carbide end mills, it was suggested that the order of importance in terms of their effects are depth of chip, feed and speed.

In this study, Varatharajulu, Duraiselvam [14] evaluated the impact of processing parameters during surface milling of AA-6082 alloy. In the study where the depth of chip, feed and spindle speed parameters were taken as reference, evaluations were made on the roughness, material removal rate and processing time. It was reported that with the correct combination of spindle speed, feed and depth of chip, roughness and processing time could be brought to the best level. The study by Garcia, Feix [15] is about the finish turning of 6082-T6 aluminum alloy with an uncoated carbide tool under dry and reduced quantity lubricant (RQL) conditions. The study showed that the use of RQL was superior to the dry condition by reducing both surface roughness and tool wear. Beșliu and Tamașag [16] evaluated the impact of cooling and cutting conditions on surface quality during machining of AA6082-T6 aluminum alloy. Although the MQL method gives better results than dry conditions, it was stated that the results obtained at some feed rates are not stable. In this study,

Table 1. Chemical composition-AA 6082 [23]

Element	%Al	%Fe	%Cu	%Mn	%Mg	%Cr	%Ni	%Zn	%Ti	%Ga	%V	%Si
% weight	96.5	0.47	0.1	0.55	1.15	0.17	0.013	0.09	0.019	0.012	0.017	0.85

Quintana, Gomez [17] evaluated the impact of feed and tool diameter used in milling operations of aluminum 6082 alloy on cycle time, forces, roughness and dimensional accuracy. One of the study results is that the best surface quality and dimensional accuracy are obtained when low feed rate and large diameter cutting tools are used. Yigit [18] investigated the effect of coolant/lubricant medium on tool wear, cutting forces and surface roughness during machining of 6082 aluminum alloy at different cutting speeds. Compared to dry cutting, MQL stood out with lower wear and longer life. Patel and Deshpande [19] studied the effects of machining parameters on surface roughness (Ra) and material removal rate (MRR) in turning process of aluminum 6082 alloy. It is emphasized that the optimum parameters for the lowest roughness and the highest metal removal rate are 1.5 mm corner radius, 0.142 mm/rev feed rate, 1235 rpm spindle speed. Solanki and Jain [20] studied on the effect of process parameters speed, feed and depth of chip on response variables-Material Removal Rate (MRR) and Surface Roughness (Ra) for aluminum-6082 material. It was stated that the most effective parameters were feed for roughness and depth of chip for MRR. The study by Aydın [21] is about the changes in cutting force and cutting power at depths of cut lower than the tool nose radius during turning of AA6082-T4 aluminum alloy. It has been shown by both Finite Element Analysis and Experimental study that chip depth has a considerable impact on forces and speed has a considerable impact on power. In the study investigating the optimization of cutting parameters on surface roughness and material removal rate (MRR) in turning process of Aluminum Alloy 6082 (AA6082), Aryan, John [22] reported that spindle speed is one of the most effect parameters on MRR and roughness. Although these studies have provided valuable insights, a comprehensive analysis combining the effects of tool nose radius with detailed cutting parameters on both surface roughness and cutting forces under conventional dry turning conditions remains limited.

The aim of this study was to evaluate the effect of various machining parameters on cutting forces and surface roughness in machining AA 6082 aluminum alloy using 0.8 and 0.4 corner radius cutting tools. In the literature, some important gaps have been observed in the studies on the machinability of AA6082 aluminum alloy. While only the effect of machining parameters is commonly evaluated, this study provides a broader perspective by taking into account the significant effect of tool corner radius. In this context, the data obtained can be a direct reference for both academic research and industrial applications. In this research, the effects of different levels of cutting speed and feed parameters were investigated

according to a full factorial experimental design and ANOVA analysis and (S/N) ratios were utilized to determine the best turning environments.

2. Materials and Methods

2.1. Workpiece Material

AA 6082 aluminum alloy (Seykoç, Kocaeli, Turkey) with a length of 500 mm and a diameter of 50 mm, which is widely used among alloys, was utilized as the workpiece material in the experimental study. The chemical characteristics of the workpiece are shown in ▶Table 1 and the physical and mechanical properties are given in ▶Table 2.

Table 2. Physical and Mechanical Properties of AA6082 Alloy [23]

Property	Value
Tensile Stress (Mpa)	310
Yield Stress (Mpa)	285
Length (%)	10
Hardness ($Hv_{0.2}$)	115

2.2. Experiments, Cutting Tools and Cutting Parameters

Cutting tools were selected in accordance with ISO 3685 with TiC coated CCMT 09T308-304 and CCMT 09T304-304 (Korloy, Seoul, Republic of Korea) series cutting tools according to the widely preferred applications in the manufacturing industry [24]. In accordance with the purpose of the experiment and according to the hypothesis established by examining the studies in the literature, the parameters were selected taking into account both the suggestions of the tool company and the material properties. Tools were changed in each run of the machining experiments. The cutting-edge length is 9 mm, the cutting tool clearance angle was 7° degrees and the insert thickness was 4.97 mm. Two different types of cutting tools were used, with a corner radius of 0.8 mm and a corner radius of 0.4 mm. In the cutting experiments, a full factorial experimental design was utilized to determine the speed, feed and depth of chip parameters/levels. Full factorial experimental design is considered to be an optimal approach as it evaluates all possible combinations of cutting parameters given a small number of factors [25-27]. The first step in designing the study is to determine the processing parameters that could effect the responses. After determining the parameters with their levels, the experimental design was created for all possible combinations. In the

next step, the specified parameter and level combination was tested and the experimental results were evaluated. When ▶Table 3 shows the determined processing parameters with their levels, ▶Figure 1 shows an overview of the study.

Figure 1. Overview of the study
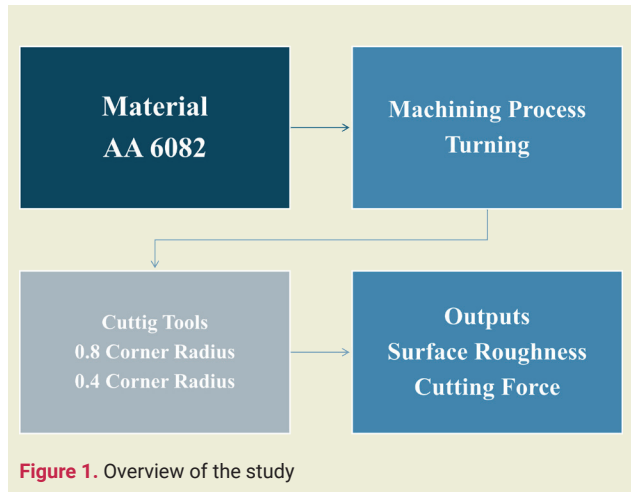
Table 3. Experiment parameters

Exp. No	Cutting Speed	Feed Rate	Chip Depth
	(m/min)	(mm/rev)	(mm)
1	65	0.1	0.25
2	105	0.1	0.25
3	65	0.1	0.5
4	105	0.1	0.5
5	65	0.2	0.25
6	105	0.2	0.25
7	65	0.2	0.5
8	105	0.2	0.5

As seen in the literature, the "smaller is better" approach for the S/N ratio is preferred for quality characteristics where it is desired to keep the obtained measurement values at the lowest level [28]. When determining the optimum levels of machining parameters, the values of cutting force and surface roughness should be the smallest in order to increase productivity. Therefore, in the calculation of the S/N ratios, the objective function of the "smaller is better" case of the performance characteristic given in Eq.1 was used.

$$S/N = -10log\left(\frac{1}{n}\sum_{i=1}^{n}Y_i^2\right) \quad (1)$$

ANOVA was applied to the experimental results at 95% (α=0.05) confidence level to determine the effect levels of machining parameters on force and roughness. Optimization studies and variance analysis were carried out with the help of Minitab program.

1.1. Measurement of Cutting Forces and Surface Roughness of Machine Tool

A total of 16 machining experiments were studied out using a conventional De Lorenzo S547-8899 lathe available at Selcuk University Faculty of Technology. Table 4 presents specifications of it. Forces were measured with a KISTLER 9275 dynamometer (Kistler Instrumente AG, Winterthur, Switzerland). For the cutting forces, the force values obtained during cutting were averaged and recorded in the computer environment. After the experiment, the surface roughness values were measured from three different points with a measuring length of 5.6 mm using a Mahr Perthometer M1 (Mahr, Göttingen, Germany) device and evaluated by averaging them. Surface roughness measurements are customized according to DIN EN ISO 4287. In light of all this, Figure 2 shows a graphical summary of the experimental process.

Table 4. Specification of lathe

Features	Value
Maximum workpiece diameter	460 mm
Distance between chuck and tailstock	1500 mm
Spindle speed range	25-1800 rev/min
Spindle speed number	12 piece
Feed range	0.04 -2.46 mm
Number of feeds	122 piece
Maximum tool holder size	25x25 mm
Motor power	5.5 kW

3. Results and Discussions

Cutting experiments were carried out on conventional lathe with 0.4-0.8 mm corner radius cutting tool forms depending on the variation in machining parameters. The surface roughness values on the machined parts and the cutting forces generated during machining were measured and the parameters effecting these values and their relationships with each other were interpreted.

3.1. Evaluation of Surface Roughness

The average roughness values in microns obtained from turning tests with cutting tools coded CCMT 09T308-304 and CCMT 09T304-304 with machining parameters were given graphically in ▶Figure 3. In ▶Figure 3, the first parameter that drawed attention in general was the feed rate; it has been seen that the roughness increased with the increase in the feed. This result can be explained by utilizing the ideal roughness equation given in Eq. 2 [29, 30]. As can be seen from the equation expressed as surface roughness (Ra: μm), feed rate (f: mm/rev) and tool corner radius (r_ε: mm), surface roughness and feed were directly proportional to each other. In other words, the variation in feed rate directly effected the roughness of the surface. The main reason for this was that at low feed rates, the amount of chips removed
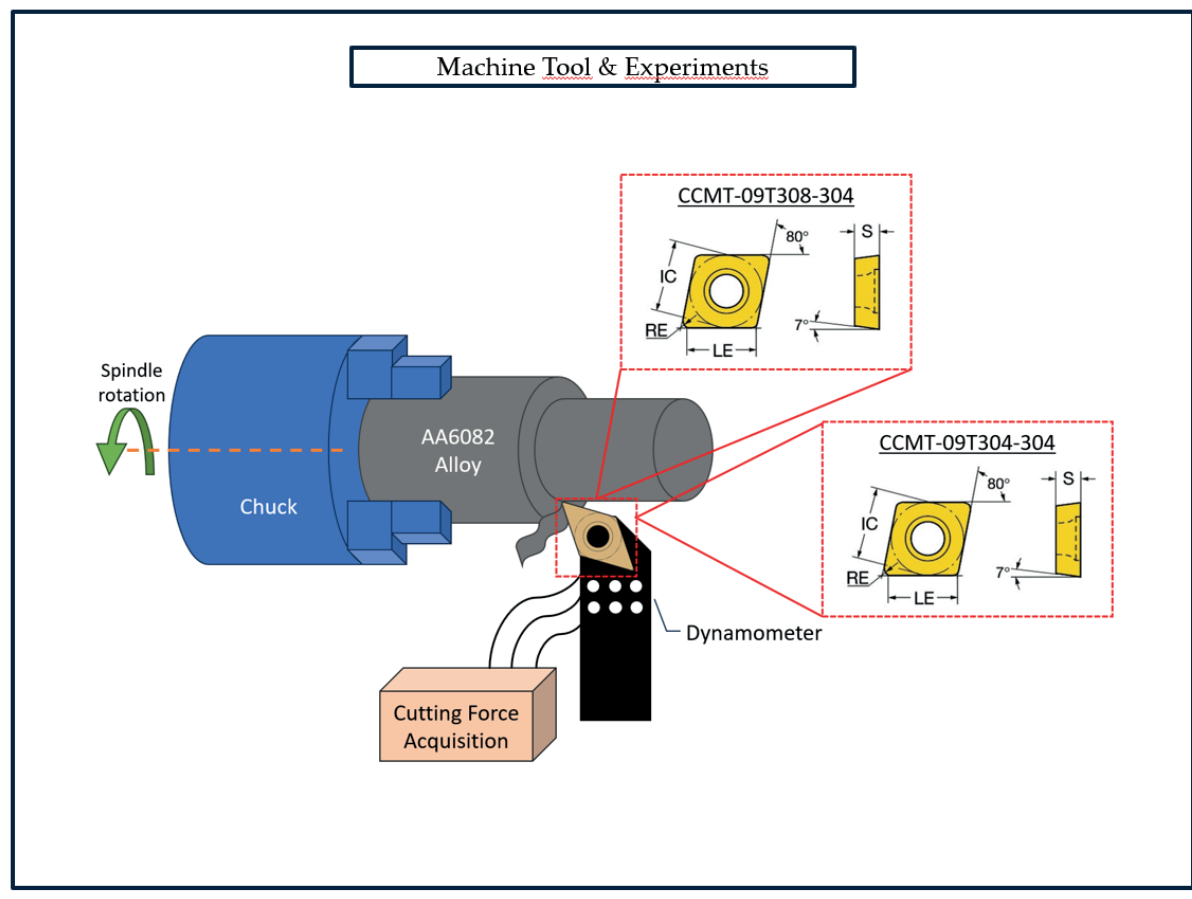
Figure 2. Graphical summary of the experimental process

by the cutting tool per feed rate was small and the surface was machined more smoothly, whereas when the feed increased, the tool removed larger chips and larger grooves were formed on the surface and these groove caused an increase in the roughness of the part surface [31-34]. In addition, this can increase the friction between the workpiece and the cutting tool, leading to heat build-up in the machining zone and an increase in wear and a decrease in cutting tool life, resulting in faster cutting edge deterioration, reduced machining capability and undesirable surface finish [35-37]. It has been observed from the graph that the roughness increased with increasing feed rate for both tools with 0.8 and 0.4 corner radius. The best surface quality was observed on surfaces machined with 0.8 corner radius cutting tools and the worst surface quality was observed on surfaces machined with 0.4 corner radius cutting tools. This was since when machining high feed rates with a small corner radius tool, the cutting tool contacts the workpiece more and increases the cutting forces. It was thought that the tool with a corner radius of 0.4 causes more deterioration on the workpiece surface than the tool with a corner radius of 0.8, as a result of high vibration formation with increasing cutting forces [38].

$$R_a = \frac{0.0321 \times f^2}{r_\varepsilon} \qquad (2)$$

It has known that the increase in temperature in the cutting zone with the increase in speed was among the factors that facilitate chip flow. However, the effect of temperature more than the expected levels was thought to cause plastic deformation on the surface of the material in AA 6082 aluminum alloy. Therefore, it can be concluded that the deformation reflects negatively on the surface structure and worsens the surface quality. Similar experimental results were found in the literature [39-42]. However, in a study, it was reported that the most effective cutting parameter on roughness values was cutting speed and according to the analysis results, it was stated that the most effective parameter with the highest contribution rate on surface roughness was again cutting speed [43]. In another study, it was emphasized that the surface roughness value decreased with increasing cutting speed, and it was stated that the chip-to-tool contact length shortened with the increase in cutting speed, and as a result, deformations decreased [44]. Looking at the roughness graph in this study, it was observed that the increase in speed had a negative effect on the surface quality in the results of the experiments performed with two different corner radiuses. As can be seen in the graph, the lowest roughness occurred in the experiments with two corner radius at a cutting speed of 65 m/min. It can also be seen from the graph that machining with a 0.4 corner radius

cutting tool produces more roughness on the surface than machining with a 0.8 corner radius cutting tool. The reason for this was thought to be that the 0.8 mm corner radius distributes the cutting forces better and provides a smoother surface compared to smaller corner radius [45, 46]. In a study on the turning of AA 6082 T4 alloy [47], the corner radius of the cutting tools were determined as 0.4 mm and 0.8 mm and it was found that the cutting forces were distributed more evenly, especially in tools with 0.8 mm corner radius.

When the graph has been interpreted to evaluate the effect of the depth of cut on surface roughness, it has been seen that surface roughness improves as depth of cut increases. In ductile materials such as AA 6082 aluminum alloy, it was thought that the probability of chip sticking (BUE) occurring was high when the depth of cut was low. In the literature, it was quite possible to come across studies where this situation caused irregularities on the surface and results in undesirable surface quality [48, 49]. However, in this study, it can be said that when the depth of cut is increased, chip removal becomes more controlled and BUE formation, i.e. sticking to the tool edge, decreases and as a result, a smoother surface is obtained. In the experiments with 0.4 and 0.8 corner radius, as can be seen in the graph, improvements in surface roughness occurred with increasing the depth of cut. However, contrary to the other studies, in the machining with 0.4 corner radius, the roughness increased slightly on the surface when the speed of 105 m/min, 0.2 mm/rev feed was changed from 0.25 mm chip depth to 0.5 mm chip depth under the same conditions. This is thought to be due to the fact that small corner radius make it difficult to break chips at high chip depths, which leads to undesirable chip agglomeration and worsens the surface quality [50]. According to the graphical evaluation results of the turning experiments performed with cutting speed,

feed rate, chip depth and 0.4-0.8 corner radius tool, machining with 0.8 corner radius tool produced better surface quality on AA 6082 aluminum material.

The S/N ratio is called the quality characteristic that constitutes the main decision mechanism. The S/N ratio, an analysis specific to the statistical technique, is the ratio of a signal sampled with humidity and ambient temperature to the background noise factor. [51-53]. By calculating the S/N ratio, the optimum machining parameters can be estimated [54-58]. Since the surface roughness value was desired to be minimum, S/N ratios were calculated according to the *smaller is better* property. The analysis result graphs were given in ▶**Figure 4** and ▶**Figure 5** for tools with 0.8 and 0.4 corner radius, respectively. When the S/N ratios graph for 0.8 corner radius was analyzed in ▶**Figure 4**, it was understood that the factor with the largest change for roughness was feed (0.1, 0.2 mm/rev). The feed factor was followed by the cutting speed and chip depth factors. The least change was observed in the chip depth factor (0.25, 0.5 mm). A similar situation has been also valid for the S/N ratios graph for 0.4 corner radius given in ▶**Figure 5**. When the S/N ratios graph was analyzed, the biggest change between the ratios was seen in the feed rate factor and the change in the chip depth factor was the lowest. ANOVA analysis has been used to determine whether the independent variable has a significant effect on the dependent variables [59]. As a result of the analysis for surface roughness, ANOVA analysis was performed to see the influence of the factors.

The results of the analysis for 0.8 and 0.4 corner radius were given in ▶**Table 5** and ▶**Table 6** respectively. When the ANOVA analysis for 0.8 corner radius were analyzed in ▶**Table 5**, it has been seen that the feed rate and cutting speed factors were statistically significant for S/N ratios ($p < 0.05$), but the chip depth factor wss
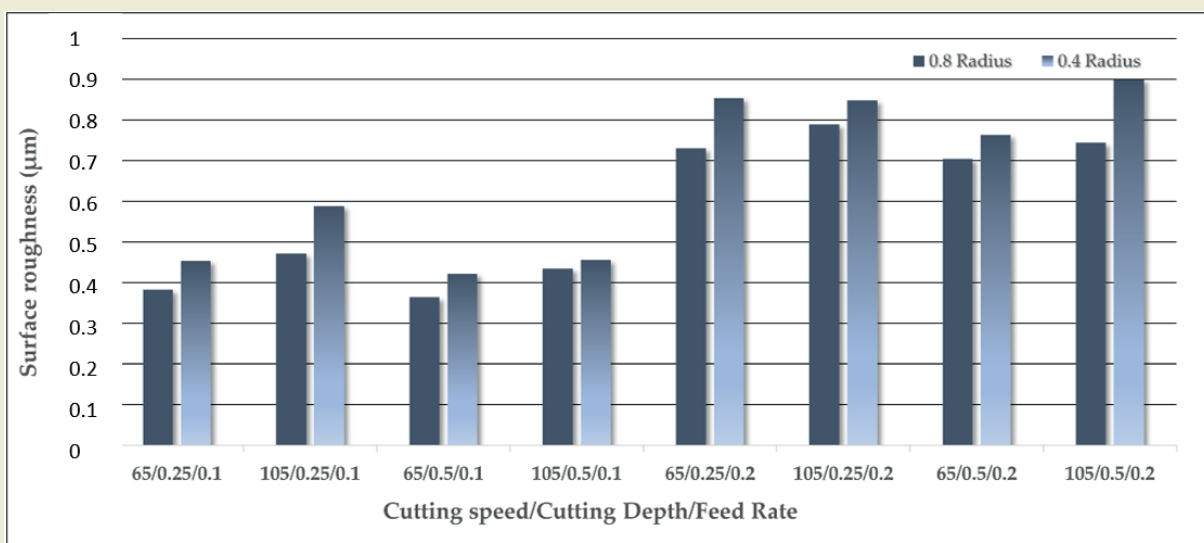

Figure 3. Surface roughness variation vs. cutting speed, chip depth and feed rate
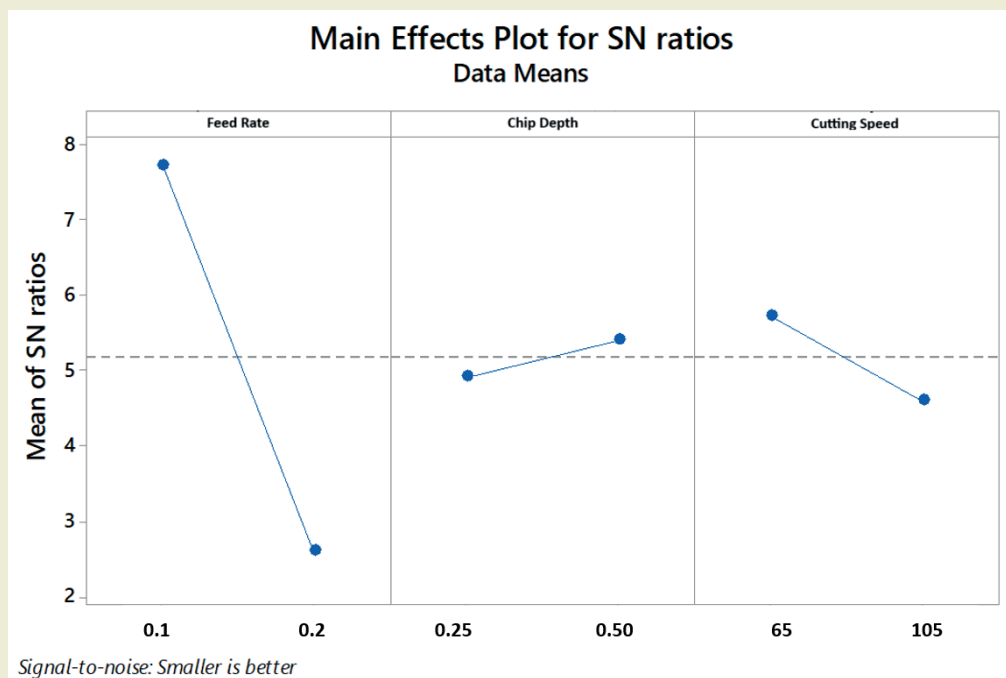
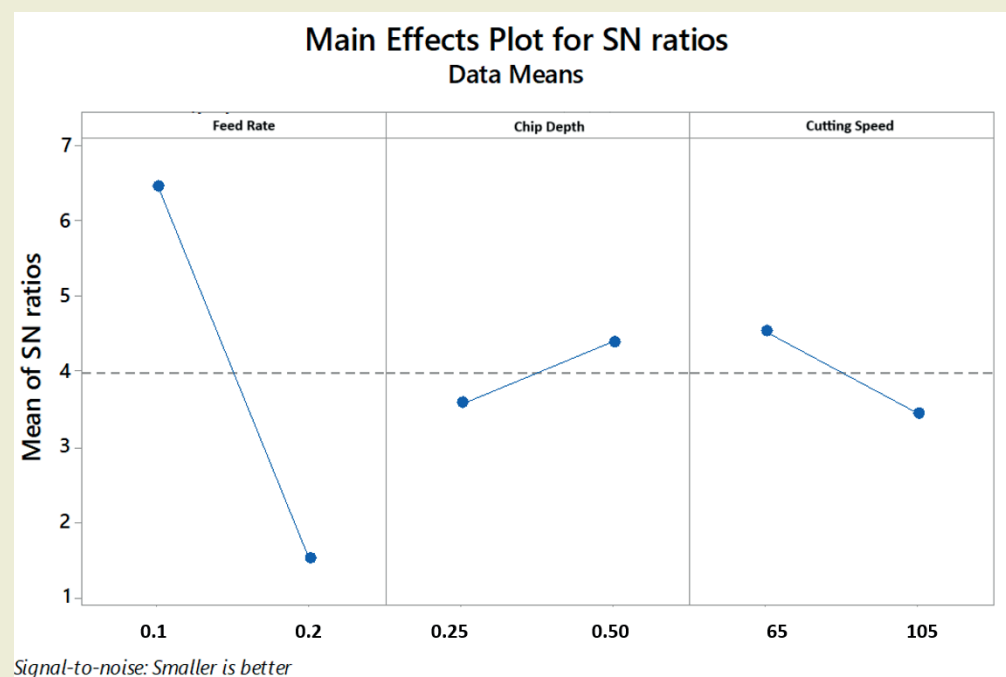**Figure 4.** Main effects of S/N ratios for surface roughness – 0.8 corner radius

Figure 5. Main effects of S/N ratios for surface roughness – 0.4 corner Radius

not significant ($p>0.05$). In addition, when the percentage effects of the factors were analyzed: 93.5% for feed, 4.5% for speed and 0.8% for depth of chip. Also, the coefficient of determination (R-Sq(adj)) for the model was found to be 98.00%.

When the ANOVA analysis for 0.4 corner radius was analyzed in ▶**Table 6**, it was seen that the feed rate factor was statistically significant for S/N ratios ($p<0.05$), but the cutting speed and chip depth factors were not significant ($p>0.05$). In addition, it was understood that the highest percentage factor effect was the feed rate

factor with 89.1% and the coefficient of determination (R-Sq(adj)) for the model was 92.92%. It can be seen that the experimental results have a high accuracy and according to the ANOVA table for both end radius, the feed factor was the most important factor for roughness. This point of view was in accordance with the literature [60-63].

3.2. Evaluation of Cutting Force

Cutting force (N) values obtained from turning experiments with cutting tools coded CCMT 09T308-304 and

CCMT 09T304-304 with machining parameters are given graphically in ▶Figure 6. Looking at the graph, it has been observed that the cutting forces increase with the increase in feed. This could be explained by the effect of the increase in the load on the tool at higher feed rates [64, 65]. It has been understood from the graph that the forces increase with the increase in feed in machines with both different corner radius. However, it could be seen that the lowest force value had occurred at 105 m/min speed, 0.25 mm chip depth and 0.1 mm/rev feed with 0.8 corner radius tool, while the highest cutting force value had occurred at 105 m/min speed, 0.5 mm chip depth and 0.2 mm/rev feed with 0.4 corner radius tool. It has been thought that the reason for this situation was that in machining with a tool with a smaller corner radius, the load was concentrated on a smaller area due to the smaller contact surface of the tool with the workpiece and the cutting forces increased as a result of the increase in feed rate [38, 66]. When the graph was analyzed, it has been seen that the force values increased with the increase in the depth of chip parameter. This can be explained that tool wear occured due to the increase in the tool-workpiece contact time, resulting in a decrease in the performance of the tool. Due to the decreased tool performance, the machine zone has more loaded, resulting in an increase in cutting forces. Studies similar to this situation are available in the literature [67, 68]. It could be understood from the graph that the cutting force values increase with increasing chip depth in both 0.4 and 0.8 corner radius machining. However, it has realized that the lowest value in the cutting force form in the combination of a speed of 105 m/min, a chip depth of 0.25 mm and a feed of 0.1 mm/rev with a 0.8 corner radius tool. This has thought to be due to the fact that the forces were evenly distributed due to the wider contact surface of the tool in machining with higher corner radius [11, 26, 69, 70].

In the graph, when the cutting force results were analyzed according to the cutting speed variation, it has seen that different cutting force values occur at different tool corner radius.

In machining with 0.8 corner radius, the force has decreased as the speed increased, while in machining with 0.4 corner radius, the force has increased as the cutting speed increased. This can be explained that the contact area of the 0.8 corner radius was wider, which results in less friction in the machining area and therefore reduces the cutting forces. However, during machining with 0.4 corner radius, it has been observed that since the contact surface of the tool was narrower, it can applied more friction on the machining surface, causing an increase in cutting forces.[71, 72].

According to the results of the graphical evaluation of turning experiments performed with cutting speed, feed, chip depth and 0.4-0.8 corner radius tool; lower cutting forces were obtained as a result of machining with 0.8 corner radius tool in AA 6082 aluminum material.

The analysis result graphs according to the cutting force has been given in ▶Figure 7 and ▶Figure 8 for tools with 0.8 and 0.4 corner radius, respectively. When the S/N ratios graph for 0.8 corner radius was analyzed in ▶Figure 7, it can be understood that the factor with the largest variation for the cutting force was the chip depth (0.25, 0.5 mm). The chip depth factor has been followed by the feed and speed factors. The least variation has been observed in the cutting speed factor (65, 105 m/min). When the graph of S/N ratios for tools with 0.4 corner radius was analyzed in ▶Figure 8, the biggest variation between the ratios has been seen in the feed factor, while the variation in the speed factor was the lowest. As a result of the analysis for cutting

Table 5. ANOVA table for surface roughness - 0.8 corner radius

Source	DF	Seq SS	Adj SS	Adj MS	F	P	PC (%)
Feed rate	1	52.6205	52.6205	52.6205	327.41	0.000	93.5
Chip depth	1	0.4777	0.4777	0.4777	2.97	0.60	0.8
Cutting speed	1	2.5335	2.5335	2.5335	15.76	0.017	4.5
Residual Error	4	0.6429	0.6429	0.1607			1.2
Total	7	56.2746					100
R-Sq(adj): 98.00%							

Table 6. ANOVA table for surface roughness - 0.4 corner radius

Source	DF	Seq SS	Adj SS	Adj MS	F	P	PC (%)
Feed rate	1	48.739	4.739	48.7393	88.18	0.001	89.1
Chip depth	1	1.357	1.357	1.3568	2.45	0.192	2.5
Cutting speed	1	2.314	2.314	2.3143	4.19	0.110	4.3
Residual Error	4	2.211	2.211	0.5527			4.1
Total	7	54.621					100
R-Sq(adj): 92.92%							

force, ANOVA analysis was performed to see the effect of the factors.

The results of the analysis were given in ▶**Table 7** and ▶**Table 8** for 0.8 and 0.4 corner radius, respectively. When the ANOVA analysis for 0.8 corner radius has been analyzed in ▶**Table 7**, it was seen that the chip depth and feed rate factors were statistically significant for S/N ratios ($p<0.05$), but the cutting speed factor was not significant ($p>0.05$). Also, when the percentage effects of the factors were analyzed: 48.5% for depth of cut, 41.7% for feed rate and 1.5% for cutting speed. Also, the coefficient of determination (R-Sq(adj)) for the model was found to be 85.51%.

When ANOVA analysis for 0.4 corner radius has been analyzed in ▶**Table 8**, it was seen that feed and chip depth factors were statistically significant for S/N ratios ($p<0.05$), while cutting speed factor was not significant ($p>0.05$). It was also understood that the highest percentage factor effect was the feed rate factor with 54.9% and the coefficient of determination (R-Sq(adj)) for the model was 76.92%. When ANOVA results were analyzed according to the cutting force, it was observed that the most important factor for 0.8 corner radius was the chip depth, while for 0.4 corner radius it was the feed rate factor. In the results of the analysis, it was thought that in machining with a cutting tool with a corner radius of 0.8 mm, due to the large contact surface, it caused the tool to contact with more material during the chip removal process, and in this case, chip depth has stand out as the most important factor for cutting forces [36,
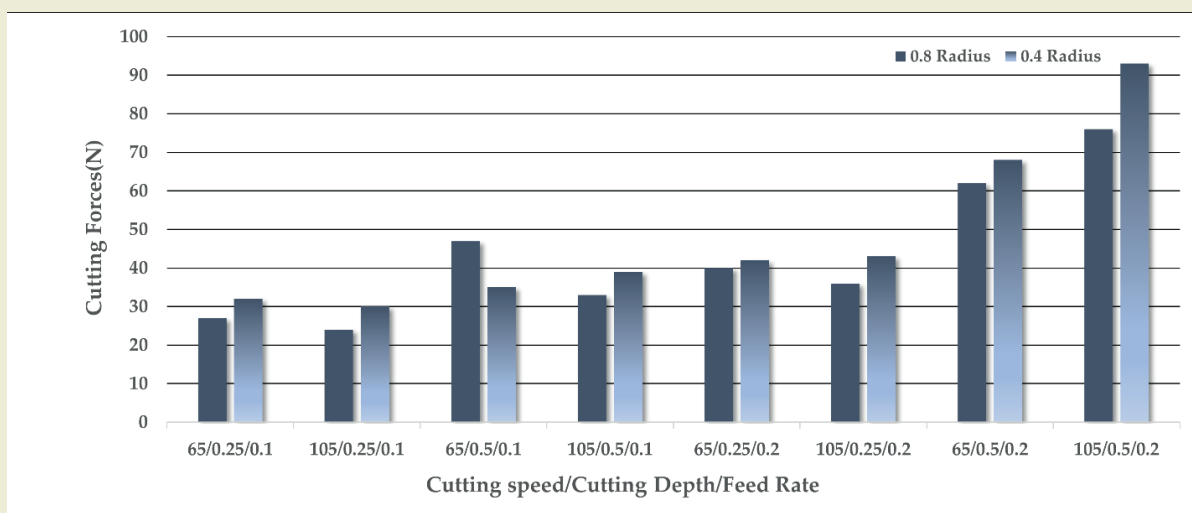

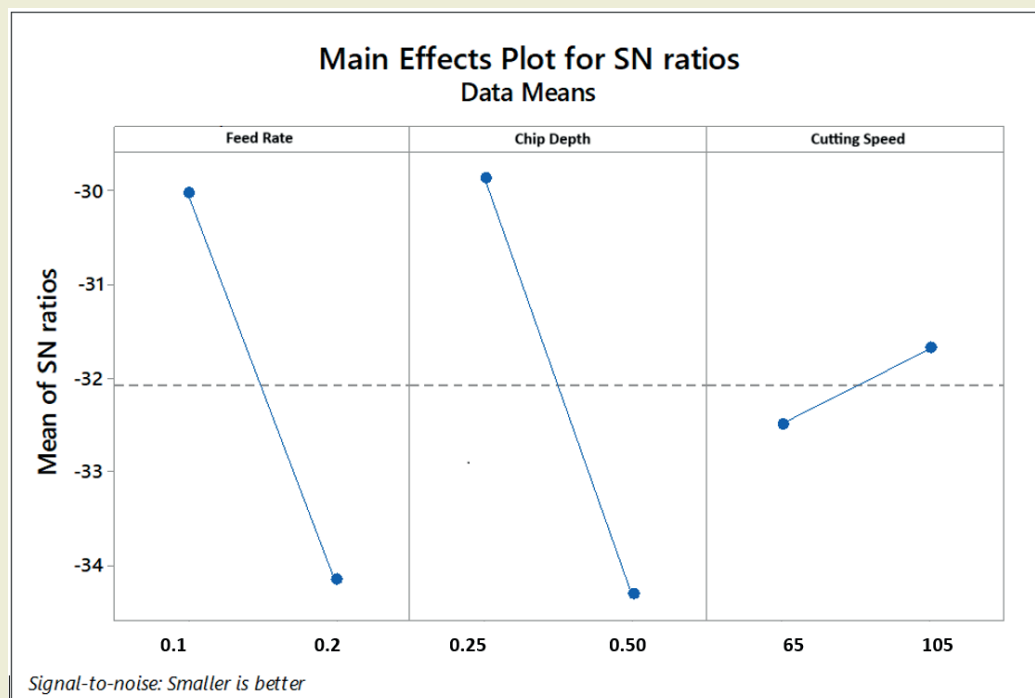**Figure 6.** Cutting Force variation vs. cutting speed, chip depth and feed rate

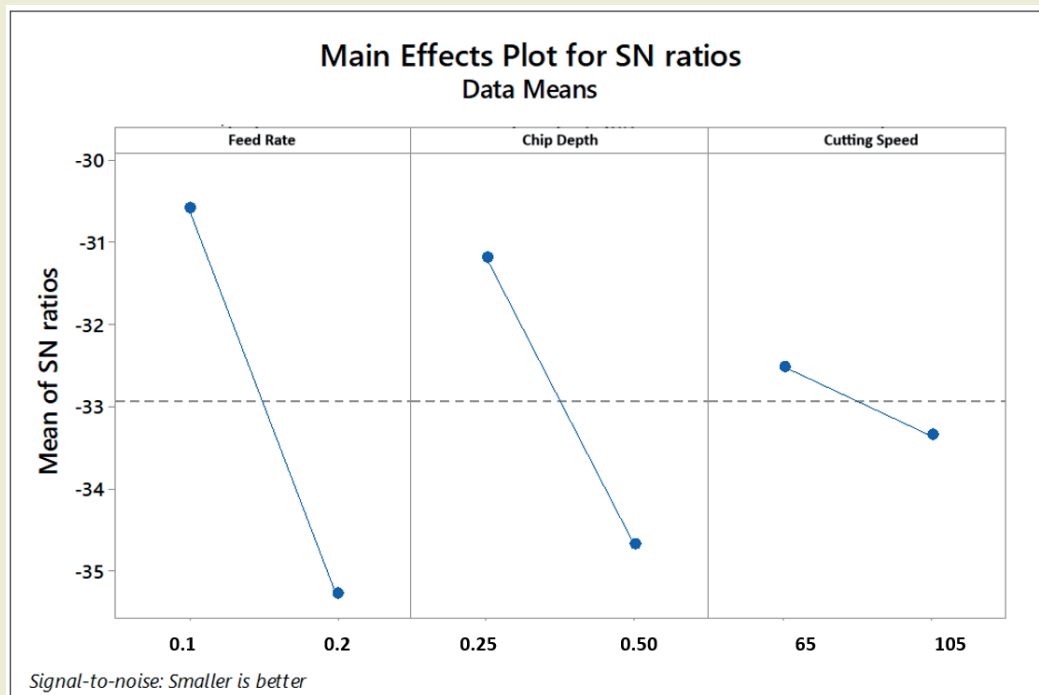**Figure 7.** Main effects of S/N ratios for cutting force – 0.8 corner radius

Figure 8. Main effects of S/N ratios for cutting force – 0.4 corner radius

Table 7. ANOVA table for cutting force - 0.8 corner radius

Source	DF	Seq SS	Adj SS	Adj MS	F	P	PC (%)
Feed rate	1	34.394	34.394	34.394	20.14	0.011	41.7
Chip depth	1	39.951	39.951	39.951	23.39	0.008	48.5
Cutting speed	1	1.313	1.313	1.313	0.77	0.430	1.5
Residual Error	4	6.832	6.832	1.708			8.3
Total	7	82.490					100
R-Sq(adj): 85.51%							

Table 8. ANOVA table for cutting force - 0.8 corner radius

Source	DF	Seq SS	Adj SS	Adj MS	F	P	PC (%)
Feed rate	1	44,209	44,209	44,209	16,66	0,015	54.9
Chip depth	1	24,300	24,300	24,300	9,16	0,039	30.2
Cutting speed	1	1,364	1,364	1,364	0,51	0,513	1.7
Residual Error	4	10,614	10,614	2,653			13.2
Total	7	80,486					100
R-Sq(adj): 76.92%							

73, 74]. In machining with a 0.4 mm corner radius tool, it was observed that changes in feed rate become more dominant in force values, since the contact area of the tool was reduced [32, 75, 76].

4. Conclusions

The important findings obtained in the study carried out to investigate the cutting forces and surface roughness depending on the machining parameters in the AA 6082 aluminum alloy on a conventional lathe with tools with two different radius are summarized below:

- 0.8 and 0.4 corner radius cutting tools, the results of machining with 0.8 corner radius cutting tool showed better results than machining with 0.4 corner radius cutting tool in terms of both roughness and force values.

- According to the graphical evaluation results, the highest surface roughness value was observed at 105 m/min cutting speed, 0.5 mm chip depth and

0.2 mm/rev feed rate with 0.4 corner radius tool, while the lowest surface roughness value occurred at 65 m/min cutting speed, 0.5 mm chip depth and 0.1 mm/rev feed rate with 0.8 corner radius tool.

- According to the results of the graphical evaluation for cutting forces, the highest cutting force value was observed at 105 m/min cutting speed, 0.5 mm chip depth and 0.2 mm/rev feed rate with 0.4 corner radius tool, while the lowest cutting force value occurred at 65 m/min cutting speed, 0.25 mm chip depth and 0.1 mm/rev feed rate with 0.8 corner radius tool.

- The best roughness results were obtained with tools with 0.8 corner radius and the worst roughness results were obtained with tools with 0.4 corner radius. For both cutting tools, the roughness increased with an increasing feed.

- In the experiments with 0.8 and 0.4 corner radius cutting tools, roughness decreased with an increasing chip depth. However, when the speed was 105 m/min and the feed was 0.2 mm and the chip depth increased from 0.25 to 0.5 for the tool with 0.4 corner radius, the surface roughness values did not decrease and even increased slightly contrary to this general behavior.

- For all cutting tools, surface roughness increased with increasing speed. It was evaluated that the selected speed values in the roughness values were low to provide the expected improvement.

- ANOVA analysis revealed that the feed and speed factors should be taken into consideration primarily for both cutting tools in reducing the surface roughness in turning AA 6082 aluminum alloy.

- The lowest S/N ratios obtained as a result of analysis (smaller is better) in obtaining the lowest surface roughness were determined by the factors and levels of feed (0.2 mm / rpm), chip depth (0.5 mm) and speed (105 m / min) for both different tools.

- In terms of cutting force, the tool with 0.8 corner radius showed the best performance, while the worst performance was obtained with the tool with 0.4 corner radius. For both cutting tools, the cutting forces increased continuously with increasing feed rate and chip depth.

- With increasing the speed, the cutting forces decreased for the tool with 0.8 corner radius. The same was not observed for machining with a tool with a 0.4 corner radius, on the contrary, the forces increased.

- According to the results of ANOVA analysis in reducing the cutting force in turning AA 6082 aluminum alloy, it was found that for the tool with 0.8 corner radius, the factors of chip depth and feed rate should be considered first, while for the tool with 0.4 corner radius, the factor of feed rate should be considered first and then chip depth.

- The lowest S/N ratios obtained as a result of analysis (smaller is better) in obtaining the lowest cutting force were determined at the factors and levels of feed (0.2 mm/rev), chip depth (0.5 mm) and speed (65 m/min) for the tool with 0.8 corner radius. For the tool with 0.4 corner radius, the factors and levels of feed (0.2 mm/rev), chip depth (0.5 mm) and speed (105 m/min) were determined.

- In addition to the cutting tool geometry, additional factors such as the approach angle of the tool to the machined material and whether it is coated or not have an effect on surface roughness. However, although these aspects were not evaluated in this study, it is foreseen that they will provide opportunities for future research. More extensive studies can be carried out in which the effects of more variables on more cutting parameters/levels can be interactively evaluated and optimized.

- This study systematically investigated the influence of tool corner radius and machining parameters on the machinability of AA6082 aluminum alloy and provided original experimental data to the literature. The findings on the inter-correlation between cutting forces and surface roughness can provide a solid basis for future modeling and optimization studies. Through an industrial point of view, it has become possible to increase production efficiency by determining the optimum tool corner radius and machining conditions. In this context, the study can be an important reference for both academic research and practical production processes.

Research ethics

Not applicable.

Author contributions

Conceptualization: [Ayşe Sena Yamaner, Bahar Sayın Kul], Methodology: [Ayşe Sena Yamaner], Formal Analysis: [Ayşe Sena Yamaner, Bahar Sayın Kul], Investigation: [Ayşe Sena Yamaner, Bahar Sayın Kul], Resources: [Ayşe Sena Yamaner, Bahar Sayın Kul], Data Curation: [Ayşe Sena Yamaner, Bahar Sayın Kul], Writing – Original Draft Preparation: [Ayşe Sena Yamaner, Bahar Sayın Kul], Writing - Review & Editing: [Bahar Sayın Kul], Visualization: [Ayşe Sena Yamaner], Supervision: [Bahar Sayın Kul], Project Administration: [Bahar Sayın Kul], Funding Acquisition: [Bahar Sayın Kul]

Competing interests

The author(s) state(s) no conflict of interest.

Research funding

None declared.

Data availability

The raw data can be obtained on request from the corresponding author.

Peer-review

Externally peer-reviewed.

Orcid

Ayşe Sena Yamaner https://orcid.org/0009-0009-0536-996X
Bahar Sayın Kul https://orcid.org/0000-0002-7899-7088

References

[1] Korhonen, H., Koistinen, A., & Lappalainen, R. (2018). Improvements in the thread cutting torque for a 6082-T6 aluminum-based alloy with tapping tools utilizing diamond coating. Machining Science and Technology, 22(4), 696–728.

[2] Vishwas, C., et al. (2019). Study on surface roughness in minimum quantity lubrication turning of Al-6082/SiC metal matrix composites. Applied Mechanics and Materials, 895, 127–133.

[3] Saravanan, K., & Mahendran, S. (2020). Aluminium 6082-boron carbide composite materials preparation and investigate mechanical-electrical properties with CNC turning. Materials Today: Proceedings, 21, 93–97.

[4] Jebaraj, M., et al. (2019). Experimental study of the influence of the process parameters in the milling of Al6082-T6 alloy. Materials and Manufacturing Processes, 34(12), 1411–1427.

[5] Yapan, Y. F., et al. (2024). Machining and sustainability performance comparison for the milling process of Al6082 alloy under various minimum quantity lubrication conditions. International Journal of Precision Engineering and Manufacturing-Green Technology, 1–22.

[6] Chowdhury, S. R., Das, P. P., & Chakraborty, S. (2023). Optimization of CNC turning of aluminium 6082-T6 alloy using fuzzy multi-criteria decision making methods: A comparative study. International Journal on Interactive Design and Manufacturing (IJIDeM), 17(3), 1047–1066.

[7] Singh, M., et al. (2015). Optimization of process parameters of aluminum alloy (Al-6082 T-6) machined on CNC lathe machine for low surface roughness. J Mater Sci Eng, 4(6), 2169–0022.

[8] Turan, İ., et al. (2025). Prediction and Modelling with Taguchi, ANN and ANFIS of Optimum Machining Parameters in Drilling of Al 6082-T6 Alloy. Journal of Manufacturing and Materials Processing, 9(3), 92.

[9] Işik, U., Demir, H., & Özlü, B. (2024). Multi-objective optimization of process parameters for surface quality and geometric tolerances of AlSi10Mg samples produced by additive manufacturing method using Taguchi-based gray relational analysis. Arabian Journal for Science and Engineering, 1–19.

[10] Özlü, B. (2021). Sleipner soğuk iş takım çeliğinin tornalanmasında kesme parametrelerinin kesme kuvveti, yüzey pürüzlülüğü ve talaş şekli üzerine etkisinin incelenmesi. Gazi Üniversitesi Mühendislik Mimarlık Fakültesi Dergisi, 36(3), 1241–1252.

[11] Binali, R., et al. (2025). A Holistic Perspective on Sustainable Machining of Al6082: Synergistic Effects of Nano-Enhanced Bio-Lubricants. Machines, 13(4), 293.

[12] Kartal, F., Yerlikaya, Z., & Gökkaya, H. (2017). Effects of machining parameters on surface roughness and macro surface characteristics when the machining of Al-6082 T6 alloy using AWJT. Measurement, 95, 216–222.

[13] Stanojković, J., & Radovanović, M. (2022). Influence of the cutting parameters on force, moment and surface roughness in the end milling of aluminum 6082-T6. Facta Universitatis, Series: Mechanical Engineering, 20(1), 157–165.

[14] Varatharajulu, M., et al. (2021). Experimental investigation of the effect of independent parameters in the face milling of aluminum 6082 alloy. Transactions of the Indian Institute of Metals, 74, 659–677.

[15] Garcia, R. F., et al. (2019). Optimization of cutting parameters for finish turning of 6082-T6 aluminum alloy under dry and RQL conditions. Journal of the Brazilian Society of Mechanical Sciences and Engineering, 41, 1–10.

[16] Beşliu, I., & Tamaşag, I. (n.d.). Effect of cooling condition over surface quality in turning of aluminium alloy 6082-T6. IOP Conference Series: Materials Science and Engineering. IOP Publishing.

[17] Quintana, G., et al. (2010). Influence of cutting parameters on cycle time, surface roughness, dimensional error and cutting forces in milling operations on aluminium 6082 sculptured surface geometry. International Journal of Machining and Machinability of Materials, 8(3–4), 339–355.

[18] Yigit, R. (2014). An experimental investigation of effect of minimum quantity lubrication in machining 6082 aluminum alloy. Kovove Materialy-Metallic Materials, 52(1).

[19] Patel, M. T., & Deshpande, V. A. (2014). Experimental investigation of effect of process parameters on MRR and surface roughness in turning operation on conventional lathe machine for aluminum 6082 grade material using Taguchi method. Journal of Engineering Research and Applications, 4(1), 177–185.

[20] Solanki, M., & Jain, A. (2021). Optimization of material removal rate and surface roughness using Taguchi based multi-criteria decision making (MCDM) technique for turning of Al-6082. Proceedings on Engineering, 3(3), 303–318.

[21] Aydın, K. (2023). Investigating Cutting Force and Cutting Power When Turning AA6082-T4 Alloy at Cutting Depths Smaller Than Tool Nose Radius. Kahramanmaraş Sütçü İmam Üniversitesi Mühendislik Bilimleri Dergisi, 26(4), 972–982.

[22] Aryan, R., et al. (2017). Optimization of turning parameters of AL-Alloy 6082 using Taguchi method. International Journal of Advance Research and Innovation, 5(2), 268–275.

[23] Doruk, E. (2015). AA 6082 alüminyum alaşımının yorulma davranışı üzerine temper durumunun etkisi [Master's thesis, Fen Bilimleri Enstitüsü].

[24] International Organization for Standardization. (1993). *ISO 3685: Tool-life testing with single-point turning tools*.

[25] Kechagias, J. D., et al. (2020). A comparative investigation of Taguchi and full factorial design for machinability prediction in turning of a titanium alloy. Measurement, 151, 107213.

[26] Binali, R., Yaldız, S., & Neşeli, S. (2024). Finite element analysis and statistical investigation of S960QL structure steel machinability with milling method. Journal of the Brazilian Society of Mechanical Sciences and Engineering, 46(5), 260.

[27] Güneş, A., et al. (2021). Optimization study on surface roughness and tribological behavior of recycled cast iron reinforced bronze MMCs produced by hot pressing. Materials, 14(12), 3364.

[28] Taguchi, G. (1987). System of experimental design; engineering methods to optimize quality and minimize costs.

[29] Jawahir, I., Qureshi, N., & Arsecularatne, J. (1992). On the interrelationships of some machinability parameters in finish turning with cermet chip forming tool inserts. International Journal of Machine Tools and Manufacture, 32(5), 709–723.

[30] Hagiwara, M., Chen, S., & Jawahir, I. (2009). Contour finish turning operations with coated grooved tools: Optimization of machining performance. Journal of Materials Processing Technology, 209(1), 332–342.

[31] Taylan, F., & Oral, N. (2018). Tİ-6AL-4V eli malzemesinin tornalama işleminde yüksek basınçlı jet soğutmanın yüzey pürüzlülüğüne etkisi. Uluslararası Teknolojik Bilimler Dergisi, 10(1), 31–46.

[32] Albayrak, S., Yeşildal, F., & Yıldırım, C. (2020). SAE 4140 Çeliğin Tornalanmasında Kesme Parametrelerinin Ses Seviyesi ve Yüzey Pürüzlüğüne Etkileri: Parametrelerin Optimizasyonu. Journal of the Institute of Science and Technology, 10(4), 2759–2769.

[33] Uğur, L. (2019). 7075 Alüminyum Malzemesinin Frezelenmesinde Yüzey Pürüzlülüğünün Yanıt Yüzey Metodu İle Optimizasyonu. Erzincan University Journal of Science and Technology, 12(1), 326–335.

[34] Binali, R. (2024). Experimental and machine learning comparison for measurement the machinability of nickel based alloy in pursuit of sustainability. Measurement, 236, 115142.

[35] Thamizhmanii, S., et al. (2019). Effect of feed rate on difficult to cut metals on surface roughness and tool wear using surface treated and untreated tools. Procedia Manufacturing, 30, 216–223.

[36] Demirpolat, H., et al. (2023). AISI 52100 Rulman Çeliğinin Tornalanmasında İşleme Parametrelerinin Yüzey Pürüzlülüğü, Kesme Sıcaklığı ve Kesme Kuvveti Üzerindeki Etkilerinin İncelenmesi. İmalat Teknolojileri ve Uygulamaları, 4(3), 179–189.

[37] Kuttolamadom, M., Hamzehlouia, S., & Mears, L. (2010). Effect of machining feed on surface roughness in cutting 6061 aluminum. SAE International Journal of Materials and Manufacturing, 3(1), 108–119.

[38] Binali, R., & Kuntoğlu, M. (2023). Evaluation of Machining Parameters Affecting Cutting Forces in Dry Turning of GGG50 Ductile Cast Iron. Türk Doğa ve Fen Dergisi, 12(2), 55–60.

[39] Sahoo, P., Pratap, A., & Bandyopadhyay, A. (2017). Modeling and optimization of surface roughness and tool vibration in CNC turning of Aluminum alloy using hybrid RSM-WPCA methodology. International Journal of Industrial Engineering Computations, 8(3), 385–398.

[40] İrizalp, S., et al. (2024). AA7475-T7351 ve AA2219-T851 Alaşımlarının Frezelenmesinde Kesici Takım Kaplamalarının ve Kesme Parametrelerinin Yüzey Pürüzlülüğü Üzerine Etkisinin Deneysel Olarak İncelenmesi. Fırat Üniversitesi Mühendislik Bilimleri Dergisi, 36(1), 85–95.

[41] Gökkaya, H. (2011). AA5052 Alaşiminin Işlenmesinde Işleme Parametrelerinin Kesme Kuvveti ve Yüzey Pürüzlülüğüne Etkisinin Deneysel Olarak İncelenmesi. Pamukkale Üniversitesi Mühendislik Bilimleri Dergisi, 12(3), 295–301.

[42] Yusuf, M., et al. (2012). Optimization of cutting parameters on turning process based on surface roughness using response surface methodology. Applied Mechanics and Materials, 117, 1561–1565.

[43] Pul, M. (2020). AI 1070/TiB2 Kompozitlerin Tornalanmasında TiB2 Takviye Miktarının Esas Kesme Kuvveti Ve Yüzey Pürüzlülüğüne Etkisi. Düzce Üniversitesi Bilim ve Teknoloji Dergisi, 8(1), 754–764.

[44] Tekaslan, Ö., et al. (2011). AISI 304 östenitik paslanmaz çeliklerin titanyum karbür kaplamalı kesici takım ile tornalama işleminde kesme kuvvetlerinin incelenmesi. Pamukkale Üniversitesi Mühendislik Bilimleri Dergisi, 13(2), 135–144.

[45] Gökkaya, H., Sur, G., & Dilipak, H. (2006). Kaplamasız Sementit Karbür Kesici Takım Ve Kesme Parametrelerinin Yüzey Pürüzlülüğüne Etkisinin Deneysel Olarak İncelenmesi. Pamukkale Üniversitesi Mühendislik Bilimleri Dergisi, 12(1), 59–64.

[46] Turgut, Y., & Çakmak, İ. (2019). AISI 1040 çeliğinin frezelenmesinde talaş kırıcı formunun yüzey pürüzlülüğü ve kesme kuvvetlerine etkisinin araştırılması. Gazi University Journal of Science Part C: Design and Technology, 7(2), 482–494.

[47] Yağmur, S., Kaya, M. K., & Şeker, U. (2021). AA-6082 T4 Alaşımının Tornalamasında Çok Kristalli Elmas (ÇKE) Takımlara Uygulanan Talaş Kırıcı Formlarının Kesme Kuvvetleri Üzerindeki Etkilerinin Araştırılması. Gazi Mühendislik Bilimleri Dergisi, 7(1), 51–57.

[48] Gökkaya, H. (2010). The Effects of Machining Parameters on Cutting Forces, Surface Roughness, Built-Up Edge (BUE) and Built-Up Layer (BUL) During Machining AA2014 (T4) Alloy. Journal of Mechanical Engineering/Strojniški Vestnik, 56(9), 584-593.

[49] Dişbudak, T., & Şensoy, S. (2014). 7075 Alüminyum alaşımının tornalamasında kesme parametrelerinin yüzey pürüzlülüğüne etkilerinin analizi. Mühendislik ve Teknoloji Bilimleri Dergisi, 2(1), 13–29.

[50] Güllü, A., Karabulut, Ş., & Güldaş, A. (2008). INCONEL 718 süper alaşımların işlenmesinde talaş kırılma problemleri ve talaş kırıcı tasarımı. Gazi Üniversitesi Mühendislik Mimarlık Fakültesi Dergisi, 23(1), 157-164.

[51] Gürbüz, H., & Gönülaçar, Y. E. (2021). Farklı kesme parametreleri ve MQL debilerinde elde edilen deneysel değerlerin S/N oranları ve YSA ile analizi. Politeknik Dergisi, 24(3), 1093–1107.

[52] Aydın, E. (2023). Taguchi optimizasyon metodunun imalat mühendisliği alanında kullanımı: Minitab örneği, 28(3), 1049-1068.

[53] Binali, R. (2023). Parametric optimization of cutting force and temperature in finite element milling of AISI P20 steel. Journal of Materials and Mechatronics: A, 4(1), 244–256.

[54] Roy, R. (1990). Taguchi method. Van Nostran Reinhold.

[55] Binali, R., Yaldız, S., & Neşeli, S. (2022). Parametric optimization for machinability parameters of S960QL structural steel during milling by finite elements, 21(1), 26-31.

[56] Binali, R., & Kuntoğlu, M. (2022). An in-depth analysis on the surface roughness variations during turning of GGG50 ductile cast iron. Doğu Fen Bilimleri Dergisi, 5(2), 41–49.

[57] Kuntoğlu, M., & Aslan, A. (2021). AISI 5140 Çeliğinin tornalanması esnasında yaklaşma açısı ve kesme parametrelerinin işlenebilirliğe etkisinin incelenmesi. Politeknik Dergisi, 1–1.

[58] Mutlu, B., et al. (2022). Machinability of CoCrMo Alloy used in Biomedical applications: Investigation of Cutting Tool Type. Gazi Mühendislik Bilimleri Dergisi, 8(2), 215–227.

[59] Nevalainen, J., & Oja, H. (2006). SAS/IML macros for a multivariate analysis of variance based on spatial signs. Journal of Statistical Software, 16, 1–17.

[60] Gürbüz, H., & Baday, Ş. (2019). Optimization of Effect of Chuck and Tailstock Pressure on Surface Roughness and Vibration with Taguchi Method in CNC Lathes. Bilecik Şeyh Edebali University Journal of Science, 6(2), 119–134.

[61] Kayır, Y., Aslan, S., & Aytürk, A. (2013). AISI 316Ti paslanmaz çeliğin tornalanmasında kesici uç etkisinin Taguchi yöntemi ile analizi. Gazi Üniversitesi Mühendislik Mimarlık Fakültesi Dergisi, 28(2).

[62] Zeyvelı, M., & Demır, H. (2009). AISI 01 soğuk iş takım çeliğinin işlenebilirliğinin kesme kuvvetleri ve yüzey pürüzlülüğü açısından araştırılması. Engineering Sciences, 4(3), 323–331.

[63] Özlü, B., Akgün, M., & Demir, H. (2019). AA 6061 Alaşımının tornalanmasında kesme parametrelerinin yüzey pürüzlülüğü üzerine etkisinin analizi ve optimizasyonu. Gazi Mühendislik Bilimleri Dergisi, 5(2), 151–158.

[64] Kuntoğlu, M., & Sağlam, H. (2016). On-line Tool Breakage Detection Using Acoustic Emission, Cutting Force and Temperature Signals in Turning. IOSR Journal of Mechanical and Civil Engineering, 13, 100–103.

[65] Memiş, F., & Turgut, Y. (2020). AISI 2205 Dubleks Paslanmaz Çeliğin CNC Torna Tezgahında İşlenmesinde Yüzey Pürüzlülüğü ve Kesme Kuvvetlerinin Deneysel Araştırılması. İmalat Teknolojileri ve Uygulamaları, 1(1), 22–33.

[66] Hasçelik, A., & Aslantaş, K. (n.d.). Mikro tornalama işleminde kenar radyüs etkisinin sonlu elemanlar yöntemiyle modellenmesi. https://core.ac.uk/download/pdf/286916096.pdf

[67] Abdullah, K., & Şeker, U. (2004). Talaş derinliğinin kesici takım gerilmelerine etkisi. Makine Teknolojileri Elektronik Dergisi, 1, 23–29.

[68] Güven, S., et al. (2023, June 10-12). Tornalama operasyonunda farklı işleme parametrelerinin kesme kuvveti ve sıcaklığı üzerine etkisinin sonlu elemanlar analizi ile incelenmesi [The investigation of

the effects of different machining parameters on cutting force and temperature in turning operations via finite element analysis]. 11th International Congress on Engineering, Architecture and Design Proceedings (Vol. 1, pp. 239-248). İstanbul, Türkiye.

[69] Gök, K., Erdem, M., & Gök, A. (2010). AISI 1006 Çeliğinin Tornalama Sürecinde Kesici Takım Uç Yarıçapının Kesme Sıcaklığı Ve Kesme Kuvveti Üzerindeki Etkisinin Numerik Olarak İncelenmesi. TÜBAV Bilim Dergisi, 4(1), 1–8.

[70] Gupta, M. K., et al. (2022). Cutting forces and temperature measurements in cryogenic assisted turning of AA2024-T351 alloy: An experimentally validated simulation approach. Measurement, 188, 110594.

[71] Şahan, Ö. (2019). Ti6Al4V alaşımının mikro tornalanması ve kesme kuvvetlerinin mekanistik modellenmesi (Yüksek lisans tezi, Afyon Kocatepe Üniversitesi, Fen Bilimleri Enstitüsü, Makine Mühendisliği Anabilim Dalı).

[72] Aslantaş, K., & Hasçelik, A. (n.d.). Mikro tornalama işleminde kenar radyüs etkisinin sonlu elemanlar yöntemiyle modellenmesi. https://core.ac.uk/download/pdf/286916096.pdf

[73] Çakmak, İ., & Turgut, Y. (2019). Investigation of the effect of chip breaker form on surface roughness and cutting forces in AISI 1040 steel milling. Gazi Üniversitesi Fen Bilimleri Dergisi Part C: Tasarım ve Teknoloji, 7(2), 482–494.

[74] Bozkurt, C. A. (n.d.). Talaşlı imalat sürecinde kesici takım performansının iyileştirilmesine yönelik yeni stratejilerin araştırılması [Doctoral dissertation, Fen Bilimleri Enstitüsü].

[75] Ateş, N. (2009). Kaplamalı Kesici Takımları Erken Aşınma Davranışlarının İncelenmesi [Doctoral dissertation, Sakarya University].

[76] Yılmaz, E., Güngör, F., & Hartomacıoğlu, S. (2019). AISI 4340 malzemesinin torna ile işlemesinde gri ilişkisel analiz yöntemi kullanılarak uygun takım tutucu (kater) seçimine karar verilmesi. Beykent Üniversitesi Fen ve Mühendislik Bilimleri Dergisi, 12(2), 7–13.

The hole-bearing behavior of laminated composites under double-shear tension and pin-crush loading

Kenan Cinar[1]* (iD)

[1]Tekirdağ Namık Kemal University, Çorlu Faculty of Engineering, Department of Mechanical Engineering, Çorlu, Türkiye

Abstract: The bearing performance of holes in laminated composite materials is a critical research area due to their increasing use in aerospace and structural applications. This study investigates the mechanical behavior of hole-bearing in laminated composites, focusing on failure mechanisms, load distribution, and the influence of laminate stacking sequences on bearing performance. Finite element analysis (FEA) and experimental testing were used to examine stress concentration around the hole. Additionally, the digital image correlation (DIC) method was employed to monitor the strain field in the pin-bearing zone during the pin-crush test. Results indicate that fiber orientation significantly affects load-bearing capacity, with notable differences between unidirectional (UD) and cross-ply (XP) laminates. A comparison between double-shear tensile loading and pin crush loading for XP and UD samples with 16 plies reveals distinct differences in load-bearing capacity and failure behavior. In the tensile test, XP-16 samples exhibited a gradual increase in load, reaching a peak of approximately 14 kN, followed by a gradual decline. Conversely, the pin-crush test resulted in a lower peak load of 9 kN and exhibited more catastrophic failure, characterized by a sudden drop in load. In contrast, UD samples displayed similar behavior under both loading conditions, with differences observed only at peak load values.

Keywords: fiber reinforced composites; hole bearing; finite element analysis (FEA); Hashin's failure theory.

1. Introduction

Laminated composite materials are widely used in aerospace, automotive, and marine applications due to their superior strength-to-weight ratio, tailored mechanical properties, and excellent fatigue performance. One critical design aspect for bolted or riveted joint applications in these composites is their bearing behavior, which governs the load transfer efficiency and overall joint performance. The performance of hole bearings in laminated composites differs significantly from that in traditional metallic materials, primarily due to the anisotropic nature of composites. The mechanical behavior of laminated composites is influenced by several factors, including the fiber orientation, ply stacking sequence, laminate thickness, and the geometry of the hole. These factors lead to complex stress distributions, which can significantly affect the bearing strength and the potential for damage initiation around the hole, such as delamination, matrix cracking, and fiber pull-out. Over the past decades, significant research has been dedicated to understanding and predicting the

bearing response of laminated composites, both experimentally and through finite element modeling (FEM).

Experimental investigations have extensively analyzed the bearing response of laminated composites, highlighting the role of material properties, lay-up configurations, and geometrical parameters. Early studies demonstrated the sensitivity of bearing strength to fiber orientation, resin properties, and ply thickness [1-7]. For instance, Furtado et al. [1] found that increasing ply thickness leads to more complex failure regions, with extensive delamination, matrix cracking, and fiber splitting near the hole. Higher ply thickness significantly reduces both the bearing load at the first load drop and the ultimate bearing load. Thin-ply laminates outperformed baseline laminates, with 21% higher initiation and 10% higher maximum bearing stresses, while thick-ply laminates showed reduced strengths. The superior performance of thin-ply laminates is attributed to their enhanced damage suppression, higher in-situ strengths, and better ply constraining. Experimental findings [5, 6] emphasized that bolted joints with ap-

---

propriate preload enhance bearing strength by minimizing local damage and delamination. Lim et al. [6] examined the fatigue behavior of bolted joints in $[\pm\theta/0_8]_s$ laminates, considering ply angle θ and bolt clamping pressure, and compared results with $[0_2/\pm45_3/90_2]_s$ laminates optimized for static loading. They found that laminates whose major plies are stacked in the axial direction are suitable for bolted joints under fatigue loads if appropriate clamping pressure is applied. Khashaba et al. [7] highlighted that ±45° layers enhance bearing load and displacement, while 90° layers resist pin displacement and increase energy absorption through interlaminar shear, improving durability and delaying sudden failure. Additionally, 0° layers maximize ultimate load capacity and apparent bearing stiffness, contributing to structural reliability.

Understanding failure mechanisms is critical for optimizing bearing performance. Experimental observations have identified three primary failure modes: bearing, shear-out, and net-tension [4]. Bearing failure, characterized by compressive deformation around the hole, is the most desirable due to its progressive nature and higher load-carrying capacity. In contrast, shear-out and net-tension failures are brittle and catastrophic. From a geometrical perspective, net-tension failure occurs when the specimen's width is too narrow to alleviate high normal stress gradients, corresponding to a low width-to-diameter (w/d) ratio. Shear-out failure arises in laminates that have sufficient width to resist net-tension failure but lack adequate free edge distance to relieve high shear stresses along the shear-out plane, indicated by a low edge-to-diameter (e/d) ratio. In both net-tension and shear-out failure modes, the compressive stresses at the bearing plane are insufficient to cause significant fiber failure before these modes occur. Bearing failure, on the other hand, results from compressive stresses and involves matrix cracking, fiber micro-buckling, kinking, and substantial delamination [8].

Non-destructive evaluation techniques, such as X-ray computed tomography (CT) [9] and digital image correlation (DIC) [10-12], have been employed to characterize damage evolution in laminated composites under bearing loads. Broutelle et al. [10] investigated damage mechanisms in an oxide/oxide ceramic matrix composite bearing using the balanced quarter hole (BQH) test, enables direct observation of damage progression during bearing failure. Unlike standard bearing tests, which rely on post-mortem analysis potentially affected by cutting operations, their setup uses high-speed cameras for real-time monitoring and damage chronology. The setup's validity was confirmed through comparisons with standard tests. Two stacking sequences were analyzed, considering the effects of material microstructure and machining. Results revealed that matrix cracks appeared before the load drop, initiating delamination and kink bands, which ultimately led to failure.

FEM has emerged as a powerful tool for predicting the bearing behavior of laminated composites, offering insights into stress distributions and failure mechanisms. Early models employed linear elastic analyses to estimate stress concentrations around fastener holes [13, 14]. However, these models failed to capture the non-linear damage progression and material degradation observed in experiments. Advancements in FEM have incorporated progressive damage models (PDMs) to simulate the initiation and growth of matrix cracking, fiber breakage, and delamination [15-22]. Hashin's failure criteria [15, 16, 20] and cohesive zone models [17,18, 20] are widely used for damage prediction in composites. For instance, Qingyuan et al. [20] developed a 3D FEM framework integrating PDMs to predict bearing strengths and observed a strong correlation with experimental data. Further developments include multi-scale modeling approaches, which bridge the microscale (fiber-matrix interactions) and macroscale (laminate response) [19]. Shipsha and Burman [22] developed a multi-scale FEM model to study the impact of fiber misalignment on bearing strength, showing that local defects significantly reduce load capacity. Instead of explicitly modeling fiber bundles, the model used stiffness matrix rotations to account for bundle waviness, reducing computational costs. It incorporated LaRC04 failure criteria and an energy-based damage evolution model, accurately predicting damage mechanisms, stress levels, and failure progression, although kinking predictions were slightly conservative. The model effectively captured both intra- and inter-laminar progressive damage, offering a balance of simplicity and predictive accuracy. Parametric studies using FEM have explored the effects of various factors on bearing performance. For example, the effect of the washer type and initial bolt tension on bearing failure was investigated by Qingyuan et al. [20]. A comparison of the bearing failure states in composite bolted joints with different washers revealed that washers significantly expand the damage range, with larger washers having a more pronounced effect. However, washers reduce delamination damage due to their suppression of peak pressure and redistribution of pressure. Regarding initial bolt tension, joints with higher tension exhibited more severe matrix and delamination damage, as the increased tension delays the reduction of structural load during tensile loading. This delay allows for greater damage accumulation before failure. High initial bolt tension improves bearing strength, delays failure onset, and enhances the load-carrying capacity of joints. Recent studies have focused on the enhancement of bearing strengths using fiber continuity around holes [23, 24].

This study explores the mechanical behavior of hole-bearing laminated composites, emphasizing failure mechanisms, load distribution, and the impact of laminate stacking sequence on bearing performance under double-shear tensile loading and pin-crush loading. A combined approach of finite element analysis (FEA) and experimental testing is employed to investigate stress concentration around the hole. The Hashin failure theory is utilized in the FEA simulations to model damage mechanisms accurately. Additionally,

the digital image correlation (DIC) method is applied to monitor the strain field in the pin-bearing zone during the pin-crush test, providing detailed insights into the deformation and failure processes.

2. Experimental and numerical procedures

2.1. Materials and manufacturing of the samples

The composite samples used in this study were fabricated using AS4/8552 unidirectional prepreg material, a high-performance carbon fiber reinforced epoxy system commonly used in aerospace and structural applications. The AS4 fibers, made of carbon, have a tensile strength of approximately 4433 MPa and a modulus of elasticity of 231 GPa. The matrix is made of the 8552 epoxy resin, known for its excellent mechanical properties and resistance to thermal degradation. The composite laminates were manufactured using the prepreg lay-up technique, where the AS4/8552 prepreg sheets, which are pre-impregnated with epoxy resin, were cut to the required dimensions for the stacking sequences.

The laminates were designed with various stacking sequences to study the effect of fiber orientation and ply number on the bearing behavior. The stacking sequences used in this study include: $[0]_{16}$, $[0/90]_{2S}$, and $[0/90]_{4S}$, where the notation indicates the number of plies and fiber orientation. Specifically, $[0]_{16}$ represent unidirectional laminates with 16 plies, respectively, all oriented at 0° to the laminate plane. The $[0/90]_{2S}$, and $[0/90]_{4S}$ sequences represent cross-ply laminates, with fibers oriented at 0° and 90° to the laminate plane in varying numbers of plies. The samples manufactured are given in ▶**Table 1**.

The lay-up process involved carefully placing each prepreg ply on a mold to maintain fiber orientation and ensure uniform resin distribution. The prepreg sheets

**Table 1.** The samples manufactured, their sizes and stacking sequences (i=1,2,3).

Bearing test	Stacking sequences	Thickness (mm)	Width (mm)	Length (mm)
XP-8-Si	$[0/90]_{2s}$	1.5±0.05	36±0.1	100±0.1
XP-16- Si	$[0/90]_{4s}$	3±0.05	36±0.1	100±0.1
UD-16- Si	$[0]_{16}$	3±0.05	36±0.1	100±0.1
Pin-crush test				
XP-16- Si	$[0/90]_{4s}$	3±0.05	25±0.1	100±0.1
UD-16- Si	$[0]_{16}$	3±0.05	25±0.1	100±0.1

were layered in the desired stacking sequence, and each layer was lightly rolled to eliminate any air pockets and improve fiber-to-matrix bonding. Once the lay-up was completed, the laminate was cured in an autoclave at 120 °C for 30 minutes and followed by 180 °C for 2 hours under 7 bar pressure to ensure full resin polymerization and optimal fiber-matrix bonding. After curing, the laminates were trimmed into 100 mm × 36 mm (25 mm for pin-crush test) specimens and 6 mm diameter hole was drilled in the specified region (18 mm from the edge of the sample), as stated in the ASTM D5961. The drilling process was done carefully to prevent damage to the fibers or matrix and minimize stress concentrations around the hole. The holes were drilled using an unused TiAlN coated carbide drill bit with a 118-degree point angle, operated at a rotational speed of ~1500 rpm and a feed speed of ~100 mm/min. Visual inspection of the drilled holes revealed no observable delamination around the hole edges, as illustrated in ▶**Figure 1b**. Therefore, quantitative measurement of delamination diameter was not performed in this study. Nevertheless, future investigations may benefit from incorporating tomography-based delamination evaluation methods to further assess hole quality and damage resistance. The edges of the specimens were grinded
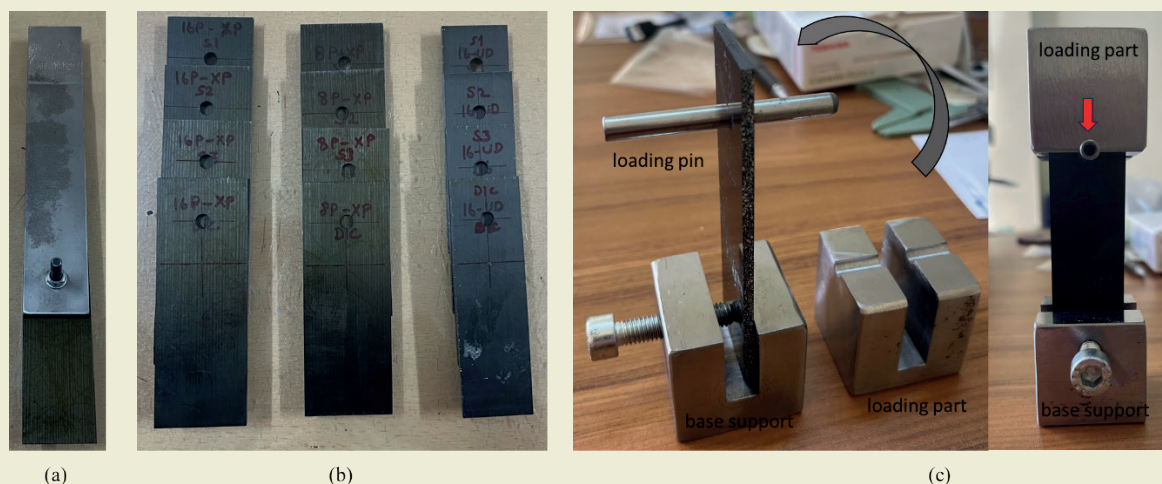
Figure 1. a) the bearing test fixture b) test samples and c) specifically designed test fixture for pin-crush test.
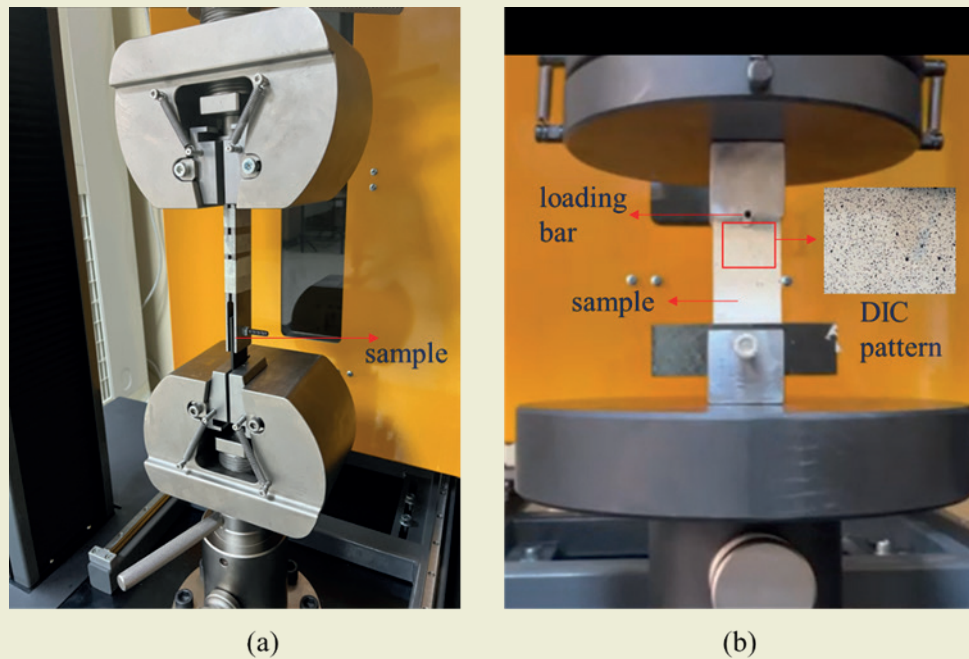
Figure. 2 a) Double-shear tensile test set-up b) strain field measurement set-up under pin-crush test

using sand papers to ensure uniform loading during testing. A special fixture as stated in the test standard (ASTM D5961) was fabricated to conduct the bearing tests, as shown in ▶**Figure 1a**. Three tests were done for each configuration. ▶**Figure 1c** presents the experimental setup used for the pin-crush test. The fixture consists of a base support with a V-groove to hold the composite specimen in place and a loading part that applies compressive force through a cylindrical pin inserted into the hole of the specimen. For Digital Image Correlation (DIC) measurements, the loading support was specifically designed with a half-hole configuration to ensure that the damage progression around the hole could be clearly captured without obstruction during the pin-crush test.

2.2. Double-shear tensile and pin-crush tests

The double-shear tensile test (bearing test) is a widely used experimental method to evaluate the performance of composite laminates under localized bearing loads, typically applied through a bolt or pin. In this study, the test was conducted using a UVE tensile test machine (200 kN) at a speed of 1 mm/min, adhering to the ASTM D5961 standard, as shown in ▶**Figure 2a**. A specially designed fixture was used to securely hold the specimens and ensure accurate load transfer, as specified in the standard. The test setup allows the investigation of the bearing strength, stiffness, and failure modes of composite materials, offering insights into their ability to withstand concentrated loads in bolted joint applications. The displacement was measured directly from the machine, capturing the mechanical response of the specimens under gradually increasing loads.

For pin-crush tests, Digital Image Correlation (DIC) was employed to capture full-field strain and displacement distributions on the specimen's surface during the test, as shown in ▶**Figure 2b**. The GOM software was used for DIC data acquisition and analysis, providing high-resolution measurements of strain evolution and damage progression. By correlating the DIC results with the load-displacement data, a detailed understanding of the material's local and global deformation behavior was achieved. This integration of bearing testing with DIC allows for a comprehensive characterization of the material's mechanical performance, highlighting critical regions of stress concentration and failure initiation in composite laminates.

2.3. Finite element analysis

▶**Figure 3** illustrates the finite element (FE) models for two different mechanical tests: the double-shear tensile test (▶**Figure 3a**) and a pin-crush test (▶**Figure 3b**). The FE mesh consists of structured and unstructured elements, with finer meshing in the regions of high stress concentration, particularly around the hole where the load is applied. The number of nodes and elements are given in ▶**Table 2**. The structured elements appear in the flat plate regions, where hexahedral meshes are used in a grid-like pattern. The unstructured elements are seen around the hole, where irregular meshing is necessary to capture stress concentrations and complex deformations. In the bearing test model in ▶**Figure 3**(a), boundary conditions were applied to ensure symmetry along the z-direction and the y-direction, restricting displacement at the edges. Thus, 8 plies were modeled. The load is applied in the x-direction with a prescribed

displacement of 4 mm at the contact region. The top region is clamped to replicate experimental constraints, and contact interactions are defined between the pin and the hole surface to capture localized deformation behavior.

In the pin-crush test model in ▶**Figure 3**(b), the boundary conditions differ to reflect a crushing scenario where the load is applied in the x-direction with a displacement of 2.5 mm. The structure is supported at the bottom, preventing rigid body motion in x-direction. The mesh refinement around the hole and the surrounding region indicates the need for accurate stress-strain predictions in highly deformed areas. The middle section of the image highlights the detailed meshing of the curved surface, which is crucial for capturing nonlinear deformations and contact effects. Both models are designed to study the material behavior under different loading conditions, providing insights into failure mechanisms such as local crushing, shear-out, or bearing failure in composite plates.

Table 2. The number of elements and nodes

Bearing analysis	Number of elements	Number of nodes
XP-8-FEM	633	1247
XP-16-FEM	2331	3319
UD-16-FEM	2331	3319
Pin-crush analysis		
XP-16-FEM	4954	5883
UD-16-FEM	4954	5883

Eight-node quadrilateral in-plane general-purpose continuum shell elements (SC8R) were used to model the lamina. To improve computational efficiency, the fixed mass scaling option in ABAQUS/Explicit [25] was activated at the start of the analysis with a scaling factor of 1000. The lamina was assumed to exhibit transversely isotropic linear elastic behavior. Hashin's damage initiation criteria were applied to predict the onset of damage, considering four distinct and uncoupled damage initiation modes, defined as follows:

$$F_f^t = \left(\frac{\sigma_{11}}{X^T}\right)^2 + \left(\frac{\tau_{12}}{S^L}\right)^2 \text{ Fiber tension } (\sigma_{11} \geq 0) \quad (1)$$

$$F_f^c = \left(\frac{\sigma_{11}}{X^C}\right)^2 \quad \text{Fiber compression} \quad (\sigma_{11} < 0) \quad (2)$$

$$F_m^t = \left(\frac{\sigma_{22}}{Y^T}\right)^2 + \left(\frac{\tau_{12}}{S^L}\right)^2 \text{ Matrix tension}$$
$$(\sigma_{22} \geq 0) \quad (3)$$

$$F_m^c = \frac{1}{Y^C}\left[\left(\frac{Y^C}{2S^T}\right)^2 - 1\right](\sigma_{22}) + \frac{1}{2(S^T)^2}(\sigma_{22})^2 + \frac{1}{(S^L)^2}(\sigma_{12}^2)$$

Matrix compression $(\sigma_{22} < 0)$ (4)

where, X^T and X^c are the longitudinal tensile and com-

pressive strengths, Y^T and Y^C are the transverse tensile and compressive strengths, S^L and S^T are the longitudinal and transverse shear strength, σ_{ij} $(i = 1, 2)$ are the components of the stress tensor, α is a coefficient which determines the contribution of the shear stress to the fiber tensile criterion. The mechanical properties of a unidirectional AS4/8552 lamina are given in ▶**Table 3**. It should be noted that inter-laminar damage (delamination) was not considered in this model due to computational burden of the analysis.

Table 3. AS4/8552 material properties [26]

Property	Value	Units
Ply elastic properties		
E_1	137100	MPa
$E_2 = E_3$	8800	MPa
$G_{12} = G_{13}$	4900	MPa
G_{23}	5400	MPa
$\upsilon_{12} = \upsilon_{13}$	0.314	
υ_{23}	0.487	
Ply strength properties		
X^T	2106.4	MPa
X^C	1675.9	MPa
Y^T	74.2	MPa
Y^T	322.0	MPa
S^L	110.4	MPa
Ply fracture energies		
G_{1+}	125.0	kJ/m²
G_{1-}	61.0	kJ/m²
G_{2+}	0.3	kJ/m²
G_6	0.87	kJ/m²

3. Results and Discussions

3.1. Double-shear tensile test (bearing test)

The load-displacement curve in ▶**Figure 4** represents the bearing response of composite laminates under ASTM D5961 testing conditions. The laminates tested include cross-ply (XP) laminates with 8 and 16 total lamina and unidirectional laminates with 16 total laminas denoted as XP-8, XP-16 and UD-16, respectively. The average maximum bearing forces and standard deviations for the tested specimens were calculated as follows: XP-8: 5679.6 ± 294.1 N, XP-16: 14832.9 ± 517.6 N, and UD-16: 5439.6 ± 128.7 N. The black curves correspond to XP-16 samples, which exhibit higher peak loads, indicating superior bearing strength due to the increased number of a lamina. In contrast, the red curves represent XP-8 samples, which show lower peak loads, reflecting their reduced bearing capacity. Both laminate types demonstrate typical behavior under bearing loads, with an initial linear region followed

by a peak and a gradual decline, indicative of material damage or failure mechanisms of matrix tensile failure, matrix and fiber crushing/fracture and delamination. The UD-16 laminates exhibit significantly lower peak loads and abrupt post-peak drops, indicative of brittle failure mechanism due to transverse matrix cracking. This comparison underscores the critical role of laminate architecture in influencing the bearing strength

and failure mechanisms of composite materials, with cross-ply laminates providing enhanced performance over unidirectional ones in bearing applications.

The failure modes observed in laminated composites under a bearing test can vary depending on the laminate stacking sequence and loading conditions. Net-tension failure occurs when the specimen fractures across
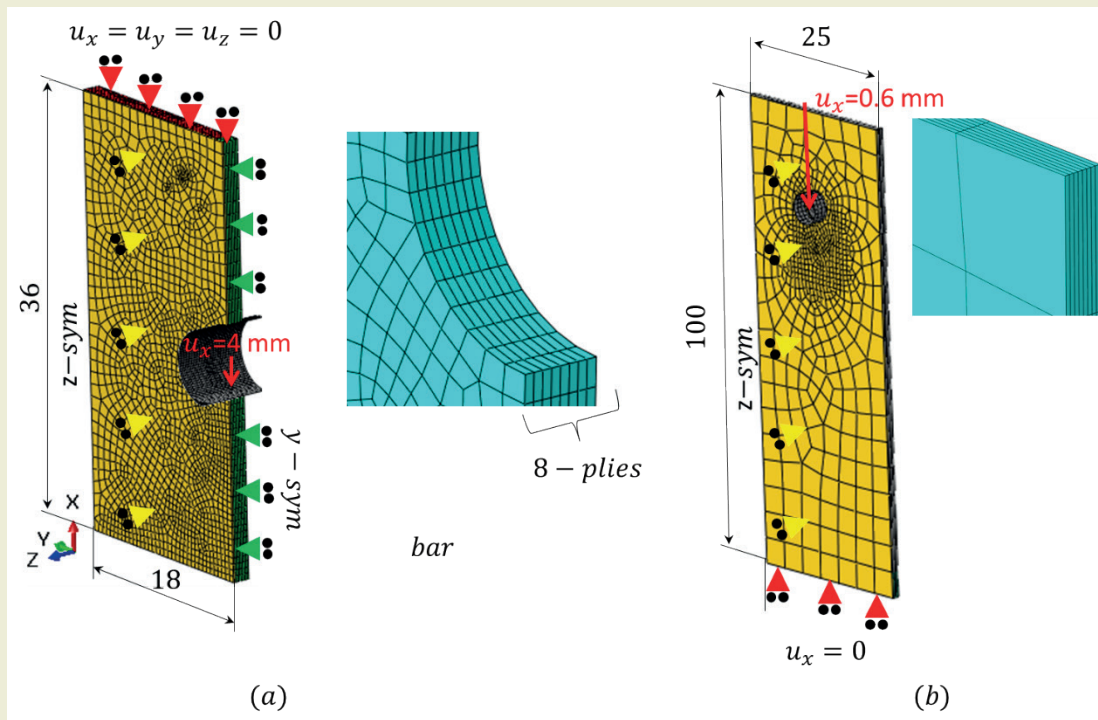
Figure 3. Finite element mesh, loading and boundary conditions a) bearing test model, b) pin-crush test model
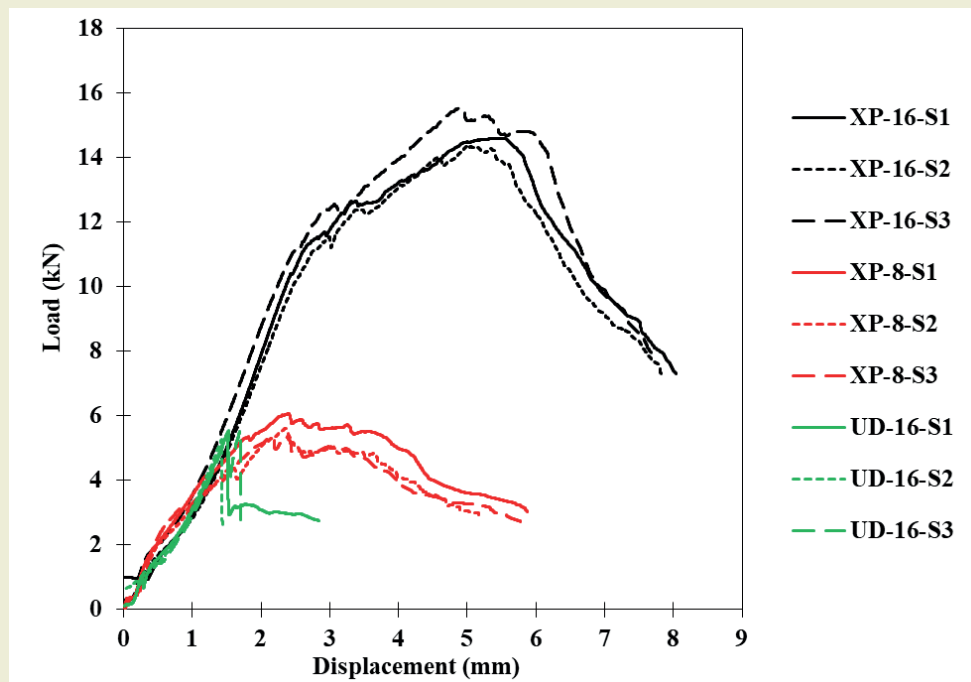
Figure 4. Load-displacement response of bearing tests for XP and UD samples with 8 and 16 plies.

its width due to excessive tensile stresses, leading to brittle failure, which is often seen in laminates with lower bearing strength [4, 8]. This failure mode was occurred in UD laminates, as shown in ▶Figure 5c. In many cases, mixed failure modes are observed, where a combination of bearing, net-tension, and shear-out failure occurs depending on the laminate stacking and test conditions. Bearing failure is characterized by progressive damage around the hole due to high localized stresses, often occurring in thicker laminates like 8-XP and 16-XP as shown in ▶Figure 5 a and 5b. The cross-ply specimens in this study exhibit signs of shear-out and bearing failure, indicating a complex interaction of

Figure 5. Failure of samples under bearing test a) 8-XP, b) 16-XP, and c) UD-16

stress distributions around the hole [4, 8].

3.2. Pin-crush tests

The pin-crush loading results for XP and UD samples with 16 plies in ▶Figure 6 show distinct differences in load-bearing capacity and failure behavior. The XP-16 reaches a higher peak load compared to the UD-16. The average maximum pin-crush forces and standard deviations for the tested specimens were calculated as follows: XP-16: 9227.5 ± 803.3 N, and UD-16: 6629.4 ± 320.3 N. Additionally, the XP sample exhibits a more gradual decline after reaching peak load, maintaining a significant load-carrying capacity (~5000 N) over a larger displacement range (~1–5 mm). This suggests a more progressive failure mechanism, likely due to enhanced load redistribution in the XP laminate. In contrast, the UD sample experiences a sharp load drop immediately after peak load, with rapid degradation beyond 1.5 mm displacement. This indicates a more brittle failure mode, where damage accumulates quickly, leading to catastrophic failure with minimal residual load-bearing capacity. Overall, the XP sample outperforms the UD sample in terms of both peak load and post-peak load retention, making it more resistant to crushing-induced damage. The improved performance of the XP laminate could be attributed to its stacking sequence, which likely enhances its resistance to through-thickness shear and progressive damage mechanisms.

This Digital Image Correlation (DIC) image in ▶Figure 7 presents the strain distribution (ε_y) in the laminated composite specimen of 16-XP undergoing the pin-crush test. The sequence of images from left to right and top to bottom suggests a progressive loading scenario, where strain concentration around the hole increases with load application. Initially, the specimen shows a uniform strain distribution with minimal localized deformation. As the load increases, strain accumulation becomes evident around the contact region between the hole and the pin, primarily in the upper part, where compressive forces are dominant. The color scale indicates that strain values transition from low (red) to high deformation (blue), with negative strain representing compression. In the intermediate stages, strain localization spreads radially from the hole, with higher deformation at the upper contact edge. The bottom edge of the hole remains relatively less affected initially, but as loading progresses, shear bands and deformation extend downward, indicating material yielding and potential bearing failure initiation. In the final images, significant localized damage appears below the hole, with clear signs of fiber-matrix separation or delamination, particularly in the lower part, suggesting shear-out failure progression. The highest strain zones (blue regions) indicate areas susceptible to crack initiation and failure propagation.

The sequence of images in ▶Figure 8 illustrates the evolution of transverse strain (ε_x) over time during a pin crushing test on a unidirectional (UD-16) laminate.
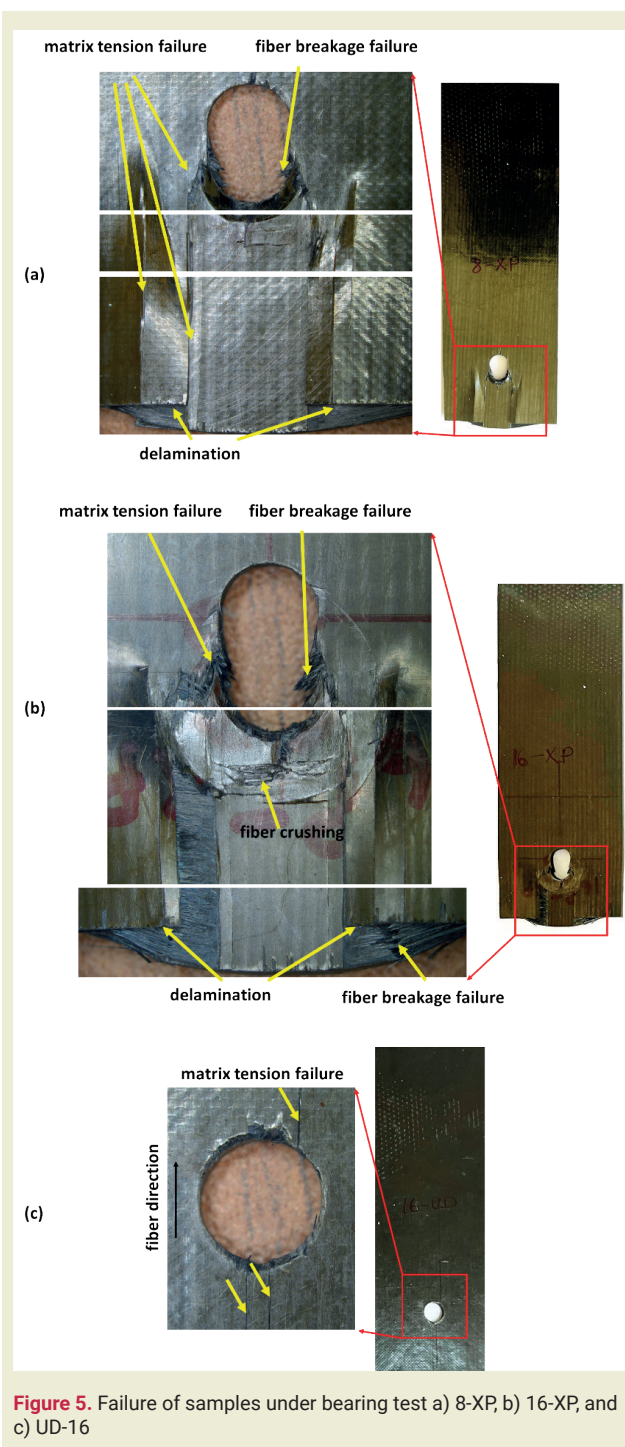
Initially, the strain distribution is relatively uniform across the specimen, with minimal localized deformation. As the test progresses, strain concentration develops directly beneath the pin, forming a vertical band of increasing tensile strain, as shown by the transition from green to yellow and red. This strain localization suggests the onset of matrix damage along the loading path. In the later stages, a significant crack propagates downward, characterized by high tensile strain (red regions) along the failure path. The final image reveals a fully developed fracture matrix crack. The test results highlight the brittle nature of the unidirectional
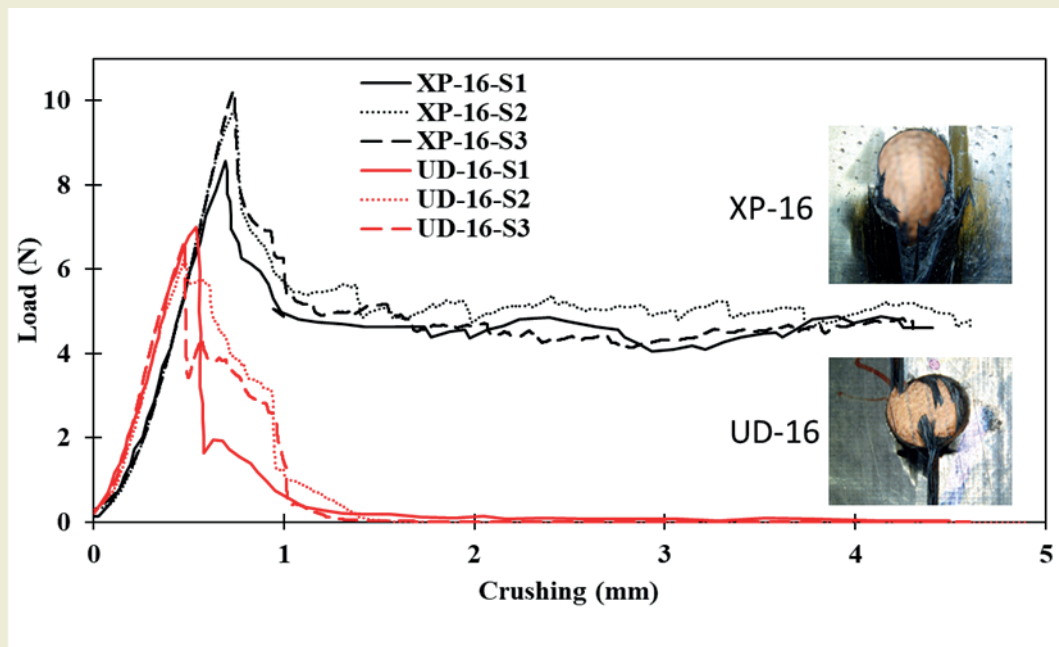
Figure 6. Load-crushing response of under specifically designed fixture for UD and XP samples of 16 plies.
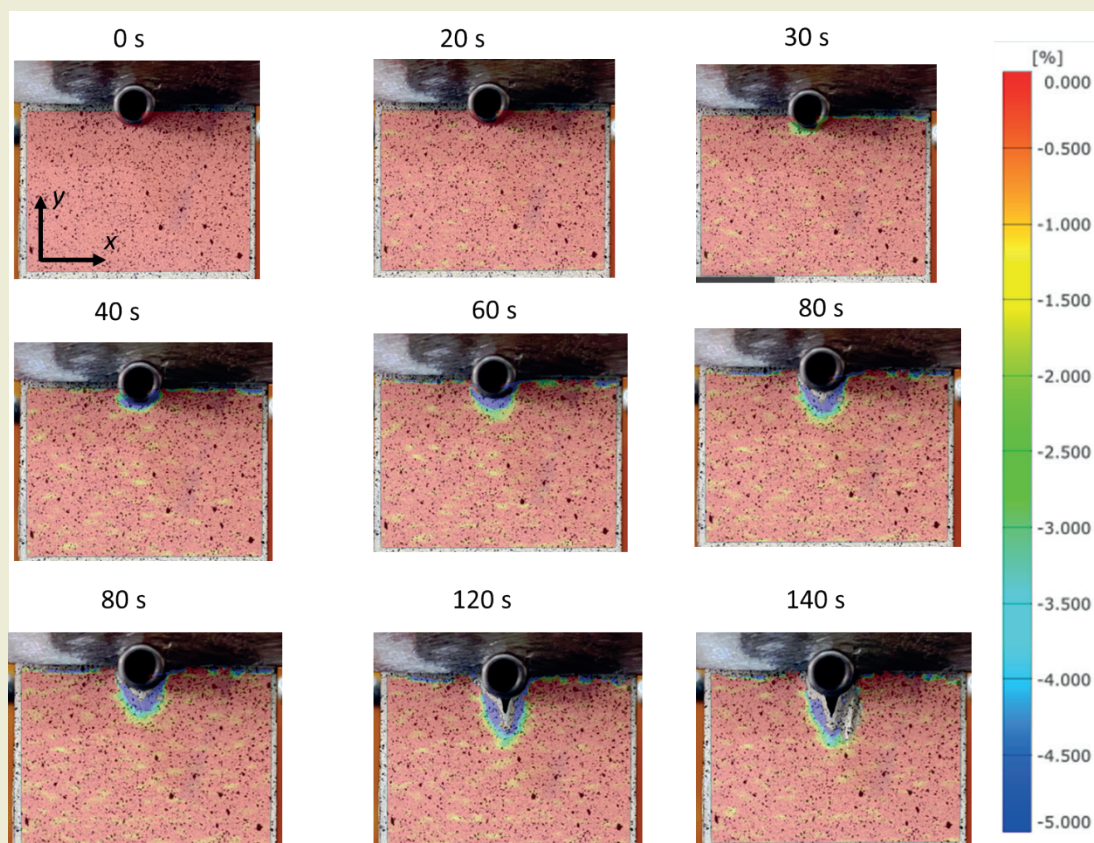
Figure 7. Change in (ε_y) with time under pin-crush test for XP-16 sample.

composite under pin crushing, where failure occurs through crack initiation at the contact point, followed by rapid crack propagation along the fiber direction. The strain distribution suggests that load transfer is primarily concentrated along the vertical axis, leading to localized damage and eventual material failure.

This sequence of images in ▶**Figure 9** illustrates the evolution of vertical strain (ε_y) over time during a pin crushing test on a unidirectional (UD-16) laminate. As the test progresses, localized strain concentration develops around the pin contact area, shown by the transition from red to green and blue regions. These areas indicate increasing compressive strain directly beneath the pin and slight tensile effects near the edges. In the later stages, strain localization intensifies along the failure path, forming a vertical crack propagating downward. The results highlight that the UD laminate primarily experiences compressive loading along the vertical axis, with failure initiating at the contact point and progressing due to local crushing and splitting. Unlike the horizontal strain (ε_x), which exhibited more tensile behavior in the crack path, the vertical strain field remains mostly compressive, supporting the observation that failure is dominated by localized crushing and transverse matrix cracking.

3.3. Finite element analysis

To ensure the reliability of the finite element model, a mesh convergence analysis was conducted by varying the global mesh size (GMS) around the hole region. Three mesh densities were considered: GMS = 2 mm, 1 mm, and 0.5 mm, as illustrated in the inset of ▶**Figure 10**. The corresponding load-displacement curves show that as the mesh was refined, the numerical results became more stable and converged. Specifically, the model with GMS = 0.5 mm showed only slight variation in peak load compared to the 1 mm mesh, indicating that the solution had sufficiently converged. Based on this analysis, GMS = 1 mm was selected for further simulations, providing a good balance between computational accuracy and efficiency.

Figure 11 shows the load-displacement curve from the double-shear tensile test which illustrates the mechanical response of UD-16 samples, comparing experimental result with finite element method (FEM) prediction. Both curves exhibit an initial linear increase, followed by a peak and subsequent softening. The FEM prediction (UD-16-FEM) closely follow the experimental trends (dotted lines), indicating that the finite element model effectively captures the material response. However, some deviations are noticeable, particularly in the post-peak region, which could be attributed to factors such as material property variability, damage evolution modeling, or experimental uncertainties. The brittle nature of unidirectional laminates under bearing loading may cause these fluctuations, and the FEM model appears to slightly underestimate the peak load, failing to capture premature damage initiation in the real test specimens. Failure progression can also be seen in
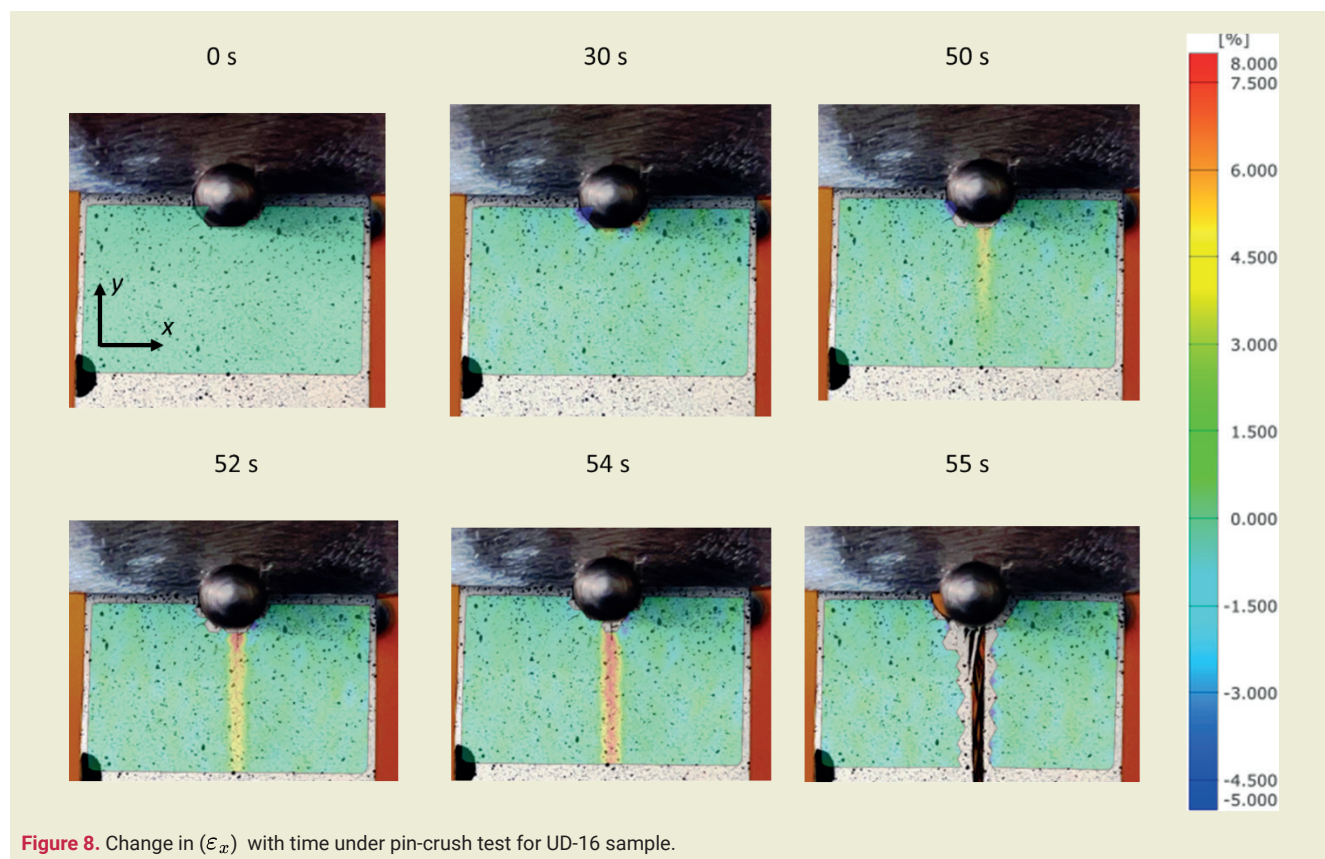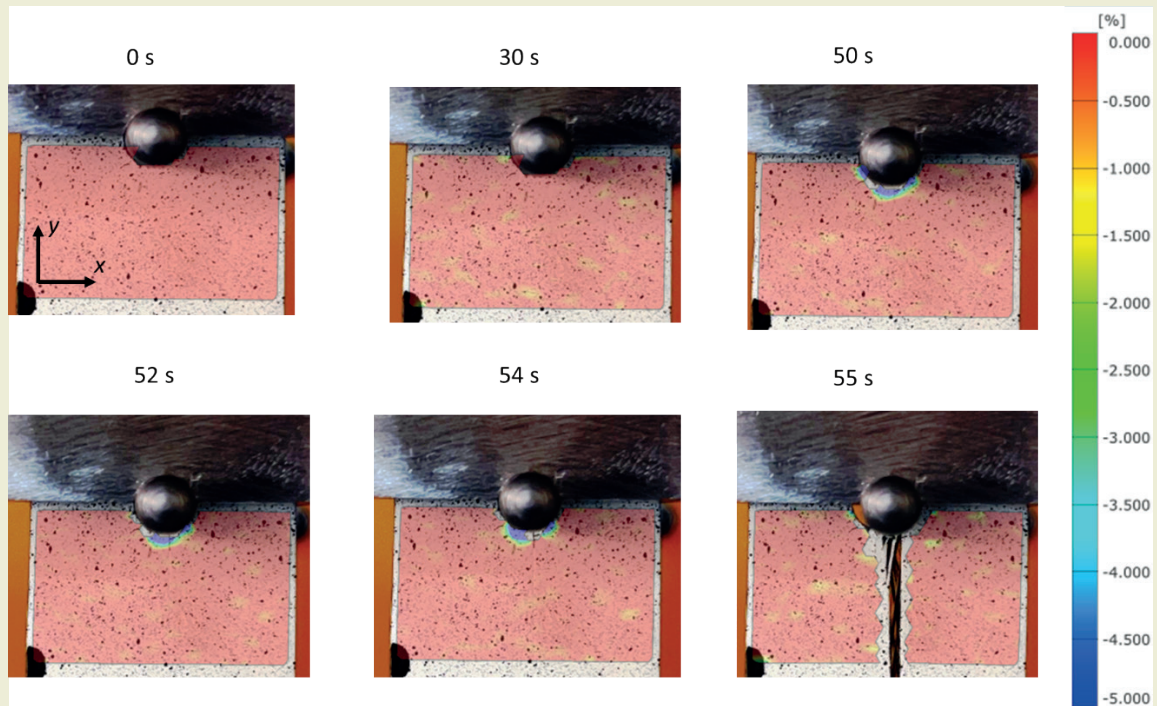

**Figure 8.** Change in (ε_x) with time under pin-crush test for UD-16 sample.

►**Figure 11**. Hashin's matrix tensile failure index with displacement and load was represented. The progression of matrix tensile failure initiated beneath the bolt shaft region and propagated downward.

►**Figure 12** presents the results of a bearing test for the XP-8 specimen, including both experimental (XP-

8-S2) and finite element model (XP-8-FEM) curves. The load-displacement graph shows that the FEM simulation closely follows the experimental trend, capturing the key load peaks and progressive failure behavior. However, some discrepancies exist, particularly in the post-peak region, where the experimental curve exhibits a more gradual decline, whereas the FEM model

Figure 9. Change in (ε_y) with time under pin-crush test for UD-16 sample.
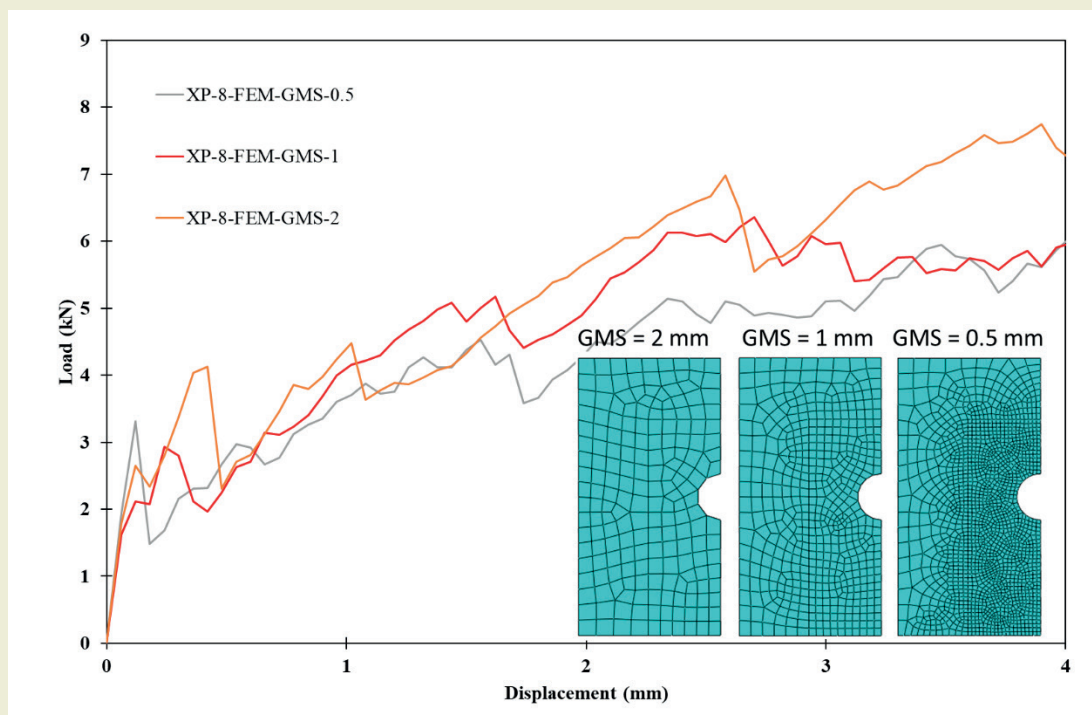
Figure 10. Mesh convergence analysis for the XP-8 specimen showing the effect of global mesh size (GMS = 2 mm, 1 mm, and 0.5 mm) on the load−displacement response.

maintains higher load levels before dropping. The peak load values are relatively close, with the FEM predicting a slightly higher failure load compared to the experiment. The Hashin failure modes in the image provide a detailed progression of damage during the bearing test. Initially, matrix tension failure occurs around the notch and spreads along the loading path as the displacement increases, indicating the onset of damage due to transverse tensile stresses. At higher load levels, matrix compression failure becomes prominent, particularly in regions experiencing compressive stresses, leading to material crushing. As the load continues to increase, fiber tension failure becomes more evident, especially in areas subject to axial stretching along the fiber direction. In the final stages, fiber tension failure becomes widespread, contributing to the reduction in load-bearing capacity. Additionally, fiber compression failure is observed near the notch where localized compressive stresses cause fiber kinking and instability. Overall, the FEM model effectively captures the initiation and evolution of these failure modes, with matrix failures occurring first, followed by fiber failures as the load increases. The FEM results correlate well with the experimental observations, but slight discrepancies in failure evolution suggest room for further refinement in the material modeling, particularly in the representation of damage propagation and softening behavior.

▶**Figure 13** presents the results of a bearing test for the XP-16 specimen, including both experimental (XP-16-S1) and finite element model (XP-16-FEM) curves. The load-displacement curves demonstrate a strong correlation between the experimental and simulated results, validating the accuracy of the FEM model in predicting the material's response under double-shear tensile test. Both curves exhibited an initial linear elastic region, followed by a non-linear phase indicative of progressive damage, culminating in a load drop signifying failure. The load-displacement curve at the top illustrates a strong correlation between the two, with numbered points corresponding to specific stages of damage. Below, the image is segmented into four rows representing different Hashin failure modes: matrix tension, matrix compression, fiber tension, and fiber compression. Each column, numbered 1 through 10, corresponds to a specific displacement and load value, showing the evolution of damage over time. Initially, matrix tension damage is observed, followed by matrix compression, then fiber tension, and finally fiber compression, indicating a sequential progression of failure mechanisms. The contour plots within each segment visually represent the failure index distribution, with color gradients indicating the severity of damage for each mode. The numerical values below each column specify the displacement in millimeters and the corresponding load values, providing a quantitative measure of the material's response. It is important to note that the number of frames shown for each failure mode in ▶**Figures 12 and 13** differs between specimens. For the XP-8 specimen (▶**Figure 12**), seven critical points were selected along the load-displacement curve based on noticeable changes in slope or load drops that indicate key stages in the damage evolution. In contrast, ten such points were identified for the XP-16 specimen (▶**Figure**
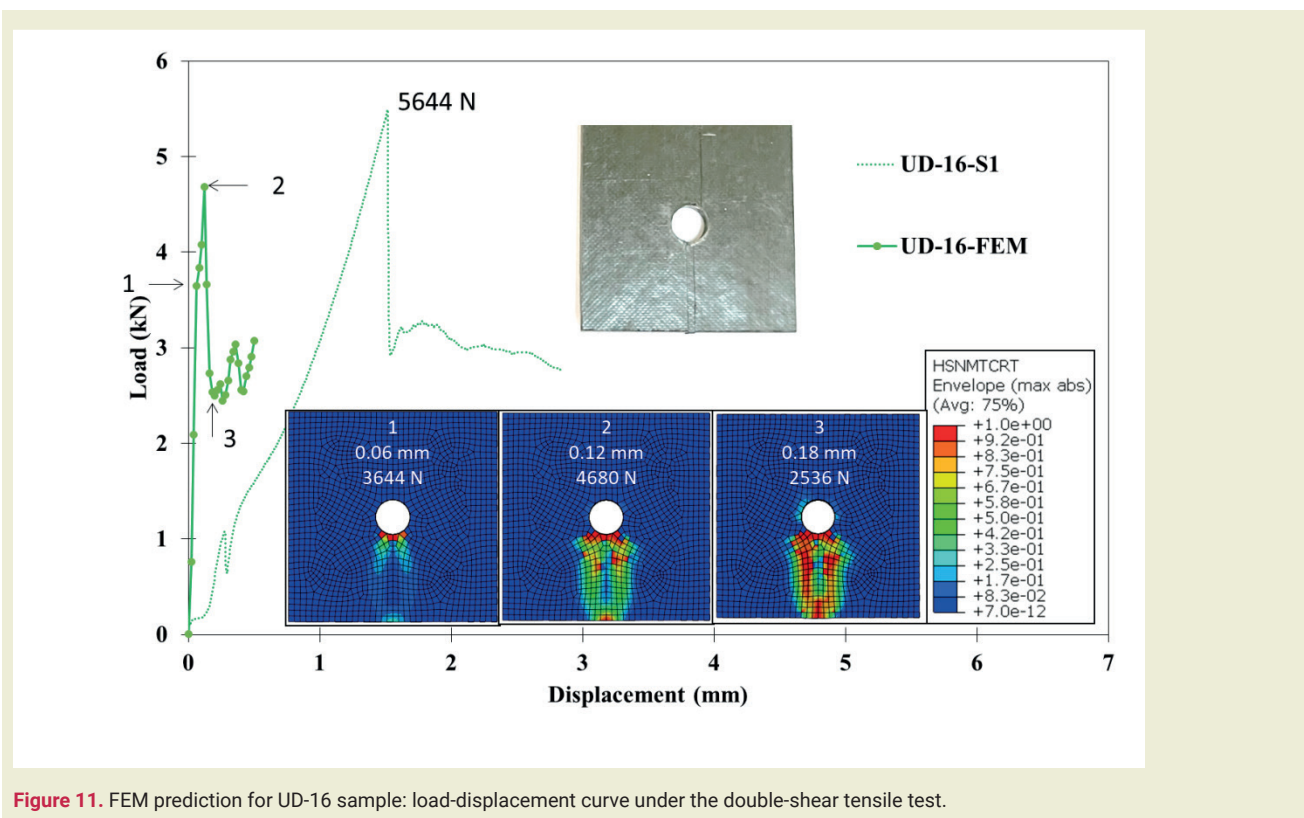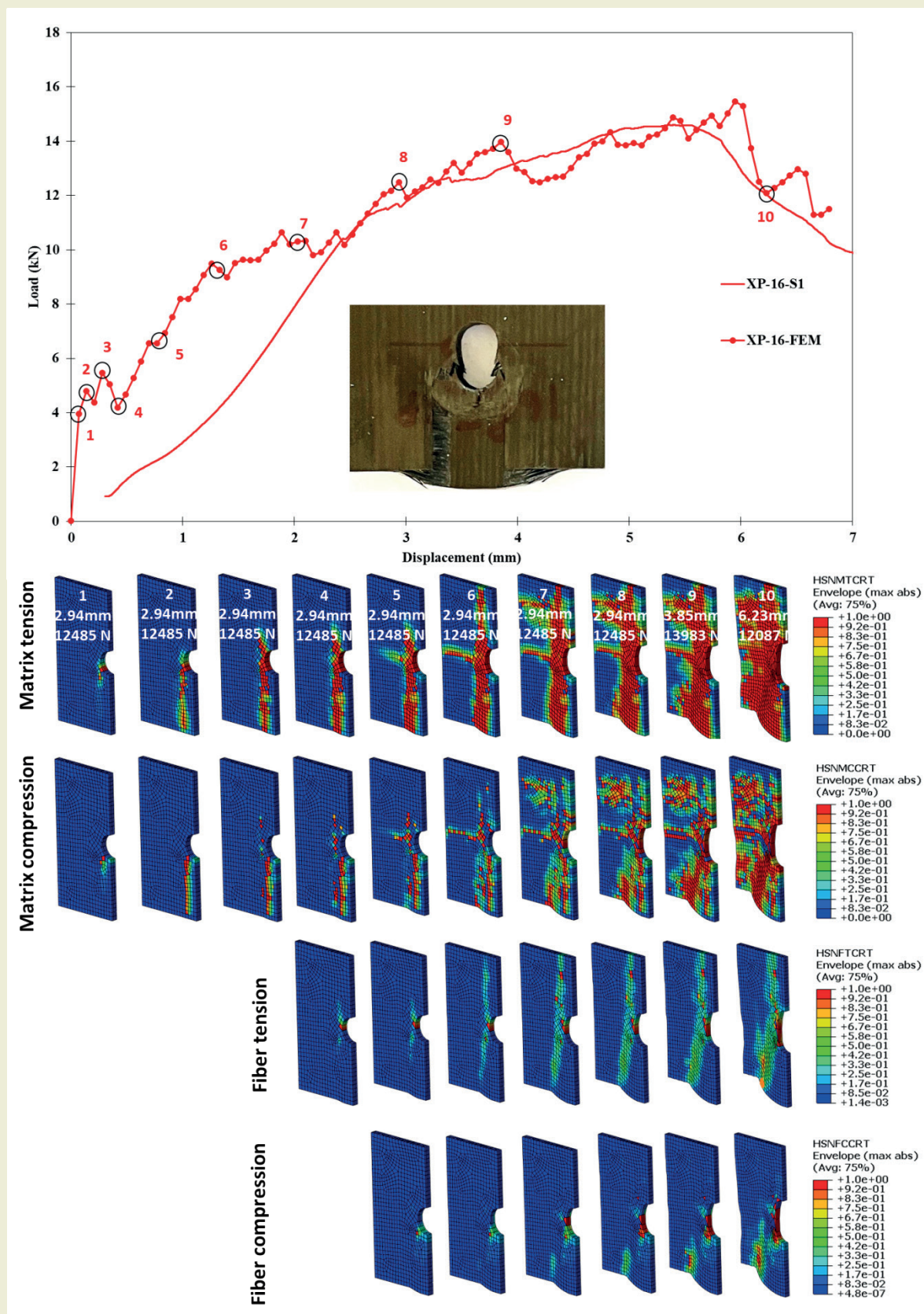

Figure 11. FEM prediction for UD-16 sample: load-displacement curve under the double-shear tensile test.
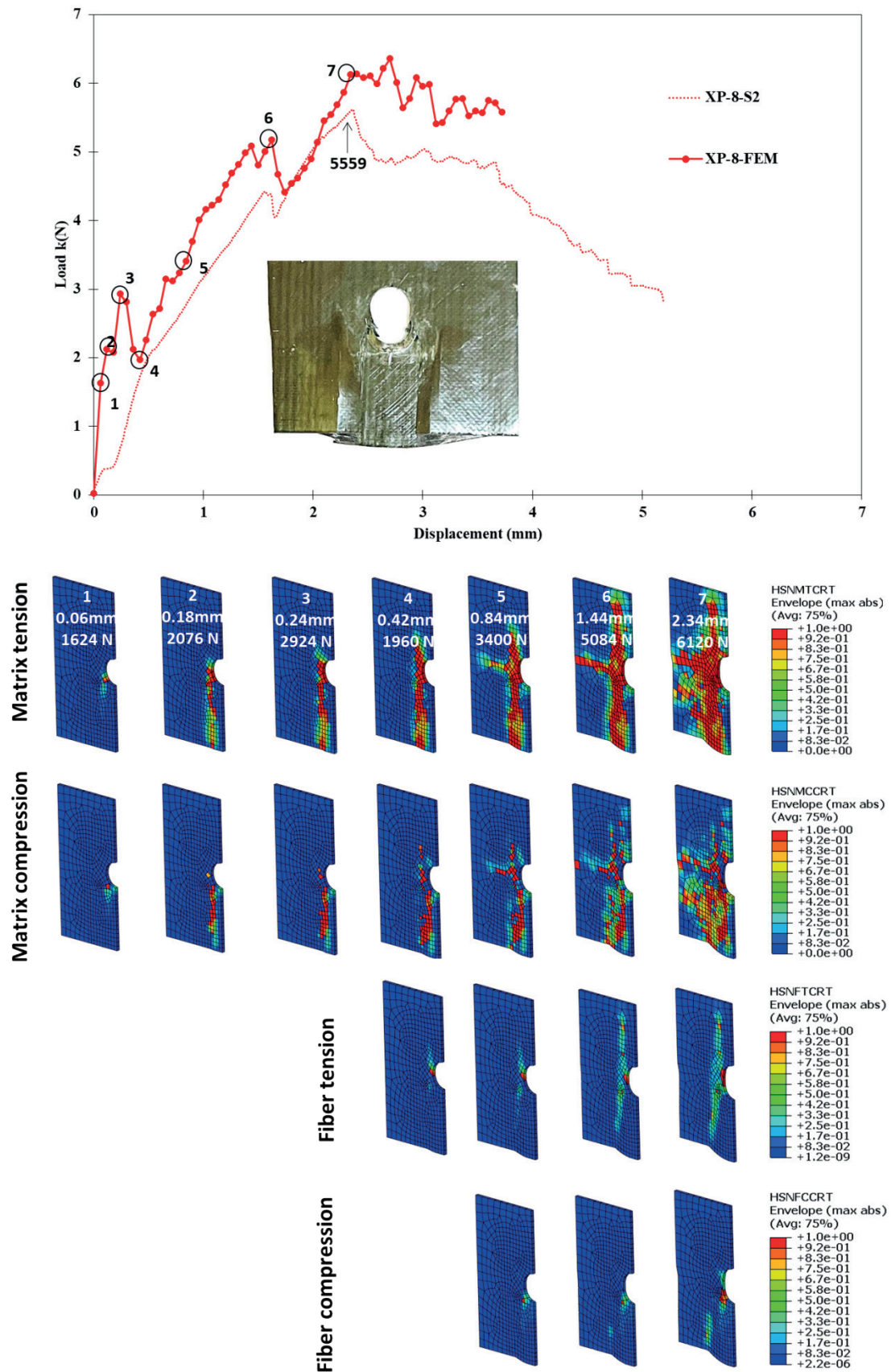
Figure 12. Comparison of FEM predictions and experimental results for the XP-8 specimen: Load–displacement response under double-shear tensile testing

Figure 13. Comparison of FEM predictions and experimental results for the XP-16 specimen: Load–displacement response under double-shear tensile testing

13). As a result, each row in ▶**Figure 12** includes seven frames, while ▶**Figure 13** contains ten. This segmentation strategy reflects the specimen-specific damage progression representative visualization of failure development at significant mechanical events.

The load-displacement graph presents the pin-crush test results for cross-ply (XP) and unidirectional (UD) laminates with 16 plies, comparing experimental (EXP) and finite element (FEM) data, as shown in ▶**Figure 14**. Both XP and UD laminates exhibit an initial load increase followed by a peak and subsequent drop, characteristic of composite failure. The XP-16 laminates show higher peak loads than UD-16 laminates in both experimental and FEM results, indicating superior load-carrying capacity due to the cross-ply layup. While the FEM predictions generally follow experimental trends, some deviations are observed. The XP-16-FEM and UD-16-FEM overestimates the peak load compared to test one. In the modelling section, it was noted that delamination was not considered in the model due to computational burden. The higher values of FEM predictions may be come from this phenomenon. Additionally, the XP-16 laminates exhibit a more gradual load drop after peak, while the UD-16 laminates experience more abrupt failure, especially in experimental results.

4. Conclusions

This study investigated the bearing and pin-crush behaviors of cross-ply (XP) and unidirectional (UD) composite laminates through both experimental testing and finite element analysis (FEM). The results highlight the significant influence of laminate architecture on the mechanical response and failure mechanisms under these loading conditions. In bearing tests, XP laminates (XP-8 and XP-16) demonstrated superior load-carrying capacity compared to UD-16 laminates, attributed to the enhanced load redistribution and resistance to through-thickness shear provided by the cross-ply layup. The UD-16 laminates exhibited brittle failure, characterized by abrupt load drops and transverse matrix cracking, reflecting their inherent susceptibility to crack propagation along the fiber direction. The FEM simulations effectively captured the general trends of the experimental data, validating the models' ability to predict the bearing response and failure initiation. However, discrepancies in the post-peak regions suggest the need for further refinement in material modeling, particularly concerning damage propagation and softening behavior. Pin-crush tests further emphasized the performance advantages of XP-16 laminates, which exhibited higher peak loads and a more gradual post-peak load decline compared to UD-16 laminates. The XP-16 laminates demonstrated a progressive failure mechanism, while the UD-16 laminates experienced brittle failure with rapid damage accumulation. Digital Image Correlation (DIC) analysis revealed distinct strain distributions and failure modes for each laminate type, with XP-16 showing progressive strain accumulation and shear-out failure, and UD-16 displaying localized compressive strain and brittle crack propagation. FEM simulations of the pin-crush tests showed good qualitative agreement with experimental results, but quantitative discrepancies, especially in peak load predictions and post-peak behavior, indicate the need for improved material modeling.
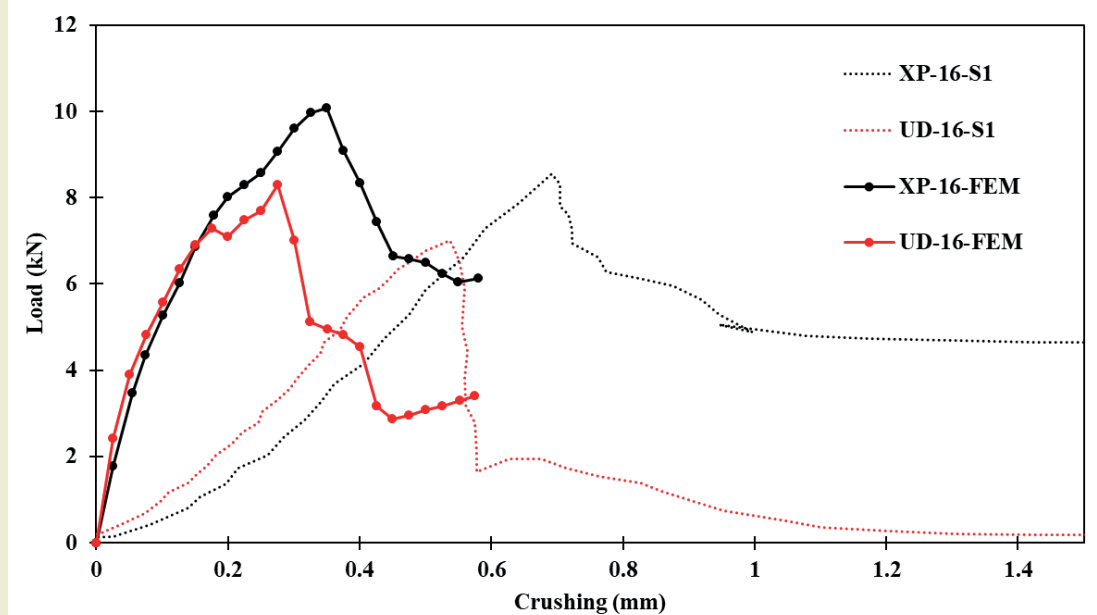

Figure 14. FEM prediction for UD-16 and XP-16 sample: load-displacement curve under the pin-crush test.

Research ethics

Not applicable.

Author contributions

The author solely conducted all stages of this research.

Competing interests

The author states no conflict of interest.

Research funding

None declared.

Data availability

The raw data can be obtained on request from the corresponding author.

Peer-review

Externally peer-reviewed.

Orcid

Kenan Cinar https://orcid.org/0000-0001-7402-2032

References

[1] Furtado, C., Tavares, R. P., Arteiro, A., Xavier, J., Linde, P., Wardle, B. L., & Camanho, P. P. (2021). Effects of ply thickness and architecture on the strength of composite sub-structures. Composite Structures, 256, 113061. https://doi.org/10.1016/j.compstruct.2020.113061

[2] Okutan, B., & Karakuzu, R. (2003). The strength of pinned joints in laminated composites. Composites Science and Technology, 63(6), 893-905. https://doi.org/10.1016/S0266-3538(02)00313-5

[3] Cameron, C. J., Larsson, J., Loukil, M. S., Murtagh, T., & Wennhage, P. (2021). Bearing strength performance of mixed thin/thick-ply, quasi-isotropic composite laminates. Composite Structures, 261, 113312. https://doi.org/10.1016/j.compstruct.2020.113312

[4] [Okutan Baba] Okutan Baba, B. (2006). Behavior of pin-loaded laminated composites. Experimental Mechanics, 46, 589-600. https://doi.org/10.1007/s11340-006-8735-z

[5] Sen, F., Pakdil, M., Sayman, O., & Benli, S. (2008). Experimental failure analysis of mechanically fastened joints with clearance in composite laminates under preload. Materials & Design, 29(6), 1159-1169. https://doi.org/10.1016/j.matdes.2007.05.009

[6] Lim, T. S., & Kim, B. C. (2006). Fatigue characteristics of the bolted joints for unidirectional composite laminates. Composite Structures, 72(1), 58-68. https://doi.org/10.1016/j.compstruct.2004.10.013

[7] Khashaba, U. A., Sebaey, T. A., & Alnefaie, K. A. (2013). Failure and reliability analysis of pinned-joints composite laminates: Effects of stacking sequences. Composites Part B: Engineering, 45(1), 1694-1703. https://doi.org/10.1016/j.compositesb.2012.09.066

[8] Ataş, A., & Soutis, C. (2013). Subcritical damage mechanisms of bolted joints in CFRP composite laminates. Composites Part B: Engineering, 54, 20-27. https://doi.org/10.1016/j.compositesb.2013.04.071

[9] Xiao, Y., & Ishikawa, T. (2005). Bearing strength and failure behavior of bolted composite joints (part I: Experimental investigation). Composites Science and Technology, 65(7-8), 1022-1031. https://doi.org/10.1016/j.compscitech.2005.02.011

[10] Broutelle, M., Lachaud, F., Barrièrre, L., Daidié, A., Chardonneau, A., & Bouillon, F. (2020). Bearing damage identification in oxide/oxide ceramic matrix composite with a new test design. Composite Structures, 236, 111902. https://doi.org/10.1016/j.compstruct.2020.111902

[11] Zhuang, F., Chen, P., Arteiro, A., & Camanho, P. P. (2019). Mesoscale modelling of damage in half-hole pin bearing composite laminate specimens. Composite Structures, 214, 191-213. https://doi.org/10.1016/j.compstruct.2019.01.06

[12] Sola, C., Castanié, B., Michel, L., Lachaud, F., Delabie, A., & Mermoz, E. (2016). On the role of kinking in the bearing failure of composite laminates. Composite Structures, 141, 184-193. https://doi.org/10.1016/j.compstruct.2016.01.058

[13] Ireman, T. (1998). Three-dimensional stress analysis of bolted single-lap composite joints. Composite Structures, 43(3), 195-216. https://doi.org/10.1016/S0263-8223(98)00103-2

[14] McCarthy, M., McCarthy, C. T., Lawlor, V. P., & Stanley, W. F. (2005). Three-dimensional finite element analysis of single-bolt, single-lap composite bolted joints: part I—model development and validation. Composite Structures, 71(2), 140-158. https://doi.org/10.1016/j.compstruct.2004.09.024

[15] Tserpes, K. I., Papanikos, P., & Kermanidis, T. H. (2001). A three-dimensional progressive damage model for bolted joints in composite laminates subjected to tensile loading. Fatigue & Fracture of Engineering Materials & Structures, 24(10), 663-675. https://doi.org/10.1046/j.1460-2695.2001.00424.x

[16] Montagne, B., Lachaud, F., Paroissien, E., Martini, D., & Congourdeau, F. (2020). Failure analysis of single lap composite laminate bolted joints: Comparison of experimental and numerical tests. Composite Structures, 238, 111949. https://doi.org/10.1016/j.compstruct.2020.111949

[17] Hu, X. F., Haris, A., Ridha, M., Tan, V. B. C., & Tay, T. E. (2018). Progressive failure of bolted single-lap joints of woven fibre-reinforced composites. Composite Structures, 189, 443-454. https://doi.org/10.1016/j.compstruct.2018.01.104

[18] Wang, J., Qin, T., Mekala, N. R., Li, Y., Heidari-Rarani, M., & Schröder, K. U. (2022). Three-dimensional progressive damage and failure analysis of double-lap composite bolted joints under quasi-static tensile loading. Composite Structures, 285, 115227. https://doi.org/10.1016/j.compstruct.2022.115227

[19] Nerilli, F., & Vairo, G. (2017). Progressive damage in composite bolted joints via a computational micromechanical approach. Composites Part B: Engineering, 111, 357-371. https://doi.org/10.1016/j.compositesb.2016.11.056

[20] Qingyuan, L., Zhao, Y., Yan, C., Liu, Y., & Pan, W. (2024). Progressive bearing failure analysis and strength prediction method for the initial assembly and tensile process of composite bolted joints. Composites Part A: Applied Science and Manufacturing, 187, 108476. https://doi.org/10.1016/j.compositesa.2024.108476

[21] Joseph, A. P., Davidson, P., & Waas, A. M. (2018). Progressive dama-

ge and failure analysis of single lap shear and double lap shear bolted joints. Composites Part A: Applied Science and Manufacturing, 113, 264-274. https://doi.org/10.1016/j.compositesa.2018.07.01

[22] Shipsha, A., & Burman, M. (2020). Failure mechanisms in NCF composite bolted joints: Experiments and FE model. Composites Part B: Engineering, 192, 107950. https://doi.org/10.1016/j.compositesb.2020.107950

[23] Cinar, K. (2024). Enhancement of laminate open-hole tensile strength by considering fiber waviness around holes. Journal of Manufacturing Processes, 131, 766-780. https://doi.org/10.1016/j.jmapro.2024.09.079

[24] Li, A., Zhang, H., & Yang, D. (2025). Bearing performance and progressive failure analysis of bolted joint in 3D printed pseudo-woven CFRP composite with fibre steering. Composites Part A: Applied Science and Manufacturing, 188, 108526. https://doi.org/10.1016/j.compositesa.2024.108526

[25] Abaqus Analysis User's. Manual. Online Documentation Help: Dassault Systemes; 2016

[26] Falcó, O., Ávila, R.L., Tijs, B., & Lopes C.S. (2018). Modelling and simulation methodology for unidirectional composite laminates in a Virtual Test Lab framework, Composite Structures, 190, 137-159. https://doi.org/10.1016/j.compstruct.2018.02.016

Low velocity impact responses of symmetric and asymmetric curved foam core sandwich panels

Fatih Balıkoğlu[1] (iD)**, Tayfur Kerem Demircioğlu[1]*** (iD)**, Berkan Hızarcı[2]** (iD)**, Mehmet Özer[3]** (iD)

[1]Balıkesir University, Mechanical Engineering Department, 10300, Balıkesir, Türkiye
[2]Tofaş Turkish Automobile Factory, Türkiye
[3]Balıkesir University, Bigadiç Vocational School, Transportation Services Department 10440, Balıkesir, Türkiye

Abstract: This work aims to experimentally examine the effects of various fiber reinforcements on the low-speed impact load responses of curved sandwich composites. Plain woven E-glass, 8H satin S2-glass, plain and twill woven carbon fiber reinforcements with the same areal weight were used as face sheets and PVC foam as core material in the fabrication of sandwich composites. A low-speed impact testing apparatus including a hemispherical impactor was used to conduct low-speed impact tests at various energy levels. Impact energy levels were determined for rebound, penetration, and total perforation of the specimens. Twill woven carbon exhibited superior performance for low-velocity impact damage resistance and tolerance in comparison with plain woven carbon and glass fibers. The absorbed impact energy decreased with the asymmetrical arrangement, and the sandwich specimens with twill-woven face sheets showed the best performance among the symmetrical and asymmetrical panels.

Keywords: low-velocity impact; sandwich composite; curvature; damage.

1. Introduction

The aerospace, maritime, automotive, and other industries employ sandwich composites for lightweight constructions. They have excellent thermal insulation, sound insulation, fire protection, and moisture resistance, as well as high specific strength, stiffness, and energy absorption [1-3]. A sandwich panel is composed of two rigid, thin and strong outer layers and a lightweight core in between them. The core material resists shear stresses, while the face sheets bear tensile and compressive loads [4]. Additionally, the curved structure distributes loads more effectively under bending or torsional stresses than a flat form [5].

Curved constructions include, for example: many parts of a helicopter, such as the fuselage, wings, tail sections, propeller, canopy, ballistic helmets and shields, can be considered as the application of curved composite panels. Several studies on the impact characteristics of curved laminate composite panels were conducted recently [6]. Low velocity impact behaviors of GFRP and CFRP composite laminates with single curve were com-

pared by Seifoori et al. [7] using impactors with flat, spherical and conical tips. An increase in contact area was found to reduce both the contact time and the midpoint deflection. Compared to GFRP composites of the same thickness and curvature, cylindrical CFRP were more rigid. At intermediate impact velocities, Usta et al. [8,9] studied the influence of thickness and curvature on the performance of flat and cylindrical CFRP composite laminates. It was found that curved samples exhibit higher penetration depths compared to flat panels that are equal in thickness and area. Arachchige and Ghasemnejad [10] investigated the after-impact behavior of a CFRP composite with a cylindrical geometry under low-velocity impact by a rigid spherical impactor. The author's analytical models yielded parameters for composite laminates with varying thicknesses of curvature.

Only a few studies were reported in the literature regarding low-velocity impact tests on sandwich composite panels with curvature. Reis, P. N et al. [11] noticed an improvement of around 20.8% in energy recovery due to the hybridization of the carbon layer with the

Kevlar layer for cylindrical sandwich shell composites. Additionally, an approximately 44.8% increase in recovered energy was achieved by incorporating the cork core into carbon laminate composites. In another work, the impact responses of curved sandwich composites with varying surface geometries produced by incorporating rubber between glass fiber fabrics were experimentally and numerically evaluated. It was found that curved sandwich panels had higher delamination areas and lower impact strength than flat panels [12]. Zhang, Y. and Zhou, Y. [13] compared the performance of curved sandwich panels against bird strike using cage, foam and cage-foam, hybrid core structures. It was found that the use of cage materials as the core in curved sandwich structures resulted in a higher resistance to impact, reduced contact force and residual kinetic energy of the bird and reduced the deformation of the backing layer. B. Arachchige and H. Ghasemne-ja [14] proposed an analytical model to simulate the low-velocity impact response of curved sandwich composites with foam core. The relationship between the increase in plate curvature and the increase in energy absorption of curved sandwich structures was verified by comparing numerical and analytical models. The effect of using graded foam materials on the impact behavior of sandwich composites with curvature and flat panels was explored in previous studies. It was found that the puncture energies of curved panels with uniform foam structure were higher than flat panels. However, the performance of panels with graded foam varied depending on the specific configuration of the foam layers [15]. In another study, the effects of artificial layer-core interface damage and curvature on the impact response of sandwich beams were investigated. It was found that the contact forces of sandwich beams without artificial damage increased with increasing curvature angle but decreased in damaged ones [16]. Yurdaskal M. and Baba B. [17] investigated the impact behavior and impact-induced damage modes of curved and planar sandwich composites consisting of E-glass/epoxy face sheet and PVC foam core. The failure modes varied depending on the geometry of the samples (curved or flat) and the amount of impact energy. In addition, more energy was absorbed during penetration process as the curvature radius of the sandwich panels was reduced. Liu et al. [18] investigated the effect of the radius of curvature of sandwich composites consisting of E-glass/epoxy face sheet and PVC foam core on the low-velocity impact test results. During the low-velocity impact tests, the contact forces increased while the displacement values decreased as the PVC core thickness and radius of curvature increased; however, the opposite was observed in the panels containing PVC foam with less wall thickness.

Recent study demonstrated the crucial role of radius and angle of curvature in the impact behavior of composite sandwich panels and the design of these structures. The papers provide a basic summary of the investigation of material and geometric effects on low-velocity impact responses, highlighting the difficulties of obtaining ac-curate results with flat panels in curved zones. Moreover, to the author's knowledge, no research has been reported in the literature on the low-velocity impact behavior of symmetric and asymmetric curved sandwich composites with varying face sheet materials. Consequently, the outcomes of this study address a gap in both scientific and practical fields and provide a foundation for future investigations, particularly numerical studies. For this purpose, this study aimed to investigate the effects of face sheet material on the contact force, absorbed energy and failure modes of curved sandwich composites under low-velocity impact tests.

2. Materials and Methods

2.1. Production of sandwich composites

Steel molds with a diameter of 250 mm were used to manufacture curved sandwich composites. Flat PVC foams (Airex® C70.75) were heated in an oven at 130 °C for 45 minutes to produce their cylindrical forms (▶Figure 1). Sandbags were put on the foam as a weight. Heating temperatures and durations for thermoforming were set in accordance with the manufacturer's specifications. The detailed information is available in the Airex Processing Guidelines data sheet [19]. Plain woven E-glass, 8H satin S2-glass, plain and twill carbon fiber fabrics are used as reinforcement materials. The densities of E-glass, S2-glass, and carbon fibers are 2.55 g/cm³, 2.49 g/cm³, and 1.79 g/cm³, respectively. The layer thicknesses of carbon, E-glass and S-glass fabrics are 0.327 mm, 0.15 mm and 0.12 mm, respectively [20]. In addition, the stiffness and strength values of these fibers are different [21]. Therefore, it is possible to compare the performances of face sheets with different mechanical properties in curved structures. For face sheets, HexForce® brand yarn type EC9 E-glass and SC9 S2-glass fiber woven fabrics were preferred. Profabric® brand plain and twill carbon woven fibers produced from Tenax-E HTA 40 3k and Carbon Fiber HT 3k 200tex yarns were used. In this way, the influence of the weaving pattern of carbon fiber on impact resistance was investigated. In asymmetric structures, fibers with higher mechanical properties were placed

Table 1. Preheat-treated PVC sandwich specimen fabrication characteristics with various face sheets.

Specimen	Upper face sheet (Impact side)	Lower face sheet	Curvature [mm]	PVC [mm]
PC	Plain carbon	Plain carbon	250	15
TC	Twill carbon	Twill carbon		
SC	S-Glass	S-Glass		
EC	E-Glass	E-Glass		
PEC	Plain carbon	E-Glass		
TEC	Twill carbon	E-Glass		
SEC	S-Glass	E-Glass		

in the top face sheet, while E-glass fibers were used in the bottom face sheet to improve elastic energy absorption by providing more displacement upon impact. The fibers' areal weights were maintained constant and employed at 200 g/m2. Epoxy resin (Hexion LR285 resin and LH287 hardener) was employed throughout fabrication. The hand lay-up method was chosen as the manufacturing technique (▶**Figure 2**). Impact tests were conducted on seven types of sandwich composites using different stacking configurations, including four symmetrical and three asymmetrical specimens. Details of the sandwich specimens are presented in ▶**Table 1**.

2.2. Drop weight test

The drop weight experiments were carried out using an Instron CEAST-9350 system (▶**Figure 3a**). The load sensor has a maximum capacity of 90 kN. The impact resistance of the sandwich specimens was measured in a test environment in accordance with the ISO 6603 standard. The impact data was obtained by dropping a hemispherical impact tool onto the convex surfaces of curved sandwich beam specimens. The clamping mechanism was specifically designed to hold curved specimens (▶**Figure 3b**). The bottom portion featured panels with a curvature radius, but the top section was built

around the panel thickness (▶**Figure 3c**). The sandwich specimens were evaluated at room temperature with impact energy values of 15 J, 30 J, and 90 J. Low velocity impact energies were determined at these energy levels to ensure rebound, penetration, and complete perforation of curved composites. For each energy level, at least three specimens were tested.

3. Results and Discussions

This section evaluated the force-displacement and energy-time curves of curved sandwich specimens and analyzed post-impact damage photographs.

3.1. Force-displacement curves

Figure 4 shows force-displacement graphs for curved sandwich composites. The curves showed single or double peaks depending on the variation in impact energy. The peaks of the force-displacement graphs are given in ▶**Figure 5**. The initial contact forces in the TC specimens are the highest among the symmetric sandwich panels at all energy levels. The superior low-speed impact resistance of twill-woven carbon textiles compared to plain-woven types aligns with earlier studies [22].
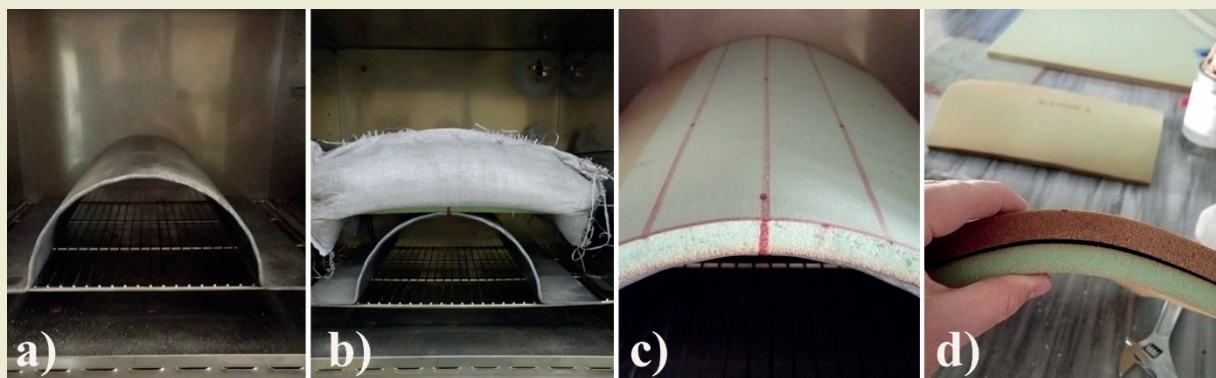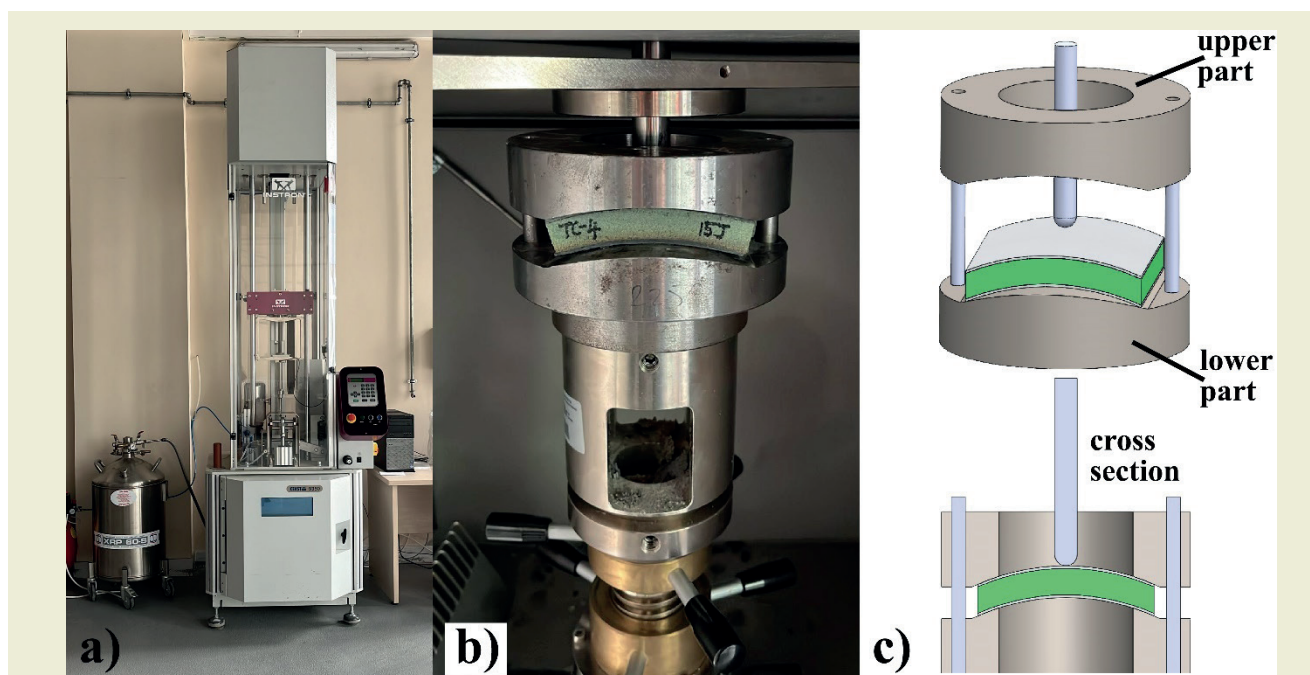

Figure 1. The process of pre-heating flat PVC foam materials. a) curved steel sheet mold, b) putting sandbags on PVC foam, c) and d) curved PVC foam parts after treatment.
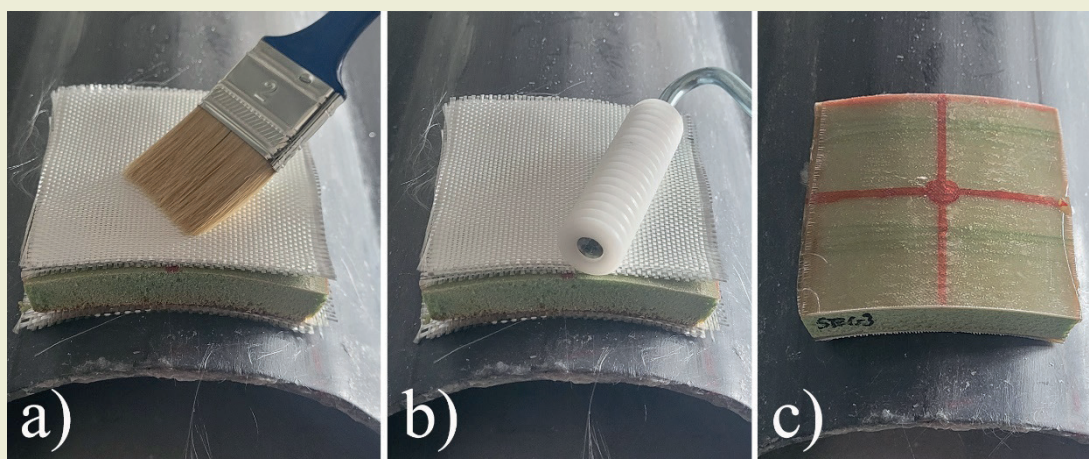
Figure 2. Production of sandwich composite specimens by hand lay-up method a) resin impregnation, b) air removal by rolling, c) sandwich specimen after curing.

Figure 3. a) Instron CEAST-9350 drop weight impact testing equipment, b) placing of curved specimens in the testing device, c) schematic view of testing apparatus.

This result shows the effect of the weave structure on the impact behavior. The contact forces of the SC panels were higher than the EC specimens at different energy levels. In this case, it is due to the higher impact resistance of S2-glass fibers compared to E-glass [23]. Furthermore, the SC specimens had larger contact forces than the PC panels, which supported the literature [24, 25]. PC and TC specimens including plain weave and twill weave carbon fibers originally exhibited a more rigid response. In addition, the second peaks are higher in the force-displacement graphs of PC and TC specimens. This scenario opposed to EC and SC specimens containing glass fiber, with greater initial contact forces. At 15 J impact energy, rebounding was seen in EC, PC, SC and TC specimens. At 30 J impact energy values, the second peak was only shown in the PC specimen. In other specimens, the impact tip penetrated the PVC foam core material and remained stuck. At 90 J impact energy, all specimens suffered complete perforation damage. The force-displacement curves show that the impact force after perforation never drops to zero due to friction between the impactor and the specimen [26]. In asymmetrical panels, the initial stiffness of the top face sheet materials, namely plain and twill woven carbon PEC and TEC specimens, was increased. The second peak had a greater value than the initial contact force just in the PEC sample within the asymmetrical specimens. This result is consistent with previous research, indicating that glass fiber reinforcements have better impact resistance than plain woven carbon textiles [27]. The first peaks in TEC and SEC specimens showed higher values. This suggested an increase in the initial penetration resistance. PEC showed resistance in the bottom face sheet to prevent total perfora-

tion. The penetration values of the impact tip into the specimens at different energy values were determined from the force-displacement graphs. At 15 J impact energy, the impact tip penetration depths of the EC, PC, SC and TC specimens were determined as 9.328 mm, 9.960 mm, 10.575 mm and 7.251 mm, respectively. The penetration depths of the impact tip in PEC, SEC, and TEC specimens with an energy value of 15J are 11.592 mm, 8.823 mm, and 8.010 mm, respectively. At the 30 J energy level, the impact tip clearly penetrated the foam core material and stopped in all panels. At 30 J impact energy, the penetration depths of the impact tip into the EC, PC, SC, and TC specimens were measured as 19.405 mm, 19.631 mm, 19.876 mm and 14.013 mm, respectively. As the penetration increased, the damage resistance of the curved sample consisting of twill carbon became noticeable. In the PEC, SEC, and TEC specimens, penetration depths were determined at 21.447 mm, 16.797 mm, and 15.39 mm, respectively, at an energy level of 30 J. The asymmetrical configuration of carbon-reinforced sandwich specimens with E-glass bottom face sheets resulted in an increased penetration depth. Additionally, SEC panel was superior to the SC specimen in terms of impact resistance and penetration depth.

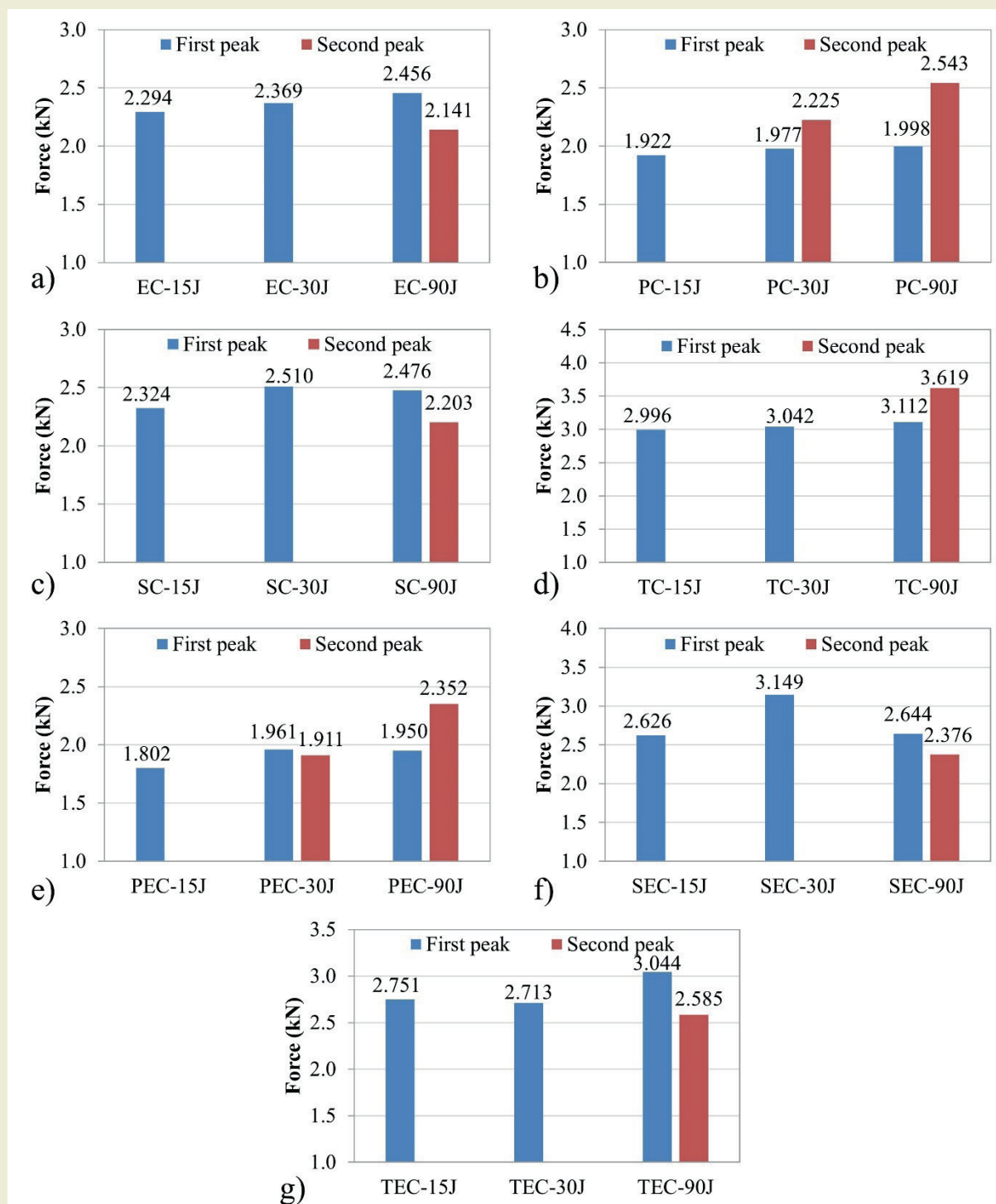### 3.2. Energy absorption-time curves

The energy absorbed by sandwich specimens under impact load equals to the area under the force-displacement curve. The energy absorption-time curves of the curved sandwich samples subjected to varying impact energies showed different shapes, as shown in ▶**Figure 6**. At a 15 J impact load, the energy curves of
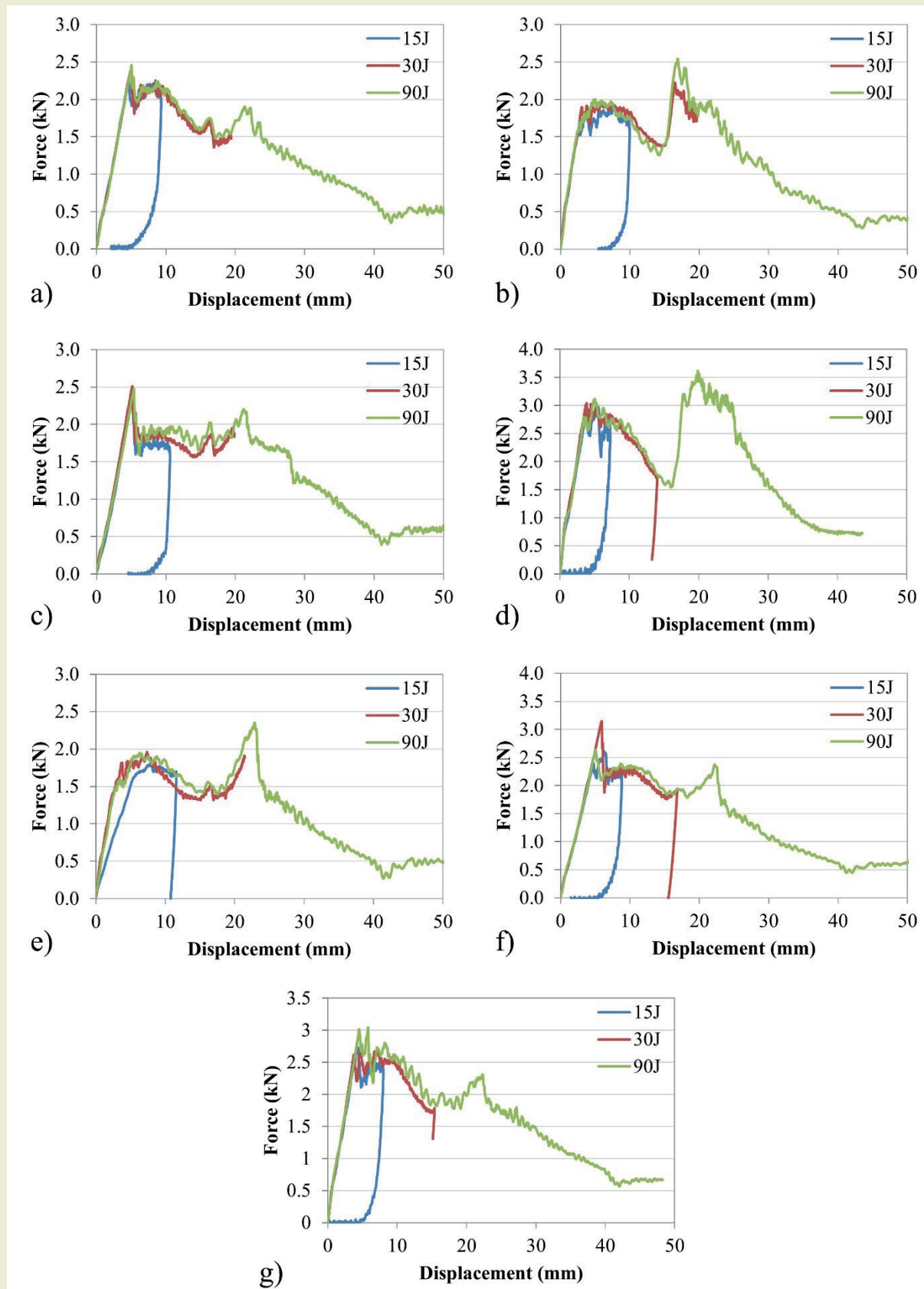
Figure 4. Force-displacement curves of curved sandwich specimens a) EC, b) PC, c) SC, d) TC, e) PEC, f) SEC, g) TEC.

curved sandwich specimens exhibited a rise with time, followed by a slight decrease after reaching the peak. This is related to rebounding. Elastically, some energy is recovered during the impact. Asymmetric sandwich composites showed rebound behavior like that of symmetric composites at an impact energy of 15 J. At an impact energy of 30 J, the rate of energy absorption decreased after the breakage of the upper face sheet, allowing the PVC foam to absorb energy via compres-

sion. Curved symmetric and asymmetric specimens exhibited entirely plastic behavior, indicating the absence of rebounding. In all sandwich panels, the energy absorption rate increased due to the impactor reaching the lower faces sheet at 90 J of impact energy. The energy absorption rate experienced a gradual decrease as the lower face sheet was damaged, causing the curve to tend to be horizontal. At a total impact energy of 90J enough for a perforation, the curved panel specimens

Figure 5. Peak contact forces of curved sandwich specimens a) EC, b) PC, c) SC, d) TC, e) PEC, f) SEC, g) TEC.
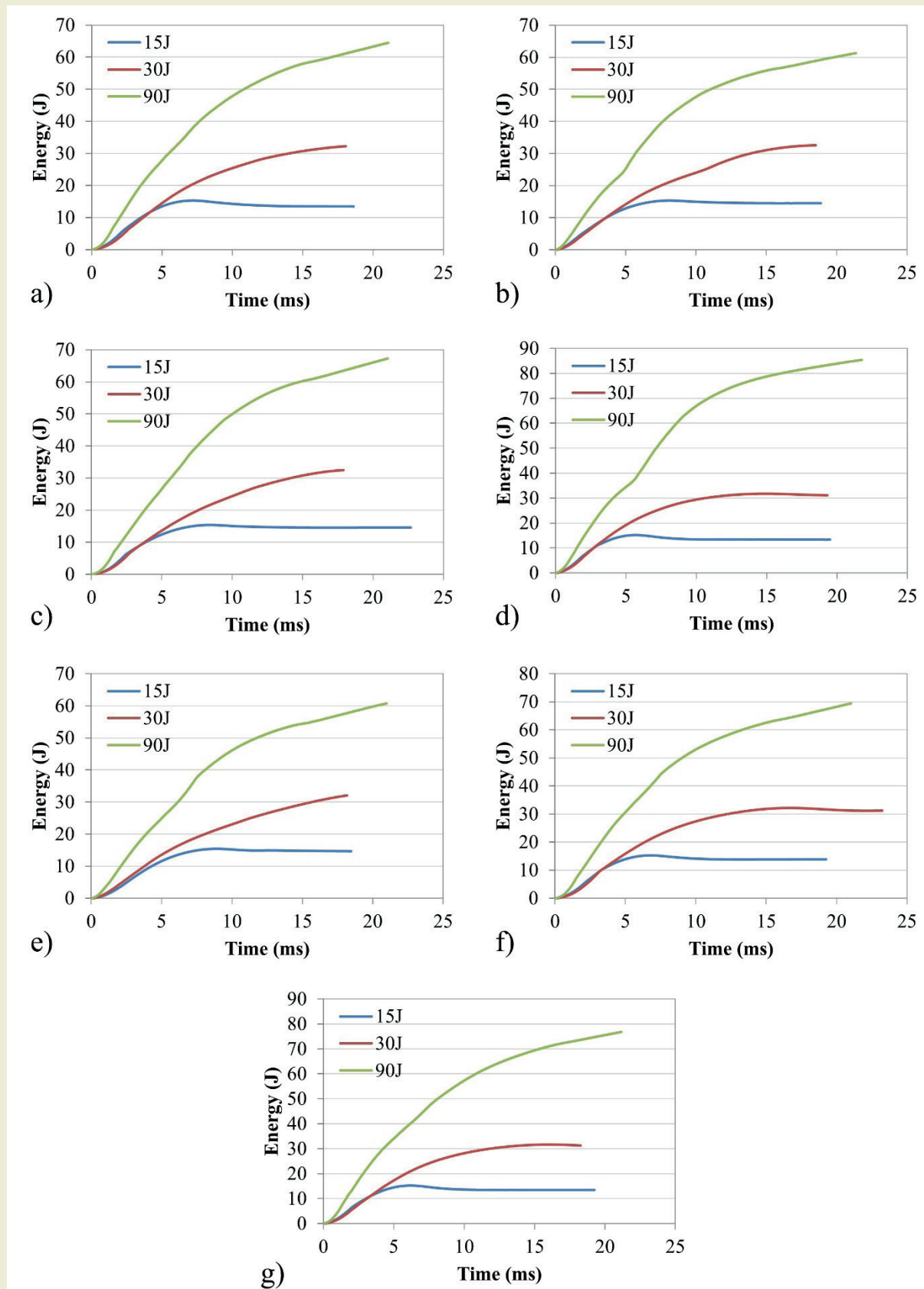
Figure 6. Energy absorption-time curves of curved specimens a) EC, b) PC, c) SC, d) TC, e) PEC, f) SEC, g) TEC.

exhibited similar curves. As can be seen in ▶**Figure 7**, at energy levels of 15 J and 30 J, the impact energy was completely absorbed in all specimens. However, it is crucial to consider that the path of the impactor in the specimens at these energy levels varies from one specimen to another. Therefore, the energy levels required for the impactor to completely perforate the specimens were found to be different (▶**Figure 7**). The standard deviation of the contact forces and absorbed energy at 15 J and 30 J in the samples were found to be negligible. The standard deviations of the perforation energy (90J) values for EC, PC, SC, and TC symmetric specimens were ±2.9, ±1.7, ±3.8, and ±6.5, respectively, whereas for PEC, SEC, and TEC specimens, these were ±1.1, ±4.2, and ±5.4. The contact forces obtained during complete perforation showed standard deviation values of ±66.1, ±148.5, ±111.4, and ±264.1 for symmetrical EC, PC, SC, and TC samples, and ±185.7, ±251.7, and ±350.7 for asymmetrical PEC, SEC, and TEC specimens. The twill carbon-reinforced specimen exhibited the maximum energy absorption through complete perforation in both symmetrical and asymmetrical panels. The perforation energy values of asymmetrical panels were lower than those of symmetrical panels (▶**Figure 7**).

3.3. Post-impact section views

This section experimentally evaluated the failure modes of impact sandwich panels. ▶**Figure 8** shows damage section photos of curved sandwich composites after impact loads. Examination of the impacted regions indicates that the modes of failure are dependent on the properties of the sheet material or the symmetric/asymmetric arrangement of the sandwich panel. In the symmetric and asymmetric curved specimens,
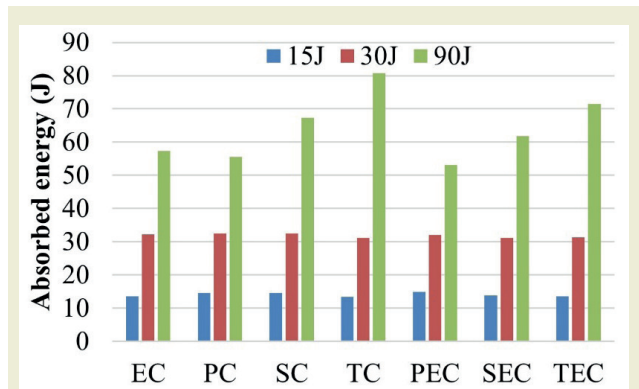

Figure 7. Absorbed impact energy values of curved specimens.

significant upper face fiber breakage, core crushing and fracture damage occurred at 15 J and 30 J impact energies (▶**Figure 8a-d**). At 30 J impact energy, the upper face sheets of the symmetric PC and TC specimens were completely perforated. In PC and TC specimens, interlayer delamination in the bottom face sheets at an energy value of 90 J is more noticeable than in other symmetric specimens. Glass fibers can withstand higher deformations before fracture, thus minimizing the spread of cracks to the inner plies [28]. The asymmetric PEC and TEC specimens showed a lower resistance to low velocity impact damage. It was noted that the delamination damage in the bottom face sheets of PEC and TEC specimens was less severe than that of their symmetric counterparts (▶**Figure 8e, g**). It can be said that the E-glass bottom face sheet in the PEC specimen resisted total perforation failure.
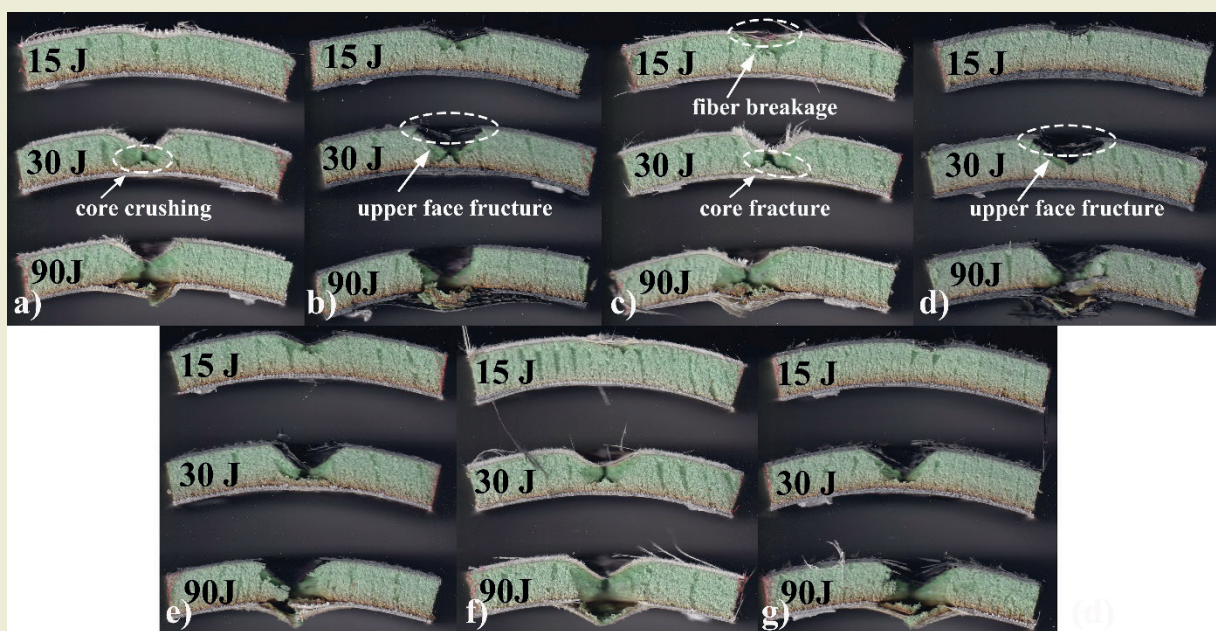

Figure 8. Damage section images of curved sandwich specimens after impact test
a) EC, b) PC, c) SC, d) TC, e) PEC, f) SEC, g) TEC.

4. Conclusions

This work experimentally investigated the effect of fiber reinforcement used in the face sheets on the low-speed impact load responses of curved foam core sandwich composites. The Twill carbon fiber woven face sheet showed the highest penetration resistance under low velocity impact loads, whereas the plain-woven carbon fiber sandwich specimen had the lowest impact resistance. The impact strength and energy absorption capacity decreased in asymmetric sandwich specimens. The use of S-glass and twill carbon in the impact direction of asymmetrical specimens improved initial impact resistance. The use of E-glass as the lower face sheet instead of plain-woven carbon fabric improved the perforation resistance in asymmetric specimens. This scenario provides details on resistance to penetration and perforation damage in cases of asymmetrical arrangement. Future study might include interlayer hybridization of the top and bottom face sheets of curved sandwich composites subjected to low-velocity impacts.

Acknowledgments

Research ethics

Not applicable.

Author contributions

Conceptualization: [Fatih Balikoğlu], Methodology: [Fatih Balikoğlu, Tayfur Kerem Demircioğlu], Investigation: [Fatih Balikoğlu, Tayfur Kerem Demircioğlu Mehmet Özer, Berkan Hizarci], Data Curation: [Tayfur Kerem Demircioğlu, Berkan Hizarci], Writing - Original Draft Preparation: [Fatih Balikoğlu], Writing - Review & Editing: [Fatih Balikoğlu, Tayfur Kerem Demircioğlu], Visualization: [Tayfur Kerem Demi

Competing interests

The author(s) state(s) no conflict of interest.

Research funding

Data availability

The raw data can be obtained on request from the corresponding author.

Peer-review

Externally peer-reviewed.

References

[1] Al-Shamary, A. K. J., Karakuzu, R., & Özdemir, O. (2016). Low-velocity impact response of sandwich composites with different foam core configurations. Journal of Sandwich Structures & Materials, 18(6), 754-768. https://doi.org/10.1177/1099636216653267

[2] Atas, C., & Potoğlu, U. (2016). The effect of face-sheet thickness on low-velocity impact response of sandwich composites with foam cores. Journal of Sandwich Structures & Materials, 18(2), 215-228. https://doi.org/10.1177/1099636215613775

[3] Caprino, G., & Teti, R. (1994). Impact and post-impact behavior of foam core sandwich structures. Composite Structures, 29(1), 47-55. https://doi.org/10.1016/0263-8223(94)90035-3

[4] Harizi, W., Anjoul, J., Santamaría, V. A. A., Aboura, Z., & Briand, V. (2021). Mechanical behavior of carbon-reinforced thermoplastic sandwich composites with several core types during three-point bending tests. Composite Structures, 262, 113590. https://doi.org/10.1016/j.compstruct.2021.113590

[5] Xie, H., Hou, X., Fang, H., Zhang, S., Wang, Z., He, P., Yu, F. (2024). Flexural behavior evaluation of PET foam core curved sandwich beam: Experimental study and numerical simulation. Construction and Building Materials, 414, 135000. https://doi.org/10.1016/j.conbuildmat.2024.135000

[6] Usta, F., Türkmen, H. S., & Scarpa, F. (2022). High-velocity impact resistance of doubly curved sandwich panels with re-entrant honeycomb and foam core. International Journal of Impact Engineering, 165, 104230. https://doi.org/10.1016/j.ijimpeng.2022.104230

[7] Seifoori, S., Parrany, A. M., & Mirzarahmani, S. (2021). Impact damage detection in CFRP and GFRP curved composite laminates subjected to low-velocity impacts. Composite Structures, 261, 113278. https://doi.org/10.1016/j.compstruct.2020.113278

[8] Usta, F., Mullaoglu, F., Türkmen, H. S., Balkan, D., Mecitoglu, Z., Kurtaran, H., & Akay, E. (2016). Effects of thickness and curvature on impact behaviour of composite panels. Procedia engineering, 167, 216-222. https://doi.org/10.1016/j.proeng.2016.11.690

[9] Usta, F., Türkmen, H. S., & Scarpa, F. (2019). Toroidal Sandwich Panels with Auxetic Core Under Impact Loads: Numerical Simulations. In 2019 9th International Conference on Recent Advances in Space Technologies (RAST), 25-28. https://doi.org/10.1109/RAST.2019.8767843

[10] Arachchige, B., & Ghasemnejad, H. (2017). Post impact analysis of damaged variable-stiffness curved composite plates. Composite Structures, 166, 12-21. https://doi.org/10.1016/j.compstruct.2017.01.018

[11] Reis, P. N., Coelho, C. A., & Navalho, F. V. (2021). Impact response of composite sandwich cylindrical shells. Applied Sciences, 11(22), 10958. https://doi.org/10.3390/app112210958

[12] Albayrak, M., Kaman, M. O., & Bozkurt, I. (2023). Experimental and numerical investigation of the geometrical effect on low velocity impact behavior for curved composites with a rubber interlayer. Applied Composite Materials, 30(2), 507-538. https://doi.org/10.1007/s10443-022-10094-5

[13] Zhang, Y., & Zhou, Y. (2023). Investigation of bird-strike resistance of composite sandwich curved plates with lattice/foam cores. Thin-Walled Structures, 182, 110203. https://doi.org/10.1016/j.tws.2022.110203

[14] Arachchige, B., & Ghasemnejad, H. (2018). Effect of variable core stiffness on the impact response of curved sandwich plates. Composite Structures, 200, 565-578. https://doi.org/10.1016/j.compstruct.2018.05.150

[15] Baba, B. O. (2017). Curved sandwich composites with layer-wise graded cores under impact loads. Composite Structures, 159, 1-11. https://doi.org/10.1016/j.compstruct.2016.09.054

[16] Baba, B. O. (2013). Impact response of sandwich beams with various curvatures and debonds. Journal of Sandwich Structures & Materials, 15(2), 137-155. https://doi.org/10.1177/1099636212460543

[17] Yurddaskal, M., & Baba, B. O. (2016). The effect of curvature on the impact response of foam-based sandwich composite panels. Steel and Composite Structure, 20(5), 983-997. https://doi.org/10.12989/scs.2016.20.5.983

[18] Liu, C., Ma, C., & Gao, X. (2023). Study on impact behavior of glass fiber/PVC curved sandwich structure composites. Polymer Composites, 44(1), 365-376. https://doi.org/10.1002/pc.27102

[19] Airex Processing Guidelines. (accessed date: 12 March 2025). https://www.3accorematerials.com/uploads/documents/AIREX-Processing-Guidelines_09.2020.pdf

[20] Dost Kimya, (accessed date: 12 March 2025). https://www.dostkimya.com/tr/urunler/kompozit-malzemeler/cam-fiber-kumaslar, https://www.dostkimya.com/tr/urunler/kompozit-malzemeler/karbon-fiber-kumaslar

[21] Yao, Y., Zhu, D., Zhang, H., Li, G., & Mobasher, B. (2016). Tensile behaviors of basalt, carbon, glass, and aramid fabrics under various strain rates. Journal of Materials in Civil Engineering, 28(9), 04016081. https://doi.org/10.1061/(ASCE)MT.1943-5533.0001587

[22] Karahan, M., & Karahan, N. (2014). Effect of weaving structure and hybridization on the low-velocity impact behavior of woven carbon-epoxy composites. Fibres & Textiles in Eastern Europe, 105(3), 109-115.

[23] Al-Shamary, A. K. J., Abed, A. R. N., & Karakuzu, R. (2024). A comparative study on ballistic impact behaviors of glass/epoxy composites. Mechanics of Advanced Materials and Structures, 31(30), 13341-13350. https://doi.org/10.1080/15376494.2023.2256003

[24] Hosur, M. V., Adbullah, M., & Jeelani, S. (2005). Studies on the low-velocity impact response of woven hybrid composites. Composite Structures, 67(3), 253-262. https://doi.org/10.1016/j.compstruct.2004.07.024

[25] Vasudevan, A., Senthil Kumaran, S., Naresh, K., & Velmurugan, R. (2020). Layer-wise damage prediction in carbon/Kevlar/S-glass/E-glass fibre reinforced epoxy hybrid composites under low-velocity impact loading using advanced 3D computed tomography. International Journal of Crashworthiness, 25(1), 9-23. https://doi.org/10.1080/13588265.2018.1511234

[26] Atas, C., & Sevim, C. (2010). On the impact response of sandwich composites with cores of balsa wood and PVC foam. Composite Structures, 93(1), 40-48. https://doi.org/10.1016/j.compstruct.2010.06.018

[27] Saylık, A., & Temiz, Ş. (2022). Low-speed impact behavior of fiber-reinforced polymer-based glass, carbon, and glass/carbon hybrid composites. Materials Testing, 64(6), 820-831. https://doi.org/10.1515/mt-2021-2179

[28] Enfedaque, A., Molina-Aldareguía, J. M., Gálvez, F., González, C., & Llorca, J. (2010). Effect of glass fiber hybridization on the behavior under impact of woven carbon fiber/epoxy laminates. Journal of composite materials, 44(25), 3051-3068. https://doi.org/10.1177/002199831036960

Impact of structural and CFD analysis on the cost of biogas-fueled gas engine exhaust pipes

Rabia Kaymaz[1] (iD), Mine Ak[1] (iD), Kürşat Tanrıver[1*] (iD)

[1] Istanbul Health and Technology University, Faculty of Engineering and Natural Sciences, Department of Mechatronics Engineering, Istanbul, Türkiye

Abstract: In this study, the effects of exhaust pipe design used in biogas-fueled cogeneration systems on engineering performance and cost were investigated. First, the existing system was analyzed by field work, and then structural analysis was applied with CFD (Computational Fluid Dynamics). The exhaust pipe route, pipe diameter, and material thickness of the existing system were evaluated, and design improvements were suggested. It was determined that the shorter pipeline application with the changes made in the pipe route and layout reduced pressure losses. Despite the use of an exhaust pipe with a smaller diameter and made of thinner material in the proposed new design, compliance with the standards was ensured, and it was shown to be safe against wind loads with finite element analysis. Considering the calculated maximum wind load of 5.52 kN and the weight of the system, the maximum stress value was calculated as 108.691 MPa as a result of the Von Mises stress analysis applied to the exhaust pipe system in the finite element analysis. This value showed that the system was 1.56 times safer. In the deformation analysis, the maximum displacement value was measured as 0.13 mm, and this value is ideal. In the cost analysis, it was determined that the proposed new system provides a cost reduction of approximately 53% compared to the existing system. The results obtained emphasize the importance of engineering analysis in exhaust pipe design, and show the applicability of the approach to increase economic and environmental sustainability in industrial facilities.

Keywords: Biogas installation; CFD analysis; exhaust pipe design; energy efficiency; cogeneration; structural analysis

1. Introduction

In the face of growing global energy demand and escalating environmental concerns, the transition to renewable and sustainable energy sources has become more critical than ever. Among these, biogas technologies have emerged as a particularly valuable solution for their dual role in waste management, and energy production. By transforming organic waste—ranging from agricultural residues, to industrial effluents—into combustible gas through anaerobic digestion, biogas plants offer a cleaner alternative to fossil fuels, while also contributing to the reduction of greenhouse gas emissions and promoting a circular economy.

Biogas plants appear as a sustainable solution where organic waste is converted into energy through fermentation. Biogas, which can be obtained from different sources ranging from agricultural waste to domestic and industrial waste, provides an alternative to fossil fuels while also offering environmental benefits such as waste management, and reduction of greenhouse gas emissions.

To maximize the energy yield from biogas, cogeneration systems (Combined Heat and Power - CHP) are frequently employed. These systems enable the simultaneous production of electricity and usable thermal energy, significantly improving the overall efficiency of biogas plants. However, the effectiveness of cogeneration systems heavily depends on the performance of their subsystems, one of the most critical being the exhaust infrastructure. The gases formed in biogas plants are used for electricity production in solutions such as cogeneration systems. In addition to electricity production, cogeneration systems are pioneers in increasing efficiency by utilizing the heat of the exhaust gas released into the atmosphere.

One of the most critical components of cogeneration

systems is the exhaust pipes that come into play during the use of the energy obtained. Exhaust pipes directly affect system safety and efficiency by properly transferring the combustion gases of the biogas burned in generators or engines out of the facility. Thanks to correctly designed and constructed exhaust pipes with appropriate materials, exhaust gases are released safely into the atmosphere. Otherwise, inadequate management of exhaust gas can lead to problems such as environmental pollution, unwanted gas accumulation in or around the facility, and efficiency losses.

While cogeneration systems have been widely adopted in many sectors, insufficient attention is often paid to the exhaust pipe design, which can result in pressure losses, heat dissipation inefficiencies, and environmental hazards. Properly engineered exhaust pipes not only optimize gas flow and minimize backpressure, but also help in complying with stringent emission regulations, both at the national and international levels. Despite the wealth of literature addressing cogeneration performance and emissions, studies that investigate the mechanical and thermofluidic behavior of exhaust pipes using CFD (Computational Fluid Dynamics) and structural analysis in a biogas-specific context remain limited.

In this manuscript, the cost effect of exhaust pipe design principles was effectively investigated by performing CFD (Computational Fluid Dynamics) and structural analysis on exhaust pipes in biogas-fueled cogeneration systems.

Moreover, the study evaluates how exhaust system components can be optimized to meet ISO and local regulatory standards, providing insights into improvement methodologies for future system implementations. By reviewing state-of-the-art research, including applications of exhaust design in industrial furnaces, transport vehicles, and maritime systems, the manuscript establishes a multidisciplinary foundation for understanding and enhancing flue gas management in renewable energy contexts.

In addition, how exhaust systems can be brought into compliance with local and international standards and possible improvement methods will be discussed. Thus, it is aimed to make biogas plants safer, more efficient, and sustainable by adopting correct applications from both engineering and environmental perspectives. The importance of exhaust pipe design stems from the fact that it directly affects the overall performance of the system by regulating gas flow and minimizing pressure losses. In this context, the analyses and design improvements made within the scope of the project aim to contribute to the more efficient operation of cogeneration systems.

Cogeneration systems provide simultaneous production of both heat and electricity from the primary energy source [1]. Studies in the literature have examined the effects of exhaust pipe design on system efficiency and cost with different methods and have drawn attention to the importance of optimizing design parameters.

The study by Tanrıver and Ay [2] used computational fluid dynamics (CFD) analyses and structural optimization methods to understand how it affects the spread of infection in refuse chute throw pipes, and to improve its design. Chootrakul Siripaiboon et al. [3] show that CFD methods are used together with experimental studies in separation gasifiers with integrated syngas burners. Experimental verification of the temperature and syngas composition values obtained in combustion, pyrolysis, gasification, and drying zones provides an important roadmap for increasing gasification efficiency and reducing emissions. Similarly, CFD-based flow and heat transfer analyses are carried out to improve natural gas, air, and flue gas channels in tower type zinc refining furnaces; it is aimed to increase combustion efficiency and thermal homogeneity in zinc refining processes [4].

In steam boilers, the method of flue gas recirculation, although the impact on system performance in controlling the temperature of reheated steam is subject to debate, there are studies suggesting that it significantly shapes the thermal efficiency of steam boilers and emission control [5]. Moreover, ash accumulation in heat exchangers can significantly change the radiation properties of the flue gas-particle mixture and, lead to significant decreases in heat transfer efficiency. Therefore, the development of dynamic accumulation models and non-gray radiation analyses can contribute to the design and optimization of waste heat recovery devices [6].

On the other hand, in terms of energy efficiency and emission reduction in the transportation and maritime sector, it can be shown that the gases in the exhaust systems cause an energy loss of approximately 25%, but it is possible to recover this energy by using thermoelectric generators [7, 8].

It has been shown that emission control can be performed with real-time data using deep learning-based time series approaches for monitoring and predicting exhaust pipe emissions from heavy trucks in road transport [9]. Exhaust pipe vibration analysis is also a critical issue in terms of reliability and durability in the automotive industry, and stress and failure points in flanges or other components can be detected with modal and random vibration analysis [10].

Nejatzadegan et al. [11] investigated the efficiency between the exhaust manifold and engine parts according to two different types of exhaust manifolds. Hasan Üstün Başaran [12] conducted a study to determine the relationship between exhaust gas and temperature in diesel engine systems. In their study, they showed that delayed fuel injection moderately improved the exhaust temperature. Zhang et al. [13] showed that when flue gas waste heat is applied together with an absorption heat pump and staged heat recovery technologies, boil-

er efficiency can be increased by more than 12%. Shi et al. [14] have conducted an alternative study to the traditional exhaust cooling systems used in diesel engines. The study not only complies with safety standards, but also provides fuel savings of over 4%. In addition, it has shown superiority in terms of environmental and performance by offering up to 90% emission reduction. Li et al. [15] studied the use and cost effectiveness of devices required for air pollution control in flue gas of coal-fired plants. Tomasz Kalak [16] has shown that industrial waste biomass can be an environmentally friendly, low-cost, and sustainable energy source that can be used as an alternative to fossil fuels in the production of electricity and heat, and can be efficiently evaluated with different conversion methods.

These literature reviews have provided a solid theoretical basis by supporting the engineering tools and design approaches used in the project. Existing studies clearly demonstrate the importance of parameters such as gas flow rate, pressure loss, and material selection in the project. In the light of this information in the literature, the problems aimed to be solved during the project process have been clearly revealed.

Ultimately, the aim of this research is to present a cost-benefit analysis of alternative exhaust designs in a real-world biogas cogeneration facility. The comparative evaluation of existing systems and newly proposed configurations is intended to offer engineers, plant designers, and decision-makers practical guidance in making sustainable, safe, and economically viable design choices. Through this study, we hope to underscore the broader role of intelligent engineering in advancing the efficiency and reliability of renewable energy systems.

The purpose of this article is to reveal the efficiency of the exhaust pipe design used in cogeneration systems in terms of engineering and cost within the entire system. For this purpose, an existing biogas-fueled cogeneration plant was examined, the design deficiencies of these existing systems were determined, and a new system was proposed. A cost analysis was performed by comparing the existing system with the proposed new design. Thus, it is aimed to provide readers, designers, and engineers with a new perspective on exhaust pipe design, demonstrating that design changes can lead to more cost-effective and efficient engineering solutions.

lows both domestic and industrial waste to be disposed of without harming the environment. The facility offers services such as waste incineration, biogas production, hazardous waste storage, and energy production. The facility uses cogeneration systems to recover the energy generated during waste disposal, and generates electricity and heat. The facility converts organic waste into an energy source by using the anaerobic digestion method during the biogas production process. The stored biogas is transmitted to the cogeneration engines. The electrical energy generated in the engines is transferred to the grid, while the heat released is used in energy systems or in-plant operations. The cogeneration system of the facility is shown in ▶**Figure 1**.

Figure 1. Biogas fueled cogeneration unit a) General view b) Gas Engine

2. Site Inspection

2.1. Biogas Plant

In order to increase the effectiveness of this study, a field study was conducted at the Izaydas (Izmit Waste and Residues Treatment, Incineration and Evaluation Inc.) facility. Izaydas is the first hazardous and industrial waste incineration and disposal facility in Turkey. Operating under the Kocaeli Metropolitan Municipality, the facility has an integrated infrastructure that al-

2.2. Exhaust Pipe Production Facility

An inspection was carried out at the Rotek Exhaust Pipe System factory to observe the exhaust pipe production on site. In the inspections, it was seen that the designers manufactured the exhaust pipe in accordance with EN 1856-1 [17] standards. In the exhaust pipe design, the exhaust pipe height, diameter, and material are determined based on EN 13384 [18] standard. Different types of exhaust pipes are shown in ▶**Figure 2**.

**Figure 2.** Types of exhaust pipes a) General view b) Insulated pipe

exhaust gas [22]. Considering these references, a 1 mm thick Ø180 mm diameter AISI 304 stainless steel exhaust pipe was selected. 50 mm thick, 80 kg/m3 density rock wool thermal insulation was applied on the inner pipe. As the outermost coating, an exhaust pipe made of 0.50 mm thick AISI 430 quality stainless steel was selected in order to ensure that the exhaust pipe is located outside the building and is resistant to rain effects.
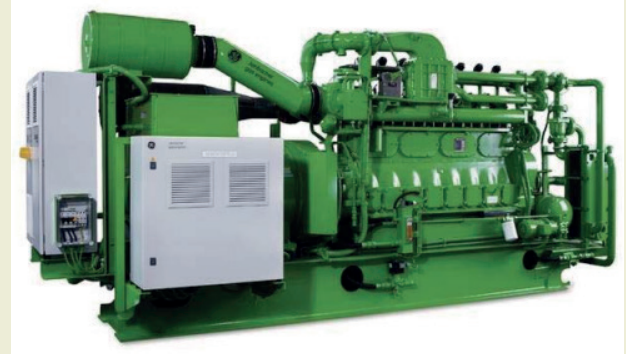
Figure 3. General Electric Jenbacher J 208 GS-C21 Gas Engine

Table 1. Gas Engine Data Sheet

Parameter	Unit	Value
Exhaust gas temperature at full load	°C	508
Exhaust gas temperature at bmep = 12.4 [bar]	°C	~527
Exhaust gas temperature at bmep = 8.3 [bar]	°C	~546
Exhaust gas mass flow rate, wet	kg/h	1.858
Exhaust gas mass flow rate, dry	kg/h	1.725
Exhaust gas volume, wet	Nm³/h	1.444
Exhaust gas volume, dry	Nm³/h	1.278
Max. admissible exhaust back pressure after engine	mbar	60

3. Material and Method

3.1. Material

The main source of CFD analysis in cogeneration plants is the gas engine. Calculations are made by considering the data sheet information given according to the type of gas engine. In this manuscript, the J 208 GS/C21 General Electric Jenbacher gas engine is used as the gas engine. The J 208 GS/C21 is a gas engine with approximately 330 kW electricity and 480 kW heat production capacity. Thanks to the cogeneration (CHP) system, total energy efficiency can reach 85-90% [19]. The engine offers flexibility by operating with various combustible gases such as biogas and natural gas. The biogas produced by the plant from organic waste is converted into energy by this engine. The gas engine is shown in ▶**Figure 3** and the data sheet parameters are shown in ▶**Table 1**.

CE certified high temperature and corrosion resistant products in accordance with EN 1856 -1 [17] and EN 1859 [20, 21] standards were selected for the exhaust pipes of the system. Since these products are made of stainless steel, they are resistant to corrosion from the

3.2. Method

In order to evaluate the effects of exhaust pipe design on energy efficiency and cost effectiveness, software performing CFD analysis was used, taking EN 13384-1 [18] standard as reference. Kesa Aladin program [23, 24], which was also used in previous studies, was used to optimize gas flow, pressure loss, and diameter calculations for exhaust pipe design. Solidworks was used for 3D design of exhaust pipe, and Solidworks Simulation [25, 26] software, which can be used in structural analysis, was used for static analysis. Wind load equations expressed in TS 498 standard [27] were used in structural analysis [28, 29, 30]. Cost analysis was performed using Excel program for Material Quantity and Cost Analysis.

4. Results and Discussion

4.1. Exhaust Pipe Calculation and CFD Analysis

The full-load operating parameters of the Janbacher J 208 GS-C 25 gas engine used in the system are report-

ed by the manufacturer. In addition to the gas engine data sheet information, the information provided by the boiler and silencer manufacturer is presented in ▶**Table 2**. The total thermal capacity of the gas engine (851 kW), exhaust flow rate (1858 kg/h), exhaust outlet temperature (508 °C), and pressure losses in the exhaust pipe system are shown in detail.

Table 2. Data Summary for CFD analysis

Motor Type: Janbacher Gas Engine J 208 GS-C 25		
Specification	Full Load	Unit
Thermal capacity (Total)	851	kW
Exhaust gas mass flow rate	1858	kg/h
Exhaust gas temperature	508	°C
Max. admissible exhaust back pressure	6	kPa
Boiler inlet temperature	508	°C
Boiler outlet temperature	161	°C
Boiler pressure loss	0.95	kPa
Silencer pressure loss	1	kPa

4.1.1 The Existing System

The current system is shown in ▶**Figure 4**. The system consists of a gas engine, boiler, muffler, and exhaust pipe. The exhaust pipe has a section with a diameter of Ø 273 mm and another section with a diameter of Ø 219 mm. To ensure the exhaust pipe remains self-supporting, its thickness has been increased, and it has been supported by a base plate and flags mounted on the cabinet.

The performance analysis of the existing exhaust pipe design, based on the information in ▶**Table 2** and ▶**Figure 4**, was performed using the Kesa Aladin software in accordance with EN 13384-1 standard. The calculation result is shown in ▶**Figure 5**.

According to the calculation results, it has been shown that the current exhaust pipe design complies with the standards by meeting both temperature and pressure requirements.

4.1.2 The Proposed New System

Within the scope of the originality of this study, improvements have been made to the existing design. Ac-
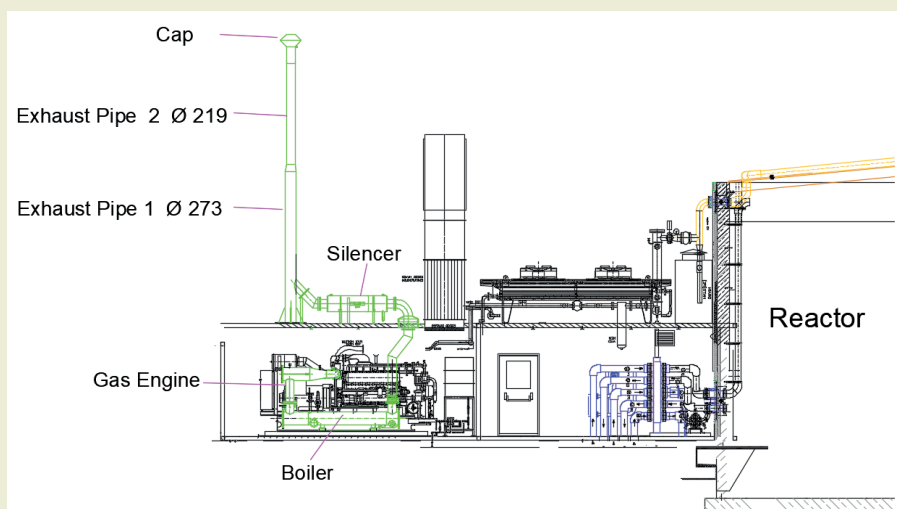
Figure 4. The Existing System Design

Figure 5. Results of the exhaust cross-section calculations for the existing system

cordingly, the existing silencer is positioned horizontally, whereas the silencer in the proposed improvement is designed vertically. This way, the length of the exhaust pipe route is reduced, which will decrease the exhaust pipe lengths and resistance losses. The reduction in length and resistance losses represents an engineering improvement and thus leads to more optimal draft. The proposed new system is shown in ▶**Figure 6**.

Based on the information in ▶**Table 2** and ▶**Figure 6**, the performance analysis of the existing exhaust pipe design was performed with Kesa Aladin software in accordance with EN 13384-1 standard. The calculation result is shown in ▶**Figure 7**.

According to the calculation results, with the route modification, it has been observed that draft is achieved in the proposed new exhaust pipe design by selecting an exhaust pipe diameter of Ø180 mm, and that it complies with the standards by meeting both temperature and pressure requirements.

4.2. Wind Load Calculation and Structural Analysis for The Proposed New System

4.2.1 Load Calculation for Wind Load Analysis

Wind load values are needed to evaluate the durability of the exhaust pipe and silencer design used in the project. The wind pressure acting on the upper surface of the structure is given in the equation below [27].

$$W = C_p q \tag{1}$$

Here, q is the wind pressure (Wind pressure and Suction pressure) (kN/m²), and C_p is the suction coefficient.

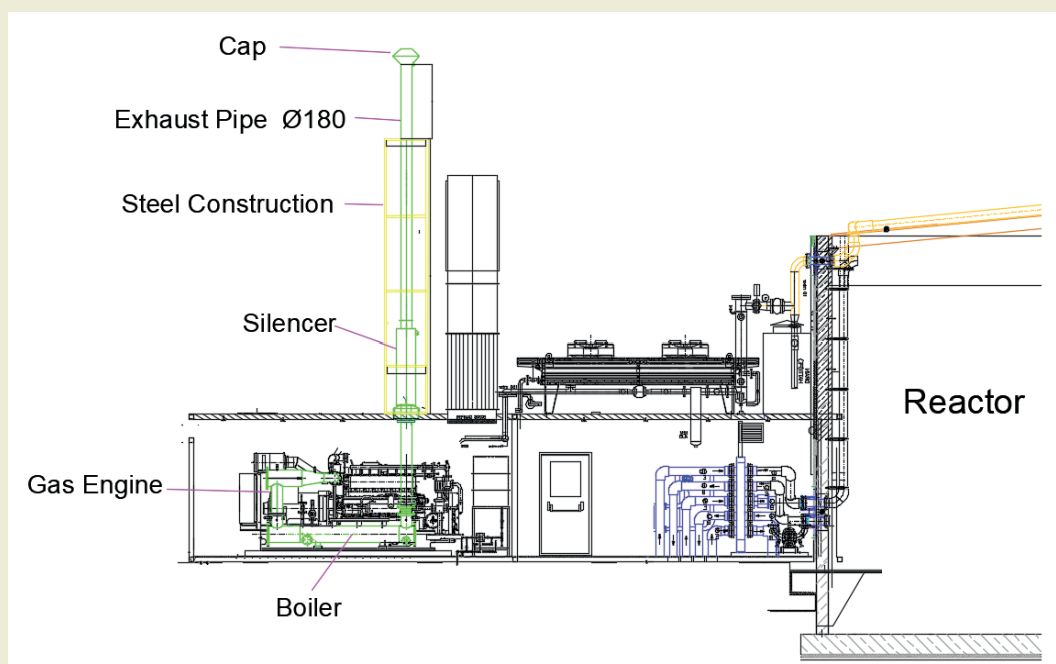**Figure 6.** Design of The Proposed New System

Figure 7. Results of The Exhaust Cross-Section Calculations for The Proposed New System

C_p is determined depending on the different wind directions for the surface under consideration. Wind pressure acts perpendicularly to the surface. In tower type structures such as exhaust pipes, this value is taken as 1.6. Thus, wind pressure in the exhaust pipes is expressed as follows [27].

$$W = 1.6 \ q \tag{2}$$

Wind pressure is determined by the following equation.

$$q = \frac{\rho \, v^2}{2g} \tag{3}$$

If the approximate unit volume mass of air is taken as q = 1.25 kg/m³, and the acceleration due to gravity is substituted in m/s², the wind pressure is expressed in the following equation.

$$q = \frac{v^2}{1600} \tag{4}$$

Although different wind speeds may occur due to local topographic conditions, in general, the wind speed is shown in ▶Table 3, according to the values specified in TS 498 September 2021 standard [27], based on the structure's height above the ground. This table also summarizes the wind pressure associated with the speed, in practical terms.

Due to local topographic conditions, different wind speeds may occur, and these speeds may deviate from the given values. Therefore, considering that the wind effect will be severe in structures located at high alti-

Table 3. Summary of Wind Speed and Wind Pressure Based on Height [27].

Height above ground (m)	Wind speed v (m/s)	Wind pressure q (kN/m²)
0 ~ 8	28	0.5
9 ~ 20	36	0.8
21 ~ 100	42	1.1
> 100	46	1.3

tudes or on steep slopes, the wind pressure should be taken as q = 1.1 kN/m² [27].

Taking into account the wind pressure, the wind load acting on the exhaust pipe system is calculated using the following equation.
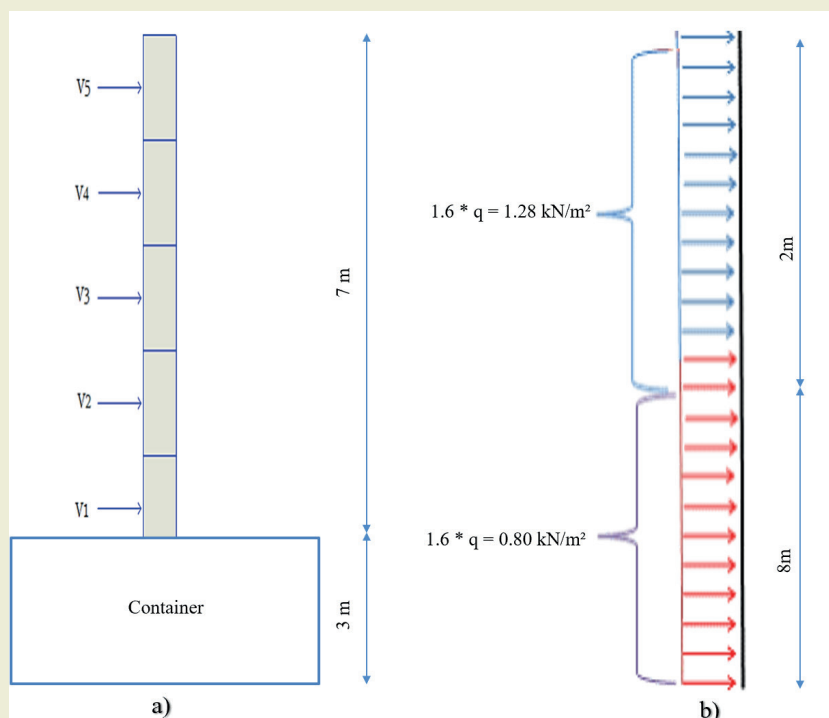
$$F_n = q \, c \, H \tag{5}$$

$$F_n = \frac{v^2}{1600} \, c \, H \tag{6}$$

$$C = \pi \, D_2 \tag{7}$$

$$D_2 = D_1 + 2 \, t_i \tag{8}$$

Here, v represents the wind speed at different heights and speeds, F_n represents the wind load, H represents the ground height, c represents the exhaust pipe outer wall perimeter, t_i represents the insulation thickness,

Figure 8. Schematic representation a) Exhaust Pipe b) Wind Pressure

D_1 represents the pipe inner diameter, and D_2 represents the pipe outer diameter after the insulation coating.

Here, when D_1 is taken as 180 mm and t_i as 50 mm, D_2 has been determined as 280 mm. The distribution of the wind load on the exhaust pipe is schematically shown in ▶Figure 8. Since the length of the proposed new exhaust pipe on the cabinet is 7 m, the load distribution has been considered accordingly.

As seen here, different wind loads are effective in the first 5 m and the following 2 m lengths of the exhaust pipe, due to the change in wind speed. Therefore, customized wind load calculations are shown in the equations below. Thus, wind load calculations are made for different wind speed ($\mathcal{V}$) and ground height (H) combinations.

$$F_1 = 1.6 \ v_1^2 \ c \ H_1 \tag{9}$$

$$F_2 = 1.6 \ v_2^2 \ cH_2 \tag{10}$$

Here, v_1= 28 m/s, H_1 = 8 m, v_2 = 36m/s, H_2 =2 m, so F_1=5.52 kN, and F_2=2.28 kN are found.

4.2.2 Structural Analysis

In the above section, the wind load calculations and the weight of the system have been defined as a force on the exhaust system in the structural analysis module. Although it is possible to apply different loads to different regions in accordance with the standards, in this project, a single force of 5.52 kN, the maximum wind load-critical load, has been applied equally across the entire system. The purpose of selecting the critical load in the calculations is to test the maximum durability in all areas of the exhaust pipe design.

Before the structural analysis, the 3D design of the exhaust pipe was made in the academic-student module of the Solidworks program. The 3D design is shown in ▶Figure 9.

The 3D design of the exhaust pipe was created in the SolidWorks (academic-student simulation model) program, and the steel construction was included in the simulation model as fixed to the ground. A total of 167691 nodes and 83229 elements were used in the analysis. In addition, mesh quality analysis was performed in the study. Mesh quality was found to be a minimum of 0.052 and maximum 0.99. The Fixed Support, Mesh structure, and load definitions have been established. While defining the loads, wind load and system weight were taken into account. Wind load was defined in the program so that it would apply to both the exhaust pipe and the construction. The Fixed Support, mesh structure, and load definitions are provided in ▶Figure 10.

Carbon steel (S275JR) has been used in the design of the construction and silencer, while AISI 304 grade stainless steel materials have been used for the exhaust pipe. These materials have been defined within the SolidWorks simulation module. Subsequently, finite element analysis was performed. The finite element analysis is shown in ▶Figure 11.
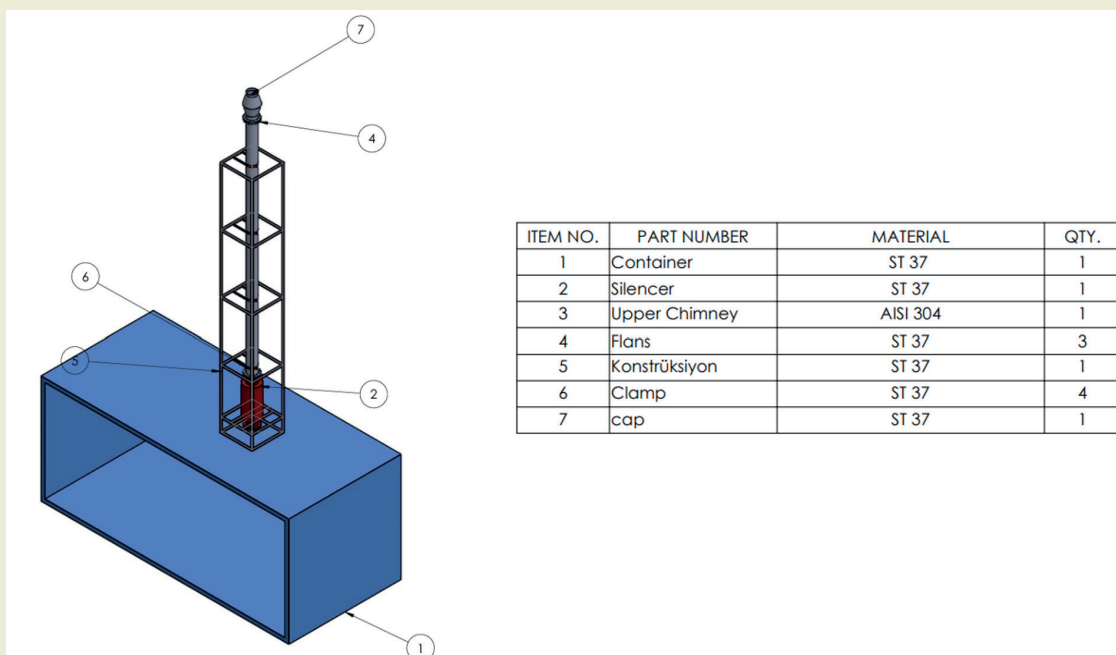

ITEM NO.	PART NUMBER	MATERIAL	QTY.
1	Container	ST 37	1
2	Silencer	ST 37	1
3	Upper Chimney	AISI 304	1
4	Flans	ST 37	3
5	Konstrüksiyon	ST 37	1
6	Clamp	ST 37	4
7	cap	ST 37	1

Figure 9. Exhaust Design for The Proposed New System

Accordingly, the maximum stress on the exhaust pipe was found to be 108.691 MPa according to the Von Mises criterion. This value is within safe limits compared to the yield strength of the steel material used (170 MPa). Thus, it was seen that the exhaust pipe is approximately 1.56 times more resistant to the loads caused by wind and the weight of the system. In the deformation analysis, the displacement and strain values of the exhaust pipe were examined in detail. With the rise of the exhaust pipe upwards, it was determined that the displacement values in some areas were a maximum of 0.13 mm. This value is within acceptable limits for the system and does not threaten the stability of the design.

4.3 Exhaust Design Cost Relationship

The proposed new exhaust system has shown that it

meets the system requirements in terms of both CFD and structural analysis, just like the existing working exhaust system, even when the pipe route is reduced. In this section, cost analysis is performed by comparing the costs of the proposed new system that meets the system requirements with the existing system. The cost of the existing system is shown in ▶Table 4, and the cost of the proposed new system is shown in ▶Table 5.

As a result of the cost analysis, it was determined that the total cost of the existing exhaust pipe system was 5,133.00 USD. However, thanks to the design optimizations and savings in material usage, the cost was reduced to 2,402.80 USD. This means a cost reduction of approximately 53%. This saving was achieved by opti-
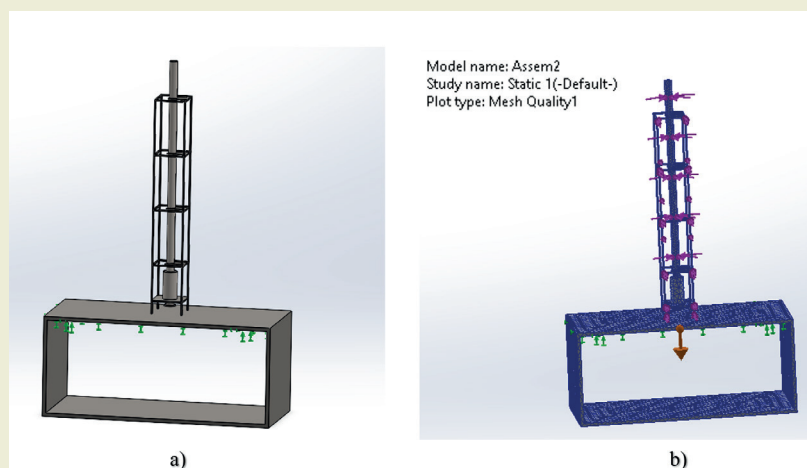

Figure 10. Design definitions: a) Fixed support b) Mesh configuration and load definitions
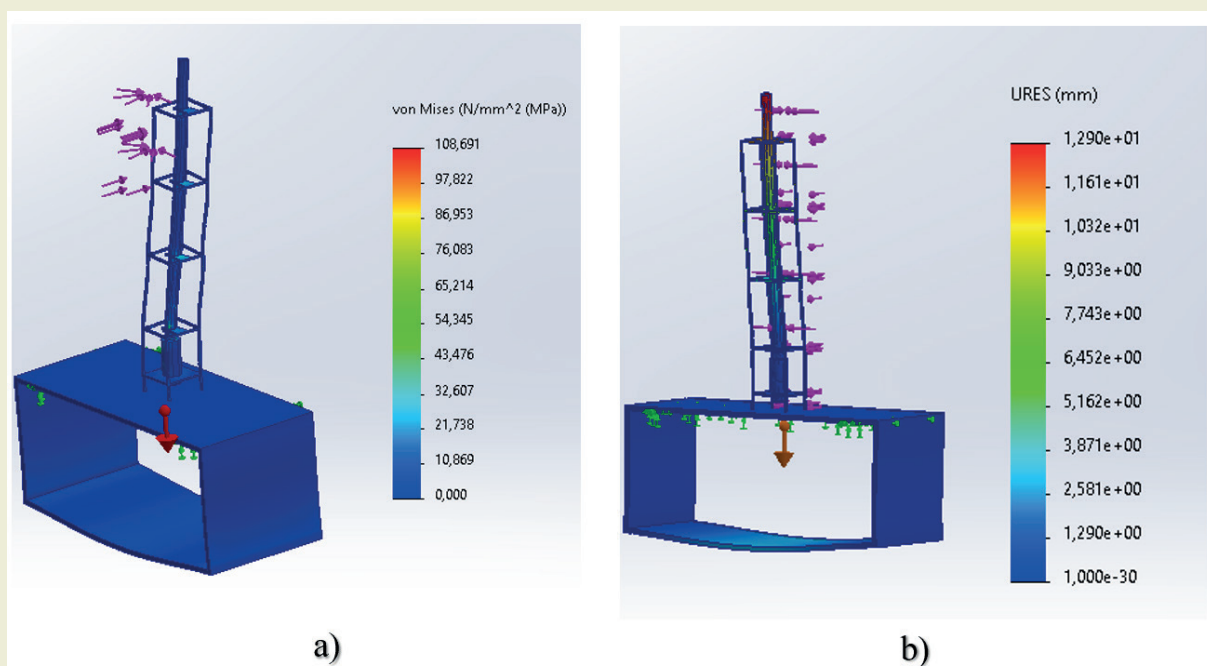

Figure 11. Finite element analysis: a) Von Mises b) Deformation

Table 4. The Cost of The Existing System

No	Description	Quantity	Unit	Total
	Vertical Sistem			
1	Ø 219 Length module	3.0	pc	$270.00
2	Ø 219 Adaptor	1.0	pc	$90.00
3	Ø 219 Cap	3.0	pc	$675.00
4	Ø 273 Length module	3.0	pc	$300.00
5	Ø 273 Condense module	1.0	pc	$120.00
6	Ø 273 Te Module	1.0	pc	$120.00
7	Ø 273 Base plate and ribs support	1.0	pc	$846.00
8	Ø 273 Flanges	0.0	pc	$0.00
	Connection pipe			
9	Ø 219 Length module	7.0	pc	$630.00
10	Ø 219 Adaptor	2.0	pc	$180.00
11	Ø 219 Te module	2.0	pc	$216.00
12	Ø 219 Dirsek 90	2.0	pc	$216.00
13	Ø 219 Dirsek 45	3.0	pc	$270.00
14	Ø 219 Flanges	10.0	pc	$1,200.00
	Total amount:			$5,133.00

Table 5. The Cost of The Proposed New System

No	Description	Quantity	Unit	Total
	Vertical Sistem			
1	Ø 180 Length module	6.0	pc	$168.80
2	Ø 180 Cap	3.0	pc	$210.00
3	Ø 180 Condense module	1.0	pc	$33.60
4	Ø 180 Te Module	1.0	pc	$33.60
5	Ø 180 Flanges	4.0	pc	$480.00
6	Ø 180 Steel construction	1.0	pc	$500.00
	Connection pipe			
7	Ø 180 Length module	2.0	pc	$56.00
8	Ø 180 Adaptor	2.0	pc	$56.00
9	Ø 180 Dirsek 90	1.0	pc	$33.60
10	Ø 180 Te Module	2.0	pc	$112.00
11	Ø 180 Flanges	6.0	pc	$720.00
	Total amount:			$2,402.80

mizing elements such as CFD analysis, structural analysis, exhaust length, exhaust pipe diameter, material thickness, and elbow design. Achieving the same durability and efficiency targets with less material usage offers a significant advantage in terms of both economic and environmental sustainability. This study clearly demonstrates the potential benefits of cost-effective design applications in industrial facilities.

The cost analysis in this study shows that the cost analysis of exhaust design is of great importance in terms of increasing recycling rates by encouraging cogeneration systems, achieving energy efficiency targets, and com-plying with environmental sustainability principles.

5. Conclusions

As a result of the examinations and analyses, it has been revealed that the correct design and positioning of exhaust pipes used in biogas-fueled cogeneration systems are of critical importance in terms of both efficiency and cost. In the current system, the horizontally positioned silencer and long exhaust pipe line increase pressure losses and cause unnecessary material usage, making the design costly. The proposed new design, thanks to the shorter pipe route, not only met the required standards but also achieved a safe structure by using much smaller diameter and material thickness.

The data collected during the field survey and the proposed new system were evaluated using CFD and structural analysis methods; the results obtained showed that there were significant improvements that directly affected the system efficiency and cost. In the current system, it was observed that the gas engine exhaust operating at 508 °C and 1858 kg/h flow (total 851 kW thermal capacity) was carried by two different pipe sections with diameters of 273 mm and 219 mm. In the analysis of this design, it was determined using the Kesa Aladin software that it complied with the standards in terms of pressure losses and gas flow, but created high costs due to unnecessary material usage.

On the other hand, in the new proposed system, the exhaust line was shortened by positioning the silencer vertically, the diameter was optimized as Ø180 mm and the material thickness was reduced. In the CFD analysis, it was seen that the temperature and pressure conditions required by the standards were also provided with this new design. Solidworks Simulation was used in structural analyses; under the wind load (critical condition defined as approximately 5.52 kN) and the weight of the system, a maximum Von Mises stress of 108.691 MPa was calculated. This value corresponds to a safety factor of approximately 1.56 when the material yield strength (170 MPa) is taken into account. The maximum displacement under the same conditions was determined to be only 0.13 mm, thus confirming that the design has sufficient stability.

The cost analysis results are one of the most striking findings in the project. While the total cost of the existing system was calculated as 5,133 USD, this amount was reduced to 2,402.80 USD with the new proposed design. A cost reduction of approximately 53% has been achieved, demonstrating that the use of a shorter exhaust route, smaller diameter, and thinner material not only ensures compliance with standards but also provides a significant economic advantage.

As a result, the new design approach, which is verified both in terms of fluid dynamics and structural aspects, combines efficiency, safety and economic criteria in

a holistic way. This study reveals that it is possible to achieve high performance at lower costs in biogas-fueled cogeneration plants and that the same method can be generalized in similar applications.

In future studies, long-term performance of high temperature and corrosion effects can be investigated by using advanced material combinations or multi-layer exhaust systems. In this context, processing the obtained data with optimization algorithms will allow for more comprehensive improvement of exhaust systems in terms of both cost and energy efficiency. Thus, adopting the same methods in similar biogas and cogeneration plants will provide a guiding approach for both operators and engineering applications.

Research ethics

Ethical approval not required.

Author contributions

Conceptualization: [Rabia Kaymaz], Methodology: [Kursat Tanriver], Formal Analysis: [Kursat Tanriver], Investigation: [Kursat Tanriver], Resources: [Rabia Kaymaz], Data Curation: [Kursat Tanriver], Writing - Original Draft Preparation: [Rabia Kaymaz], Writing - Review & Editing: [Mine Ak], Visualization: [Mine Ak], Supervision: [Mine Ak], Project Administration: [Mine Ak]

Orcid

Rabia Kaymaz https://orcid.org/0009-0008-0912-1374
Mine Ak https://orcid.org/0000-0003-1131-5529
Kürşat Tanrıver https://orcid.org/0000-0002-1723-4108

References

[1] Man, S. S., Lee, W. K. H., Chan, A. H. S., & Tsang, S. N. H. (2023). The economic and environmental evaluations of combined heat and power systems in buildings with different contexts: A systematic review. Applied Sciences, 13(6), 3855. https://doi.org/10.3390/app13063855

[2] Tanrıver, K., & Ay, M. (2024). Modifying the refuse chute design to prevent infection spread: Engineering analysis and optimization. Applied Sciences, 14(21), 9638. https://doi.org/10.3390/app14219638

[3] Siripaiboon, C., Sitthichirachat, P., Sarabhorn, P., Somkeattikul, K., Areeprasert, C., & Scala, F. (2025). Design, CFD simulation, and experimental verification of a novel fixed-bed decoupling gasifier with an integrated syngas burner using high-temperature flue gas. Process Safety and Environmental Protection, 196, 106883. https://doi.org/10.1016/j.psep.2025.106883

[4] Huang, Z., Liu, L., Wang, Z., Wang, C., Liu, Y., Liu, B., Zheng, G., & Yan, H. (2025). CFD analysis of flow and heat transfer enhancement in a tower-type zinc refining furnace with novel structural designs. Applied Thermal Engineering, 263, 125327. https://doi.org/10.1016/j.applthermaleng.2024.125327

[5] Alhashem, A., Almutairi, A. S., & Almokmesh, S. F. (2025). Flue gas recirculation in steam boilers: A comprehensive assessment strategy for energy optimization and efficiency enhancement. Processes, 13(2), 395. https://doi.org/10.3390/pr13020395

[6] An, R., & Zhang, X. (2025). Evaluation of weighted-sum-of-gray-gases models and radiation characteristics analysis for gas-ash particle mixture in ash deposition. Applied Thermal Engineering, 267, 125820. https://doi.org/10.1016/j.applthermaleng.2025.125820

[7] Yolus, A., Kayan, G., Yılmaz, Ş., & Tıkız, I. (2022). Recovery waste heat on exhaust of ship with thermoelectric generators. Journal of Maritime Research: Amphora, 1(1), 43–59.

[8] Sharma, G., Kumar, J., Sharma, S., Singh, G., Singh, J., Sharma, A., Chohan, J. S., Kumar, R., & Obaid, A. J. (2022). Performance of diesel engine having waste heat recovery system fixed on stainless steel made exhaust gas pipe. Materials Today: Proceedings, 48(5), 1141–1146. https://doi.org/10.1016/j.matpr.2021.07.511

[9] Li, Z., Zhang, X., & Dong, Z. (2023). TSF-transformer: A time series forecasting model for exhaust gas emission using transformer. Applied Intelligence, 53, 17211–17225. https://doi.org/10.1007/s10489-022-04326-1

[10] Kumar, A., Chaudhary, S. K., & Kumar, R. (2024). Vibrational analysis of an exhaust pipe flange with rib using ANSYS software. In A. De, P. P. Mukherjee, S. Pati, & A. Biswas (Eds.), Recent Trends in Mechanical Engineering. ICRAME 2024. Lecture Notes in Mechanical Engineering (pp. 67–78). Springer. https://doi.org/10.1007/978-981-97-7535-4_7

[11] Nejatzadegan, F., Sobhani, V., Pahlavan, M., & Dehghan, A. (2025). Effect of exhaust manifold geometry design on the performance of an internal combustion engine. International Communications in Heat and Mass Transfer, 162, 108593. https://doi.org/10.1016/j.icheatmasstransfer.2025.108593

[12] Başaran, H. Ü. (2024). Enhanced after-treatment warm up in diesel vehicles through modulating fuel injection and exhaust valve closure timing. European Mechanical Science, 8(2), 93–103. https://doi.org/10.26701/ems.1441861

[13] Zhang, S., Shen, M., Kang, Y., & Tang, Z. (2025). The design and experimental study of a deep-condensing waste heat recovery system for boiler flue gas based on Baoneng Heating Plant. Processes, 13(2), 306. https://doi.org/10.3390/pr13020306

[14] Shi, Z., Wei, H., Li, G., Wang, Y., Li, Q., Zheng, X., Song, K., Chen, C., Ma, C., Mozumder, S. A., & Basher, M. K. (2025). Research and analy-

sis of explosion-proof diesel engine performance based on different exhaust gas cooling systems. Energies, 18(3), 610. https://doi.org/10.3390/en18030610

[15] Li, Y., Yu, J., Liu, Y., Huang, R., Wang, Z., & Zhao, Y. (2022). A review on removal of mercury from flue gas utilizing existing air pollutant control devices (APCDs). Journal of Hazardous Materials, 427, 128132. https://doi.org/10.1016/j.jhazmat.2021.128132

[16] Kalak, T. (2023). Potential use of industrial biomass waste as a sustainable energy source in the future. Energies, 16(4), 1783. https://doi.org/10.3390/en16041783

[17] European Committee for Standardization. (2009). EN 1856-1: Chimneys — Requirements for metal chimneys — Part 1: System chimney products. Brussels, Belgium.

[18] European Committee for Standardization. (2022). EN 13384-1: Chimneys — Thermal and fluid dynamic calculation methods — Part 1: Chimneys serving one heating appliance. Brussels, Belgium.

[19] Jenbacher. (2025). Jenbacher J208 Gas Engine. Retrieved February 23, 2025, from https://www.jenbacher.com/en/gas-engines/type-2/j208

[20] European Committee for Standardization. (2009). EN 1859: Chimneys — Metal chimneys — Test methods. Brussels, Belgium.

[21] Tanrıver, K., & Ay, M. (2024). Investigation of flue gas temperature effects in natural gas fueled systems: Experimental thermal performance and structural optimization. International Journal of Heat and Fluid Flow, 107, 109428. https://doi.org/10.1016/j.ijheatfluidflow.2024.109428

[22] Reza Kashyzadeh, K., Ridha, W. K. M., & Ghorbani, S. (2025). The influence of nanocoatings on the wear, corrosion, and erosion properties of AISI 304 and AISI 316L stainless steels: A critical review regarding hydro turbines. Corrosion and Materials Degradation, 6(6), 10006. https://doi.org/10.3390/cmd6010006

[23] Kaymaz, R., Tanrıver, K., & Ak, M. (2025). Chimney installation and thermal-flow analysis in cogeneration systems. Paper presented at the 2nd International Texas Congress on Advanced Scientific Research and Innovation, January 27–28, Houston, Texas.

[24] Tanrıver, K., & Ay, M. (2020). Comparison of calculation programs in a stainless-steel chimney application. Euroasia Journal of Mathematics, Engineering, Natural Medical Sciences International Indexed Refereed, 7(10), 97–111.

[25] Ali, F. A., Hamandi, S. J., & Mohammed-Salih, H. S. (2025). Introducing a novel orthodontic bracket holder with a SolidWorks-based semiautomatic positioner tested via finite element analysis. Discover Applied Sciences, 7, 153. https://doi.org/10.1007/s42452-024-06368-1

[26] Uličný, M. M., Cigánek, J., Kutiš, V., Kučera, E., & Šedivý, J. (2025). Modeling and co-simulation of fuzzy logic controller for artificial cybernetic hand. Multimodal Technologies and Interaction, 9(2), 12. https://doi.org/10.3390/mti9020012

[27] Turkish Standards Institute. (2021). TS 498: Calculation values of loads to be taken into account in the sizing of buildings. Ankara, Turkey.

[28] Yüksel, S., Şirin, T. B., Ay, M., Uçar, M., & Kurt, M. (2024). A study on end mill tool geometry parameters for end milling of 316 L: Finite element analysis and response surface methodology optimization based on resultant cutting force. Journal of the Brazilian Society of Mechanical Sciences and Engineering, 46(8).

[29] Tanrıver, K., & Ay, M. (2023). Experimental, software and topological optimization study of unpredictable forces in bolted connections. Tehnički Vjesnik, 30(4), 1175–1184. https://doi.org/10.17559/TV-20221113121639

[30] Tanrıver, K., Dilibal, S., Şahin, H., & Kentli, A. (2021). A novel design on polymeric material recycling technology. Acta Scientiarum. Technology, 43, e56211.

Investigation of the effects of nanoparticle additive lubricants on the adhesive wear properties of ST37 steel and AISI304

Cemile Eylem Urhan[1] (iD) **, Kadir Gündoğan[2]*** (iD) **, Atike İnce Yardımcı[3]** (iD)

[1]Uşak University, Institute of Science, 64000, Uşak, Türkiye
[2]Uşak University, Faculty of Engineering, Department of Nanotechnology Engineering, 64000, Uşak, Türkiye
[3]Uşak University, Technology Transfer Office, 64000, Uşak, Türkiye

Abstract: In this study, the adhesive wear behavior of different metals lubricated with nanoparticle-modified oils was investigated. Two different metal samples, namely St37 steel and AISI304, were used. As the lubricant, the widely used industrial 10W-40 motor oil was selected and titanium carbide (TiC) and titanium nitride (TiN) nanoparticles were added at concentrations of 1%, 3%, and 5% by weight to improve the tribological properties. The lubricants were homogeneously mixed with the nanoparticles, and the prepared samples were subjected to wear tests using the pin-on-disk method. Tests were conducted under fixed parameters, and subsequently, the worn surfaces were analyzed in detail using SEM, EDS, FTIR, UV spectroscopy and Optical Microscopy techniques. The results demonstrated that the addition of nanoparticles reduced the coefficient of friction and increased wear resistance. Particularly, the addition of 3% TiN and TiC nanoparticles provided lower wear tracks and more homogeneous surface deformation on all metal surfaces. This study presents important findings supporting the potential of nanoparticle-reinforced lubricants to extend the service life and improve the performance of machines in industrial applications.

Keywords: Tribology, AISI304, St37 Steel, TiC, TiN

1. Introduction

With the advancement of technology, while human labor in industry is decreasing, an increase in machine usage is being observed. Developing wear-prevention strategies to enhance the durability and performance of machines has become critical. Metal materials are generally preferred in production; however, lubricants are used to reduce friction and wear between surfaces [1]. Although conventional lubricants offer many advantages, their performance can be limited under harsh conditions such as high temperature, pressure and contamination [2].

The development of nanotechnology has led to the idea of improving tribological properties by incorporating nanoparticles into lubricants. Nano-sized reinforcements have the potential to reduce friction, provide resistance to wear and extend system life. In the literature, many nanoparticles such as Nanodiamond, Carbon Nanotube (CNT), Molybdenum Disulfide (MoS_2), Silicon Dioxide (SiO_2), Alumina (Al_2O_3), Zinc Oxide (ZnO), Titanium Dioxide (TiO_2), Titanium Nitride (TiN) and Titanium (IV) Carbide (TiC) have been used as lubricant additives.

In this study, the effects of TiN and TiC nanoparticles on adhesive wear will be specifically examined. TiN reduces friction due to its high hardness and oxidation resistance [3], while TiC offers high-temperature stability and wear resistance [4]. Both nanoparticles aim to provide lower wear and longer life in contact between metal surfaces.

Lubricants can be either natural (vegetable, mineral, animal-based) or synthetic (PAO, ester, glycol-based) [5]. It is known that both types improve machine efficiency by reducing friction and wear. Tribology is the science that studies friction, wear, and lubrication phenomena, and it plays a critical role in reducing energy loss and surface damage in machines [6].

Adhesive wear occurs when contacting surfaces stick together and break apart, resulting in material loss. In

abrasive wear, hard particles wear down a softer surface. Fatigue wear develops through crack formation caused by repeated stress on the surface. Erosive wear occurs due to the impact of moving abrasive particles, while corrosive wear is caused by a combination of friction and chemical reactions [7].

Previous studies have shown that nanoparticle-enhanced lubricants significantly improve tribological performance. Wu et al. [2] reported that lubricants containing CuO, TiO$_2$ and nanodiamond additives considerably reduced both friction coefficient and wear. Similarly, Birleanu et al. [8] demonstrated that adding TiO$_2$ nanoparticles at concentrations of 0.01–0.075% improved load-carrying capacity and reduced friction. In another study conducted by Choi et al. [9], it was found that Cu nanoparticle-added lubricants reduced the coefficient of friction by up to 44% under high loads. Zhu and colleagues [10] reported that the addition of 8% Fe$_3$O$_4$ nanoparticles improved surface quality in rolling processes and significantly reduced rolling force. Padgurskas et al. [11] also showed that lubricants reinforced with Fe, Cu and Co nanoparticles decreased both the friction coefficient and wear by up to 1.5 times. Moreover, Yu et al. [12] demonstrated that MoS$_2$ nanoparticles reduced surface roughness and helped prevent adhesive wear. Wu and colleagues [13] developed ZnO@SiO$_2$ nanocomposites, which, when added to grease, reduced the coefficient of friction by 11.5% and wear by 25%. These studies strongly support that adding nanoparticles to lubricants can significantly reduce friction and wear in tribological systems. Ma et al. [14] reported that a water-based nanolubricant containing 3.0 wt.% TiO$_2$ nanoparticles reduced the coefficient of friction by 82.9% and wear by 42.7% compared to dry conditions, demonstrating significant improvements in tribological performance. Martin et al. [15] demonstrated that adding TiO$_2$ and SiO$_2$ nanoparticles to PVE lubricant reduced the coefficient of friction, with optimal performance observed at concentrations below 0.010% for TiO$_2$ and 0.005% for SiO$_2$, achieving lower COF and wear scar diameter compared to pure PVE lubricant. Liñeira del Río et al. [16] reported that adding 0.1 wt% MoS$_2$ nanoparticles to PAO4 lubricant led to a 64% reduction in friction, a 62% decrease in wear width and a 97% reduction in worn area, confirming the formation of protective tribofilms and highlighting the effectiveness of MoS$_2$ under boundary lubrication conditions. Bordo et al. [17] demonstrated that while Cu nanoparticles at 0.3% and 3.0%wt were ineffective in synthetic ester oils, their addition to mineral oil significantly reduced the coefficient of friction and enhanced antiwear performance, with optimal results observed at 0.3%wt concentration under varying contact pressures and temperatures.

2. Materials and Method

In this study, based on the information gathered from the literature, the adhesive wear behavior of lubricants modified with different nanoparticles on various metal surfaces was investigated. The experiments were conducted using specially prepared lubricants with specific metal and nanoparticle combinations and the wear performance was evaluated through tribological tests.

Two different metals commonly used in industry were selected for the experiments: St37 steel and AISI304 stainless steel. The chemical composition data of these metals were obtained from the literature and are presented in ▶**Table 1**.

Table 1. Chemical Composition of St37 Steel and AISI304 Stainless Steel (by weight %) [18]

Element	C	Si	Mn	P	S	Cr	Ni
St37	0.11	0.03	0.56	0.007	0.005	0.07	0.03
AISI304	0.034	0.55	1.33	0.03	0.01	18.50	8.44

The TiC and TiN nanoparticles used in this study had a particle size below approximately 44 microns and were supplied in -325 mesh form (completely passing through the sieve) (▶**Table 2**). This was intended to ensure better interaction with the surface and achieve homogeneous dispersion within the lubricant.

Table 2. Material Properties of TiC and TiN Nanoparticles Used in the Study

Nanoparticle	Purity	Size	Molecular Weight (g/mol)	CAS Number
TiC	%98	-325 mesh	59.88	12070-08-5
TiN	%99.5	-325 mesh	61.91	25583-20-4

The base lubricant used in this study was a motor oil with a 10W40 viscosity grade. The fundamental properties of this oil are presented in ▶**Table 3**.

Table 3. Technical Specifications of 10W40 Lubricants

	Viscosity (40 °C) mm²/s	Viscosity (100 °C) mm²/s	Viscosity Index	Density (15 °C) g/ml	Flash Point °C	Pour Point
10W40	90	13.4	150	0.882	210	-39

TiC and TiN nanoparticles were added to the base oils at different weight ratios and the ratios were given in ▶**Table 4**. Special dispersion techniques were applied to ensure the homogeneous distribution of the nanoparticles within the oil. The lubricant formulations were prepared as follows.

The prepared lubricants, both with and without additives, were applied to different metal specimens and subjected to wear tests. Tribological performance evaluations were carried out using the pin-on-disk method [19]. In this study, a steel ball (52100 SAE Bearing Steel) with a hardness range of 58–66 HRC was used as the counter surface in the pin-on-disk wear test. The tests were conducted under constant parameters to en-

Table 4. Composition of Test Samples with Nanoparticle Additives

Nano-Lubricant Name	Nanoparticle	Metal Content (g/100 ml of oil)
10w40	-	-
10w40+TiC1	TiC	0.1
10w40+TiC3	TiC	0.3
10w40+TiC5	TiC	0.5
10w40+TiN1	TiN	0.1
10w40+TiN3	TiN	0.3
10w40+TiN5	TiN	0.5

sure repeatability, and the test conditions used given ▶**Table 5**.

Each metal specimen was individually tested under standard Hz (unmodified) oil and nanoparticle-enhanced lubricants. After the wear tests, surface analyses were performed using Scanning Electron Microscopy (SEM), Energy-Dispersive X-ray Spectroscopy (EDX), Optical Microscopy, Fourier Transform Infrared Spectroscopy (FTIR) and Ultra-Violet (UV) spectroscopy. These techniques allowed for a detailed investigation of surface morphology, chemical composition changes and wear mechanisms.

3. Results and Discussion

In this study, the effects of 10W40 engine oil and the addition of TiC and TiN nanoparticles on the tribological performance of AISI304 and St37 steel specimens were investigated through pin-on-disk wear tests. The experimental results were evaluated based on both the coefficient of friction and weight loss parameters, and the interactions between material, oil and additive were thoroughly analyzed. Coefficient of Friction results are plotted in ▶**Figure 1**.

For the AISI304 sample, the average coefficient of friction in its pure (unlubricated) form was measured as 1.06. This value indicates that there is a significant level of friction between the surfaces when no lubricant is applied. When 10W40 motor oil was used, a notable reduction in the coefficient of friction was observed, decreasing to 0.84. This reduction demonstrates that the 10W40 lubricant effectively reduced direct metal-to-metal contact and improved the tribological performance.

However, when TiC nanoparticles were added to the

Table 5. Parameters used during the Pin-on-Disk wear test

Parameter	Rotational Speed (rpm)	Track Diameter (mm)	Sliding Speed (mm/s)	Duration (s)	Total Sliding Distance (mm)	Normal Load (N)	Data Acquisition Frequency (Hz)	Test Ambient Temperature (°C)
Value	600	12	377	1326	500000	6.4	50	30

Table 6. Average Friction Coefficient Results of AISI304 with 10W40 + TiC Additives

	Pure	10W40	10W40 + TiC %1	10W40 + TiC %3	10W40 + TiC %5
Average Coefficient of Friction (μ)	1.06	0.84	1.55	2.00	1.98
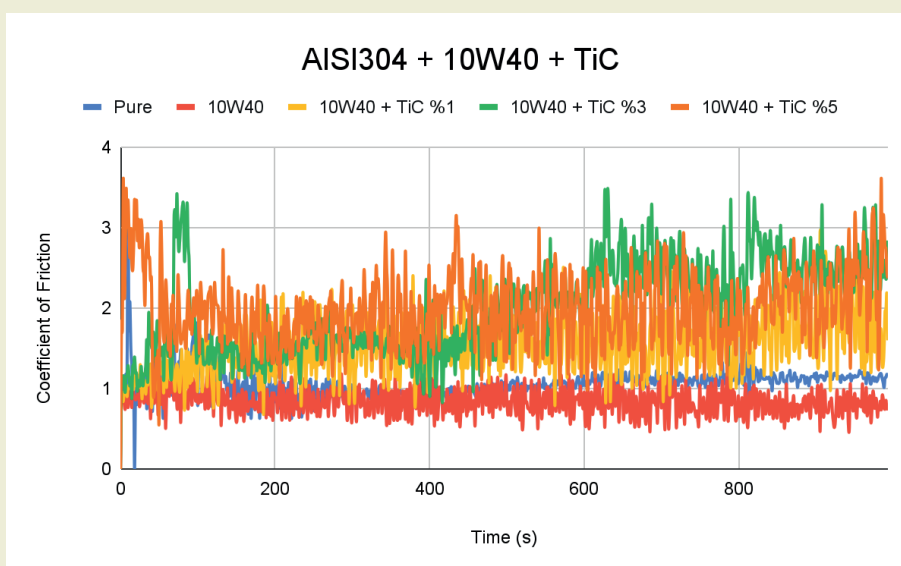
Figure 1. Coefficient of Friction Results for AISI304 with 10W40 + TiC Additives

10W40 oil, the following changes in friction coefficient were observed: with 1% TiC, the coefficient increased to 1.55; with 3% TiC, it reached 2.00; and with 5% TiC, it slightly decreased to 1.98. These results indicate that the addition of TiC nanoparticles to 10W40 oil increased the coefficient of friction on the AISI304 surface and negatively affected the tribological performance. Notably, at 3% and 5% addition rates, the coefficient of friction increased significantly compared to the use of base oil alone.

This increase can be attributed to several mechanisms. Firstly, the high concentration of TiC nanoparticles may have caused the formation of an uneven film layer on the surface, leading to micro-abrasion. Additionally, the increased amount of solid particles could have produced abrasive effects on the sliding surface, thereby raising the friction coefficient. Moreover, the high particle concentration may have increased the viscosity of the oil, negatively affecting its flow properties and preventing the formation of a stable lubricating film between the surfaces. Considering all these mechanisms together, it is evident that excessive nanoparticle addition has a detrimental impact on tribological performance. Coefficient of friction results for AISI304 with 10W40 + TiN additives are given in ▶**Figure 2**.

The average coefficient of friction for the AISI304 specimen in its pure (unlubricated) state was measured as 1.06, indicating significant friction between the surfaces under dry conditions (Table 7). When 10W40 motor oil was used, the coefficient of friction decreased notice- ably to 0.84, demonstrating that the oil formed a protective film layer between the surfaces, thereby reducing direct contact.

However, when TiN nanoparticles were added to the 10W40 oil, a significant increase in the coefficient of friction was observed: 1.82 for 1% TiN, 2.69 for 3% TiN and 2.70 for 5% TiN additions. These findings clearly show that the use of TiN nanoparticles in combination with 10W40 oil increased friction on AISI304 surfaces and negatively affected the tribological performance.

This increase can be attributed to several potential factors. Firstly, the higher concentration of nanoparticles may have led to particle accumulation and aggregation within the oil, resulting in the formation of uneven wear zones on the surface. Additionally, the dense presence of nanoparticles might have caused a micro-abrasive effect rather than acting as a protective film layer, thereby damaging the surface. Moreover, as the particle ratio increased, adverse changes in the oil's viscosity may have occurred, disrupting the lubricant's flowability, preventing sufficient film formation on the surface and ultimately leading to an increase in the coefficient of friction.

The average coefficient of friction measured for the pure AISI304 sample was found to be 1.06. In tests performed with 10W40 motor oil, the coefficient of friction decreased to 0.84, indicating that 10W40 oil provided significantly lower friction values compared to the dry condition. When TiC nanoparticles were added to the
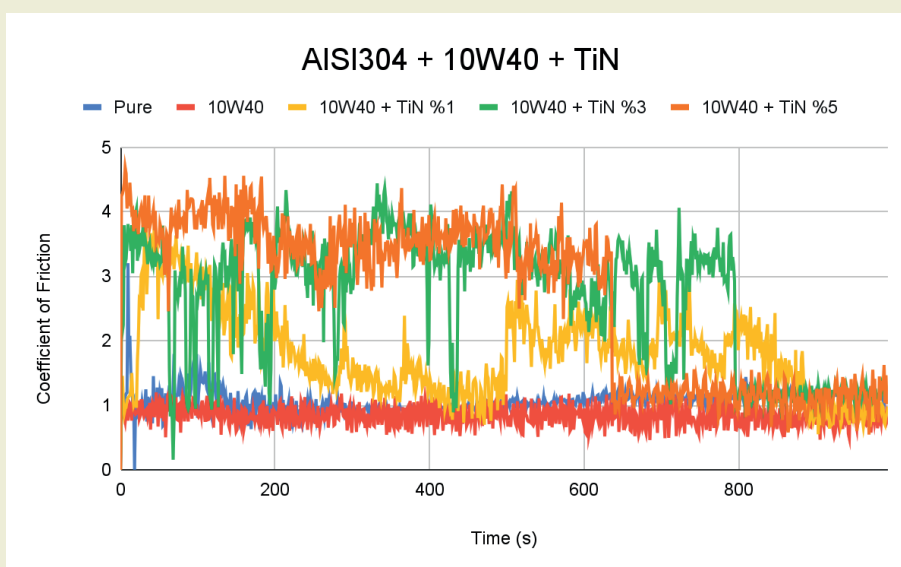

Figure 2. Coefficient of Friction Results for AISI304 with 10W40 + TiN Additives

Table 7. Average Friction Coefficient Results of AISI304 with 10W40 + TiN Additives

	Pure	10W40	10W40 + TiN %1	10W40 + TiN %3	10W40 + TiN %5
Average Coefficient of Friction (μ)	1.06	0.84	1.82	2.69	2.70

10W40 motor oil, the coefficient of friction increased to 1.55 at 1% concentration, and reached 2.00 and 1.98 at 3% and 5% concentrations, respectively. In the case of TiN in addition to 10W40 oil, high coefficients of friction were obtained: 1.82 at 1% concentration, 2.69 at 3% and 2.70 at 5%.

The weight loss values obtained from the wear tests performed on the AISI304 specimen are presented in ▶**Table 8**. The measured weight loss for the pure (unlubricated) AISI304 sample was found to be 0.0059 g. When 10W40 motor oil was used, this value significantly decreased to 0.0001 g, indicating that 10W40 oil is highly effective in minimizing wear on the AISI304 surface.

Table 8. Weight Loss Results from Wear Tests of AISI304-Based Samples with TiC and TiN Additives

AISI304	Weight Loss (g)
Pure	0.0059
10w40	0.0051
10w40+TiC1	0.0057
10w40+TiC3	0.0054
10w40+TiC5	0.0050
10w40+TiN1	0.0034
10w40+TiN3	0.0031
10w40+TiN5	0.0027

When TiC and TiN nanoparticles were added to the oil, the following changes in weight loss were observed: For 10W40 + TiC additives, the weight loss ranged between 0.0050 and 0.0057 g, showing an increase compared to pure 10W40 oil. For 10W40 + TiN additives, the weight loss remained relatively low, between 0.0027 and 0.0034 g. These findings indicate that the effect of nanoparticle additives on tribological performance depends not only on the type of additive but also on its concentration, the type of base oil, and the surface properties of the material.
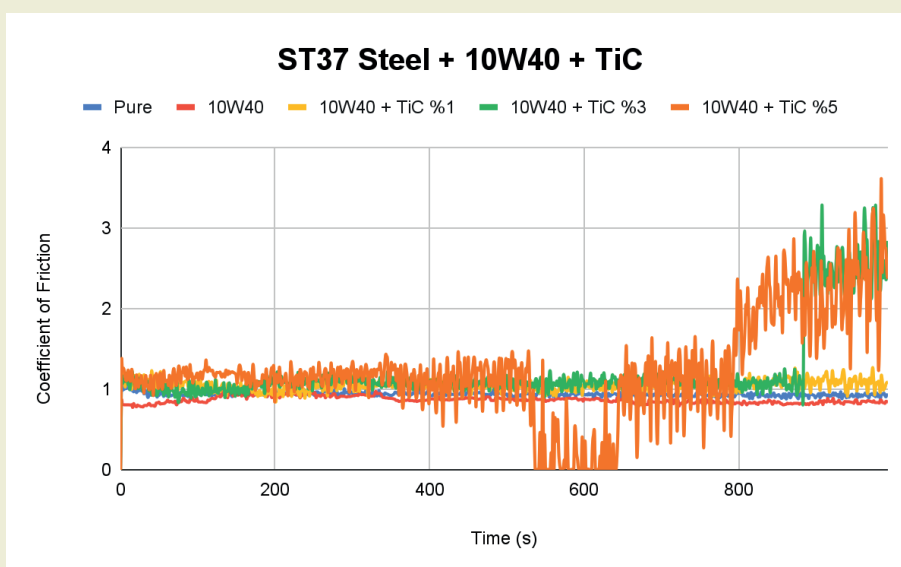
Overall, 10W40 motor oil was found to be effective in reducing the coefficient of friction. However, the addition of TiC nanoparticles increased the coefficient of friction for the AISI304 sample (▶**Figure 3**). In contrast, TiN nanoparticles improved friction performance only at a specific concentration (3%); increasing the concentration beyond this point had a negative effect on tribological performance.

In conclusion, the effectiveness of nanoparticle additives depends not only on the material and oil type but also significantly on the additive concentration. If the optimal concentration is not carefully determined, undesirable increases in friction may occur.

The average coefficients of friction obtained from the wear tests conducted on the St37 steel specimen using 10W40 motor oil and TiC (Titanium Carbide) nanoparticle additives are presented in ▶**Table 9**.

The average coefficient of friction for the pure St37 steel

Figure 3. Coefficient of Friction Results for St37 Steel with 10W40 + TiC Additives

Table 9. Average Coefficient of Friction Results for the St37 Steel Specimen Under 10W40 + TiC Additive

	Pure	10W40	10W40 + TiC %1	10W40 + TiC %3	10W40 + TiC %5
Average Coefficient of Friction (μ)	0.94	0.87	1.05	1.23	1.23

specimen was measured as 0.94. When 10W40 motor oil was used, a decrease in the coefficient of friction was observed, with the value measured at 0.87. This result indicates that the 10W40 lubricant forms a more effective film layer between the surfaces, thereby reducing friction. However, when TiC nanoparticles were added to the 10W40 motor oil, an increase in the coefficient of friction was observed: with 1% TiC additive, the coefficient rose to 1.05 and for 3% and 5% TiC additives, it was measured as 1.23.

The increase in friction with higher additive ratios suggests that TiC nanoparticles may have created an abrasive effect on the St37 steel surface, rather than forming a friction-reducing film layer. Additionally, the high particle concentration may have negatively impacted the flow properties of the oil, leading to more contact points on the surface.

In general, it was determined that the use of 10W40 motor oil alone was effective in reducing friction on the St37 steel surface. However, the addition of TiC nanoparticles resulted in increased friction with higher concentrations, negatively affecting tribological performance. These findings indicate that nanoparticle additives may not produce the desired effect in every system and that the compatibility of the additive, material and lubricant must be carefully optimized.

The average coefficients of friction obtained from the wear tests conducted on the St37 steel specimen using 10W40 motor oil and TiN (Titanium Nitride) nanoparticle additives are presented in ▶Table 10.

The average coefficient of friction for the pure St37 steel specimen was determined to be 0.94. When 10W40 motor oil was used, the coefficient of friction decreased to 0.87, indicating that the lubricant effectively reduced direct surface contact and improved tribological performance. When TiN (Titanium Nitride) nanoparticles were added to the 10W40 motor oil, the following changes in the coefficient of friction were observed: 1.05 with 1% TiN, 1.29 with 3% TiN and 1.13 with 5% TiN.

The use of TiN additives at 1% and 3% resulted in an increase in the coefficient of friction compared to pure oil (▶Figure 4). At 5% TiN, a slight improvement was observed compared to lower concentrations, but the value still remained higher than that of the base oil alone. This trend suggests that TiN nanoparticles did not achieve the desired friction-reducing effect on St37 steel surfaces when dispersed in 10W40 oil. Factors such as particle agglomeration at higher concentrations or negative changes in lubricant flow characteristics may have negatively influenced the tribological behavior.

In general, the use of pure 10W40 motor oil was effective in reducing friction on St37 steel surfaces. However, the addition of TiN nanoparticles led to an increase in friction depending on the concentration, negatively affecting overall tribological performance. These findings highlight that the effectiveness of nanoparticle additives depends not only on the type of additive but also
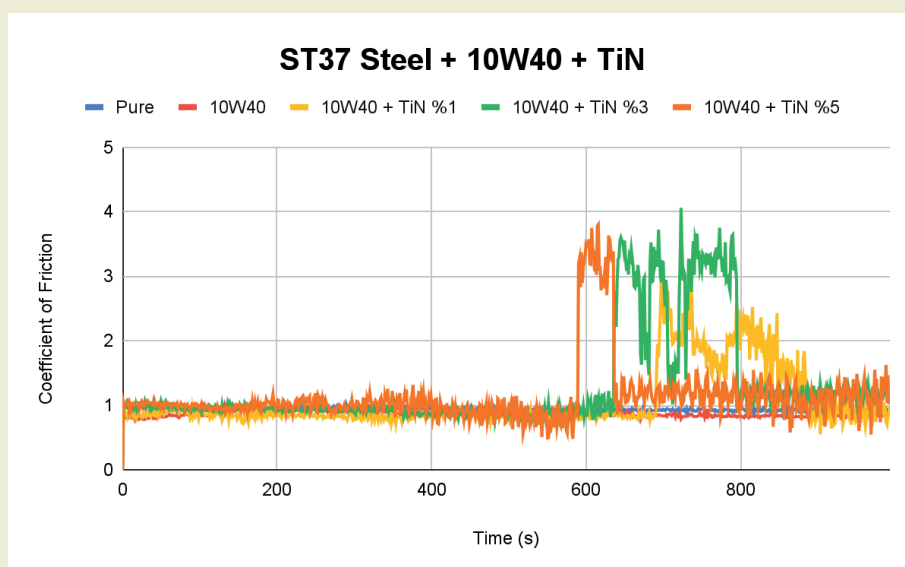

Figure 4. Coefficient of Friction Results for St37 Steel with 10W40 + TiN Additives

Table 10. Average Coefficient of Friction Results for St37 Steel Specimen Under 10W40 + TiN Additive Conditions

	Pure	10W40	10W40 + TiN %1	10W40 + TiN %3	10W40 + TiN %5
Average Coefficient of Friction (μ)	0.94	0.87	1.05	1.29	1.13

on its interaction with the lubricant and the material properties. Therefore, careful optimization of additive type and concentration is essential for achieving desired performance.

The average coefficient of friction measured for the pure St37 steel specimen was 0.94. The use of motor oil improved tribological performance by reducing friction on the specimen surfaces. When 10W40 motor oil was applied, the coefficient of friction decreased to 0.87. Upon the addition of TiC and TiN nanoparticles to the 10W40 motor oil, different trends in the coefficient of friction were observed. For TiC additives, a clear increase in friction was noted with increasing nanoparticle concentration. In 10W40 + TiC samples, the coefficient of friction was measured as 1.05 at 1% concentration and 1.23 at both 3% and 5% concentrations. This rise suggests that TiC nanoparticles did not exhibit the expected friction-reducing effect on St37 steel surfaces and may have even induced an abrasive effect.

On the other hand, the influence of TiN additives followed a different pattern. In 10W40 + TiN samples, the coefficient of friction was 1.05 at 1% TiN, 1.29 at 3% and 1.13 at 5% concentration. These results indicate that TiN nanoparticles may provide a friction-reducing effect on St37 steel when used at an optimal concentration (3%), but this effect diminishes at both lower and higher concentrations.

The wear test results for the St37 steel specimen in terms of mass loss are presented in ▶Table 11.

Table 11. Wear Loss Results for St37 Steel Specimen

St37 Steel	Weight Loss (g)
Pure	0.0013
10w40	0.0052
10w40+TiC1	0.0012
10w40+TiC3	0.0091
10w40+TiC5	0.0024
10w40+TiN1	0.0017
10w40+TiN3	0.0059
10w40+TiN5	0.0027

The wear loss measured for the pure St37 steel specimen was 0.0013 g. When 10W40 motor oil was used, the wear increased to 0.0052 g. Upon the addition of TiC and TiN nanoparticles to the oil, the wear loss values showed the following variations: For 10W40 + TiC, a very low wear loss of 0.0012 g was observed at 1% concentration; however, at 3%, the wear increased sharply to 0.0091 g, and at 5%, it decreased again to 0.0024 g. For 10W40 + TiN, the wear values generally remained low, ranging between 0.0012–0.0059 g. Titanium is widely used in various industries, especially in aviation, due to its exceptional strength, corrosion resistance, low density and favorable biocompatibility and biome-

chanical properties. The results obtained in this study prove this [20].

These findings demonstrate that the effect of nanoparticle additives on wear behavior depends not only on the type of additive, but also on the concentration used, the base oil type and the properties of the material. It is observed that TiN nanoparticles at lower concentrations can enhance wear resistance, while their effectiveness diminishes at higher concentrations. In contrast, TiC additives may increase wear loss at certain concentrations, possibly due to their abrasive effects on the surface [21].

Based on the results of this study, it is concluded that for materials like AISI304, nanoparticle additives can improve tribological performance if the additive ratio is carefully optimized. For St37 steel, low-percentage TiN additives are recommended, while TiC additives should be avoided. In the selection of lubricating oils, both friction and wear parameters should be considered. Finally, it is recommended that more comprehensive wear tests under variable load and temperature conditions be conducted in future research to evaluate the long-term performance of nanoparticle-enriched lubricant systems [22].

3D Optic microscope images were used to examine the wear mechanisms and the surface deformations were analyzed in detail in terms of abrasive and adhesive wear.

Abrasive wear typically occurs as a result of mechanical abrasion of the surface by hard particles. In the 3D microscope images, pronounced scratches, micro-pitting, and surface irregularities were observed, particularly on the pure St37 steel samples in ▶Figure 5. The images obtained for pure St37 steel revealed that the wear progressed in the form of directed and deep grooves. This type of wear mechanism is generally defined as two-body abrasive wear and tribological studies [23] have shown that this form of wear can be further intensified by the movement of abraded particles on the surface.

When reinforced lubricants were used, a significant reduction in surface wear was observed. In St37 steel specimens lubricated with oils containing 1%, 3% and 5% TiN additives, abrasive wear was found to be less pronounced. The depth of the scratches decreased and a more uniform wear pattern formed on the surface. TiN particles contributed to a more balanced wear behavior under frictional forces, leading to a more controlled wear mechanism. Lubricants with TiC additives, on the other hand, altered the wear mechanism more effectively, minimizing the impact of abrasive wear. The St37 steel specimen lubricated with 5% TiC-containing oil exhibited the least signs of abrasive wear, standing out as the sample with the best surface condition. Studies in the literature [24] have shown that TiC controls surface wear more effectively due to its high hardness and chemical stability. The high hardness prevents the

formation of micro-cuts on the surface, leading to a smoother and more uniform wear pattern.

Adhesive wear occurs as a result of the adhesion and subsequent detachment of metal surfaces. In the images, material transfer was observed particularly in certain regions of the AISI304 samples in ▶Figure 6. Although AISI304 is known for its higher resistance to adhesive wear due to its natural oxide layer, localized material accumulation and deformation were detected in the samples lubricated with non-reinforced oils.

Adhesive wear is not solely a result of mechanical damage but is also influenced by chemical and physical in-

teractions at the contact interface [25]. The incorporation of TiN and TiC additives into lubricants alters these interactions, significantly reducing metal transfer between contacting surfaces. In this study, AISI304 samples lubricated with 5% TiN and 5% TiC additives exhibited minimal adhesive wear. This observation aligns with findings from previous research, which demonstrated that TiN and TiC coatings effectively lower the coefficient of friction, thereby minimizing direct metal-to-metal contact and reducing adhesive wear. Especially for AISI304, the lubricant containing 5% TiC almost completely suppressed adhesive wear. This indicates that TiC particles act as a barrier preventing metal transfer between contact surfaces.
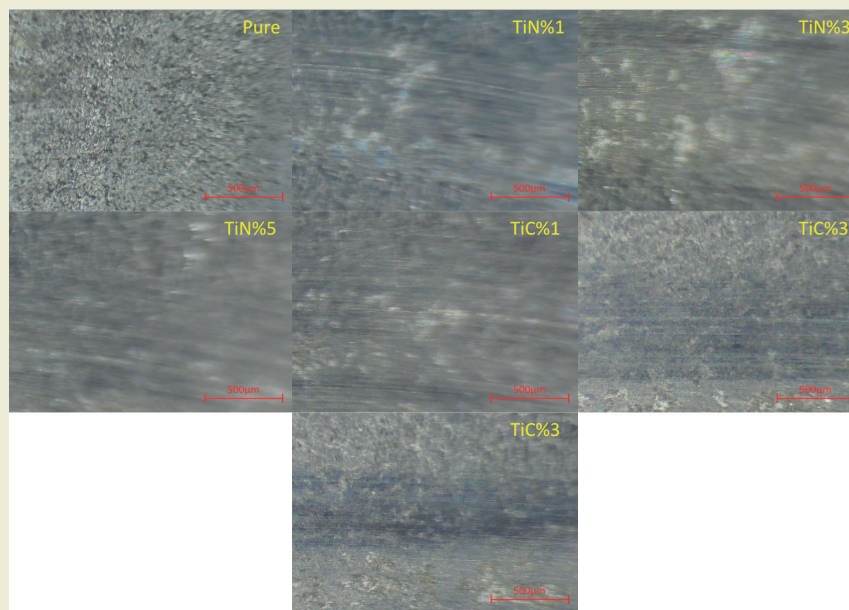
Figure 5. St37 Sample Surface Wear Analysis under 10W40 Oil with TiC and TiN Additives (3D Optical Microscopy Images)
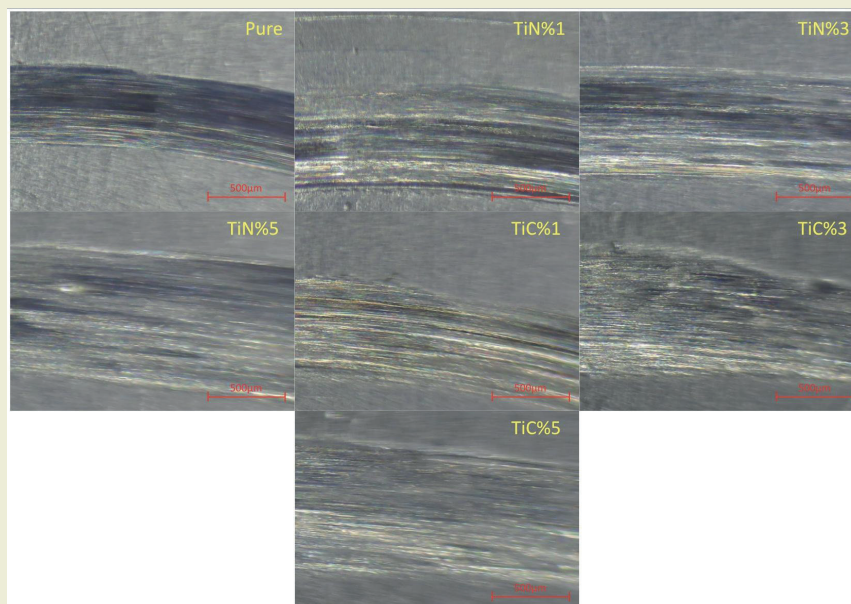
Figure 6. AISI304 Sample Surface Wear Analysis under 10W40 Oil with TiC and TiN Additives (3D Optical Microscopy Images)

SEM images of St37 and AISI304 samples at 1000X scale are given in ▶Figure 6. When the SEM image of the St37 steel plate is examined, its grains are clearly visible. Very distinct and sharply bounded grains of various sizes are observed on the St37 surface. The surface of St37 steel showed a typical low carbon steel morphology consisting of white colored ferrite and black colored pearlite phases. The microstructure of these steels mainly consists of equiaxed ferrite grains ranging from 14 µm to 18 µm and pearlite phase in varying

proportions. The proportion of pearlite phase in the microstructure is around 9% in St37 [23, 26]. The morphology of the AISI304 sample has a smoother surface appearance. There are some scratches and defects on the surface. There is a second phase consisting of small particles that appear to be homogeneously distributed on the AISI304 surface.

When the EDX analysis of the AISI304 sample and the presence of the elements in it as a weight percentage
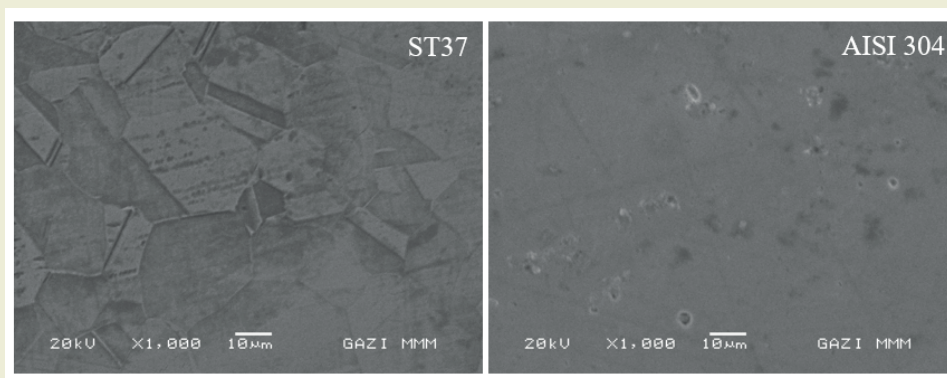
Figure 7. SEM images of St37 and AISI304 at 1000X scale
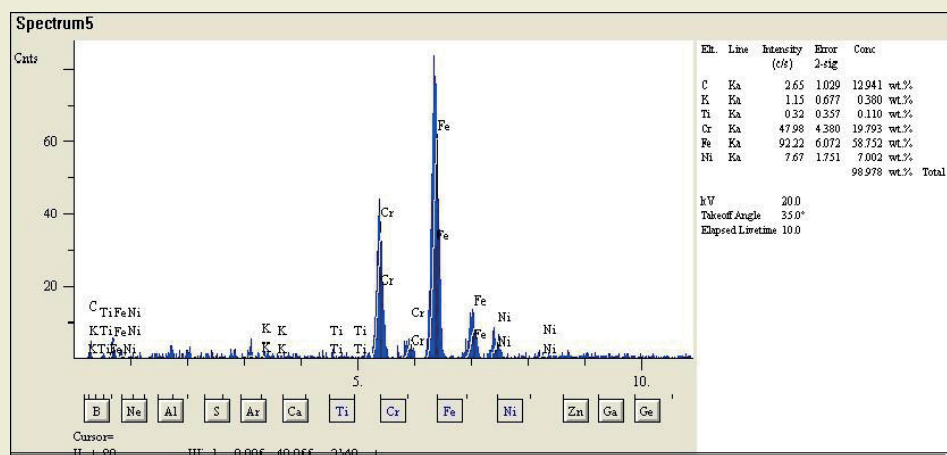
Figure 8. EDX spectrum of AISI304
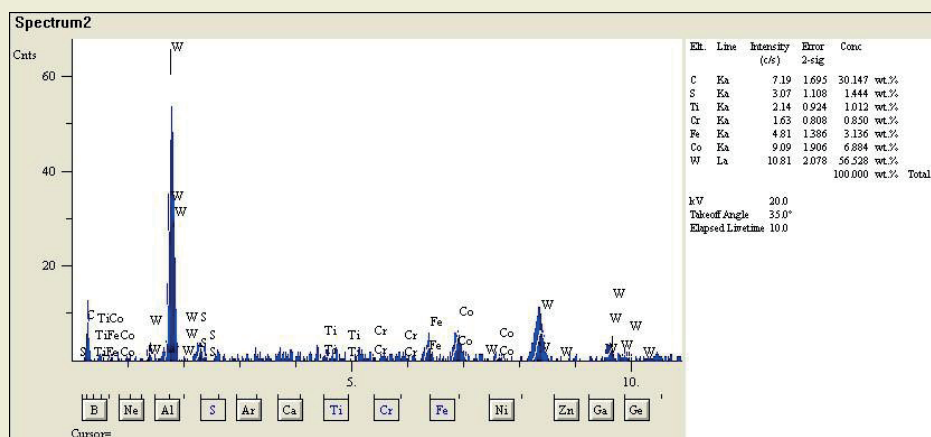

Figure 9. EDX spectrum of St37

were examined, it was observed that elements such as C, Cr, Fe and Ni were found in large amounts in the sample. Besides, the sample contains 58.752% Fe, 19.793% Cr, 12.941% C, 7.002% Ni, 0.380% K, 0.110% Ti.

The EDX elemental analysis results of the St37 sample in ▶**Figure 9** show the presence of C, S, Ti, Cr, Fe, Co, W elements in the sample. The EDX spectrum showed that the chemical composition of St37 consists of 56.528% W, 30.147% C, 6.884% Co, 3.136% Fe, 0.850% Cr, 1.012% Ti and 1.444% S elements.
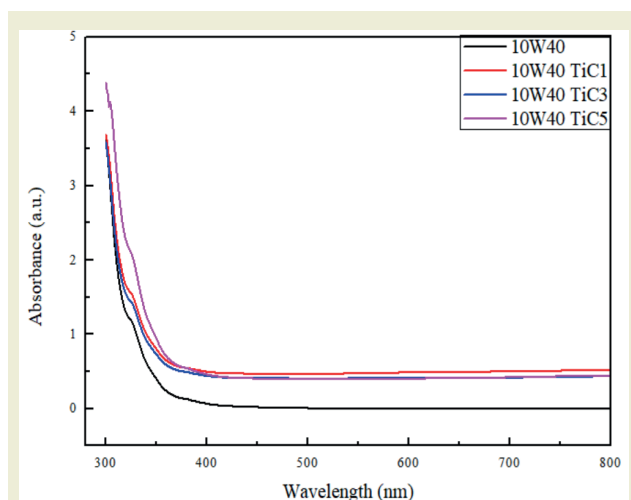
Figure 10. UV absorbance graphs of 10W40 oil including different amounts of TiC.

Another method used to characterize TiC nanoparticles dispersed in 10W40 oil is UV spectrometry. ▶**Figure 10** shows the UV absorption spectra of 10W40 oils containing 1, 3 and 5% TiC nanoparticles. The absorption of TiC nanoparticles was observed below 350 nm, similar to the literature [27]. With the increase in the TiC nanoparticle ratio in the oil, the absorption in the UV wavelength region also increased. The reason for the in-
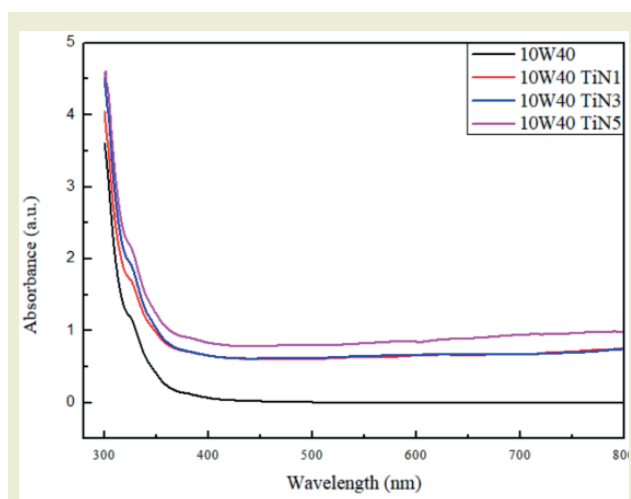
Figure 11. UV absorbance graphs of 10W40 oil including different amounts of TiN.

creased light extinction with the increased TiC amount may be due to both UV absorption of the nanoparticles and light scattering. The results showed that TiC particles are good UV absorbers.

UV–vis absorption spectra were used to characterize the deoxygenation of GO and the formation of TiN–rGO nanohybrids. ▶**Figure 11** shows the absorption spectra of 10W40 oil containing 1, 3 and 5 wt% TiN. In the UV spectrum, TiN showed a broad absorption band at between 300-350 nm, which was in agreement with the literature [28, 29]. As the TiN ratio in the oil increased, the peak shifted towards 350 nm.

4. Conclusions

This study systematically investigated the tribological performance of AISI304 and St37 steel specimens lubricated with 10W40 engine oil, both with and without TiC and TiN nanoparticle additives. The findings revealed that while the base oil alone effectively reduced friction and wear, the incorporation of nanoparticles led to varying outcomes depending on their type and concentration.

Specifically, the addition of TiC nanoparticles resulted in an increased coefficient of friction for both steel types, suggesting that at higher concentrations, TiC may induce abrasive effects rather than providing lubrication. Especially, TiN nanoparticles demonstrated a concentration-dependent behavior. At optimal concentrations, they improved wear resistance, particularly in St37 steel specimens. However, at higher concentrations, the benefits diminished, likely due to nanoparticle agglomeration and increased lubricant viscosity, which hindered effective lubrication.

Surface analyses further revealed that the wear mechanisms transitioned from predominantly adhesive in dry conditions to a combination of abrasive and adhesive when nanoparticle-enhanced lubricants were applied. Notably, TiC additives were more effective in mitigating adhesive wear in AISI304 specimens, while TiN additives provided smoother wear patterns in St37 specimens at optimal concentrations. These results indicated that nanoparticle additives can alter wear mechanisms based on their interaction with the base oil and the material surface.

Lubricants reinforced with TiN and TiC have modified the wear mechanism, effectively controlling both abrasive and adhesive wear. 3D microscope images clearly illustrate the wear mechanisms and support the contribution of reinforced lubricants to tribological performance. Weight loss data and friction coefficient results clearly demonstrate the surface protection effect provided by the additives.

As a result, in abrasive wear tests, it was observed that wear occurred in the form of deep channels and distinct

scratches in pure ST37 steel samples. When a lubricant without nanoparticle reinforcement was used, wear was more severe and uncontrolled. In adhesive wear tests, the non-reinforced lubricant could not completely prevent adhesive wear. For abrasive wear, the ST37 steel sample lubricated with 5% TiC-reinforced lubricant showed the lowest abrasive wear marks and the high hardness and chemical stability of the TiC particles prevented the formation of microcuts on the surface and minimized wear. Adhesive wear results showed that adhesive wear was almost completely suppressed in the 304 stainless steel sample lubricated with 5% TiC-reinforced lubricant. In summary, TiC particles acted as an effective barrier preventing metal transfer. 5% TiN and 5% TiC reinforcements minimized adhesive wear by reducing metal-to-metal contact.

Research ethics

Not applicable.

Author contributions

Conceptualization: [Kadir Gündoğan, Atike İnce Yardımcı, Cemile Eylem Urhan], Methodology: [Kadir Gündoğan, Atike İnce Yardımcı, Cemile Eylem Urhan], Formal Analysis: [Cemile Eylem Urhan, Kadir Gündoğan], Investigation: [Cemile Eylem Urhan, Atike İnce Yardımcı], Resources: [Kadir Gündoğan, Atike İnce Yardımcı], Data Curation: [Cemile Eylem Urhan, Kadir Gündoğan], Writing - Original Draft Preparation: [Cemile Eylem Urhan], Writing - Review & Editing: [Kadir Gündoğan, Atike İnce Yardımcı], Visualization: [Cemile Eylem Urhan, Kadir Gündoğan], Supervision: [Kadir Gündoğan, Atike İnce Yardımcı]

Competing interests

The author(s) state(s) no conflict of interest.

Data availability

The raw data can be obtained on request from the corresponding author.

Peer-review

Externally peer-reviewed.

Orcid

Cemile Eylem Urhan https://orcid.org/0000-0002-3836-9087
Kadir Gündoğan https://orcid.org/0000-0001-6742-3110
Atike İnce Yardımcı https://orcid.org/0000-0001-5482-4230

References

[1] Karabaş, O. ve Cesur İ. (2023). Farklı Motor Yağlarının Sürtünme ve Aşınma Özelliklerinin Karşılaştırmalı İncelenmesi, All Sciences Proceedings, 203.

[2] Wu, Y. Y., Tsui, W. C., ve Liu, T.C. (2007). Experimental analysis of tribological properties of lubricating oils with nanoparticle additives. Wear, 262(7–8), 819–825.

[3] Voevodin, A. A., & Zabinski, J. S. (2005). Nanocomposite and nanostructured tribological materials for space applications. Composites Science and Technology, 65(5), 741–748.

[4] Musil, J. (2000). Hard and superhard nanocomposite coatings. Surface and Coatings Technology, 125(1–3), 322–330.

[5] Rudnick, L. R. (2005). Synthetics, Mineral Oils, and Bio-Based Lubricants: Chemistry and Technology. CRS Press.

[6] Soydan, Y., & Ulukan, L. (2013). Temel Triboloji: Sürtünme, Aşınma, Yağlama Bilimi ve Teknolojisi. Tagem Kopisan Yayınevi.

[7] Bhushan, B. (2013). Introduction to Tribology. Wiley.

[8] Birleanu, C., Pustan, M., Cioaza, M., Molea, A., Popa, F., & Contiu, G. (2022). Effect of TiO$_2$ nanoparticles on the tribological properties of lubricating oil: An experimental investigation. Scientific Reports, 12, 5201.

[9] Choi, Y., Lee, C., Hwang, Y., Park, M., Lee, J., Choi, C., & Jung, M. (2009). Tribological behavior of copper nanoparticles as additives in oil. Current Applied Physics, 9(2), 124–127.

[10] Zhu, Y., Zhang, H., Li, N., & Jiang, Z. (2023). Friction and wear characteristics of Fe$_3$O$_4$ nano-additive lubricant in micro-rolling. Lubricants, 11(10), 434.

[11] Padgurskas, J., Rukuiza, R., Prosyčevas, I., & Kreivaitis, R. (2013). Tribological properties of lubricant additives of Fe, Cu and Co nanoparticles. Tribology International, 60, 224–232.

[12] Yu, R., Liu, J., & Zhou, Y. (2019). Experimental study on tribological property of MoS$_2$ nanoparticle in castor oil. Journal of Tribology, 141(10), 1.

[13] Wu, C., Li, S., Chen, Y., Yao, L., Li, X., & Ni, J. (2023). Tribological properties of chemical composite and physical mixture of ZnO and SiO$_2$ nanoparticles as grease additives. Applied Surface Science, 612, 155932.

[14] Ma, L., Ma, L., Lian, J., Wang, S., Ma, X., & Zhao, J. (2024). Tribological behavior and cold-rolling lubrication performance of water-based nanolubricants with varying concentrations of nano-TiO$_2$ additives. Lubricants, 12(11), 361.

[15] Martin, D. S. (2022). Tribological performance effect of SiO$_2$ and TiO$_2$ nanoparticles as lubricating oil additives (pp. 223–231).

[16] Liñeira del Río, J. M., Fernandes, C., & Seabra, J. H. O. (2024). Tribological improvement of low-viscosity nanolubricants: MoO$_3$, MoS$_2$, WS$_2$ and WC nanoparticles as additives. Lubricants.

[17] Borda, F. L. G., Ribeiro de Oliveira, S. J., Lazaro, L. M. S. M., & Leiróz, A. J. K. (2018). Experimental investigation of the tribological behavior of lubricants with additive containing copper nanoparticles. Tribo-

logy International, 117, 52–58.

[18] Jafarzadegan, M., Feng, A. H., Abdollah-zadeh, A., Saeid, T., Shen, J., & Assadi, H. (2012). Microstructural characterization in dissimilar friction stir welding between 304 stainless steel and St37 steel. Materials Characterization, 74, 29.

[19] Kocaman, R., & Ateş, S. (2023). Al6061 matrisli SiC, Al_2O_3 ve kömür cürufu tozu takviyeli hibrit kompozitlerin sertlik ve aşınma davranışlarının incelenmesi. International Journal of Engineering Research and Development, 15(2), 598–609.

[20] Çakır, Ö. F., & Erdem, M. (2025). Investigation of lattice geometries formed by metal powder additive manufacturing for energy absorption: A comparative study on Ti6Al4V, Inconel 718, and AISI 316L. Machines, 13(4), 316.

[21] Szabó, Á. I., Tóth, Á. D., Abdallah, H., & Hargitai, H. (2023). Experimental wear analysis of nano-sized titania particles as additives in automotive lubricants. Micro, 3(3), 715–727.

[22] Sadeghi, B., Cavaliere, P., Shabani, A., Pruncu, C. I., & Lamberti, L. (2023). Nano-scale wear: A critical review on its measuring methods and parameters affecting nano-tribology. Proceedings of the Institution of Mechanical Engineers, Part J: Journal of Engineering Tribology.

[23] Marinescu, I. D., Rowe, W. B., Dimitrov, B., & Inasaki, I. (2004). Tribology of Abrasive Machining Processes. William Andrew Publishing.

[24] Kavishwar, S., Bhaiswar, V., Kochhar, S., Fande, A., & Tandon, V.

(2024). State-of-the-art titanium carbide hard coatings: A comprehensive review of mechanical and tribological behaviour. Engineering Research Express, 6.

[25] Cozza, R. C. (2013). A study on friction coefficient and wear coefficient of coated systems submitted to micro-scale abrasion tests. Surface and Coatings Technology, 215, 224–233.

[26] İpekoğlu, G., Küçükömeroğlu, T. D., Sekban, M., & Çam, G. (2018). Sürtünme karıştırma kaynağıyla birleştirilen St37/St52 levhaların mikroyapı karakterizasyonu ve mekanik özellikleri. Dokuz Eylül Üniversitesi Mühendislik Fakültesi Fen ve Mühendislik Dergisi, 20, 471–480.

[27] Mallakpour, S., & Barati, A. (2011). Efficient preparation of hybrid nanocomposite coatings based on poly(vinyl alcohol) and silane coupling agent modified TiO_2 nanoparticles. Progress in Organic Coatings, 71(4), 391–398.

[28] Hering, N., Schreiber, K., Riedel, R., Lichtenberg, O., & Woltersdorf, J. (2001). Physical deposition of carbon doped titanium nitride film by DC magnetron sputtering for metallic implant coating use. Applied Organometallic Chemistry, 15(11), 879–886.

[29] Pareek, S., & Quamara, J. K. (2018). Dielectric and optical properties of graphitic carbon nitride–titanium dioxide nanocomposite with enhanced charge separation. Journal of Materials Science, 53, 604–612.

Unravelling quadcopter frame dynamics: A study on vibration analysis and harmonic response

Edip Öztürk[1*] iD

[1]Gaziantep University, Aeronautics and Aerospace, Aeronautics and Aerospace Engineering, 27310, Gaziantep, Türkiye

Abstract: Quadcopters are widely used rotorcraft members of the UAV family. Since they have four motors and four propellers, they are exposed to dynamic loads and vibratory motion. This study presents vibration analysis of a well-known F450 quadcopter frame. Modal analysis was performed to identify the natural frequencies and mode shapes, followed by harmonic response analysis to observe the dynamic behaviour under a periodic force. Harmonic response analysis frequency range covered all critical frequencies obtained by modal analysis. Two additional axes in addition to hovering direction were considered in order to simulate the propeller imbalance case. Numerical solution of analysis was performed by finite element method. Critical frequencies were examined in terms of motor angular velocities and compared with real life motor rpm values. Harmonic response analysis for Y-axis displacements revealed significant peaks near 222 Hz and 410 Hz, corresponding to motor speeds of approximately 12,000−24,000 RPM. For an unbalanced propeller simulated along the X-axis, significant response peaks were observed near 277 Hz and 620 Hz, corresponding to motor speeds of approximately 15,000−360,000 RPM. Similarly, for the Z-axis, peaks were observed near 200 Hz and 420 Hz, also corresponding to motor speeds of approximately 15,000−360,000 RPM. These results indicate potential risks of structural resonance during quadcopter operation, particularly under high throttle or unbalanced loading conditions.

Keywords: modal analysis; quadcopter vibration analysis; harmonic response; structural vibration

1. Introduction

Unmanned aerial vehicles, especially quadcopters, are susceptible to structural vibrations that can compromise flight stability and sensor performance. Analysing the dynamic behaviour of the frame components is critical in enhancing durability and performance. Faraz Ahmad et al. investigate the vibration characteristics of a quadcopter propeller. They design the 3D model of the propeller in Creo 2.0 and analyse it using Ansys. They compare the vibration behaviour of different materials (G-10, aluminium and CFRP) and determine the first 6 natural frequencies and mode shapes by modal analysis. As a result, they find that CFRP material exhibits higher frequency values and is more suitable for heavy loadings[1]. Bhandari et al. deal with modelling and vibration analysis of the quadcopter body frame by changing boundary conditions. Thus, the failure frequency range can be controlled. Simulation results help researchers to design quadcopter frames for heavy-duty applications[2].

Chen et al. study the structural vibration problems of multi-rotor drones in order to solve the structural damage problem of large multi-rotor manned drones. From this study, researchers find that the main vibrations of a large multi-rotor manned drone arm are low-frequency vibrations below 200Hz, and the vibrations mainly produce torsional and bending modes[3]. Kuantama et al. performed vibration analysis using the finite element method. In this analysis, it was investigated that the existence of rotational speeds in each propeller flow field will significantly affect the thrust efficiency, which may cause flight instability or body frame vibration[4]. Lostaunau et al. perform an analysis of the measured vibration of a quadcopter during hovering under varying propeller speeds and track compliance. To collect data, four accelerometers are mounted on the drone's arm. The collected data are analysed using time domain plots and spectrograms obtained from the Gabor transform[5]. Kalay and Özkul[6] investigated the role of vibrations in Unmanned Aerial Vehicles (UAVs), efficiency measurement techniques, and their effects on

performance; using theoretical and experimental methods such as frequency analysis, mode analysis, and finite element analysis, they understood the vibration dynamics of UAVs and achieved higher performance, longer operational life, and increased precision. Lalem et al.[7] investigated AI and vibration signal processing for anomaly detection in quadcopter systems; they demonstrated the effectiveness of the combination of AI and the Internet of Things (IoT) to improve fault detection and problem diagnosis in UAVs by obtaining 97.78% accuracy with Random Forest and Support Vector Machine (SVM) classifiers by extracting features from accelerometer data. Salem et al.[8] investigated the vibration analysis using multilayer perceptron artificial neural networks (MLP-ANN) to detect rotor imbalance in quadrotor UAVs, trained the MLP-ANN model by extracting time, frequency, and time-frequency domain features from accelerometer data, and detected rotor imbalance with a high accuracy of up to 99.1%.In this study, Geronel et al.[9] investigated the vibration analysis of a load connected to a quadrotor-type UAV with a shape memory alloy (SMA) spring; by analysing the natural frequencies and damping properties of the load, they evaluated the vibration isolation and adaptive damping potential of SMA springs. When the literature is examined, it is easily seen that there are not many studies on quadcopter vibration analysis. In this study, the solid model of the well-known F450 coded (▶**Figure 1**) quadcopter frame is prepared, and ABS material is assigned to the prepared model.
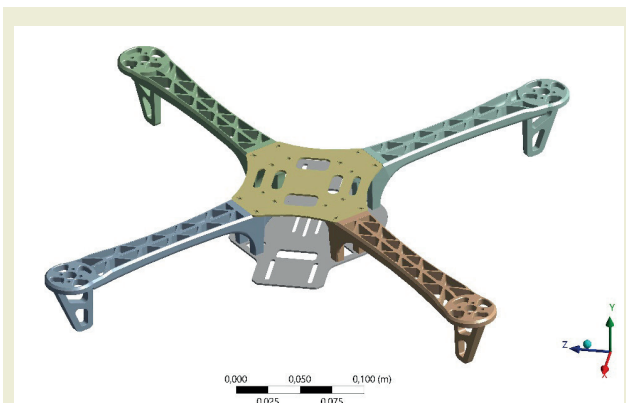

Figure 1. F450 quadcopter frame

The frame has a cross length of 450 mm and an arm length of 210 mm. ABS material has a density of 1050 kg per cubic meter volume, an elastic modulus of 2.4 GPa and a shear modulus of 0.8 GPa. Boundary conditions are determined for the model and vibration and harmonic response analysis are performed. As a result of these analyses, the critical natural frequencies and harmonic responses for the frame are determined. At the end of the study, the mode shapes related to natural frequencies and the critical frequencies obtained as a result of the harmonic response are interpreted. In addition to these, the connection between the harmonic response critical frequencies and the motor speed relations is also mentioned.

2. Materials and Methods

2.1. Modal Analysis

Modal analysis examines the dynamic properties of a structure or system in the frequency domain. Its main purpose is to determine the natural vibration frequencies of the structure and the mode shapes corresponding to these frequencies. This analysis is critical for understanding how a system or a structure will respond to external forces or vibratory motions.

If one of the natural frequencies of a structure matches the frequency of the applied external force, resonance occurs. This can lead to excessive vibrations and structural damage. Modal analysis identifies these potential resonant frequencies, allowing design changes to be made.

$$[M]\ddot{u}(t) + [K]u(t) = 0 \tag{1}$$

Modal analysis solves the mathematical free vibration equation (Equation 1). and solving the eigenvalue problem Equation 2 gives natural frequencies and mode shapes corresponding to natural frequencies[10].

$$([K] - \omega_n^2[M])\phi_n = 0 \tag{2}$$

ANSYS uses the finite element method in order to discretize geometry into smaller elements. This discretization enables a numerical solution of the structural dynamic equations[11].

Modal analysis in ANSYS begins with preparing the geometry of the quadcopter frame. Since the quadcopter frame is symmetric, a single arm of the frame is sufficient enough to perform modal analysis. Single-arm geometry is isolated, and in the modal analysis section, boundary conditions are applied. Fixed support is assigned in ▶**Figure 2** in order to model connection single arm to middle body plates.
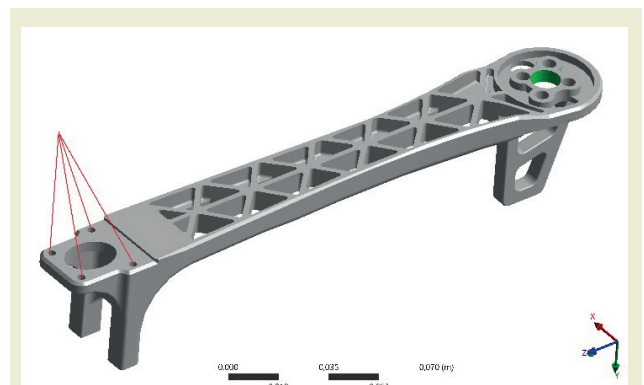

Figure 2. Fixed support locations

The main purpose of modal analysis is to obtain the natural frequencies of single arm. Therefore, external force

is not applied. A total of 38135 elements and 68200 nodes are generated at the end of the meshing operation (▶Figure 3). Skewness is selected as a mesh quality indicator. Average value of skewness is obtained as 0.42 and this value is sufficient enough to perform modal analysis.
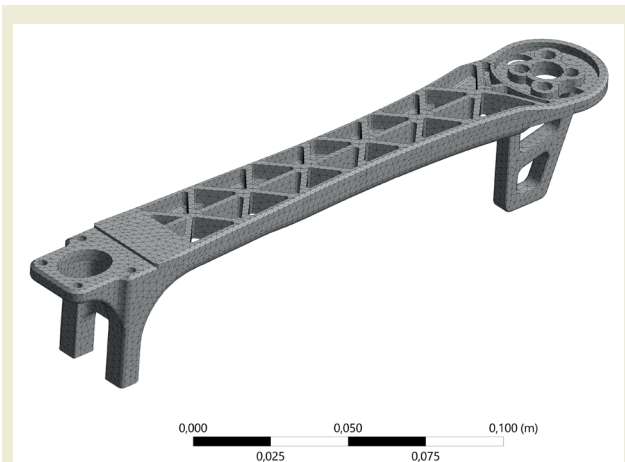
Figure 3. Mesh view

First six natural frequencies in ▶Table 1 and mode shapes corresponding to natural frequencies are obtained.

Table 1. Modal analysis results

Mode	Frequency (Hz)
1	47.018
2	135.06
3	237.77
4	270.09
5	547.44
6	761.69

In this mode, the structure essentially makes an upward-downward bending movement (▶Figure 4). This mode represents the first frequency at which vertical vibrations from engines or external factors during flight can cause resonance. Entering this frequency range, especially during take-off or landing, can lead to vibration growth.
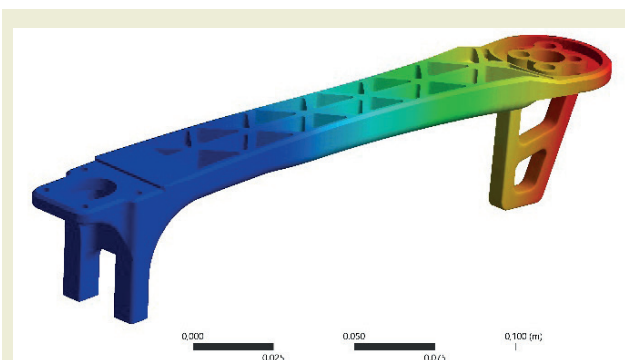

Figure 4. First mode shape

In the second mode, the structure exhibits bending behaviour in the horizontal plane (▶Figure 5). This mode represents the natural frequency that can occur in side-slip manoeuvres. It is important to understand the lateral vibrations of the body.
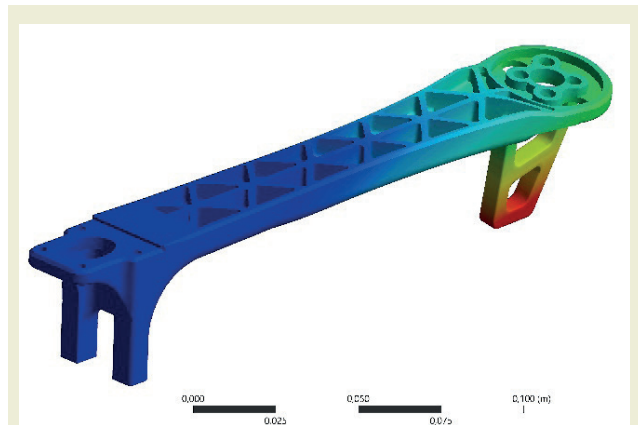

Figure 5. Second mode shape

In this mode the structure exhibits transverse torsional motion (▶Figure 6). Torsional modes can often be triggered by propeller imbalance or engine vibrations. Therefore, engine speeds close to the frequency of the third mode should be avoided.
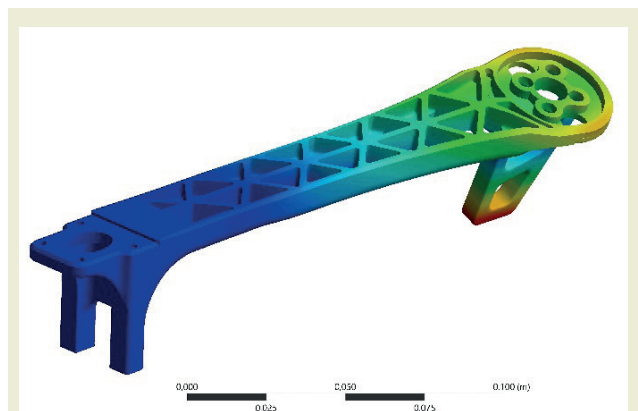

Figure 6. Third mode shape

This mode acts as a combination of the previous bending modes, with a combined bending tendency in different planes (▶Figure 7). When engines operate at high speeds, these modes can also be excited, creating simultaneous vibrations in various axes of the structure.

In the fifth mode, there is more pronounced torsion and asymmetric bending (▶Figure 8).

In this mode, a more complex vibration pattern is observed in the upper part of the structure and in the propeller mounting area (▶Figure 9).
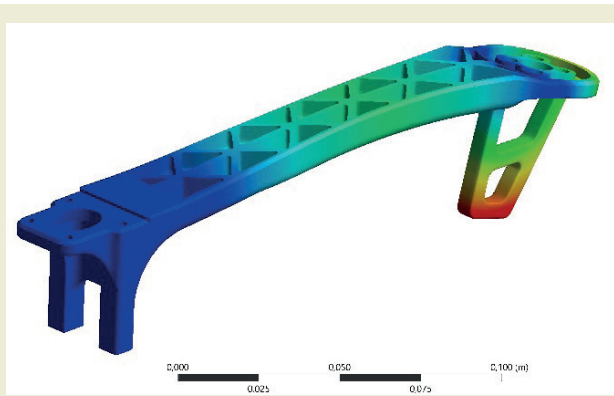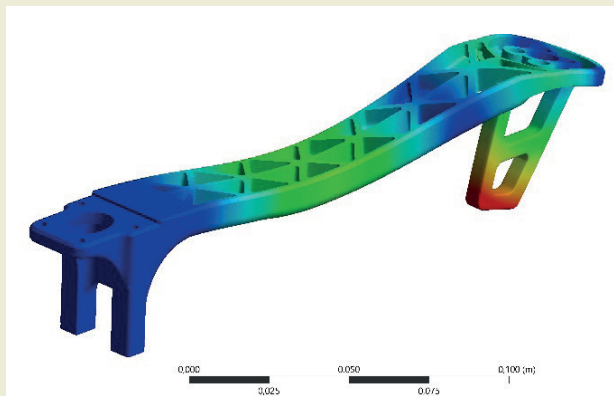
Figure 7. Fourth mode shape

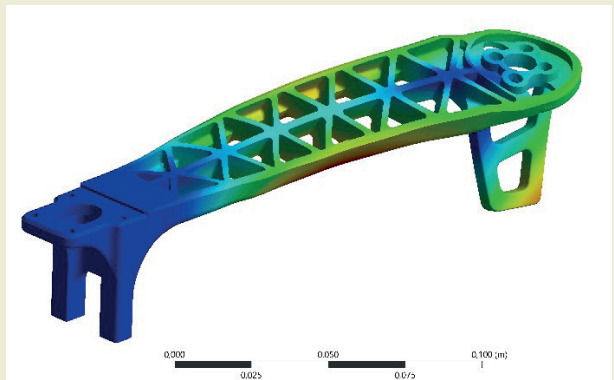**Figure 8.** Fifth mode shape

Figure 9. Sixth mode shape

2.2. Harmonic Response Analysis

Harmonic response analysis is a type of analysis used to determine the steady-state dynamic response caused by sinusoidally varying loads applied to a structure or system. This analysis is critical for understanding the structure's forced vibration behaviour at specific frequencies, determining resonant frequencies and amplitudes, and assessing structural integrity. Harmonic response analysis for a forced vibration system is modelled as in Equation 3[12].

$$[M]\ddot{u}(t) + [C]\dot{u}(t) + [K]u(t) = F(t) \tag{3}$$

Force is modelled as a constant amplitude sine wave

(Equation 4).

$$F(t) = F_0 \sin(\omega t) \tag{4}$$

System response under constant amplitude harmonic force is given in Equation 5.

$$u(t) = U\sin(\omega t + \phi) \tag{5}$$

The response amplitude is calculated using the expression in Equation 6.

$$|U| = |([K] - \omega^2[M] + i\omega[C])^{-1}F_0| \tag{6}$$

Since the frequencies to which the system responds are important rather than the magnitude of the response given by the system in the harmonic response analysis, a force of 1 N magnitude is applied as in ▶**Figure 10**. In harmonic response analysis, the 1 N load is a standardization tool to determine the frequency-dependent behaviour of the system against a unit load. This allows the results obtained to be easily scaled to other loading cases and provides a clearer understanding of the dynamic properties of the system, such as resonance, damping, and amplitude. The force applied in this direction will be used to obtain the vibration behaviours that the quadcopter will be exposed to during take-off and landing.
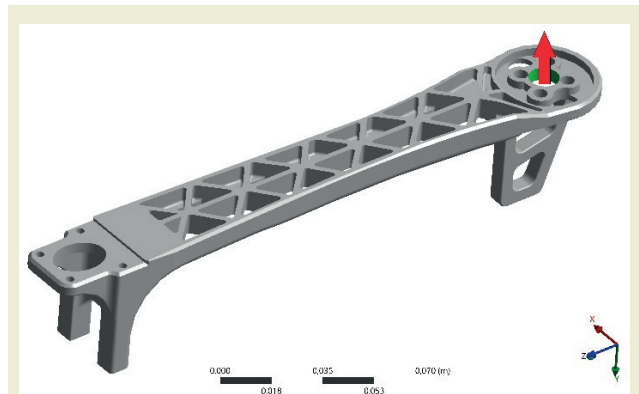

Figure 10. Force applied in the Y axis

The frequency range to be scanned in the harmonic response analysis should be selected to include the frequencies obtained as a result of the modal analysis. Therefore, the frequency range is assigned as between 20 Hz and 800 Hz. In order to determine the vibration response of the propeller due to the inhomogeneous mass distribution caused by production and the unexpected forces that will occur in the propeller imbalance situation, harmonic response analysis is performed again by applying force in the Z direction shown in ▶**Figure 11**.

In a similar way harmonic response analysis is per-

formed again by applying force in the Z direction shown in ▶**Figure 12**.
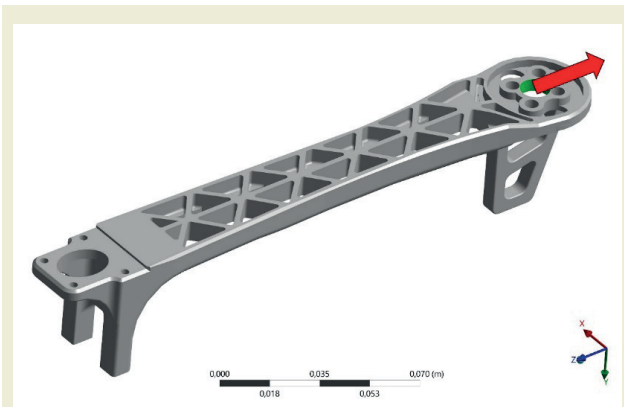

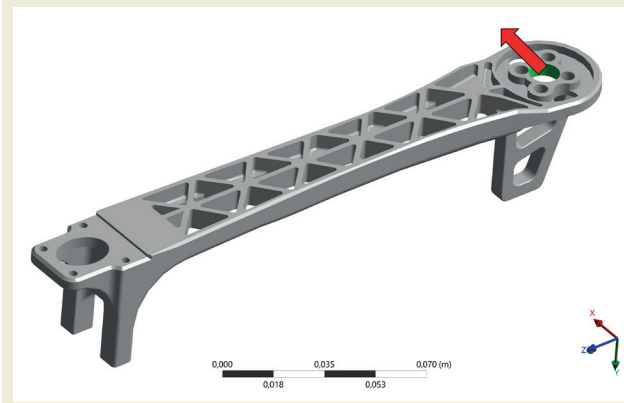**Figure 11.** Force applied in the Z axis

Figure 12. Force applied in the X axis.

3. Results and Discussions

The modal analysis revealed the first six natural frequencies of the isolated F450 arm made of ABS material. These modes include bending, torsional, and coupled vibration shapes, with the first mode appearing at approximately 47 Hz and the sixth mode at 761 Hz. The distribution and symmetry of mode shapes are consistent with cantilever-like boundary conditions and suggest that excitation in certain frequency bands can lead to dynamic amplification. The harmonic response analysis focused on Y-axis displacements, which are critical for vertical stability in flight (▶**Figure 13**). Significant response peaks were observed at frequencies near 222 Hz and 410 Hz. These correspond to motor speeds of approximately 12,000–24,000 RPM. If the quadcopter operates in this regime, resonance phenomena could amplify structural vibrations, potentially affecting flight control systems or inducing fatigue.

An unbalanced propeller scenario was simulated along the X-axis to investigate lateral vibrational effects. Significant response peaks were observed at frequencies near 277 Hz and 620 Hz (▶**Figure 14**). These correspond to motor speeds of approximately 15,000–360,000 RPM. This result indicates that lateral vibrations may still influence the camera payload or sensor accuracy during high-speed manoeuvres.

In a similar way, an unbalanced propeller scenario was simulated along the Z-axis to investigate vibrational effects. Significant response peaks were observed at frequencies near 200 Hz and 420 Hz (▶**Figure 15**). These correspond to motor speeds of approximately 15,000–
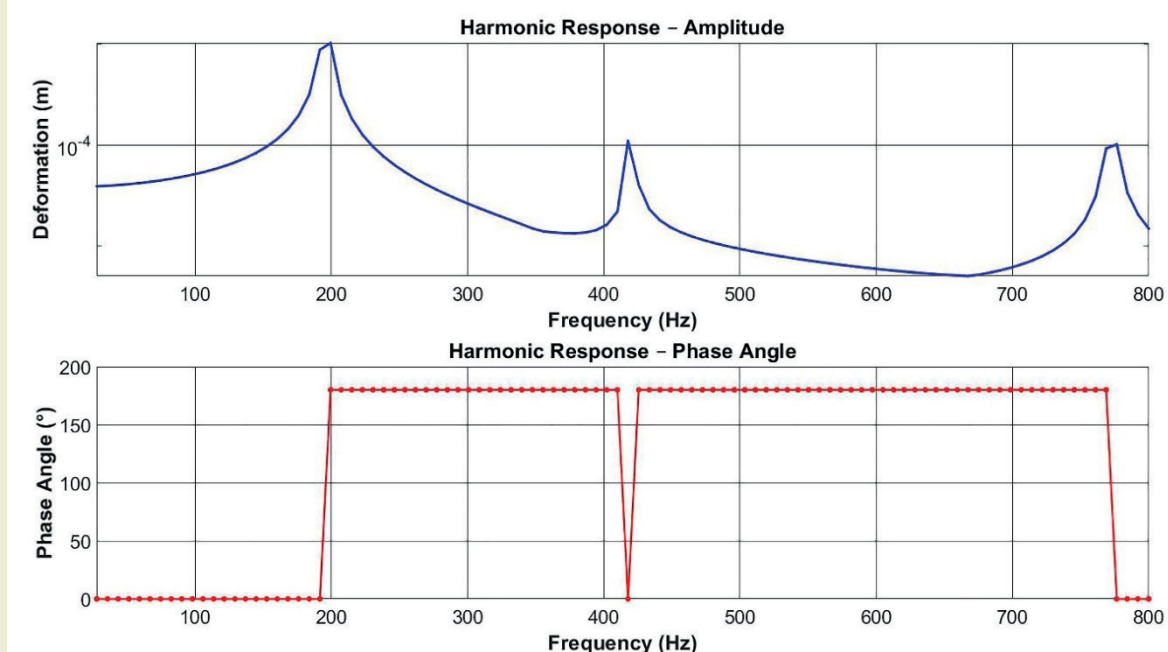

Figure 13. Harmonic response for Y direction

360,000 RPM.

It is observed that the y data results and the z data results are very close except for the phase angle. The phase angle at the peaks of the y-axis is 0 degrees, while the phase angle on the z-axis is 180 degrees. The phase angle is the angle between the applied force and the deformation.

4. Conclusions

This study conducted a detailed modal and harmonic response analysis of a single ABS arm of the F450 quadcopter frame using ANSYS. Modal results revealed key frequencies susceptible to resonance, while harmonic analysis showed significant amplitude peaks in the Y-direction within common motor speed ranges. These results indicate potential risks of structural resonance
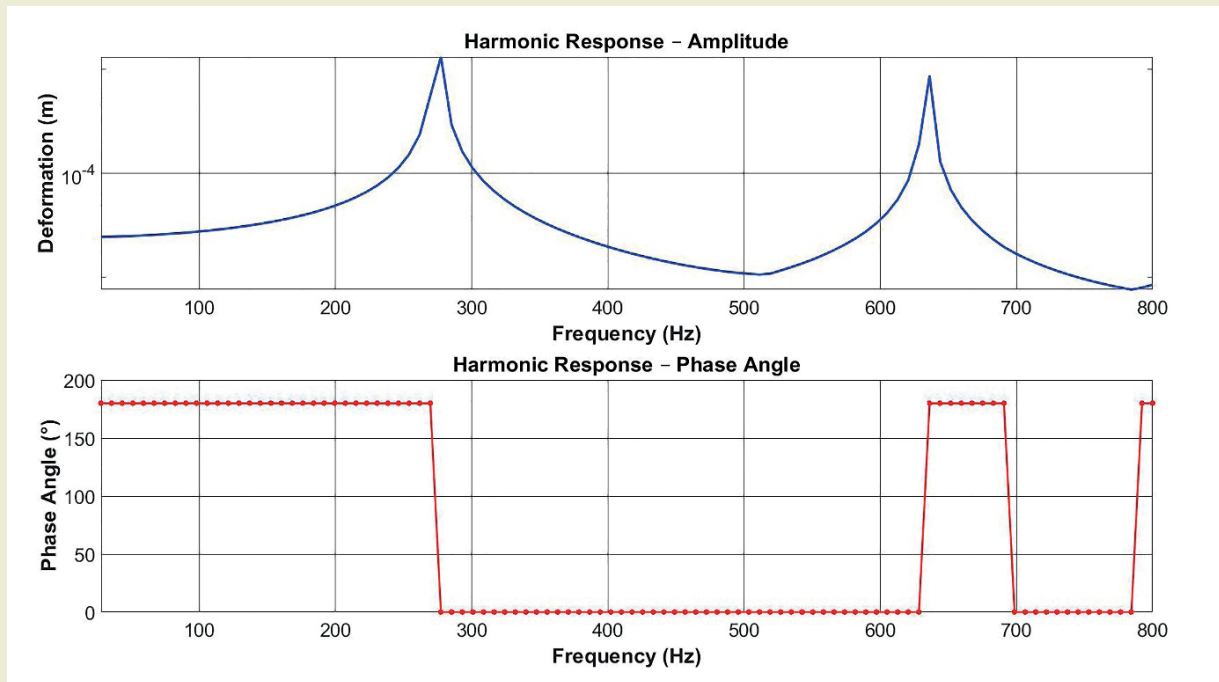

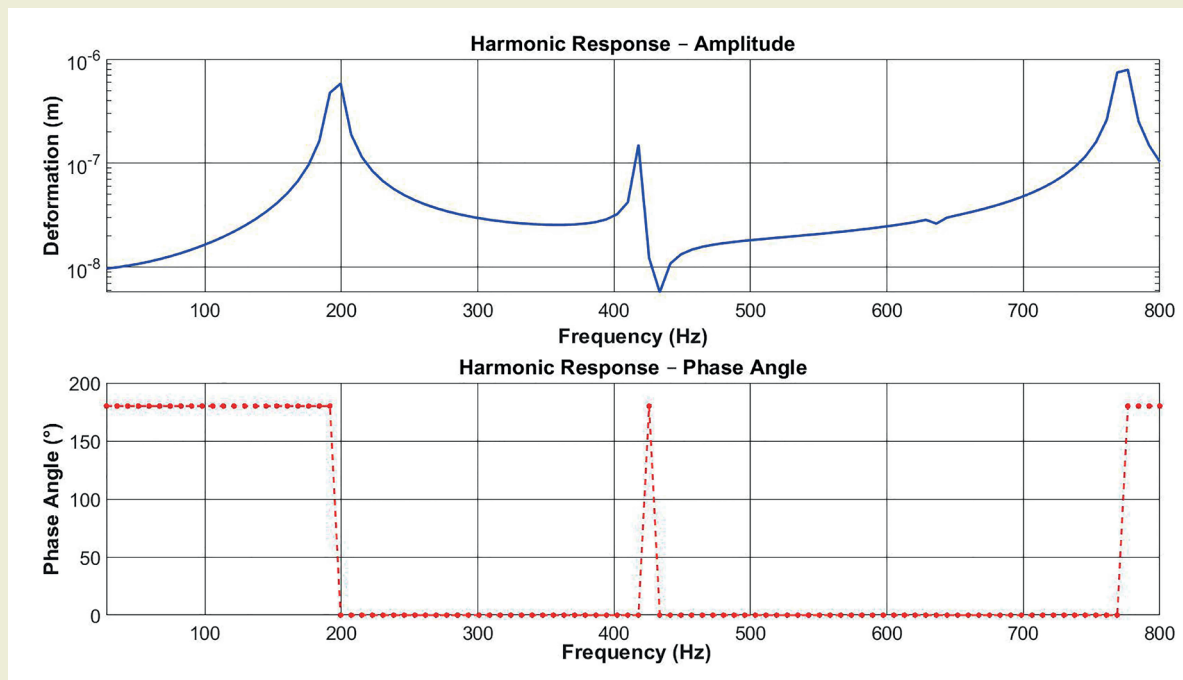**Figure 14.** Harmonic response for X direction

Figure 15. Harmonic response for Z direction

during operation, especially under high throttle or unbalanced loading.

Future studies may explore full-frame analysis, incorporate motor and propeller coupling effects, and validate results with experimental modal testing. Optimizing the frame geometry or integrating vibration-absorbing materials could further improve performance and durability.

Author contributions

The author solely conducted all stages of this research.

Orcid

Edip Öztürk https://orcid.org/0000-0002-1816-1553

References

[1] Ahmad, F., et al. (2019). Modeling and mechanical vibration characteristics analysis of a quadcopter propeller using FEA. IOP Conference Series: Materials Science and Engineering. IOP Publishing.

[2] Bhandari, A., et al. (2019). Design and vibration characteristics analysis of quadcopter body frame. International Journal of Applied Engineering Research, 14(9), 66–70.

[3] Chen, K., et al. (2023). An investigation on the structural vibrations of multi-rotor passenger drones. International Journal of Micro Air Vehicles, 15, 17568293231199097.

[4] Kuantama, E., Craciun, D., & Tarca, R. (2016). Quadcopter body frame model and analysis. Annals of the University of Oradea, 71–74.

[5] Lostaunau, O., et al. (2024). Analysis of quadcopter body frame vibration during hovering flight with variable rotor speeds. In 2024 8th International Symposium on Instrumentation Systems, Circuits and Transducers (INSCIT). IEEE.

[6] Kalay, E., & Özkul, İ. (2024). İnsansız hava araçlarında titreşimlerin rolü, verimlilik ölçüm teknikleri ve performans etkileri. Turkey Unmanned Aerial Vehicle Journal / Türkiye İnsansız Hava Araçları Dergisi, 6(2).

[7] Lalem, M. S. E. I., Ouadah, M., & Touhami, O. (2024). Anomaly detection in quadcopter systems using AI and vibration signal processing.

[8] Abdullah Salem, B. T. S., et al. (2025). Vibration analysis using multi-layer perceptron neural networks for rotor imbalance detection in quadrotor UAV. Drones, 9(2), 102.

[9] Geronel, R. S., Bueno, D., & Botez, R. M. (2022). Vibration analysis of a payload connected to quadrotor-type UAV by SMA spring. In AIAA SciTech 2022 Forum.

[10] Rao, S. S., & Yap, F. F. (1995). Mechanical vibrations (Vol. 4). Addison-Wesley.

[11] Bhavikatti, S. (2005). Finite element analysis. New Age International.

[12] Rao, S. S. (2019). Vibration of continuous systems. John Wiley & Sons.

Microstructural investigation of geopolymer composites obtained from recyclable waste materials

Hülya Temizer[1]* (ID), Özlem Çavdar[1] (ID)

[1]Gümüşhane Üniversitesi, İnşaat Mühendisliği Bölümü, 29000, Gümüşhane, Türkiye

Abstract: Today, researchers are exploring materials that could replace cement and provide solutions for utilizing waste products. In this study, a binder was formulated using 85% blast furnace slag and 15% fly ash. The marble powder and strontium as mineral wastes were incorporated as partial replacements to blast furnace slag at ratios of 5% to create geopolymer mortars. Also, titanium dioxide was added at a rate of 1%. The influence of these additives on the flexural and compressive strength of the mortars was assessed. In addition, SEM/EDX analysis was performed to examine the microstructural effects of the additives. The results showed that titanium dioxide achieved the highest compressive strength, recorded at 65.7 MPa. The SEM/EDX analysis further indicated that the samples displayed a homogeneous internal structure, suggesting a strong bond among the components within the matrix.

Keywords: Geopolymer; Blast furnace slag; Fly ash; Strontium; SEM/EDX

1. Introduction

The development and use of low-carbon or carbon-free products, as well as waste recycling, are particularly important in the construction industry. [1]. Given the environmental impacts, high production costs, and substantial energy consumption associated with Portland cement, the importance of alternative binders has become even more pronounced. In the current landscape of skyrocketing fuel costs, and the limited availability of fossil fuel resources (such as coal and natural gas), the construction industry has grown increasingly reliant on these sectors. While Portland cement remains the traditional and widely utilized binder in construction, its usage has come under scrutiny over the past decade, particularly due to its environmental ramifications. Recently, the production and application of binders known as geopolymer concrete and mortar have gained prominence [2]. Geopolymer applications have attracted interest for various reasons, including cost reductions through the use of waste materials during production, a contribution to lower CO_2 emissions, and performance characteristics comparable to those of Portland cement. However, it is essential that geopolymer binders used in this field fulfill the necessary performance expectations regarding mechanical properties, along with their

environmental benefits. Consequently, researchers have shown a keen interest in examining the chemical and physical properties of geopolymer concretes produced through various methods, alongside conducting strength and durability tests [3].

Naskar and Chakraborty [4] developed geopolymer concrete using fly ash with low calcium content, due to the negative environmental impacts associated with traditional Portland cement. In their study, they incorporated mixtures containing 0.75%, 3%, and 6% nano-silica, 0.02% carbon nanotubes, and 1% titanium dioxide as substitutes for fly ash in the concrete production process. The results of the compressive strength tests indicated that the additions of nano-silica and carbon nanotubes did not significantly enhance the compressive strength at 7 and 28 days. However, the inclusion of titanium dioxide at a concentration of 1% improved the compressive strength by up to 33% at 7 days, and 47% at 28 days. In a study by Nergis et al. [5], a coal ash-based geopolymer was synthesized using mine wastes activated with phosphoric acid. Three types of aluminosilicate sources were employed either as standalone raw materials or combined to create five different types of geopolymers activated with H_3PO_4 in a 1:1 weight ratio. The thermal behavior of the geopoly-

mers activated with H_3PO_4 was found to resemble that of those activated with a mixture of NaOH and Na_2SiO_3 within the temperature range of 20-300 °C. Furthermore, within the temperature range of 400-600 °C, the geopolymers containing mining waste exhibited exothermic reactions, while those without the addition of mining waste did not show significant phase changes. In a study by Chithambaram and Kumar [6], the impact of granulated blast furnace slag (GBFS) on the partial replacement of fly ash in geopolymer mortar production was examined. The geopolymer mortars were created using a combination of sodium hydroxide (NaOH) and sodium silicate as the alkaline activator solutions. The production process involved varying the concentrations of NaOH at 8M, 10M, 12M, and 14M, along with replacing fly ash with GBFS at different percentages: 0%, 10%, 20%, 30%, and 40%. Additionally, the study established thermal curing intervals ranging from 600°C to 1000°C for the geopolymer mortar, which utilized 100% fly ash as the sole binder. Upon reviewing the results of the geopolymer mortar made with 100% fly ash, cured at 90°C using a 12M NaOH concentration, researchers found a maximum compressive strength of 51.55 N/mm². In a study where fly ash was added to ground blast furnace slag, high calcium fly ash with a particle size of 21.26 μm, blends containing fly ash in proportions were compared with samples containing 100% ground blast furnace slag. It was reported that workability performances such as plastic viscosity, segregation resistance, and flowability increased especially in mixtures containing 40%, 50%, and 60% fly ash [7].

A group of researchers [8] explored the utilization of fly ash (FA) and granulated blast furnace slag (GBFS), both aluminosilicate by-products, in the development of geopolymer cement. They conducted a comparison of six geopolymer cement mortars with varying ratios of FA to GBFS against ordinary portland cement (OPC), and magnesium potassium phosphate cement (MPPC) mortars. The study evaluated several aspects, including workability, setting time, strength development, volume stability, and chloride permeability. The results revealed that geopolymer mortars containing a high proportion of GBFS demonstrated rapid setting and significant early strength, though they exhibited some issues with volume stability. Given these findings, it was suggested that GBFS -blended mortars could serve as a more cost-effective alternative to the higher-priced MPPC mortar. In the study conducted by Hager et al. [9], the researchers examined the impact of high temperatures on the mechanical properties and microstructure of geopolymer mortars. The investigation included blends of fly ash with blast furnace slag at four different ratios. The results showed that the mixtures without slag exhibited superior performance, particularly at elevated temperatures. Flexural strengths increased up to 200 °C but demonstrated a nearly linear decline from that point to 600 °C. This decrease was attributed to dehydration processes that occur as the temperature rises. Such dehydration results in thermal shrinkage around the aggregates, which leads to cracking. At 573 °C, the

expansion of quartz sand and the transformation between β-quartz and α-quartz formations resulted in material deformation. Notably, an increase in compressive strengths was observed after reaching 800 °C.

In a study conducted by Başpınar and Kurtuluş [10], fly ash was utilized as the primary material for a geopolymer. Hydrogen peroxide was employed as a foaming agent. Various sample series were prepared by varying the mixing ratios of fly ash and blast furnace slag. The physical and mechanical properties of these samples were tested, mineralogical and microstructural characterizations were conducted using X-ray diffraction (XRD) and scanning electron microscopy (SEM) techniques. It was found that an increased addition of blast furnace slag resulted in crack formation. However, incorporating coarse aggregate significantly reduced drying shrinkage, and helped prevent crack formation. Furthermore, it was observed that adding coarse aggregate contributed to a decrease in the density of the geopolymer foam concrete blocks. The conversion of industrial by-products into geopolymer concrete is crucial for developing environmentally sustainable structural components. In a study conducted by Raj et al. [11], dolomite and ground granulated blast furnace slag were utilized as aluminosilicate materials, while NaOH and Na_2SiO_3 solutions served as alkali activators. The study highlighted that numerous parameters influence the production of geopolymer concrete, necessitating extensive experimentation to identify the optimal sample. To address this, the Taguchi statistical method was employed to determine the effective parameters and optimal samples in geopolymer concrete production. Various parameters, such as mixture ratio, molarity, and activator ratio, were compared within the L9 test series. Upon examining results related to workability, compressive strength, and splitting tensile strength of the geopolymer samples, it was found that the binder ratio was the most significant factor. Additionally, SEM microstructure analyses revealed that these structures were more compact. In geopolymer concrete, the use of source materials with low calcium content, such as metakaolin and class F fly ash, results in the formation of sodium aluminosilicate hydrate (N-A-S-H) products. Conversely, when materials with high calcium content, like blast furnace slag and class C-fly ash, are utilized, the reaction produces calcium aluminosilicate hydrate (C-A-S-H) gel products [12]. In a study conducted by Chokkalingam et al. [13], waste ceramic powder and granulated blast furnace slag were used as geopolymer binders to examine the effects of various parameters, including binder content, ratio of main binders, ratios of alkali activator solutions, and molarity. The findings revealed that using ceramic powder as a binder on its own had a minimal impact, but when combined with slag, there were significant improvements in performance. The researchers developed an L16 orthogonal array that included five factors and four levels. The analysis of variance (ANOVA) results highlighted that the ratio of alkaline activator to binder and the percentage of slag were the most influential factors affecting the compres-

sive strengths after 28 days. In contrast, the binder content and molarity had the least effect. Microstructure analyses indicated nearly equal ratios of Ca/Si and Si/Al, suggesting the presence of similar calcium hydrates and silicate phases. This was believed to contribute to the formation of calcium silicate hydrate (C-S-H) and calcium aluminosilicate hydrate (C-A-S-H) gels, which enhance the microstructure of the geopolymer concrete. It was noted that a higher Na/Si ratio compared to Ca/Si in the structure may lead to the predominance of N-A-S-H gel over C-A-S-H gels, a characteristic influenced by the presence of marble dust.

In recent years, many studies have focused on the development of geopolymer composites using industrial by-products such as fly ash and blast furnace slag. However, the incorporation of regionally sourced, underutilized mineral wastes into geopolymer systems remains limited. This study focused on incorporating marble powder and strontium-bearing mineral waste from the Sivas region of Türkiye into geopolymer mortar. The binder for the mortar is composed of 85% blast furnace slag and 15% fly ash. Moreover, titanium dioxide was utilized as an additive. The simultaneous evaluation of these three additives under identical curing and testing conditions represents a novel comparative approach in the literature. Furthermore, the inclusion of long-term curing results (up to 90 days), supported by microstructural analysis via SEM/EDX, offers valuable insight into the time-dependent behavior of these composites. Notably, the finding that a low dosage (1%) of TiO_2 can significantly enhance early compressive strength (up to 65.7 MPa) contributes to the optimization of performance with minimal additive use. The study thus fills a crucial gap by proposing a sustainable, high-performance geopolymer system utilizing local industrial wastes with potential for practical application in earthquake-prone regions.

2. Materials and Methods

In the study, geopolymer mortars were created using 85% blast furnace slag and 15% fly ash (85BFS15FA), activated with a 10M NaOH solution at 75°C. Three different additives were incorporated into the mortar mixtures by replacing portions of the blast furnace slag. Due to the exothermic reaction of sodium hydroxide when it comes into contact with water, the solution was prepared one day in advance in glass containers to ensure it was ready for use. In addition to sodium hydroxide, sodium silicate was used as another alkaline activator. The two were combined to form a ready solution, with 70 grams of sodium hydroxide and 180 grams of sodium silicate, totaling 250 grams of alkali activator. The ratio of sodium silicate to sodium hydroxide was consistently maintained at 2.5 across all mixtures. Through preliminary tests, it was determined that a constant water ratio of 50 grams would be used in the experiments. Additionally, river sand sourced from Sivas Kızılırmak was kept constant at 1350 grams for all mixtures. The prepared samples were produced using a Hobart mixer in accordance with the TS EN 196-1 standard. They were poured into prismatic molds with dimensions of 40x40x160 mm and heat-cured in an oven for 24 hours. After that, the samples were allowed to cure at ambient temperature and kept in airtight conditions for periods of 7, 28, 56, and 90 days, leading up to the experiments.

Blast furnace slag is a by-product generated during the production of iron in blast furnaces at iron and steel manufacturing plants. The rapid cooling of this slag results in an amorphous structure. Granulated blast furnace slag is subsequently ground into a fine powder and used in
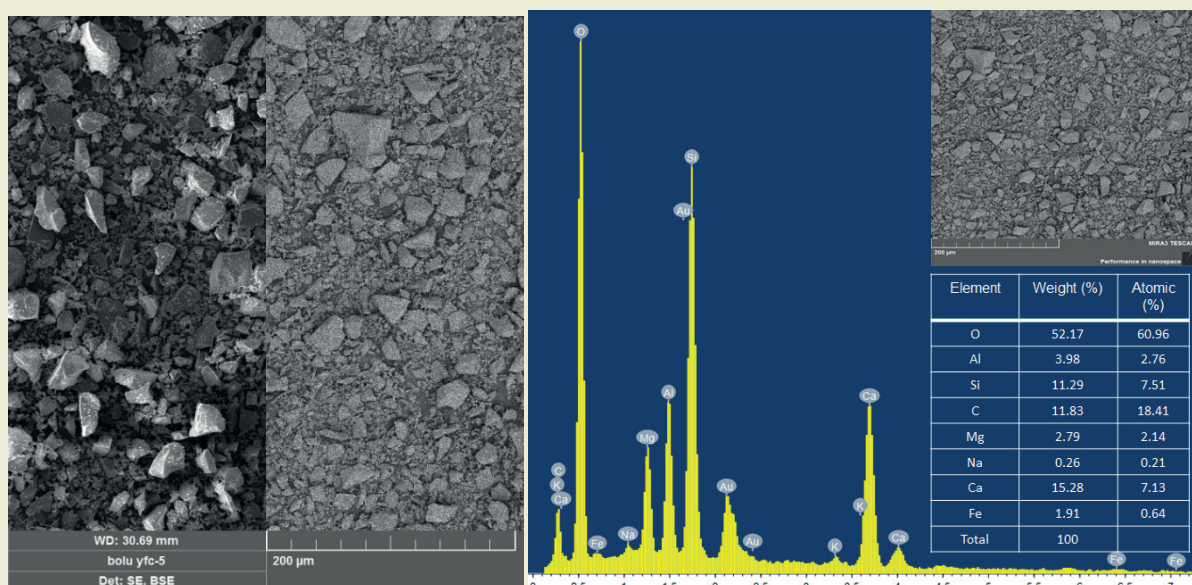

Element	Weight (%)	Atomic (%)
O	52.17	60.96
Al	3.98	2.76
Si	11.29	7.51
C	11.83	18.41
Mg	2.79	2.14
Na	0.26	0.21
Ca	15.28	7.13
Fe	1.91	0.64
Total	100	

Figure 1. SEM-EDX analysis of Bolu blast furnace slag

the formulation of concrete and mortar. For this study, the slag was procured from Bolu Cement Industry Inc. The silica + alumina + iron oxide ratio is 54.41% < 70%, which is below the minimum percentage requirement for pozzolanic activity [3]. ▶**Figure 1** presents SEM/EDX analysis of the blast furnace slag, which appears angular, finely structured, and glassy. This fine grain enhances its surface area, offering a potential advantage in terms of reactivity. The physical and chemical properties of the blast furnace slag are detailed in ▶**Table 1**.

Table 1. Physical and chemical properties of Bolu blast furnace slag

| Component	(%)
SiO_2	40.5
Al_2O_3	12.8
Fe_2O_3	1.11
CaO	35.5
MgO	5.81
K_2O	0.6
SO_3	0.22
TiO_2	0.71
Na_2O	0.7
Total	97.95
Specific Surface (cm^2/g)	5384
Moisture (%)	0.1

The Class C fly ash utilized in this experiment was obtained from the Sivas Kangal Thermal Power Plant. This material is classified as Class C (high calcareous) due to its composition, which contains over 50% SiO2, Al_2O_3, and Fe_2O_3 [14-16]. Additionally, because the CaO content exceeds 10%, these ashes are also referred to as high calcite fly ashes. Typical crystal phases present in Class C fly ashes include anhydrite ($CaSO_4$), tricalcium aluminate ($Ca_3Al_2O_6$), lime (CaO), quartz (SiO_2), periclase (MgO), mullite ($Al_6Si_2O_{13}$), merwinite ($Ca_3Mg(SiO_4)_2$), and ferrite ($(Mg, Fe)(Fe_3Al)_2O_4$). Scanning Electron Microscope (SEM) images of the fly ash reveal a structure that is spherical, glassy, and irregular. ▶**Table 2** summarizes the physical and chemical properties of the fly ash sourced from the Kangal Thermal Power Plant. ▶**Figure 2** presents SEM/EDX analysis of the fly ash.

Table 2. Physical and chemical properties of fly ash

Component	(%)
MgO	3.12
Al_2SO_3	14.2
SiO_2	35.01
SO_3	7.56
Na_2O	1.21
K_2O	1.06
CaO	25.75
Fe_2SO_3	5.42
Insoluble residue	24.21
Glow loss	6.02
Total	99.35
Physical composition	
Specific gravity (ton/m^3)	2.72
45 micron sieved balance (%)	44.3
Blain specific surface (cm^2/gr)	3320

Strontium used in the study contains 37.76% SrO as strontium ore in its structure, as waste material obtained from mining sites in the Sivas region. It contains sulestine, calcite, mica, and other minerals in its mineralological composition. The density of the stron-
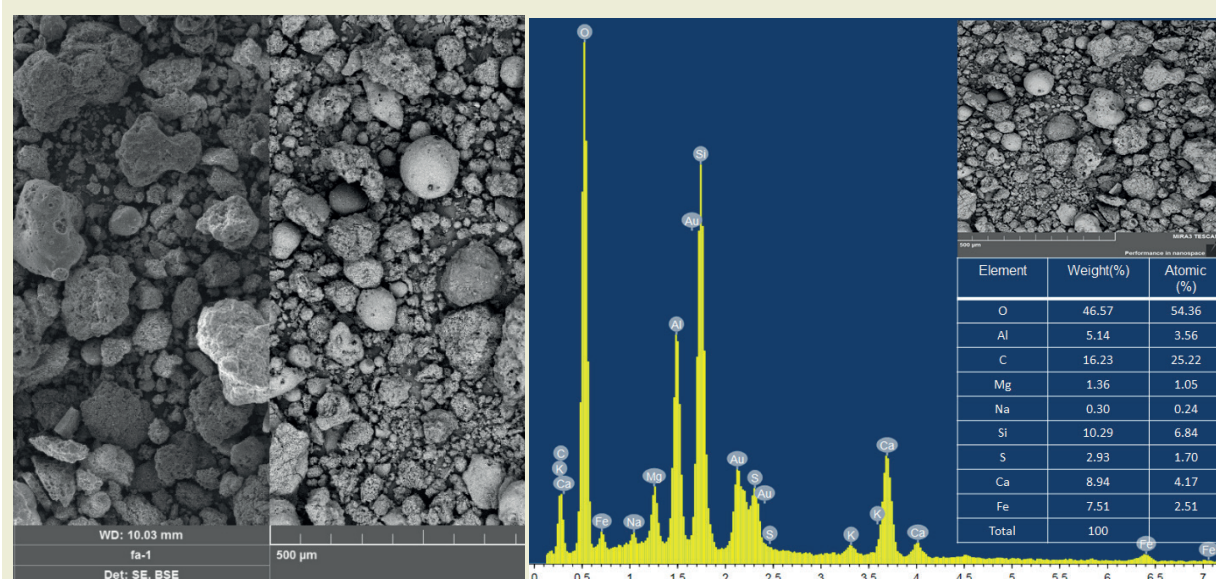
Figure 2. SEM-EDX analysis of fly ash

tium-containing mineral is 3.54 g/cm³. ▶**Figure 3** shows the photographs of the mineral taken before and after grinding. After drying and grinding, it was sieved with the help of sieve number 200, and made ready for use.
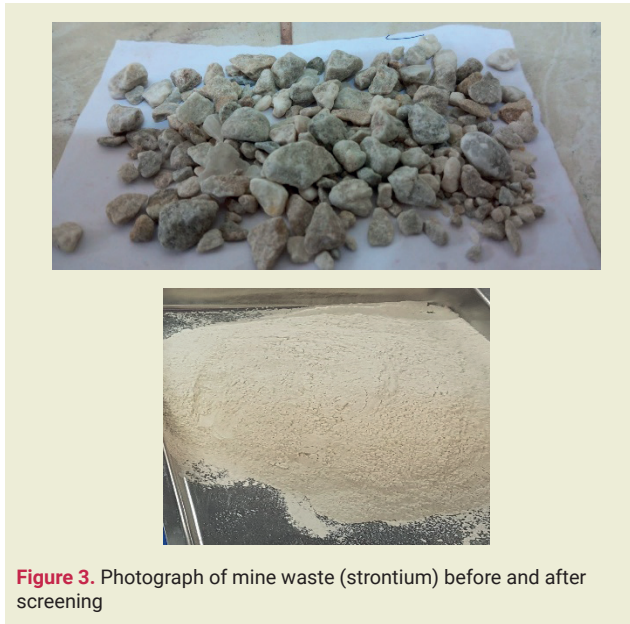

Figure 3. Photograph of mine waste (strontium) before and after screening

The physical and chemical properties of strontium are presented in ▶**Table 3**. ▶**Figure 4** shows a scanning electron microscope (SEM) image of a strontium mineral at 10.00X magnification. The analysis revealed a grain structure consisting of various sizes and different geometric shapes. Additionally, a semi-quantitative mineral analysis of this mineral was conducted using X-ray fluorescence spectrometry (XRF) at the Erciyes University Technological Research and Application Centre (TAUM), as shown in ▶**Table 3**.

The marble powder employed in the geopolymer composite for this study was sourced as industrial waste from the Özmersan marble plant in the Sivas region. After drying and grinding, the powder (▶**Figure 5**) was prepared for use by being sifted through a sieve with a mesh size of 200. The marble powder's SEM and EDX analyses, which were prepared for experiments after drying, are presented in ▶**Figure 6**. These analyses were conducted at the Advanced Technology Research and Application Centre (CÜTAM) of Sivas Cumhuriyet University. The results show that the marble powder has a semi-spherical shape and consists of particles of various sizes. Notably, the high CaO ratio in the marble powder's composition stands out during the physical and chemical property assessment. A summary of the physical and chemical properties of the marble powder is provided in ▶**Table 4**.

Table 3. XRF analysis of strontium

Components	%
SrO	37.76
SO$_3$	38.63
CaO	14.42
BaO	0.43
SiO$_2$	0.18
Al$_2$O$_3$	0.084
TiO$_2$	0.103
Fe$_2$O$_3$	0.091

Titanium dioxide nanoparticles possess specific surface areas ranging from 200 to 220 m²/g, with particle sizes below 25 nm and melting temperatures of approximately 1825 °C [17]. TiO$_2$ exhibits three distinct crystal structures: rutile, anatase, and brookite [18]. The titanium dioxide used in these experiments was sourced from the Mega Analitik firm. Scanning Electron Microscopy (SEM) images illustrating the properties of TiO$_2$ are provided in ▶**Figure 7**. These images reveal
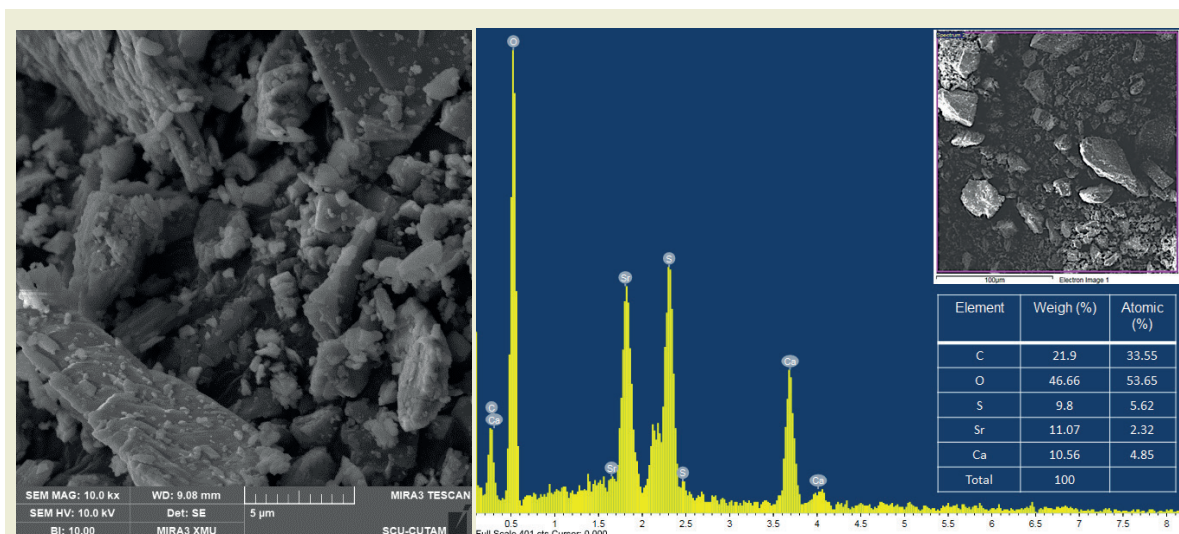

Figure 4. SEM-EDX analysis of mine waste /strontium

Figure 5. Photograph of sifted marble powder

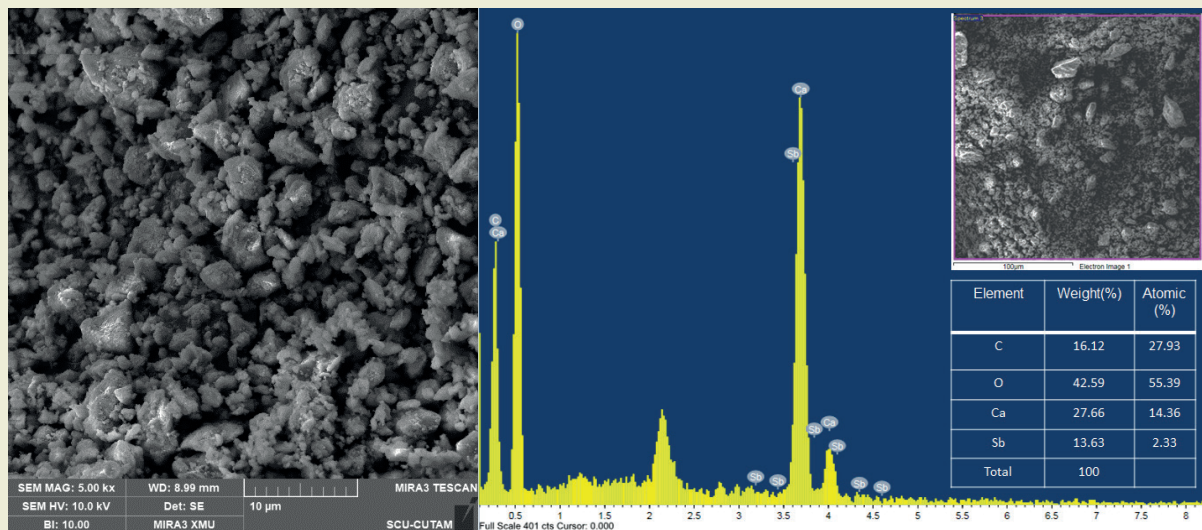that TiO_2 has a crystalline structure and predominantly spherical shapes.

Table 4. Physical and chemical properties of marble powder

| NOCHE - Travertine Components	%
Al_2O_3	0.22
CaO	54.51
FeO_3	0.11
MgO	0.41
SiO_2	0.87
Density (g/cm³)	2.69

3. Results and Discussions

The flexural and compressive strengths of the specimens at the end of the curing period are presented in ►**Figure 8** and ►**Figure 9**, respectively. This figure il-

Figure 6. SEM-EDX analysis of marble powder

Element	Weight(%)	Atomic (%)
C	16.12	27.93
O	42.59	55.39
Ca	27.66	14.36
Sb	13.63	2.33
Total	100	
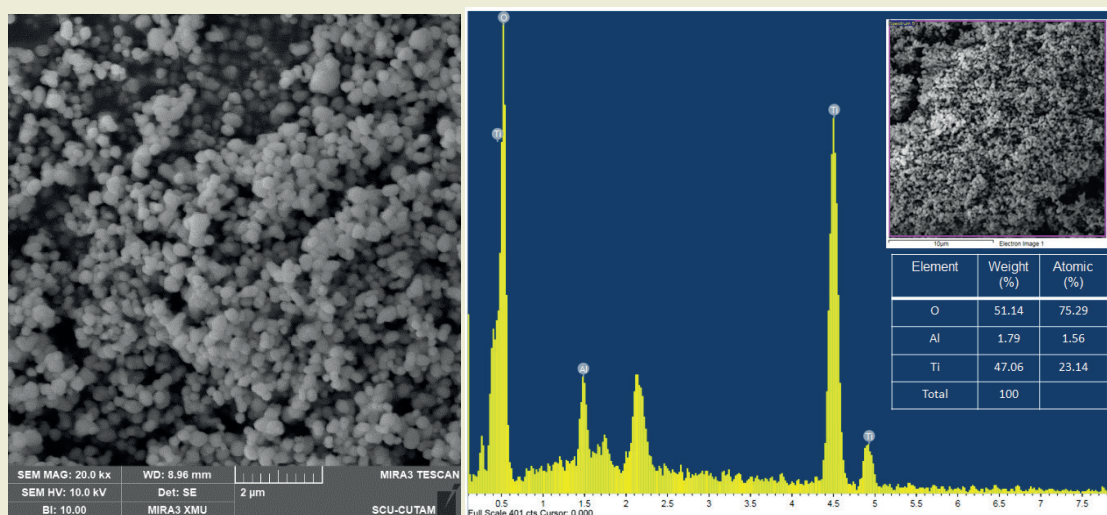
Figure 7. SEM-EDX analysis of titanium dioxide

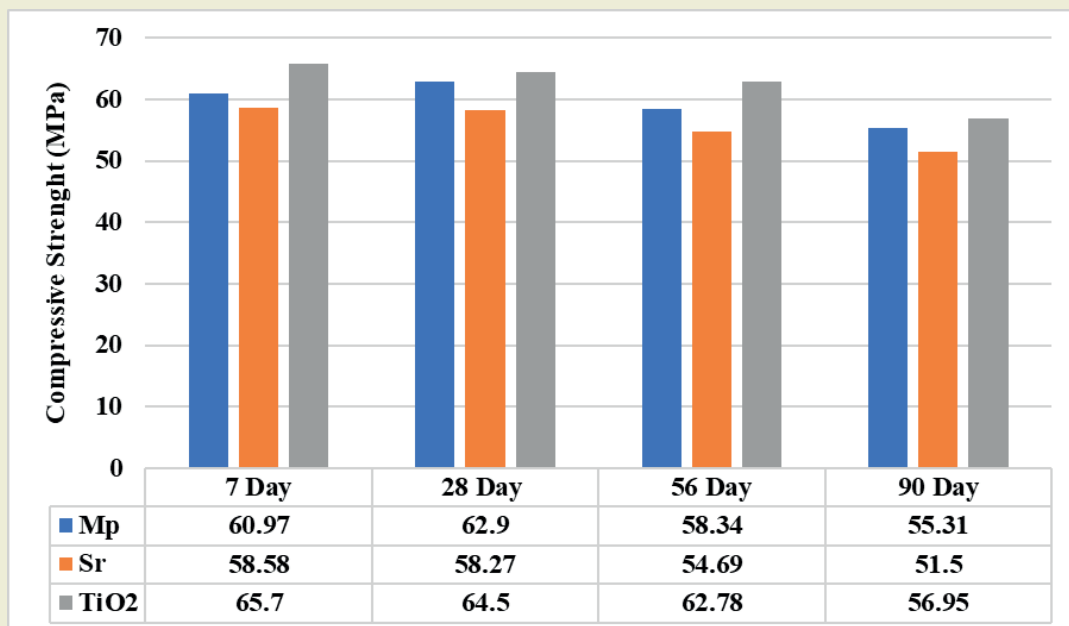| Element	Weight (%)	Atomic (%)
O	51.14	75.29
Al	1.79	1.56
Ti	47.06	23.14
Total	100	

lustrates the flexural strength results for samples cured for 7, 28, 56, and 90 days. It shows a time-dependent decrease in flexural strength. The highest flexural strength value, 10.81 MPa, was observed in the strontium-doped sample at the 7-day mark, while the lowest flexural strength, 7.66 MPa, was found in the titanium dioxide-doped sample at 90 days. Upon examining the compressive strengths, the highest value recorded was 65.7 MPa for titanium dioxide in the 7-day samples. Conversely, the lowest compressive strength, measured at 51.5 MPa, was observed for strontium in the 90-day samples. Overall, it is evident that titanium dioxide exhibits the highest compressive strength among the various additives tested. This indicates that the use of

a low concentration of 1% titanium dioxide positively influences compressive strength [19].

The SEM/EDX images of the mortars, produced by substituting 5% marble dust for blast furnace slag and fly ash as the primary binder, are presented in ▶Figure 10 for both the 7-day and 90-day samples. Analysis of the SEM/EDX images for the 7-day samples indicated a Si/Al ratio of 4.02 . In comparison, the 90-day samples revealed a Si/Al ratio of 3.92. This reduction in the Si/Al was consistent with a decline in compressive strength. When the compressive strengths of 7 and 90-day samples are examined, it is thought that the decrease in compressive strength seen in 90-day samples

	7 Day	28 Day	56 Day	90 Day
■ Mp	10.77	10.57	9.85	9.28
■ Sr	10.81	10.53	9.84	7.93
■ TiO2	10.55	10.28	9.23	7.66
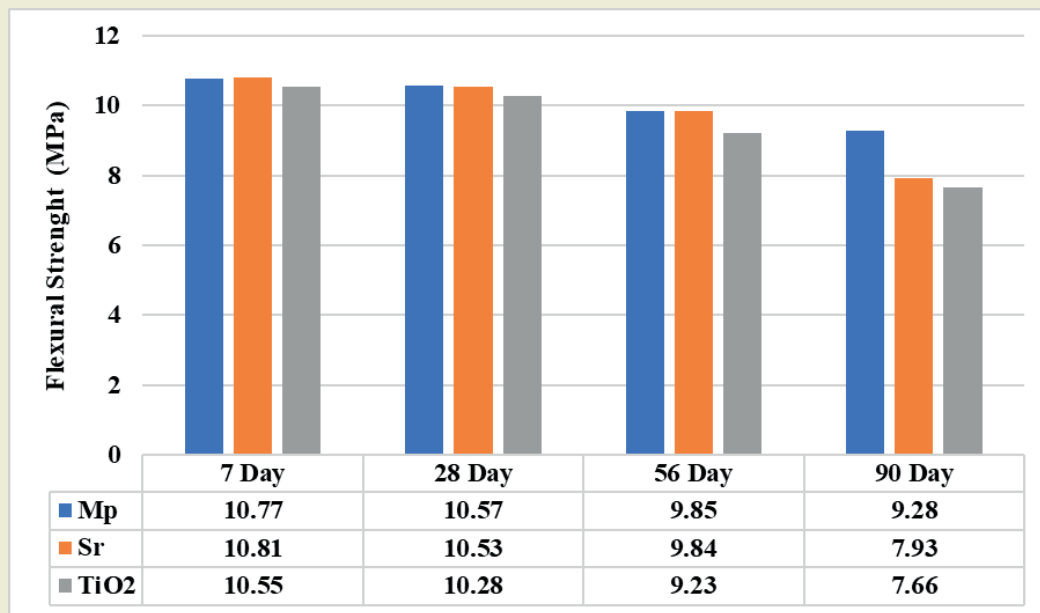
Figure 8. Flexural strengths of marble powder, strontium, and titanium dioxide

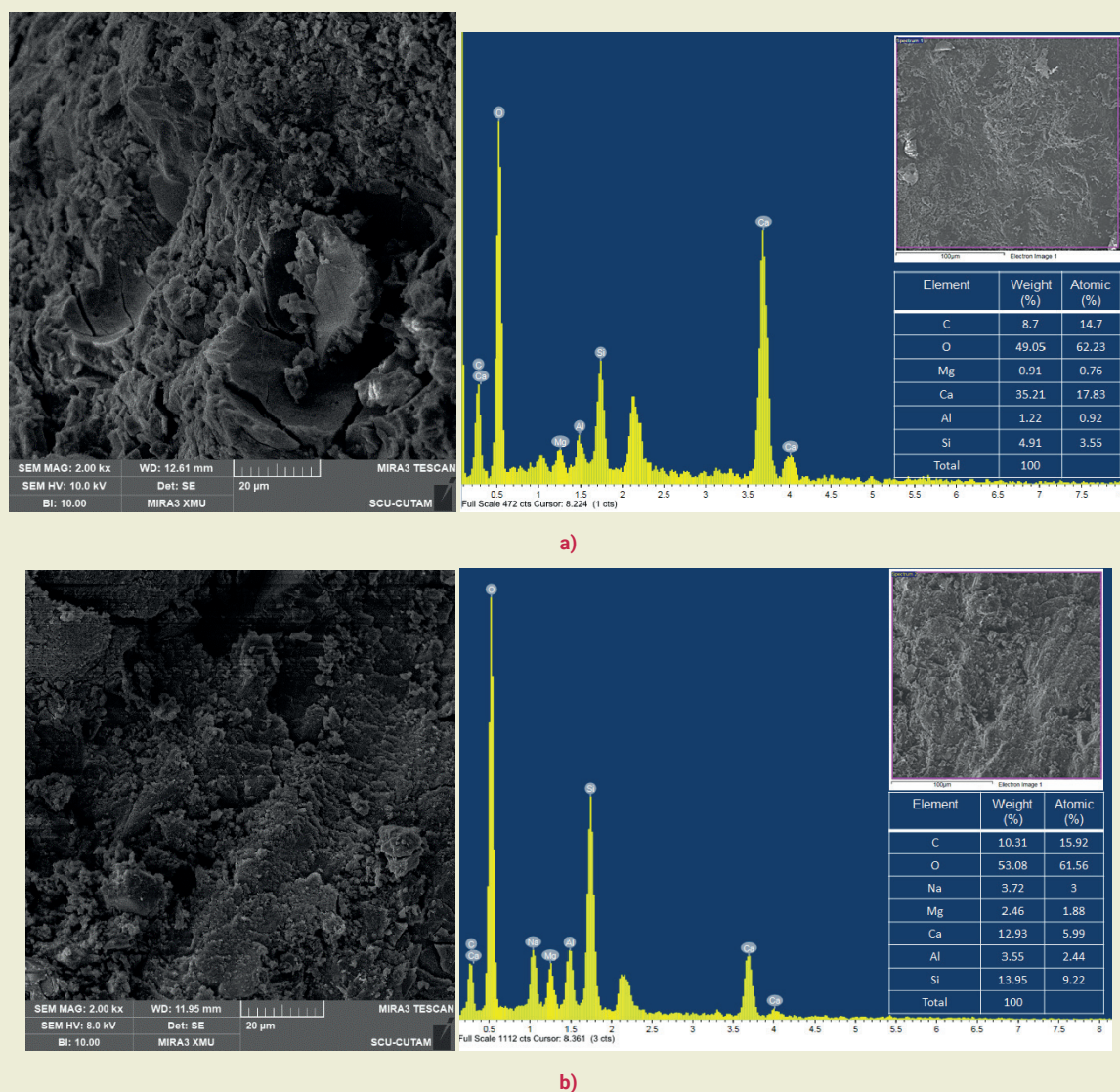|	7 Day	28 Day	56 Day	90 Day
■ Mp	60.97	62.9	58.34	55.31
■ Sr	58.58	58.27	54.69	51.5
■ TiO2	65.7	64.5	62.78	56.95

Figure 9. Compressive strengths of marble powder, strontium, and titanium dioxide

may be due to the decrease in Si/Al ratio. In addition, when SEM images were examined, it was determined that a more homogeneous structure was formed in the 7-day sample images, but unreacted particles were formed in the 90-day sample images. When 7 and 90-day compressive strengths are compared, it is thought that the decrease in compressive strength in 90-day samples may be due to the decrease in Si/Al ratio. In addition, when SEM images are examined, it is predicted that a homogeneous structure is formed in 7-day images and unreacted particles are formed in 90-day images, which may be effective on strength. It has been stated that the relatively high compressive strength of binders with high slag content is due to the density of C-A-S-H gel phases and microstructure [20-21]. On 90-day specimens, waste materials enhance microstructure densification and contribute to early strength, but may reduce strength later. [22]. It could be said that the marble powder additive is effective on the strength with its void reducing effect and Ca content. Thanks to the CaO content of marble powder, the effect of gelation on microstructural analyses is observed [23].

▶**Figure 11** shows SEM and EDX images of geopolymer mortars that include a 5% substitution of strontium in a mixture of blast furnace slag and fly ash. In the Energy Dispersive X-ray (EDX) analysis of 7-day geopolymer mortars, the silicon to aluminum (Si/Al) ratio was found to be 3.16. In contrast, the EDX analysis of 90-day geopolymer mortar samples revealed a Si/Al ratio of 5.75 on the surface. Upon examining the Scanning Electron Microscopy (SEM) images, a denser Calcium-Silicate-Aluminate-Hydrate (C-S-A-H) gel formation was observed in the 7-day geopolymer mortars with 5% strontium doping, despite the presence of micro-cracks. Similar gels were noted in the 90-day geopolymer mortars with 5% strontium doping, but it was also observed that micro-cracks appeared, particularly between the layers, along with the presence of unreacted particles.

a)

Element	Weight (%)	Atomic (%)
C	8.7	14.7
O	49.05	62.23
Mg	0.91	0.76
Ca	35.21	17.83
Al	1.22	0.92
Si	4.91	3.55
Total	100	

b)

Element	Weight (%)	Atomic (%)
C	10.31	15.92
O	53.08	61.56
Na	3.72	3
Mg	2.46	1.88
Ca	12.93	5.99
Al	3.55	2.44
Si	13.95	9.22
Total	100	

Figure 10. SEM (left) /EDX (right) images of 7 days (a) and 90 days (b) old marble powder-doped geopolymer mortar

The SEM/EDX images of geopolymer mortars with 1% titanium dioxide substitution are presented in ▶Figure 12. The Si/Al ratio was found to be 4.76 in the samples taken after 7 days, and 15.92 in those taken after 90 days. Examination of the SEM images revealed that the 7-day geopolymer mortar samples exhibited a more homogeneous internal structure compared to the 90-day samples, leading to a better bond among the components of the matrix.

4. Conclusions

In the geopolymer mortars designated as 85BFS15FA, the composition included 5% marble powder, 5% strontium, and 1% titanium dioxide. The samples were cured in an oven for 24 hours with a 10M NaOH solution at a temperature of 75°C. The findings revealed a reduction in both flexural and compressive strengths as curing time increased. Remarkably, titanium dioxide demonstrated the highest compressive strength at early ages

(specifically at 7 days). Scanning Electron Microscopy (SEM) analyses indicated that the geopolymer mortars with titanium dioxide developed gel structures, which are thought to enhance compressive strength. This effect is likely attributed to the high proportion (85%) of blast furnace slag combined with the low proportion (1%) of titanium dioxide. It was observed that TiO_2 additive, which was effective on compressive strengths, decreased flexural strengths. Especially for all additives, while the flexural strengths of the 7 and 28 day cured specimens were similar, time-dependent decreases in these values were observed.

The results of this study show that it can contribute to the recycling of local and regional wastes and sustainability issues. In addition, by presenting 3 different additives comparatively, the mechanical and microstructural differences were compared. The fact that a high strength result was obtained at early age with TiO_2 admixture at a low rate of 1% in the study showed that it can be used for low performance admixed geopolymer
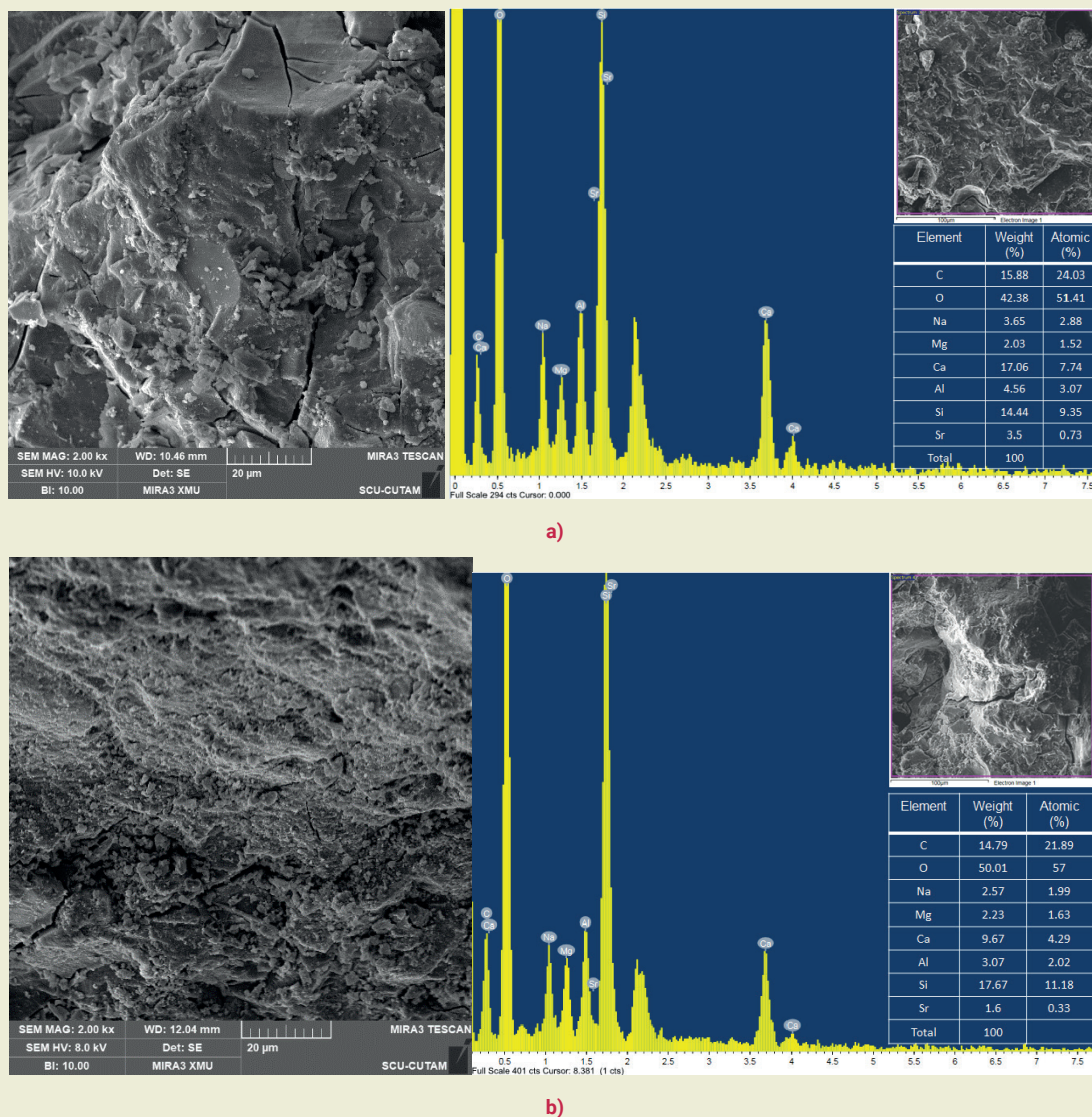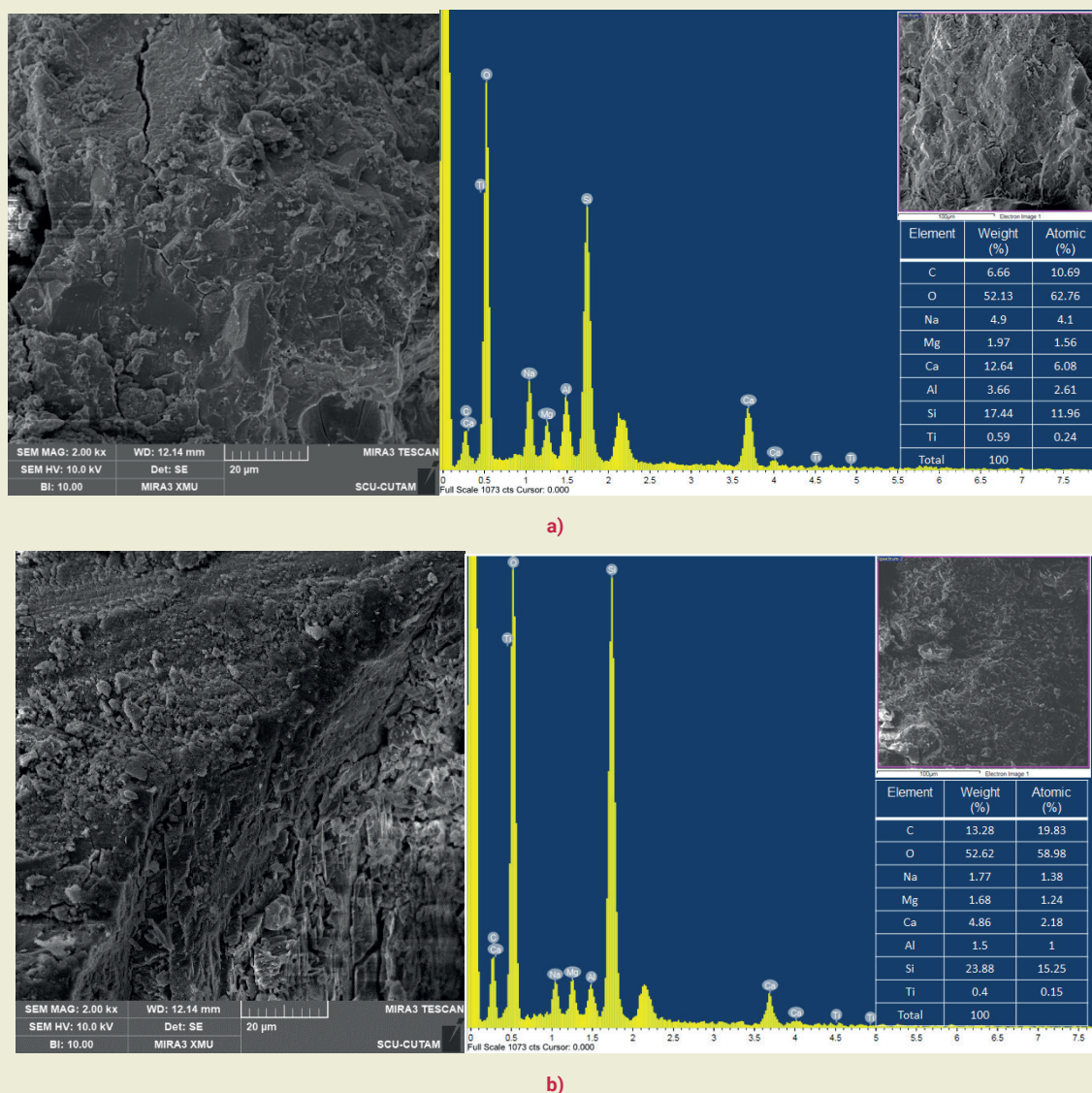

Figure 11. SEM (left)/EDX (right) images of 7 days (a) and 90 days (b) strontium-doped geopolymer mortar

Figure 12. SEM (left)/EDX (right) images of 7 days (a) and 90 days (b) TiO2 doped geopolymer mortar

concrete and mortars.

Research ethics

Not applicable.

Author contributions

Conceptualization: [Hülya Temizer,Özlem Çavdar], Methodology: [Hülya Temizer,Özlem Çavdar], Formal Analysis: [Author names], Investigation: [Hülya Temizer,Özlem Çavdar], Resources: [Hülya Temizer], Data Curation: [Hülya Temizer], Writing - Original Draft Preparation: [Hülya Temizer,Özlem Çavdar], Writing - Review & Editing: [Özlem Çavdar], Visualization: [Hülya Temizer,Özlem Çavdar], Supervision: [Özlem Çavdar], Project Administration: [Özlem Çavdar], Funding Acquisition: [Hülya Temizer,Özlem Çavdar]

Competing interests

The authors state no conflict of interest.

Data availability

The raw data can be obtained on request from the authors.

Peer-review

Externally peer-reviewed.

Orcid

Hülya Temizer https://orcid.org/0009-0001-4618-6336
Özlem Çavdar https://orcid.org/0000-0002-5459-0769

References

[1] Adak, D., Sarkar, M., & Mandal, S. (2014). Effect of nano-silica on strength and durability of fly ash based geopolymer mortar. Construction and Building Materials, 70, 453–459. https://doi.org/10.1016/j.conbuildmat.2014.07.093

[2] Çavdar, A., & Yetgin, Ş. (2009). The effect of particle fineness on properties of Portland pozzolan cement mortars. Turkish Journal of Science & Technology, 4(1).

[3] Çavdar, Ö., & Temizer, H. (2025). The regression analysis and determination of mechanical and physical properties on geopolymer composites under thermal and water curing. Thermal Science. https://doi.org/10.2298/TSCI250216091C

[4] Naskar, S., & Chakraborty, A. K. (2016). Effect of nano materials in geopolymer concrete. Perspectives in Science, 8, 273–275. https://doi.org/10.1016/j.pisc.2016.04.049

[5] Nergis, D. D. B., Vizureanu, P., Sandu, A. V., Nergis, D. P. B., & Bejinariu, C. (2022). XRD and TG-DTA study of new phosphate-based geopolymers with coal ash or metakaolin as aluminosilicate source and mine tailings addition. Materials, 15, 202. https://doi.org/10.3390/ma15010202

[6] Chithambaram, S. J., Kumar, S., & Prasad, M. M. (2019). Thermo-mechanical characteristics of geopolymer mortar. Construction and Building Materials, 213, 100–108. https://doi.org/10.1016/j.conbuildmat.2019.04.051

[7] Huseien, G. F., Sam, A. R. M. S., & Alyousef, R. (2021). Texture, morphology and strength performance of self-compacting alkali-activated concrete: Role of fly ash as GBFS replacement. Construction and Building Materials, 270, 121368. https://doi.org/10.1016/j.conbuildmat.2020.121368

[8] Shang, J., Dai, J. G., Zhao, T. J., Guo, S. Y., Zhang, P., & Mu, B. (2018). Alternation of traditional cement mortars using fly ash-based geopolymer mortars modified by slag. Journal of Cleaner Production, 203, 746–756. https://doi.org/10.1016/j.jclepro.2018.08.255

[9] Hager, I., Sitarz, M., & Mróz, K. (2021). Fly-ash based geopolymer mortar for high-temperature application: Effect of slag addition. Journal of Cleaner Production, 316, 128168. https://doi.org/10.1016/j.jclepro.2021.128168

[10] Başpınar, S., & Kurtuluş, C. (2018). Effect of composition on geopolymer foam concrete basic properties. AKÜ IJETAS, 1, 5–10.

[11] Raj, P. K. A., Sarath, D., Nagarajan, P., & Thomas, B. S. (2024). A simplified mix design for GGBS–dolomite geopolymer concrete using the Taguchi method. Iranian Journal of Science and Technology, Transactions of Civil Engineering, 48, 3189–3212. https://doi.org/10.1007/s40996-024-01354-4

[12] Yıldız, S. (2023). Investigation of mechanical and durability properties of geopolymer concretes produced with industrial by-products [PhD thesis, Kocaeli University].

[13] Chokkalingam, P., El-Hassan, H., El-Dieb, A., & El-Mir, A. (2022). Development and characterization of ceramic waste powder-slag blended geopolymer concrete designed using Taguchi method. Construction and Building Materials, 349, 128744. https://doi.org/10.1016/j.conbuildmat.2022.128744

[14] Yüksek, S., & Kaya, S. (2017). Building material production from fly ash, lime and gypsum. APJES, 5(3), 58–70.

[15] Çavdar, A., & Yetgin, Ş. (2005). The effects of trass addition ratio on strength, setting time, and soundness properties of trass–cement. Science and Engineering Journal of Fırat University, 17(4), 687–692.

[16] Çavdar, A., & Çavdar, Ö. (2024). Availability of sedimentary and volcanic rock deposits on Northeastern Turkey as concrete aggregates. Physics and Chemistry of the Earth, 134. https://doi.org/10.1016/j.pce.2024.103567

[17] Erem, A. D., & Özcan, G. (2015). Polypropylene/titanium dioxide nanocomposite fiber production and characterization. Journal of Textiles and Engineer, 22(99), 1–6. https://doi.org/10.7216/130075992015229901

[18] Mengeloğlu, F., & Çavuş, V. (2019). Effect of titanium dioxide (nm and µm TiO$_2$) on some mechanical properties of wood plastic composites. In MAS International European Conference on Mathematics-Engineering-Natural & Medical Sciences-X (pp. 1–6). İzmir, Türkiye

[19] Naskar, S ve Chakraborty, A. K. (2016). Effect Of Nano Materials in Geopolymer Concrete. Perspectives in Science, 8, 273-275. DOI:10.1016/j.pisc.2016.04.049..

[20] Mohammed, D. T., & Yaltay, N. (2024). Strength and elevated temperature resistance properties of the geopolymer paste produced with ground granulated blast furnace slag and pumice powder. Ain Shams Engineering Journal, 15(3), 102483. https://doi.org/10.1016/j.asej.2023.102483

[21] Temizer, H., & Çavdar, Ö. (2024). Effects on geopolymer mortars of the blast-furnace slags obtained from different regions. In 3rd International Conference on Contemporary Academic Research, November 10–11, Konya, Turkey.

[22] Yousuf, M., & Khan, R. A. (2021). Mechanical and microstructural characteristics of sustainable geopolymer concrete using industrial by-products. Journal of Cleaner Production, 282, 124517. https://doi.org/10.1016/j.jclepro.2020.124517

[23] Ali, M. A., & Ahmed, S. F. (2022). Utilization of marble waste in geopolymer concrete for sustainable construction. Construction and Building Materials, 320, 126212. https://doi.org/10.1016/j.conbuildmat.2021.126212